

RICE UNIVERSITY

Pairing of Fermionic ${}^6\text{Li}$ Throughout the BEC-BCS
Crossover

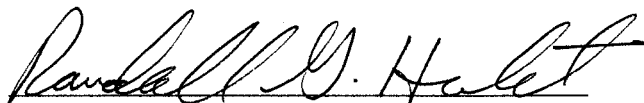
by

Guthrie Bran Partridge

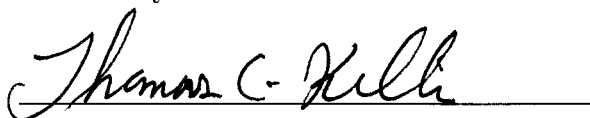
A THESIS SUBMITTED
IN PARTIAL FULFILLMENT OF THE
REQUIREMENTS FOR THE DEGREE

Doctor of Philosophy

APPROVED, THESIS COMMITTEE:



Randall G. Hulet, Chairman
Fayez Sarofim Professor of Physics and
Astronomy



Thomas C. Killian
Associate Professor of Physics and
Astronomy



Daniel Mittleman
Associate Professor of Electrical and
Computer Engineering

Houston, Texas

February, 2007

UMI Number: 3257341

INFORMATION TO USERS

The quality of this reproduction is dependent upon the quality of the copy submitted. Broken or indistinct print, colored or poor quality illustrations and photographs, print bleed-through, substandard margins, and improper alignment can adversely affect reproduction.

In the unlikely event that the author did not send a complete manuscript and there are missing pages, these will be noted. Also, if unauthorized copyright material had to be removed, a note will indicate the deletion.

UMI[®]

UMI Microform 3257341

Copyright 2007 by ProQuest Information and Learning Company.

All rights reserved. This microform edition is protected against unauthorized copying under Title 17, United States Code.

ProQuest Information and Learning Company
300 North Zeeb Road
P.O. Box 1346
Ann Arbor, MI 48106-1346

ABSTRACT

Pairing of Fermionic ${}^6\text{Li}$ Throughout the BEC-BCS Crossover

by

Guthrie Bran Partridge

The pairing of fermionic particles is an essential ingredient of superconductivity and of the superfluidity of ${}^3\text{He}$. While such phenomena are accurately described by BCS theory in the limit of weak pairing strength, a complete understanding remains elusive when pairing strength is increased, such as in high temperature superconductors. We create ultracold gases of trapped fermionic ${}^6\text{Li}$ atoms, through which we directly observe fermionic pairing. In our system, there are no impurities whatsoever, and parameters such as the number and temperature of the trapped atoms are precisely and independently controlled. In addition, a Feshbach resonance enables the continuous tuning of interaction strength and sign between the paired atoms. This control allows us to observe the smooth crossover of a molecular Bose Einstein condensate (MBEC) to a superfluid of weakly interacting Cooper pairs. With these tools, we have performed several fundamental measurements of pairing in fermionic systems.

We use optical molecular spectroscopy to precisely measure the closed-channel contribution to the many body state of paired ${}^6\text{Li}$ atoms within a broad Feshbach resonance. The magnitude of this contribution is small, and supports the concept of universality for the description of broad Feshbach resonances. Moreover, the dynamics of the excitation provide clear evidence for pairing across the BEC-BCS crossover,

and for the first time, into the weakly interacting BCS regime.

We also prepare a polarized Fermi gas with unequal numbers of two spin states of ^6Li atoms. The real-space densities of the polarized, strongly-interacting, two-component Fermi gas reveal two low temperature regimes. At the lowest temperatures, the gas separates into a phase with a uniformly paired superfluid core surrounded by a shell of normal, unpaired atoms. This phase separation is accompanied by a spatial deformation of the core. At higher temperatures, the uniformly paired core persists, though it does not deform. This temperature dependence is consistent with a tri-critical point in the phase diagram. These measurements of pairing in a polarized Fermi gas are relevant to predictions of exotic phases of quark matter and magnetized superconductors.

Acknowledgments

The work presented in this thesis represents the culmination of many different aspects of my life over the last several years. Since the bulk of the writing is devoted to the more technical side of this experience, I will take this opportunity to acknowledge both the personal and professional contributions and support that I have received from others along the way. Without such support, none of this would have been possible.

I must first thank Randy for providing guidance and knowledge. I am grateful for the opportunity to have worked in this exciting field with someone who has played such an important role throughout the course of its development. By establishing the lab where all of this work was done, he has made all of the following possible. In addition to being my advisor, Randy has been a friend who has been equally willing to discuss the pairing of fermions, or the Astros, over lunch.

I must also thank the many other people I have worked with throughout my time here. In addition to their many contributions to the actual apparatus and experiments, these people have provided friendship. This has been imperative, since I have always believed that a crucial ingredient to being able to put in all the long hours in the lab is that I am always among friends. I was first shown the ropes on my future experiment by Kevin and Andrew. Throughout our struggles to make the experiment work, these people demonstrated how to persevere through the “occasional” seemingly hopeless situation. Next came along Ramsey, who helped me to sort out the experiment upon Kevin’s departure. His attention to detail in the lab, as well as his knack for doing funny voices during late night data runs, was invaluable to this work. During the same period, I also benefitted from working with Michael. Though he didn’t set foot in the lab, he provided a very well timed theoretical grounding for our work, and thereby helped to keep us anchored to reality. Currently working on

the experiment are Yean-an and Wenhui. Along with their contributions to recent results, their willingness to learn the apparatus in a relatively brief period of time is appreciated. Outside of these people, whom I have worked with directly, there are many others. Some preceded me, such as Ian, who began the work on the apparatus I have used. Others, including Jordan, Ionut, Marin, Mark, Dan, Chris, James and Yong, work(ed) on the other side of the room, on the other apparatus.

Moving outside of the lab, I must first thank my wife, Amy. I am grateful for her forgiveness for all the times I ended up staying at work a bit longer than I said I would.* She has always provided understanding and support, all the while helping me to keep perspective as to what is really important. I might add that she has been very patient, and hardly ever reminds me how long I've been in school. I am also grateful for the continued support of my parents, who helped me get started on this whole endeavor by encouraging me to ask questions and wonder how things work. They have also instilled in me, at least in theory, the importance of balancing work with other aspects of life. I am also fortunate to have had a solid foundation provided by the rest of my family, including Grandma Vicki, Syd, Amelia, Chuck, Roxanne and all the rest.

Last, but not least, I thank all of my other friends who have helped me to maintain some semblance of balance in my life. These include my friends from the University of Arizona Drumline, who keep in touch with me despite my apparent inability to reply to an email in less than a month, as well as the friends I have made in Houston and at Rice through the sport of Ultimate, or over a drink at Valhalla. Finally, no acknowledgement section from this lab would be complete without thanking Jen and Purvez Captain for "paying forward" their friendship and generosity.

*For brevity, I include only this representative example...

Contents

Abstract	ii
Acknowledgments	iv
List of Figures	ix
List of Tables	xiii
1 Introduction	1
1.1 BEC and BCS	5
1.1.1 Role of Interactions	5
1.2 Experiments	8
1.2.1 Prior Experiments	9
1.3 Outline	11
1.3.1 The Purpose of This Work	13
2 The Apparatus	14
2.1 Overview	14
2.1.1 Dual MOT and Magnetic Trap	15
2.2 Optical Trap(s)	20
2.2.1 A Brief History of Our Optical Traps	25
2.2.2 Current Optical Trap	27
2.3 High Field	47
2.3.1 Spin Mixture	50
2.3.2 Optical Trap Evaporation Trajectories	53
3 Molecular Probe of Pairing	61
3.1 Molecules, Pairs and a Feshbach Resonance	61
3.1.1 ^6Li Feshbach Resonances	63
3.2 The Experiment	68

3.2.1	The Setup	68
3.2.2	Starting Point: Molecular Bose-Einstein Condensate	76
3.2.3	Measuring the Bare Molecular Fraction: Picking out the Pairs	81
3.2.4	Molecular Loss Rate, BEC Side	83
3.2.5	Molecular Loss Rate, BCS Side	86
3.2.6	Paired Fraction: Molecules and Beyond	88
3.3	Conclusions	92
4	Polarized Fermi Gases	94
4.1	Polarized Fermionic Systems	94
4.2	Experiments	97
4.2.1	Experimental Process	98
4.2.2	Uneven Spin Mixture	99
4.2.3	Rapid Dual Probing	103
4.3	Results	109
4.3.1	Universal Many Body Parameter, β , in an Unpolarized Gas at Unitarity	109
4.3.2	Phase Separation	115
4.3.3	Uniform Central Pairing	118
4.3.4	Deformations and Aspect Ratio	121
4.3.5	Mechanisms for Deformation	126
4.4	Critical Polarization	140
4.5	Temperature Dependence	144
4.5.1	Temperature determination	146
4.5.2	Temperature Results	149
4.6	Raise the Temperature	150
4.7	The Big(ger) Picture	154
4.7.1	Phase Diagrams	155

5	Conclusions	159
5.0.2	Outlook	160
A	Estimation of Uncertainty in Measurement of β	162
A.0.3	Measured Radius, R_z	162
A.0.4	Calculated Radius, R_{TF}	162
B	Temperature Determination of Strongly interacting Fermi Gas	166
B.1	Example Fits	170
C	Tunable Standing wave EOM	174
D	Experimental Benchmarks	178
	References	183

List of Figures

1.1	Bosons and Fermions in a Trap at $T = 0$	2
1.2	Fermi Pressure Images	4
1.3	Chemical Potential vs. Coupling Strength	7
1.4	BCS to BEC	8
1.5	Feshbach Demonstration: Bright Solitons	10
1.6	Molecules of ^6Li Formed by Field Sweep	11
2.1	Picture of Apparatus	15
2.2	MOT Laser Beam Diagram	16
2.3	Trapping and Repumping Transitions of ^6Li and ^7Li	17
2.4	Hyperfine Levels of ^6Li and ^7Li	18
2.5	Ioffe Pritchard type Magnetic Trap	19
2.6	Dressed States for Positive and Negative Detuning	22
2.7	Dipole Force vs. Detuning	23
2.8	Optically Trapped Atoms	25
2.9	Crystal Laser Optical Trap Layout	28
2.10	IPG Laser Optical Trap Layout	30
2.11	Distorted Optical Trap Beam	31
2.12	Distorted Optical Trap Beam at Focus	32
2.13	Nice Focus	33
2.14	Fitted Beam Waist	34
2.15	$\omega(z)$ vs. z , M^2	36
2.16	Measurement of Optical Trap Radial Frequency	39
2.17	Radial Frequency vs. Trap depth	41
2.18	Measurement of Optical Trap Axial Frequency	43

2.19 Contributions to Axial Potential	44
2.20 Magnetic Contribution to Axial Frequency Measurement	45
2.21 Optical Trap Loading vs. Power	48
2.22 Rabi Oscillations	51
2.23 Lifetimes of Coherent and Incoherent Spin Mixtures in Optical Trap .	52
2.24 Creation of a Spin Mixture via Multiple RF Sweeps	54
2.25 Optical Trap Power Control Diagram	55
2.26 Optical Trap Control Response Function	57
2.27 Control Voltage for a Linear Evaporation Trajectory	58
2.28 Control Voltage for an Exponential Evaporation Trajectory	59
2.29 Fitted Temperature vs. Trap depth	60
3.1 Crossing Potentials Lead to a Feshbach Resonance	62
3.2 Scattering Length of ${}^6\text{Li}$ $F = 1/2, m_F = \pm 1/2$ vs Magnetic Field . . .	64
3.3 Origin of ${}^6\text{Li}$ Feshbach Resonances	66
3.4 Zoom in on the Crossover	67
3.5 Bound-Bound Molecular Transition Frequency	69
3.6 Bound-Bound Photo-association Optical Setup	73
3.7 Atom and Molecular Probe Combining Optics	74
3.8 Bound-Bound Molecular Resonance	77
3.9 Field Dependent Transition Frequency	78
3.10 Cooling by Magnetic Field Sweep	80
3.11 Molecular BEC and Bimodal Profiles	82
3.12 Measurement Scheme of the Bare Molecular Fraction, Z	84
3.13 Depletion of Trap from Molecular Probe: BEC	85
3.14 Depletion of Trap from Molecular Probe: BCS	87
3.15 Closed Channel Amplitude, Z , vs. Magnetic Field	89
3.16 Loss Rate vs $(k_F a)^{-1}$: Order Parameter	91

4.1	Balanced and Unbalanced Fermion Systems	95
4.2	Pairing Phases in Imbalanced Fermion Systems	96
4.3	Transfers to State $ 3\rangle$	101
4.4	Creating a Polarized Gas by Transfers to a Third State	102
4.5	Optical System for Rapid Dual Probing	105
4.6	Dual Probe Timing Sequence	106
4.7	Dual Probing Resonances	107
4.8	Probe Induced Heating from Pair Breaking	108
4.9	Probe Induced Heating from Pair Breaking	109
4.10	Fermi Energy and Radius Reduced by Unitary Interactions	113
4.11	Thomas-Fermi Distributions: Fit and Theoretical	114
4.12	Measured Thomas-Fermi Radius at Unitarity	115
4.13	Phase Separated Fermi Gas at Unitarity	116
4.14	Integration of Density by Absorption Probe Beam	118
4.15	Deconvolved True Density Distribution	119
4.16	Ratio of Central Densities vs. Polarization	120
4.17	Thomas-Fermi Fit and Edge Finder in Axial Direction	123
4.18	Aspect Ratio of Deformed Gas vs. P	124
4.19	Integrated Axial Density Distributions: Measured	125
4.20	Integrated Axial Density Distributions: Calculated (LDA)	127
4.21	Integrated Axial Density, Real Potential: Calculated (LDA)	130
4.22	Integrated Radial Density, Real Potential: Calculated (LDA)	131
4.23	Integrated Axial Density, Real Potential (Filled): Calculated (LDA)	132
4.24	Integrated Radial Density, Full Potential (Filled): Calculated (LDA)	133
4.25	Integrated Axial Density, $M^2 = 5$: Calculated (LDA)	135
4.26	Integrated Radial Density, $M^2 = 5$: Calculated (LDA)	136
4.27	Predicted Effects of Surface Tension on Axial Difference Profile	138

4.28 Non-elliptical Deformation of Minority Distribution	139
4.29 Non-elliptical Core Surfaces	140
4.30 Axial Density Fits using Non-elliptical Core Surfaces	141
4.31 Predicted Deformation for Different Experimental Configurations . .	142
4.32 Critical Polarization for Phase Separation and Deformation: Profiles .	143
4.33 Ratio of Measured to Calculated Axial Radii vs P	145
4.34 Demonstration of Fermi Pressure	147
4.35 Deformations and Temperature	151
4.36 Aspect Ratio at $\tilde{T} \sim 0.2$	152
4.37 Ratio of Central Densities vs. Polarization: Increased Temperature .	153
4.38 Non-Zero Phase Diagram of Polarized Fermi Gas Showing Data . . .	156
 B.1 Fitted Temperature Calibration	 169
B.2 Fit Data: Cold	170
B.3 Finite T and $T = 0$ Column Density Profiles: Cold	171
B.4 Fit Data: Not as Cold	172
B.5 Finite T and $T = 0$ Column Density Profiles: Not as Cold	173
 C.1 Tunable EOM Drawing	 175
C.2 Tunable EOM Frequency Range	177

List of Tables

D.1	Experimental Benchmarks	179
D.2	Diode Lasers	181

Chapter 1

Introduction

The research we conduct in our lab involves confining and cooling collections of atoms of lithium to very low temperatures, usually measured in the 10-100's of nano-kelvin (1 nano-kelvin = $1/1,000,000,000$ of a degree above absolute zero). At these low temperatures, the atoms stop following the ordinary rules that we are all familiar with from our everyday lives (unless your everyday life is in the lab). Instead, their behavior is governed by the less familiar rules of quantum mechanics. At these low temperatures, the atoms cease behaving like discrete particles, and instead can be more accurately describes as waves. As the gas is cooled, these waves spread out until at sufficiently low temperatures, the characteristic size of the atom, known as the thermal de Broglie wavelength, Λ_T , becomes comparable to the spacing between the atoms,

$$\Lambda_T = \left(\frac{2\pi\hbar^2}{mk_B T} \right)^{1/2} \sim n^{-1/3}, \quad (1.1)$$

where n is the density given by the number of atoms per volume N/V . When this occurs, the gas reaches what is known as quantum degeneracy.

Now, with that in mind, a little background: The building blocks of matter come in two varieties that are distinguished by the value of the quantum mechanical expression for their intrinsic angular momentum, known as spin. Though spin is a quantum mechanical entity, it may be thought of (loosely) as being analogous to the angular momentum of a classical body, such as the Earth, spinning about its own axis. In quantum mechanics, this spin is quantized into half-integer units which means that particles may only have integer or half-integer total spin. Particles with integer spin are known as bosons, and particles with half-integer spin are known as fermions. As luck would have it, lithium atoms come in two varieties (isotopes), ^7Li , a boson, and ^6Li , a fermion.

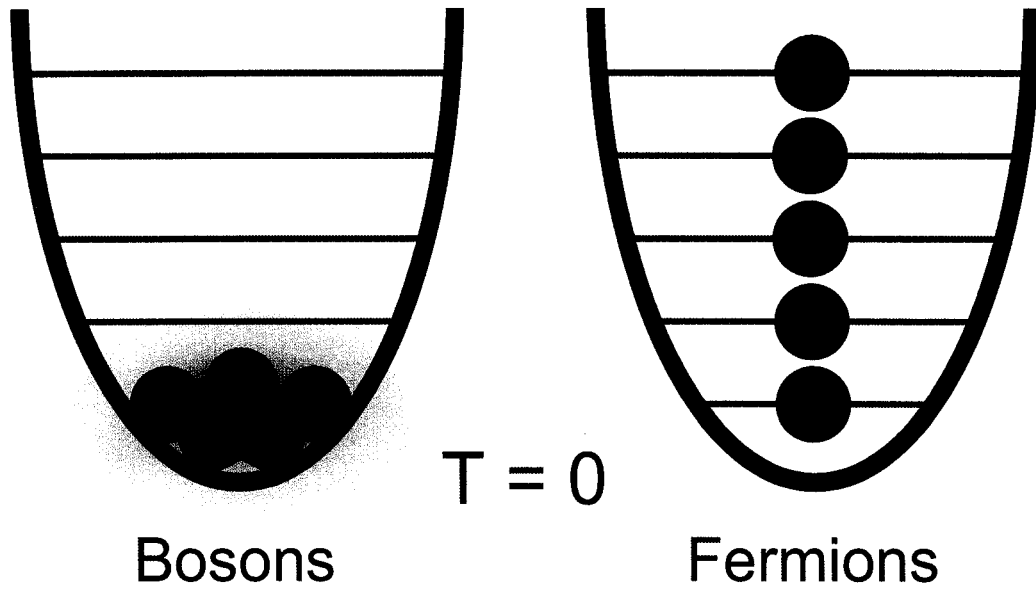


Figure 1.1 This diagram illustrates a primary difference between bosonic and fermionic particles. The left side shows a harmonic potential which contains bosonic particles at zero temperature. In this case, all the bosons fall to the lowest energy level (black lines) to form a BEC. The right side shows the behavior of indistinguishable fermionic particles at zero temperature. Since the fermions are identical, they are forbidden from occupying the same state, and instead pile up, one per level due to the Pauli exclusion principle. The energy of the highest occupied state is defined as the Fermi energy, ϵ_F , with associated Fermi temperature $T_F = \epsilon_F/k_B$, where k_B is the Boltzmann constant.

Under “normal” circumstances, these two types of lithium are very similar. When the rules of quantum mechanics take over (i.e. quantum degeneracy is reached), however, the behaviors of these two types of matter diverge. Under such circumstances, bosons are usually referred to as the more sociable of the two, as they are perfectly happy to crowd up into the same place at the same time. At very low temperatures, these bosons undergo a transition to a state known as a Bose-Einstein condensate (BEC) in which they all settle to the lowest energy possible in given system, as shown in fig. 1.1. The fermions, on the other hand, are often labeled as antisocial. This unfortunate reputation is a result of the fact that, at low temperatures, fermions refuse to interact with other fermions with which they are identical, and will not even

occupy the same place at the same time. When identical fermions are confined and cooled, the result is that they just stack up on each other, each one taking the next available unoccupied state, also shown in fig. 1.1. This behavior is described by the Pauli exclusion principle.

If we dig a little deeper, though, we find that it may not be completely fair to label the fermions as antisocial. Instead, it may be more accurate to say that they are just more particular about their partners. For example, at low temperatures, two *non*-identical fermions are perfectly happy to pair together (in fact, this is the preferred arrangement, since the paired state is at a lower energy than the unpaired). Moreover, the result of this pairing is a boson, since the sum of the half-integer fermion spins is an integer value.

While Bose-Einstein condensates in ultracold atomic gases have been around for a while (since 1995) [1–4], corresponding systems of degenerate Fermi gases have been slower in coming. (Note: this was not for lack of interest, but due instead to technical hurdles which result from the “antisocial” fermionic behavior.) The first degenerate Fermi gas arrived on the scene in 1999 [5], and subsequently in our lab in 2001 [6] (see fig. 1.2). As promised, these observations showed the effects of quantum mechanics on a macroscopic scale. In the latter case, it was verified that trapped fermionic ^6Li atoms would not occupy the same state, and as a result piled up in the trap. The resulting “Fermi pressure” that kept the atoms from falling to the center of the trap is the same exact mechanism that prevents a neutron star from collapsing in on itself due to gravity [7]. The difference was that this system was only a few feet away from us, and we could therefore probe, measure, and otherwise characterize this previously inconveniently located (outer space) state. The applicability of this trapped fermion system to other, less accessible systems, gave an early indication of the power that our model system would provide in the future.

The period of time since these events has seen the rapid growth of this field, both

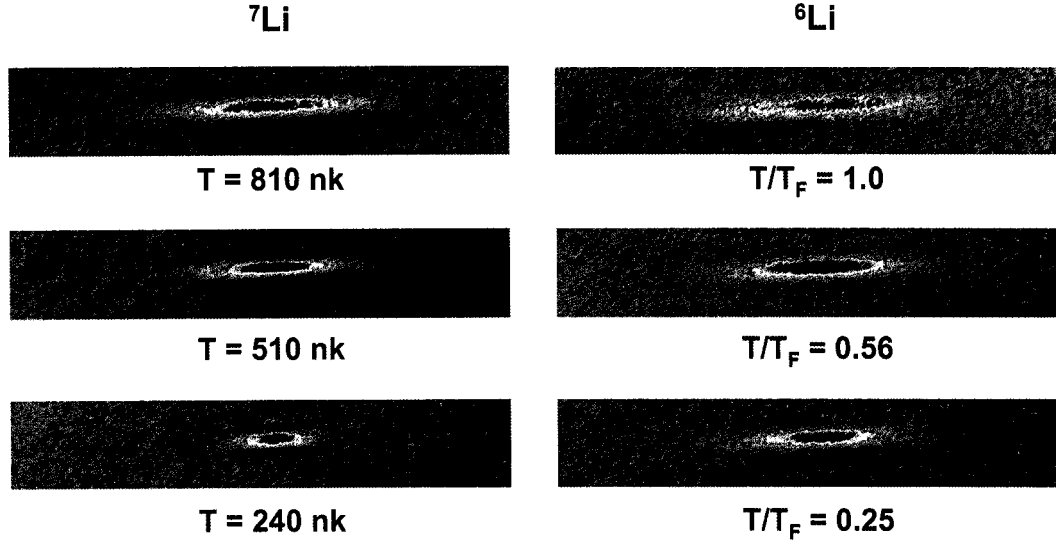


Figure 1.2 Images taken of ${}^7\text{Li}$ and ${}^6\text{Li}$ confined in a magnetic trap with decreasing temperature (top to bottom). Images that are side-by-side coexisted in the same trap. The top set of images are nearly indistinguishable since at higher temperatures, the gases of bosons and fermions are governed by classical physics. As temperature is reduced however, the gases become quantum degenerate. At this stage, the laws of quantum mechanics begin to take over and the behavior of bosons and fermions becomes different. The boson clouds on the left continue to shrink, whereas the fermion cloud size stabilizes. This stabilization is a result of Fermi pressure resulting from the Pauli exclusion principle that forbids the fermions from occupying the same trap energy level. An absolute temperature is determined from the bosons, since their distribution continues to change with the lowering of the temperature. The temperature of the fermions is referenced to T_F , the Fermi temperature, described in the caption of the previous figure (1.1). (Figure reprinted from ref. [6])

in experiment and theory, such that systems are now being investigated which go beyond atomic physics, and are contributing to the knowledge many other fields. In fact, the current experiments have progressed to the point that they are actually blurring the dividing line between bosonic and fermionic behavior. This feat is accomplished by continuously tuning the coupling strength between paired fermions. With strong coupling, the pair's behavior is bosonic, while for weak coupling, the fermionic behavior emerges.

The time since the first observation of Fermi degeneracy roughly corresponds to the time I have been in grad-school (coincidentally). This thesis will serve to tell the

story of the evolution of this field through the perspective of the experiments we have done in our own lab.

1.1 BEC and BCS

The 20th century has witnessed the emergence of the parallel phenomena of superconductivity and Bose-Einstein condensation (BEC). In 1911, Kamerlingh-Onnes discovered that at sufficiently low temperatures, the electrical resistance of mercury vanished, and it became what is known as a superconductor [8], so called because charge carrying electrons are free to move about without dissipation of energy. Similar systems are also possible where the free particles, such as atoms of ^3He , are uncharged. In either case, the substance can be generally referred to as a superfluid. It was not until 1957 that a full understanding of the mechanisms responsible for this phenomenon emerged [9]. This understanding came in the form of the BCS theory, so named for its inventors, Bardeen, Cooper and Schrieffer.

BEC's, on the other hand, made their entrance in reverse fashion, with the theory preceding the observation. In 1924-25, Einstein generalized a quantum theory, proposed by S. Bose to describe black body radiation [10], to massive particles [11]. The result of this theory was the prediction that at sufficiently low temperatures, a gas of bosonic particles would undergo a phase transition marked by the “condensation” of a macroscopic number of particles into the lowest energy ground state of the system. It was not until 1995 that BEC was experimentally observed in systems of dilute, trapped ultracold gases of alkali atoms, as mentioned earlier [1–4].

1.1.1 Role of Interactions

Due to the relationship between fermions and bosons discussed earlier, the two phenomena described above, BCS superconductivity and BEC, are not independent of one another either, and are in fact inextricably linked. In BCS theory, weakly bound pairs of electrons, called Cooper pairs, are formed. Since these pairs are comprised

of two fermions, they are themselves bosons. It is the Bose-Einstein condensation of these pairs which results in superconductivity. Whereas BCS superfluids are composed of very weakly paired fermionic particles, BEC's are formed from bosons which are deeply bound composites of fermions. For example, ^7Li , a bosonic atom, is formed from 3 protons, 4 neutrons and 3 electrons, all of which are fermions, whose half integer spins add to give an integer total value. In this case, since the fermions are very deeply bound (compared to the Fermi energy), the atom as a whole acts as a boson. As the binding energy of the composite fermions is reduced, however, there is a point where their fermionic character begins to come through. Figure 1.3, taken from ref. [12] exemplifies this behavior. In the weakly paired regime, labeled BCS, the chemical potential is equal to the Fermi energy. This is a characteristic of a non-interacting Fermi gas at $T = 0$, and is a result of the fact that when an additional fermion is added, the only place to put it is at the Fermi surface, since all the other states (trap levels, for a trapped gas) are occupied. As the pairing strength is increased, it begins to take less energy to add the particle, due to the energy gained from pairing. Finally, the interactions take over and the chemical potential goes below zero. It is at this point, where the remnant Fermi surface is lost, that the system becomes bosonic (labeled BEC). Within the in-between region (labeled PG for “pseudo-gap”, also called unitarity, or strongly interacting) the ground state is known as resonance superfluidity. Figure 1.4 also illustrates this progression from a BCS superfluid to BEC with increasing coupling strength.

It has been shown that BCS theory can be used to describe this entire system for arbitrary coupling strength, as long as the chemical potential is self consistently computed [13, 14]. As coupling strength increases, however, the precision of the predictions made with BCS theory decrease. As the theoretical capabilities for the strongly interacting region are limited, it becomes highly desirable to have an experimental system which is capable of exploring this region. This need is made more urgent by

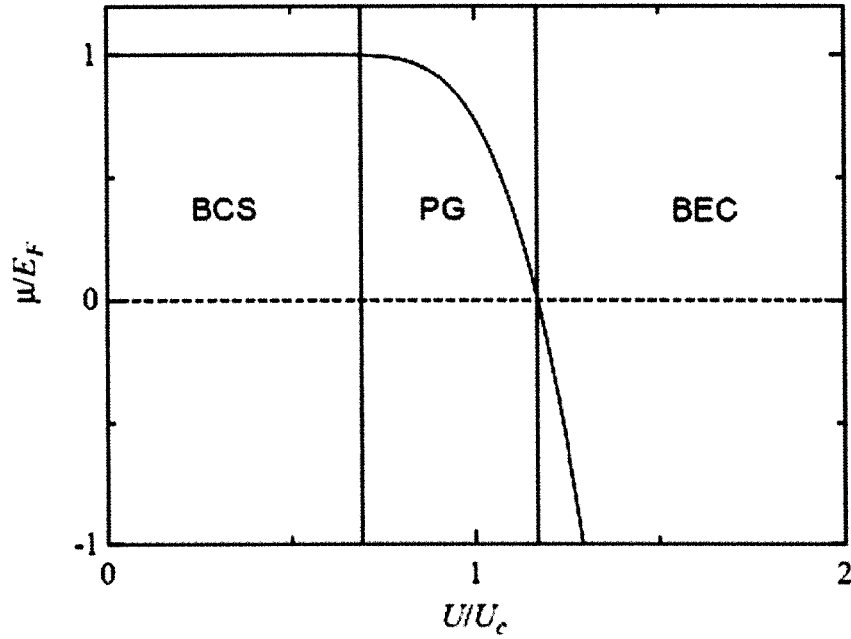


Figure 1.3 (Reprinted from ref. [12].) This plot shows the typical $T = 0$ chemical potential versus pair coupling strength for a paired Fermi gas in the BCS to the BEC regimes. For sufficiently weak coupling, the chemical potential equals the Fermi energy. This is generally called the BCS regime. As the coupling is increased, μ decreases and crosses below zero, at which point the system passes into the BEC regime. In between these extremes ($0 < \mu < E_F$), pair formation occurs at a temperature above the critical temperature for superfluidity, though the character of the system remains fermionic. This region is known as the pseudogap (PG), or crossover region. The coupling is normalized by U_c , which is the critical value of the potential for forming a two particle bound state in vacuum.

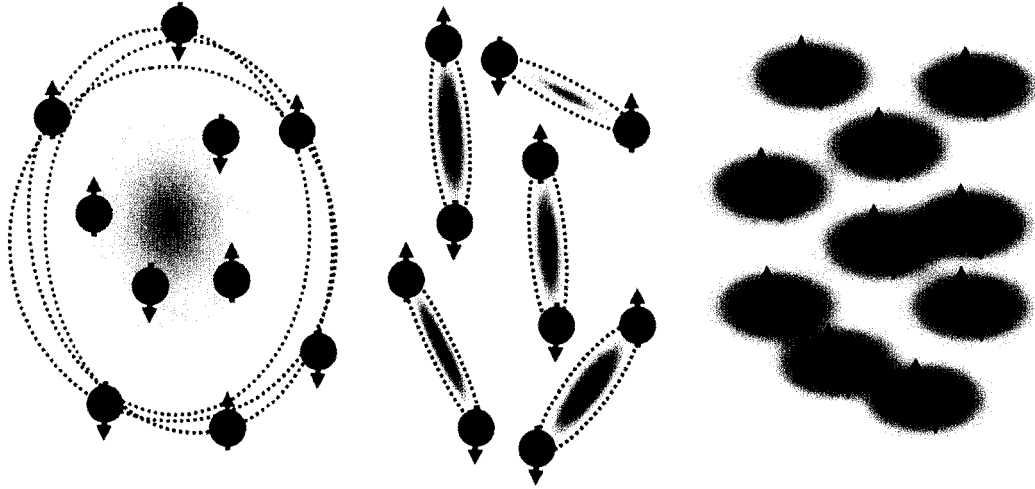


Figure 1.4 These illustrations represent the BCS (left), crossover (middle) and BEC (right) regimes. The red circles are fermionic atoms, and the small arrows show the atoms' internal spin states. Two distinct spin states are needed in such systems, since identical fermions are forbidden from interacting at low temperatures by the Pauli exclusion principle. In the BCS limit, pairing is weak, and specific pairing partners are not well defined. As coupling is increased, the pairs become increasingly more robust and better defined.

the ongoing lack of understanding of high T_c superconductivity, which is thought to operate in this regime.

1.2 Experiments

The gray area between the BEC and BCS limits is in fact where cold atom experiments, having already proven their worth through the creation of BEC's and degenerate Fermi gases, may once again enter the picture. An ideal system would be one of ultracold trapped fermionic atoms with tunable interactions. In this way, an atomic system could be set up as a clean model which could replicate the physics described the above.

As luck would have it (again), atomic physics has just the tool for the job of tuning interactions, known as a Feshbach resonance. In addition to a more detailed explanation in Chapter 3, a general introduction will be presented here (see also ref. [15]). A Feshbach resonance arises when the energy of a pair of colliding atoms (the

open channel) is tuned near that of a bound molecular state (the closed channel). Even though energy and momentum conservation do not allow the two colliding atoms to form a bound molecule, the proximity of the molecular state modifies their interaction, since they may temporarily “sample” the bound state. The result of this phenomena is to modify the s-wave scattering length, a , which determines the sign and strength of interatomic interactions in ultracold systems. For $a < 0$, attractions are attractive, while for $a > 0$, they are repulsive. Tuning may be accomplished when the open and closed channels have different magnetic moments, since their relative energies may then be tuned via the Zeeman shift associated with an external magnetic field. The field dependent scattering length $a(B)$ can be parameterized by

$$a(B) = a_{bg} \left(1 - \frac{\Delta B}{B - B_0} \right), \quad (1.2)$$

where a_{bg} is the background scattering length, B_0 is the resonance center field, and ΔB is its width [16].

1.2.1 Prior Experiments

In our first work with a Feshbach resonance, we did not use fermionic atoms, but instead created a large stable BEC of bosonic ^7Li atoms with repulsive interactions. When the scattering length was subsequently tuned to a small negative value, we observed the condensate to collapse into a train of solitons [17], as shown in fig. 1.5. Each soliton in fig. 1.5 is actually a small BEC which is held together by the attractive interactions of the atoms. This self-attraction prevents the solitons from spreading out in time, and allows them to maintain their small size, even as they propagate back and forth in the trap. This behavior provides a straightforward example of the effect of the Feshbach resonance.

The next experiment kicked off our studies of pairing of fermions. For this work we created bound molecules out of two fermionic atoms of ^6Li [18]. This was achieved by creating a mixture of two interacting spin states of ^6Li and ramping across a

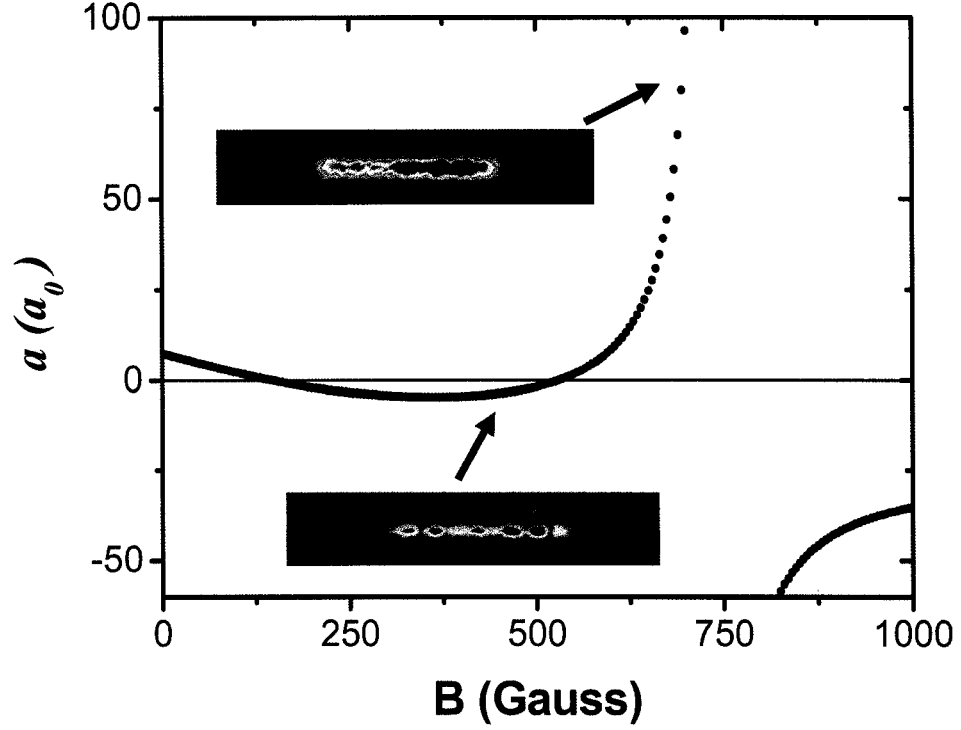


Figure 1.5 Creation of matter wave solitons of ^7Li . This experiment exemplifies the tunability of interatomic interactions using a Feshbach resonance. A large BEC of bosonic ^7Li is created at a magnetic field where the s-wave scattering length (y-axis) has been tuned to be large and positive. When the magnetic field (x-axis) is subsequently swept to a lower field where the scattering length is small and negative, the condensate collapses into a train of bright solitons. The solitons maintain their shape due to the attractive interactions between atoms. (See ref. [17].)

narrow Feshbach resonance. This sweep resulted in an adiabatic transfer of atoms to molecules, due to the avoided crossing of the molecular and atomic levels from which the resonance originates. This process is illustrated in fig. 1.6. While this experiment did not yet utilize tunable interactions, it showed that pairing of fermionic atoms could be achieved through the use of a Feshbach resonance. This established the versatility of the trapped atom system and its ability to change between bosons and fermions.

This brings us up to the current experiments which will be presented in this thesis.

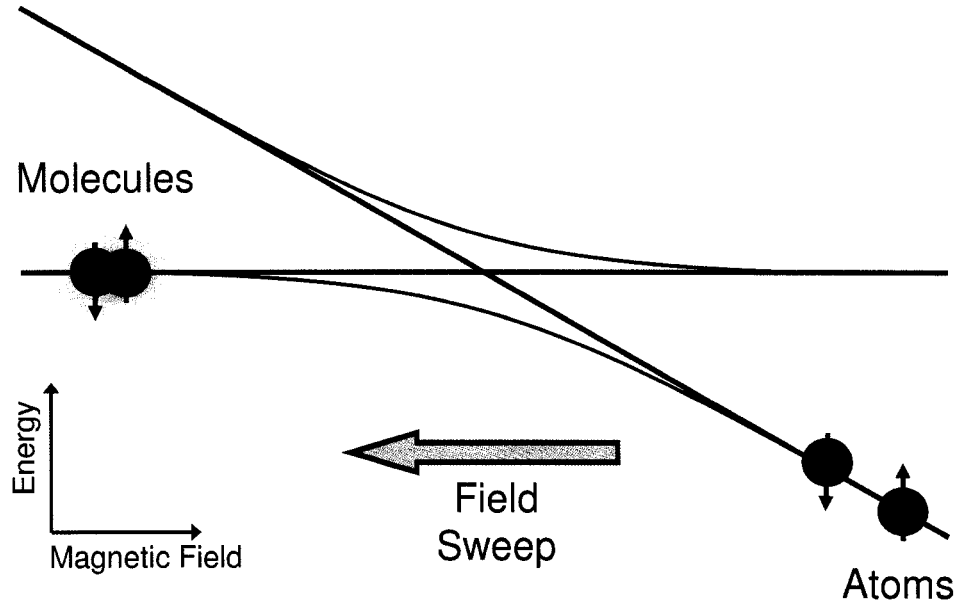


Figure 1.6 We have formed Molecules of fermionic ${}^6\text{Li}$ by a magnetic field sweep across a narrow Feshbach resonance. Since the resonance is formed by the avoided crossing of a molecular bound state with the atomic continuum, atoms may be transferred to molecules via adiabatic rapid passage. We measured a 50% transfer efficiency for this process [18]. Since the sweep is large compared to the width of the resonance, the molecules formed are much more deeply bound than the dressed molecules discussed in later chapters. Despite this, the molecules are surprisingly long lived, as they were measured to persist for up to 1 second.

These experiments will probe the BEC-BCS crossover by combining both the tuning of interactions, as in the soliton experiment, and the pairing of fermionic atoms, as in the molecular sweep experiment.

1.3 Outline

As with our research, the next step in this thesis, following the theoretical motivation, is the experimental apparatus and its implementation. I will begin, in Chapter 2, by giving an overview of the experimental apparatus and procedures used to perform the experiments. In addition, this chapter will detail the components of the apparatus that are new, or have been significantly improved since the last documentation was done, primarily in my Masters thesis [19] (2003), and in the Masters [20]

(2002) and Ph.D theses [21] (2004) of my predecessor, Kevin Strecker. This chapter will include a detailed look at the optical trap which will include the setup, as well as an in-depth characterization of the potential it forms. Beyond Chapter 2, there are other experimental and theoretical details which are more relevant to one experiment or another, and are generally located in the early parts of subsequent chapters.

In Chapter 3, we will finally get to some results. I will present a quantitative measurement of the make-up of pairs of fermionic atoms from the BEC to the BCS regimes, including the region in between, where interactions become very strong. This strongly interacting regime is of particular interest, since it is not well understood theoretically, yet may hold the key to understanding high T_c superconductors. Our measurement also shows that the strongly interacting atoms in a Feshbach resonance should exhibit the same universal behavior common to all strongly interacting Fermi systems, from nuclear, to condensed matter, to astrophysics.

This universal behavior is utilized in the following chapter as well, where we measure the universal many body parameter for a strongly interacting Fermi gas. From this point, Chapter 4 goes on to detail more experiments which were performed using paired atoms. In this case, however, we create a mismatch in the numbers of the two atomic spin states required for pairing. Such an imbalance is interesting from the point of view of many fields of physics, from magnetized superconductors, to cold dense quark matter, and neutron stars. In addition, the imbalance allows for us to study the interface which connects the regions of a gas that is part superfluid and part normal.

At the end, I have included several appendices that are used to document procedural and experimental details that are of importance, but which may have otherwise cluttered up the main chapters.

1.3.1 The Purpose of This Work

If you are still reading the introduction, then perhaps you are planning on reading the thesis in order, from front to back. That is fine, as this work is meant to tell the story of the time I have worked in the Hulet lab, from my point of view. Having read this document, the reader should have a fairly good understanding of what has been keeping me so busy for the last “several” years. So, if these things sound appealing, then keep reading.

Of course, the primary purpose of this writing is to document the work that I have done, including the historical and scientific motivation and ramifications. This document will also serve to record the techniques and procedures that I have either developed or adopted in order to achieve the goals of our research. This aspect will be most useful to my fellow lab-mates, or possibly other experimentalists following similar endeavors. If you are one of these people, then you are probably not reading this section.

When reading a document such as this, it is sometimes easy to forget that the results presented were all obtained through experimentation. I attribute this phenomenon to the fact that most of the content of this thesis is composed of things that worked, while the actual evolution of ideas to their final state, through both failures and successes, is unavoidably condensed when it is written down. (If something *really* didn’t work, I’ll write that down too, so that others may learn from my mistakes.)

All the experimental results I present were conceived in order to answer questions about the physical world. In the previous sections, I have already given a basic idea as to the general area of this physical world that we will be investigating, namely a better understanding of the mechanisms behind pairing of fermions, and the applicability of our cold atom experiments to many other diverse systems.

Chapter 2

The Apparatus

The major aspect of cold atom systems that makes them versatile in modeling and characterizing so many diverse systems is the tunability and control which they allow. Among the possibilities are control of temperature, number, density, dimensionality, and interactions. In order to take advantage of the versatility offered by these systems, we have constructed an apparatus through which we are capable of creating, containing, tuning, and measuring gases of ultracold atoms.

2.1 Overview

The substance whose atoms we cool and trap is elemental lithium, an alkali metal. Among the many reasons for choosing to work with lithium is the natural abundance of both stable bosonic ${}^7\text{Li}$ and fermionic ${}^6\text{Li}$ isotopes. Having bosons and fermions at our disposal allows for many different avenues of investigation, and since both isotopes have similar transition wavelengths, the same laser trapping technology and techniques may be used for both. Moreover, there are many Feshbach resonances at experimentally accessible fields for both isotopes.

Many of the procedures and much of the apparatus have been previously described in our papers and in various theses [6, 17–25]. Figure 2.1 shows the major components of the apparatus. We begin with a recirculating oven packed with equal amounts of ${}^6\text{Li}$ and ${}^7\text{Li}$. When the oven is heated to $\sim 400^\circ\text{C}$, a thermal beam escapes through a small opening directed into a Zeeman slower. The slowed thermal beam of atoms is then loaded into a dual magneto optical trap (MOT) that traps both ${}^6\text{Li}$ and ${}^7\text{Li}$ (fig. 2.2).

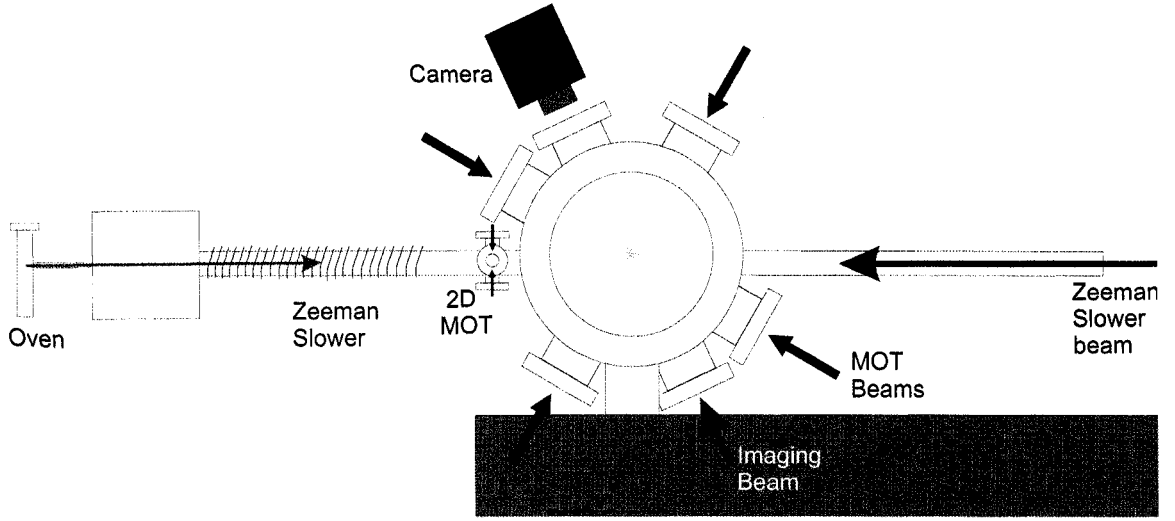


Figure 2.1 The apparatus. Lithium is emitted from the oven and slowed by a Zeeman slower to load a dual species MOT. From there, a magnetic trap is loaded and evaporatively cooled. Finally the atoms are transferred to an optical trap and imaged by absorption.

2.1.1 Dual MOT and Magnetic Trap

The dual MOT is presented in greater detail in my Master's thesis [19], however key points are discussed here as well.

The transition used to trap ${}^6\text{Li}$ (${}^7\text{Li}$) is the ${}^2\text{S}_{\frac{1}{2}} F=\frac{3}{2} (F=2) \rightarrow {}^2\text{P}_{\frac{3}{2}} F=\frac{5}{2} (F=3)$. In spectroscopic notation, these are the D2 transitions. From the level diagram (fig. 2.3), it is apparent that the transitions in the upper manifold are only separated by a frequency on order of the natural linewidth. This allows the atoms to de-excite to the $F=\frac{1}{2} (F=1)$ state. The frequency of the D2 transition of an atom in this state is approximately 230 MHz (800 MHz) detuned from the trapping laser. Since this detuning corresponds to 39γ (137γ), where $\gamma = (2\pi)5.87 \text{ MHz}$ is the natural linewidth of the $2s - 2p$ transition in lithium [27], the atom will no longer be addressed by the laser, and therefore will no longer be trapped. While this is a concern in any MOT, the close spacing of the excited states increases the probability of sending the atom to the lower, untrapped state. As a result it is necessary to include a separate repumping frequency in each of the six MOT beams to drive the atoms out of the lower

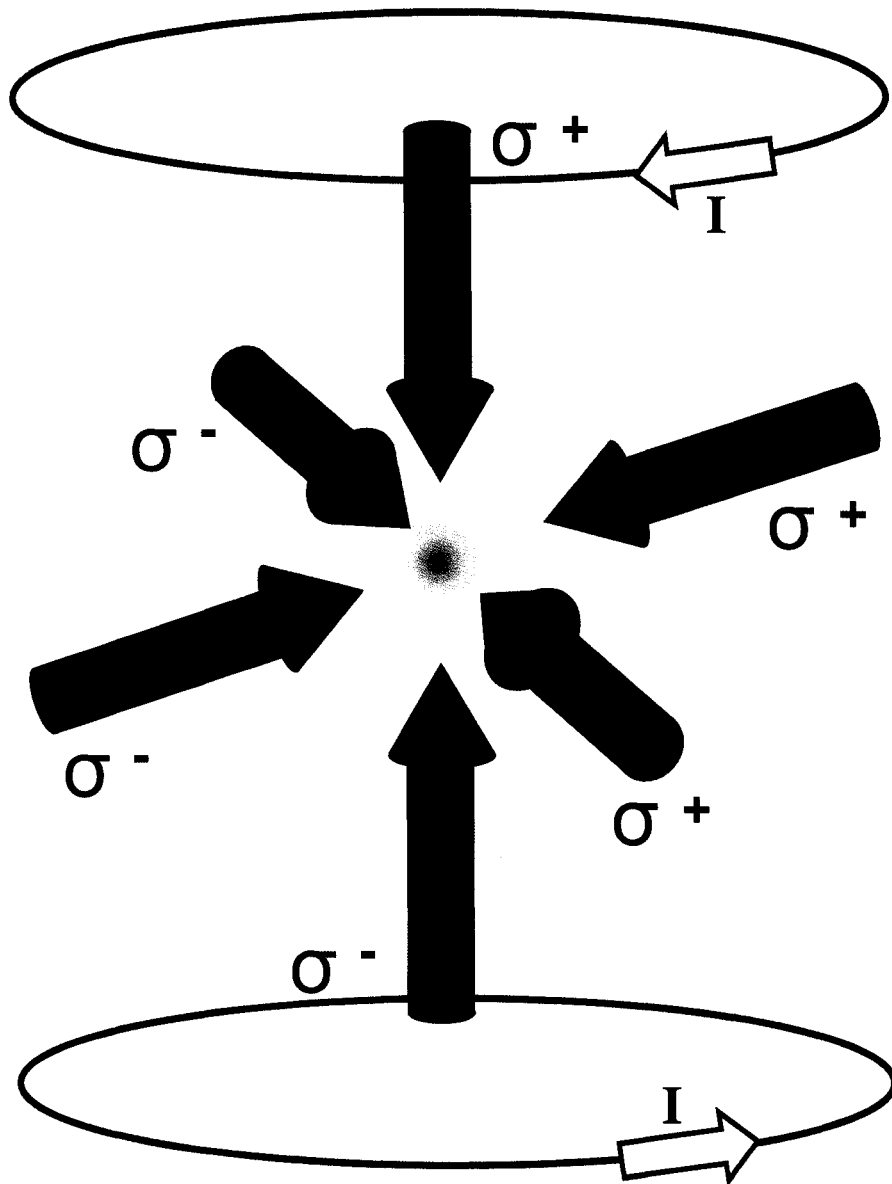


Figure 2.2 A magneto-optical trap (MOT): Circularly polarized laser beams converge on the zero of a field produced by coils in an anti-Helmholtz configuration. We create spatially overlapped MOT's of both fermionic ${}^6\text{Li}$ and bosonic ${}^7\text{Li}$.

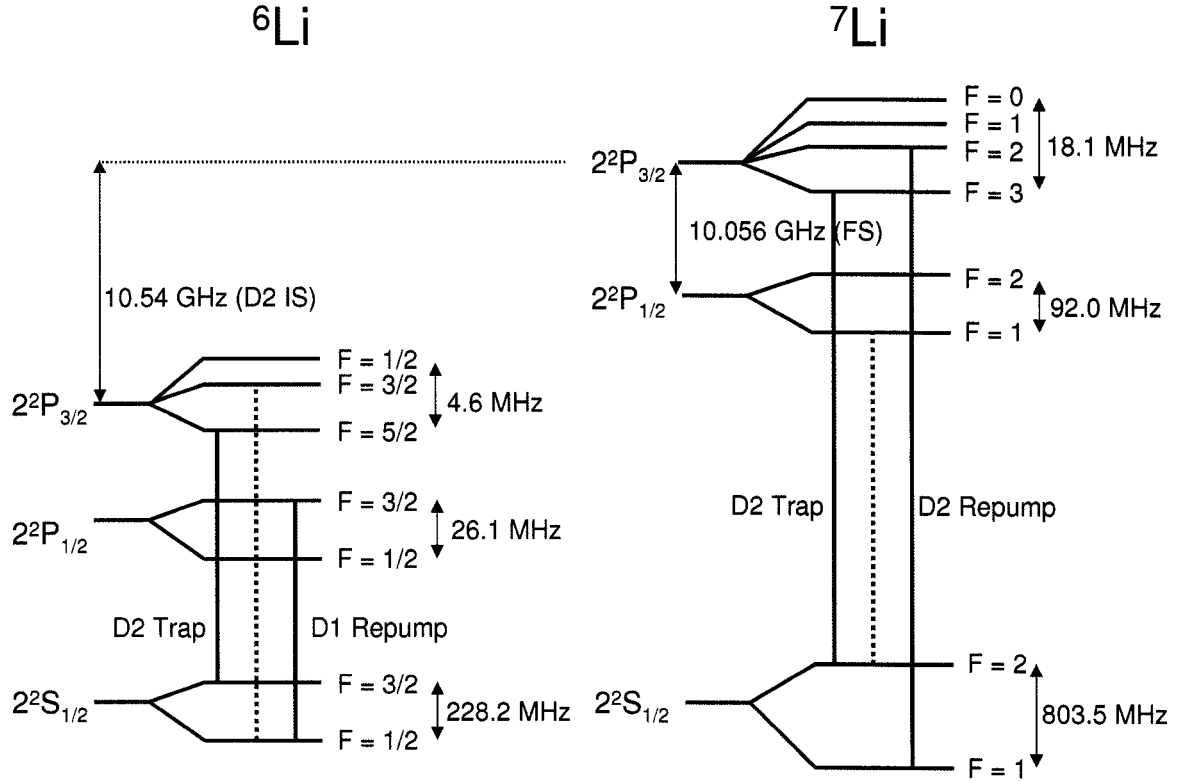


Figure 2.3 Energy level diagram for lithium, showing hyperfine structure. For the ${}^7\text{Li}$, D2 transitions are used for both trapping and repumping, while for ${}^6\text{Li}$, the D2 transition is used for trapping, and the D1 is used for repumping. The dotted line shows the frequency of the ${}^6\text{Li}$ D1 repump and the nearly resonant transition in ${}^7\text{Li}$. This coincident frequency is a result of the closeness of the isotope shift (IS) and the fine structure splitting (FS). Energy splittings are not to scale. (For lithium spectroscopic measurements, see, for example, [26] and references.)

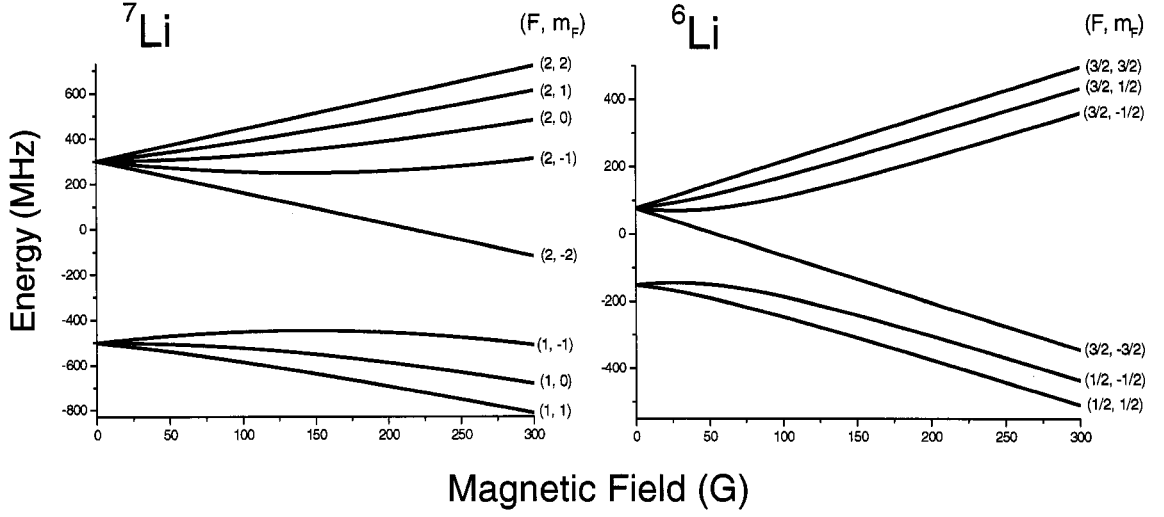


Figure 2.4 Ground state level splitting as a function of magnetic field for both lithium isotopes. Although any upward sloping, i.e. low field seeking, level may be magnetically trapped, spin exchange losses necessitate spin polarization into the topmost levels ($F = 2$, $m_F = 2$ for ${}^7\text{Li}$, and $F = 3/2$, $m_F = 3/2$ for ${}^6\text{Li}$). Note that it is common practice in the literature and in this thesis to refer to the levels of ${}^6\text{Li}$ by numbers 1 - 6, counting from the bottom. ($|1\rangle \equiv F = 1/2$, $m_F = 1/2$, $|2\rangle \equiv F = 1/2$, $m_F = -1/2$ etc.

state [21]. The simplest way to implement repumping is to modulate the trapping beams at a frequency near the splitting of the ground state. This can be achieved by using an acousto-optic modulator (AOM) or electro-optic modulator (EOM), as in the ${}^7\text{Li}$ MOT [20, 21],

Difficulty arises since there is a near overlap of this ${}^6\text{Li}$ repumping frequency ($F = \frac{1}{2}$, D2) with that of a D1 transition of ${}^7\text{Li}$. This coincidental overlap results in loss of ${}^7\text{Li}$ from the MOT when the ${}^6\text{Li}$ D2 repump is on. To circumvent this difficulty, we repump on the D1 transition of ${}^6\text{Li}$ which is far detuned from any ${}^7\text{Li}$ lines as shown in fig. 2.3. Since this frequency is ~ 10 GHz detuned from the ${}^6\text{Li}$ D2 trapping light, it necessitates another laser system, also documented in my Master's thesis [19].

Once both isotopes have been loaded into the dual MOT ($N_6 \sim 10^9$, $N_7 \sim 10^{10}$), they are optically pumped to the highest ground state hyperfine levels, shown in fig. 2.4. These states are selected because they can be magnetically trapped and are

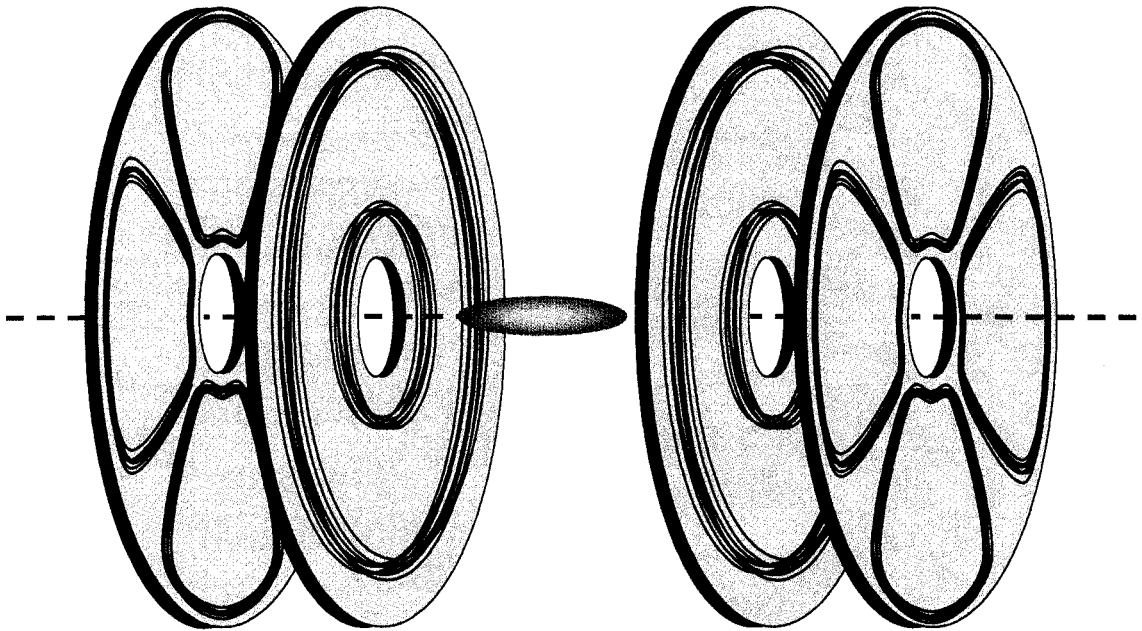


Figure 2.5 Atoms are confined in the magnetic trap which is comprised of 3 coil sets. The small circular curvature coils create a curved field with a central minimum in the long axial direction. The larger circular [anti-]bias coils produce a flat field which nearly cancels the curvature field at the center of the coils so that the center of the trap is at nearly zero field. The four 'D' shaped quadrupole coils produce a radial field gradient to provide confinement in that direction [28].

resistent to spin exchange collisions. After optical pumping, the atoms are transferred to an Ioffe-Pritchard type magnetic trap, as shown in fig. 2.5 [21]. Once in the magnetic trap, both isotopes are cooled via dual forced RF evaporation [19]. The bosonic ${}^7\text{Li}$ is necessary to mediate the rethermalizing collisions among the fermionic ${}^6\text{Li}$, which is quantum mechanically forbidden from interacting via s-wave collisions due to symmetry.

For the experiments presented in this thesis, only the fermionic ${}^6\text{Li}$ is used, and so the evaporation trajectory is set to remove all the ${}^7\text{Li}$. After a cooling cycle of approximately 55 seconds, a highly degenerate ($T/T_F \sim 0.1$, $N \sim 10^7$) cloud of ${}^6\text{Li}$ is produced.

This cooled cloud is then transferred to an all optical trap, since it provides much

more flexibility than a magnetic trap. The various optical trapping schemes we have used are described in the following section.

2.2 Optical Trap(s)

The tunability of interactions between trapped atoms is achieved through a magnetic Feshbach resonance, as described in Chapter 1. To use a magnetic Feshbach resonance, it is necessary to have control over the magnitude of the magnetic field that the atoms are subjected to. If the atoms are trapped by magnetic fields in a magnetic trap, this tunability is effectively ruled out. Moreover, many of the atomic spin (hyperfine) states of interest (such as those of ^6Li used for the experiments presented in this thesis) are high-field seekers and therefore can not be magnetically trapped in the first place. To work around these restrictions, and thereby realize the full potential of the trapped atom system, we have integrated an all optical trap to contain the atoms, regardless of their internal state or the background magnetic fields which we apply.

Optical traps work off the principle of the ac-Stark shift, where the internal energies of the atomic levels are shifted by an off-resonant light field. In particular, the time averaged electric field induces an electric dipole moment \vec{d} in the atom that interacts with the field to produce an energy shift. This can be understood through the dressed atom picture, in which the entire atom-light system is considered as one [29–31]. In the presence of the atoms and the light, dressed states, so called because the bare atomic states are “dressed” by the light field, become the relevant eigenstates of the system. If the coupling between the light and the atom is neglected ($\vec{d} = 0$), the dressed states are $|i, n\rangle$, where $i = g, e$ and refers to the ground and excited internal state of the atom, connected by the transition energy $\hbar\omega_0$, and n is the photon number which changes the energy by units of the photon energy $\hbar\omega_L$. These levels are split by the detuning energy, $\hbar\Delta$, where $\Delta = \omega_L - \omega_0$, and are shown on the left

of parts (a) and (b) of fig. 2.6.

With the addition of coupling between the atoms and light ($\vec{d} \neq 0$), the energy splitting of the dressed states becomes $\pm \frac{\hbar(\Delta^2 + \Omega^2)^{1/2}}{2}$, where Ω is the Rabi frequency of the transition, which can be written in terms of the laser intensity, I , and the saturation intensity as $\Omega = \gamma(I/I_{sat})^{1/2}$. The shifted states are a linear superposition of the dressed states $|g, n+1\rangle$ and $|e, n\rangle$, and are labeled $|1, n\rangle$ and $|2, n\rangle$. These are shown on the right of parts (a) and (b) of fig. 2.6.

If the intensity of the light field varies with position, then the gradient of the resulting position dependent energy shift leads to a dipole force which may be used to create a potential for trapping the atoms. This force is given for an atom at rest in ref. [30] as

$$\vec{F}_{dip}^{st} = -\nabla \left[\frac{\hbar\Delta}{2} \log \left(1 + \frac{\Omega^2}{2\Delta^2} \right) \right] \quad (2.1)$$

where Ω is now spatially dependent. The relevant $e \rightarrow g$ transition in lithium is the 2S to 2P transition, with wavelength $\lambda = 671$ nm and saturation intensity $I_{sat} = 5.1$ mW/cm². From eq. 2.1, we see that the direction of this force depends on the sign of the detuning of the trapping laser. Figure 2.7 (taken from [30]) shows the origin of this dependence.

From 2.1, we also see that the potential seen by the atoms is given by

$$U(r) = \frac{\hbar\Delta}{2} \log \left(1 + \frac{\Omega(r)^2}{2\Delta^2} \right) \quad (2.2)$$

(since $\vec{F} = -\nabla U$). For our implementation, $\frac{\Omega(r)^2}{2\Delta^2} \ll 1$, since the trapping laser ($\lambda = 1064 - 1080$ nm) is very far detuned from the atomic transition ($\lambda = 671$ nm). As such, we may take the first term of the expansion of the log term in Eqns. 2.1 and 2.2

$$\log \left(1 + \frac{\Omega(r)^2}{2\Delta^2} \right) = \frac{\Omega(r)^2}{2\Delta^2} + \dots \quad (2.3)$$

Now we may rewrite eq. 2.2 as

$$U(r) = \frac{\hbar\Omega(r)^2}{4\Delta} = \frac{\hbar(I/I_{sat})\gamma^2}{4\Delta}. \quad (2.4)$$

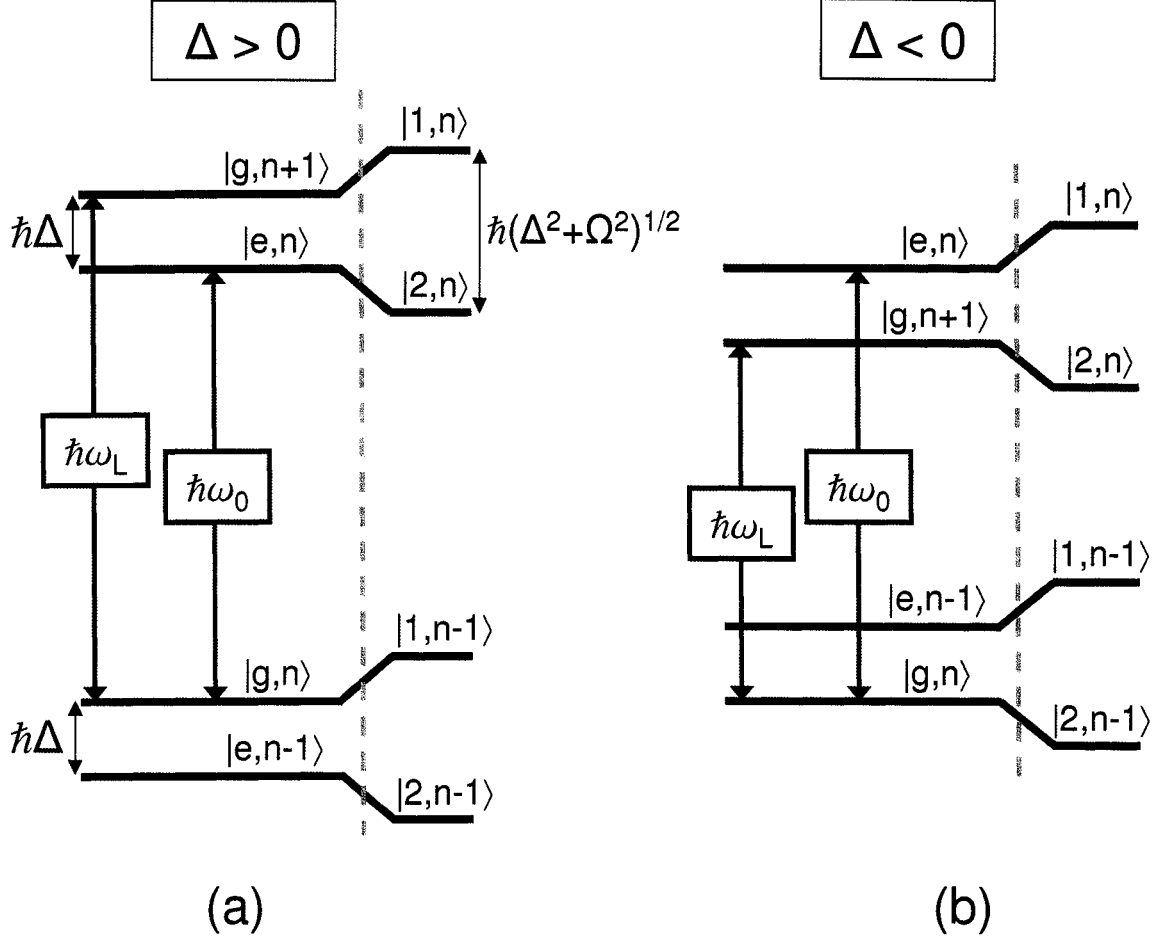


Figure 2.6 Energy levels in the dressed atom picture, shown for $\Delta > 0$ (a) and $\Delta < 0$ (b). The energy structure of dressed states of bare atoms and photons have a repeating periodic structure of manifolds separated by units of energy given by the laser frequency $\hbar\omega_L$. Within each manifold are two dressed states, the separation of which depends on the laser interaction strength with the atom. For no laser-atom coupling (left of the dashed gray lines) the states are split by the detuning energy $\hbar\Delta$. With the addition of coupling (right of the dashed gray lines), the splitting is increased to $\hbar(\Delta^2 + \Omega^2)^{1/2}$, where Ω depends on the (position dependent) intensity of the laser. This intensity dependent energy shift produces a force on the atoms (eq. 2.1) which can be used to confine them. Additionally, the sign of Δ determines whether or not the atoms are attracted to, or repulsed from, the laser beam. (see fig. 2.7)

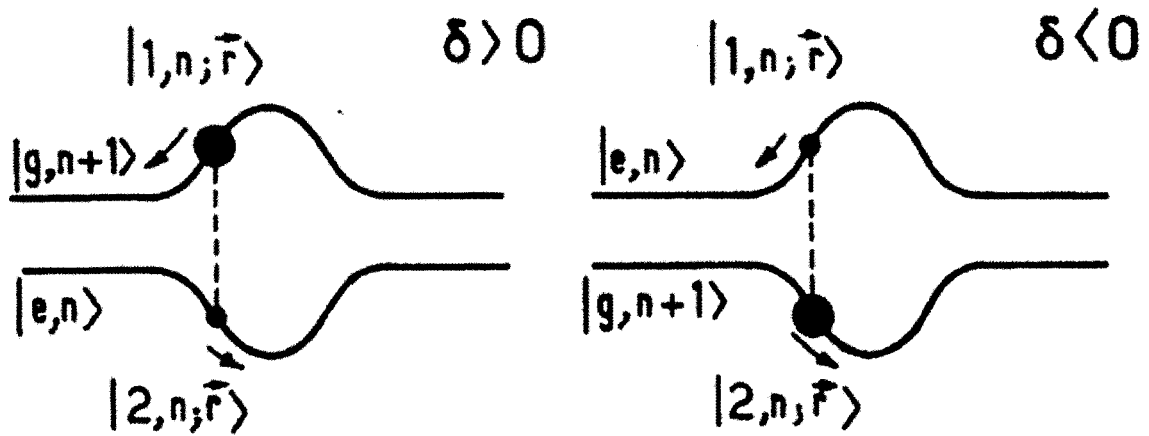


Figure 2.7 This diagram, taken from ref. [30], is useful for understanding the effect that the sign of the detuning, Δ (here written δ), has on the dipole force. These two diagrams show the same energy levels as the top half of the previous figure. The bulge in the middle represents the energy shift caused by the intensity profile of a laser beam. In each case, the $|1, n\rangle$ and $|2, n\rangle$ states are linear superposition of $|g, n+1\rangle$ and $|e, n\rangle$. The average force that the atom experiences is the force resulting from the shift of both levels $|1, n\rangle$ and $|2, n\rangle$, weighted by the relative amplitudes of the basis states $|g, n+1\rangle$ and $|e, n\rangle$. Since the laser is far from resonance, the ground state will be more populated on average, and the shift of the level that connects to the $|g, n+1\rangle$ as $\Omega \rightarrow 0$ will dominate. For the case of $\delta > 0$, the $|1, n\rangle$ level is more populated (signified by larger dot), and so the average force tends to be repulsive (shown by small arrow), while for $\delta < 0$, the $|2, n\rangle$ is the dominant level, and leads to an attractive force.

From this expression for the potential eq. 2.4, and given the geometry of a trapping beam, one may calculate the peak trap depth, typically on the order of 10's - 100's of μK for our implementation, as well as find the oscillation frequency of an atom confined in the trapping potential. These values will be computed specifically for the current trap configuration, once the optical setup and resulting beam intensity profile is presented. For now, it is sufficient to say that a single focussed red-detuned ($\Delta < 0$) beam can be used to form a potential that provides confinement in three dimensions. The distribution of the trapping potential is given by the intensity distribution of a gaussian beam

$$I(r, z) = I_0 e^{-2r^2/w(z)^2} \quad (2.5)$$

and eq. 2.4:

$$U(r, z) = \frac{\hbar(I_0 e^{-2r^2/w(z)^2}/I_{sat})\gamma^2}{4\Delta} \quad (2.6)$$

where the beam waist is given by

$$w(z) = w_o(1 + (z/R_L)^2)^{1/2}, \quad (2.7)$$

and $R_L = (\pi\omega_o^2)/(\lambda)$ is the Rayleigh length, and w_o is the beam waist at the focus.

A trap formed from such a beam has a cylindrical symmetry, with tight confinement in the radial (\hat{r}) direction, perpendicular to the beam propagation, and weaker confinement in the remaining axial (\hat{z}) direction (along the beam propagation axis) which arises due to the changing waist (eq. 2.7). Such a potential results in a cigar shaped trapped cloud, as shown in fig. 2.8.

For the experiments covered in this thesis, we have constructed such an optical trap from a red-detuned ($\Delta < 0$) laser, though in the past, we have also utilized blue detuned ($\Delta > 0$) light as well. I will briefly document the evolution of our traps in the following section.



Figure 2.8 This absorption image shows the general geometry of an optical trap formed from a single focussed red-detuned beam. The elongated shape of such a potential is evident from the distribution of the trapped atom cloud. This trap is formed from a 1080 nm beam focussed to $\sim 26 \mu\text{m}$, and will be characterized later in the chapter. In this image, there are ~ 3 million ^6Li atoms with a temperature of $\sim 6 \mu\text{K}$ confined in the trap with a trap depth of $105 \mu\text{K}$.

2.2.1 A Brief History of Our Optical Traps

Through the course of the past several years, we have actually constructed several versions of optical traps in an effort to maximize the performance and repeatability attainable in these traps.

The first optical trap used on our experiment used an infrared Nd:YAG laser (CrystaLaser IRCL-1W-1064nm) with an output of approximately 1 Watt at a wavelength $\lambda = 1064 \text{ nm}$. It was formed by focusing this laser to a $\sim 40 \mu\text{m}$ beam waist [21]. This beam waist was chosen to minimize the heating of the atom gas upon transfer, by simulating, as closely as possible, the radial potential created by the magnetic trap, from which the optical trap was loaded. While in the radial direction, this trap provided adequate confinement, in the axial direction, the potential was much flatter than that of the magnetic trap. As a result, atoms transferred to this trap were not well confined in the axial direction. To prevent this from happening, optical endcaps were formed from blue detuned light sheets (532 nm), from which the atoms were repelled. This trap was utilized for two separate experiments: the production of atomic solitons from bosonic ^7Li atoms in a Feshbach resonance [17], and later the creation of long-lived deeply bound molecules of ^6Li , by a sweep through a narrow Feshbach resonance [18]. Both these experiments, as well as the specifics of the optical trap are presented in the thesis of Kevin Strecker [21].

While this trap proved adequate for these purposes, in the end, several limitations

led to the need for improvement. First, the overlap of the red-detuned beam and the blue-detuned endcaps was sensitive, and large amounts of time was spent aligning these beams relative to each other and to the atoms. In addition, even under optimal conditions, this trap only provided on the order of $10\ \mu K$ of confinement, and therefore required transfer of a very cold pre-cooled atomic sample. This requirement resulted in degradation of repeatability, due to shot to shot or day to day performance of the rest of the apparatus. Finally, since this trap was cylindrical in shape (e.g. can shaped) the axial distribution of the atom cloud was independent of temperature, and therefore temperature determination of the sample required fitting of radial distributions, which were small and subject to optical resolution limitations. (On the other hand, this flat distribution also has interesting implications for experiments, and may have facilitated the formation of soliton trains [17], as opposed to single solitons as seen at ENS [32]). In the end, however, the difficulties outweighed the advantages and this trap was changed.

The next iteration of the optical trap involved the use of more brute force – i.e, the addition of a 20 W fiber laser (IPG Photonics YLR-20-LP) with wavelength $\lambda = 1080$ nm. With this laser, it was possible to produce a potential that was much deeper than could be realized with the 1 W Nd:YAG laser. The idea of this trap was to replace the axial confinement of the blue-detuned endcaps with a perpendicular red-detuned beam, as well as to fortify the potential formed in the radial direction with more power. This implementation is known as a crossed dipole trap. The potential of our crossed dipole trap was formed from an axial beam with waist of $\sim 50\ \mu m$ at ~ 3 W (for radial confinement) and a crossed beam of $\sim 250\ \mu m$ at ~ 15 W for axial confinement. This effectiveness of this trap was again compromised by the necessity of precise alignment between the two beams. Maintaining this alignment proved difficult as well, due to thermally driven drift of optical components (especially the switching AOM's). In the future, if other crossed beam traps are attempted, it may

be advisable to fiber couple the beams after the AOM's. This trap also suffered from an, at the time, undiagnosed problem with heating due to mechanical vibrations in the laser mount [21].

The heating associated with this laser led us to temporarily return to the 1 W laser which had been used previously. For this implementation, however, a smaller beam waist of $\sim 23\mu m$ was created. The optical setup of this trap is shown in fig. 2.9. The small beamwaist provides increased confinement in the axial direction, and so allows for the elimination of a secondary beam. This trap was used for the molecular probe experiment described in Chapter 3 of this thesis. This trap still suffered from a low trap depth which resulted in inconsistent performance on a day to day basis.

2.2.2 Current Optical Trap

The final (current) implementation of the optical trap combines the best of the previous iterations, and is improved by the lessons learned, such as it is better to transfer more atoms to the trap at the expense of heating them due to mis-matched frequencies. Moreover, once the vibration problem was discovered [21], we were free to use the 20 W fiber laser to create the optical trap. This trap is used for the experiments presented in Chapter 4, and is the best performing and most thoroughly characterized of the group.

Optical Setup

This trap is again formed by focussing the laser to a small beam waist, and so provides both radial and axial confinement with the use of a single beam. We have previously experienced heating due to vibrations from turbo-molecular pumps mounted on the apparatus, so to minimize heating due to these vibrations, this trap is built on a weighted platform that is isolated from the main optical table by vibration damping rubber. Mounting the trap table in this way has completely eliminated any measurable heating of the atoms.

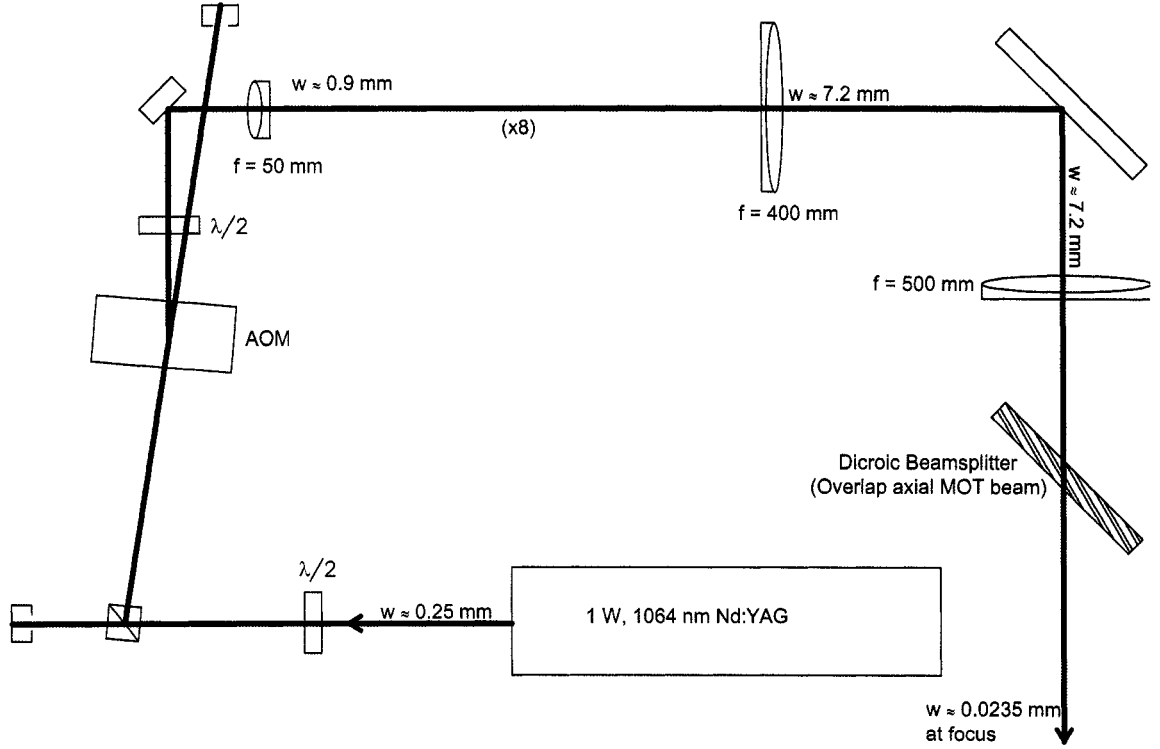


Figure 2.9 This optical trap setup was used to create a Bose-Einstein condensate of dressed molecules in a Feshbach resonance, and was utilized for the experiments measuring the bound molecular fraction of fermionic pairs presented in Chapter 3. The trap is designed around a 1 W, 1064 nm, Nd:YAG laser (CrystaLaser IRCL-1W-1064nm). A half wave plate and a polarizing beam splitter cube is used to limit the power going to the rest of the optics during initial alignment. The trap is formed from the first order of an AOM (Crystal Technology Model 3110-197). The optical power directed to the atoms is controlled by varying the RF drive power. The beam is expanded from a waist of ~ 0.9 mm to 7.2 mm by a lens pair, and then focussed onto the atoms by a 500 mm lens mounted on a 3-axis translator. The translator may be shifted to fine-tune the position of the focussed beam to overlap with the atoms. The waist at the atoms, given by $w_o = (f\lambda)/(\pi w_i)$ where $f = 500$ mm is the focussing lens, $\lambda = 1064$ nm, and $w_i = 7.2$ mm, is $23.5 \mu\text{m}$. This waist was confirmed by radial frequency measurements such as those presented later in the chapter. We have found that in order to achieve the small beam waists required to form an effective 1 beam potential, it is necessary to use high quality achromatic doublet lenses and large optics that ensure that no clipping of the beam occurs. A dichroic beamsplitter (transmits IR, reflects visible: CVI LWP series) is used to direct the beam along the same axis as the axial MOT and optical pumping beams.

Since we are focussing the beam down to a relatively small waist, minute imperfections in the optical setup can lead to significant distortions of the focus of the beam. In order to achieve a clean and symmetric beam at the focus, it is necessary to use high quality doublet lenses and large optics that eliminate the possibility of distortion or clipping of the beams. In addition all optics are mounted on short, thick (1") posts for stability. To achieve a clean focus, it is also necessary for the beam to pass exactly through the center of the lenses at normal incidence. As such, the lenses are mounted on mirror mounts that allow for tilt control. The optical setup is shown in fig. 2.10.

Even with all the precautions taken in the setup to ensure a clean focus, it is still necessary to directly verify the quality of the focussed laser beam. This is done by imaging the beam directly onto a CCD camera at and around the position of the focus. Figures 2.11, 2.12, and 2.13 show examples of such images of the trapping beam. The first two (figures 2.11, and 2.12) show commonly encountered distortions of the beam that require attention. At this time, small adjustments to the optical setup are made to produce the desired focus which should be symmetric at the focus, as well as on either side. The third image (fig. 2.13) shows an image of the beam after the optics have been adjusted to give a nice focussed spot. The gaussian fit to a cut of the third image is shown in fig. 2.14. The waist extracted from the fit is $26.0 \pm 0.5 \mu\text{m}$. These measurements also provide a useful way to determine the z position of the focus for subsequent overlap with the position of the magnetically trapped atoms.

In addition, plotting the extracted beam waist $\omega(z)$ versus focus position, z , allows us to characterize the quality of the beam. Specifically, we may extract the gaussian beam quality factor, M^2 , where M^2 is defined as the ratio of the actual focussed beam waist and the ideal waist, given by the divergence angle of the beam far from the focus [33]. With the inclusion of the M^2 parameter, the z dependence of the

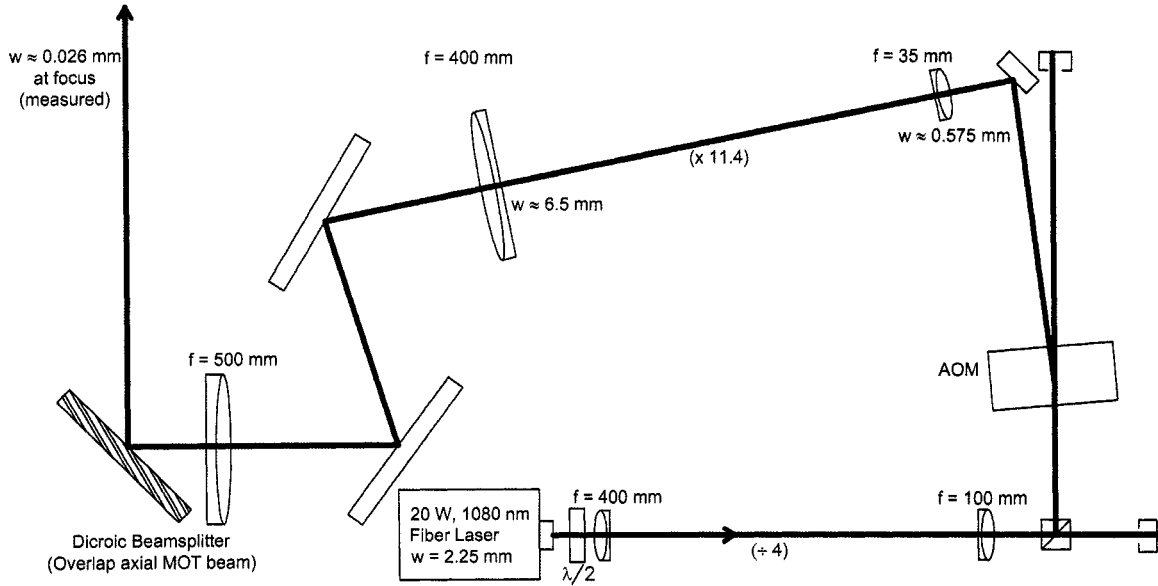


Figure 2.10 This optical trap setup is currently in use on the apparatus, and was used for the experiments described in Chapter 4. A careful characterization of the trapping potential is also provided in this chapter. This trap is improved from the previous version by the inclusion of a fiber laser (IPG Photonics YLR-20-LP) capable of outputting 2 - 20 Watts at 1080 nm. This laser allows for significantly increased trap depth. The output of the laser fiber is collimated at a beam waist of 2.25 mm, which is too large for the AOM (Crystal Technology Model 3110-197), so the beam waist is reduced a factor of four by a lens pair. A half wave plate and polarizing beam splitting cube are used to limit the optical power during the initial setup. We also find that the relative intensity stability of the laser is improved at running powers above 5 W, so the waveplate and cube are also used to dump excess power during normal operations, since the operating power in the trap is typically < 5 W, as described in the text. The first order of the AOM used to control trap power is expanded by another lens pair to a waist of 6.5 mm, which is the waist required to achieve the final trap focus of $26 \mu\text{m}$ using a 500 mm lens (again, mounted on a three axis translator). As before, all lenses are high quality doublets, and a dichroic beamsplitter (reflects IR, transmits visible: CVI SWP series) is used to direct the beam along the same axis as the axial MOT and optical pumping beams.

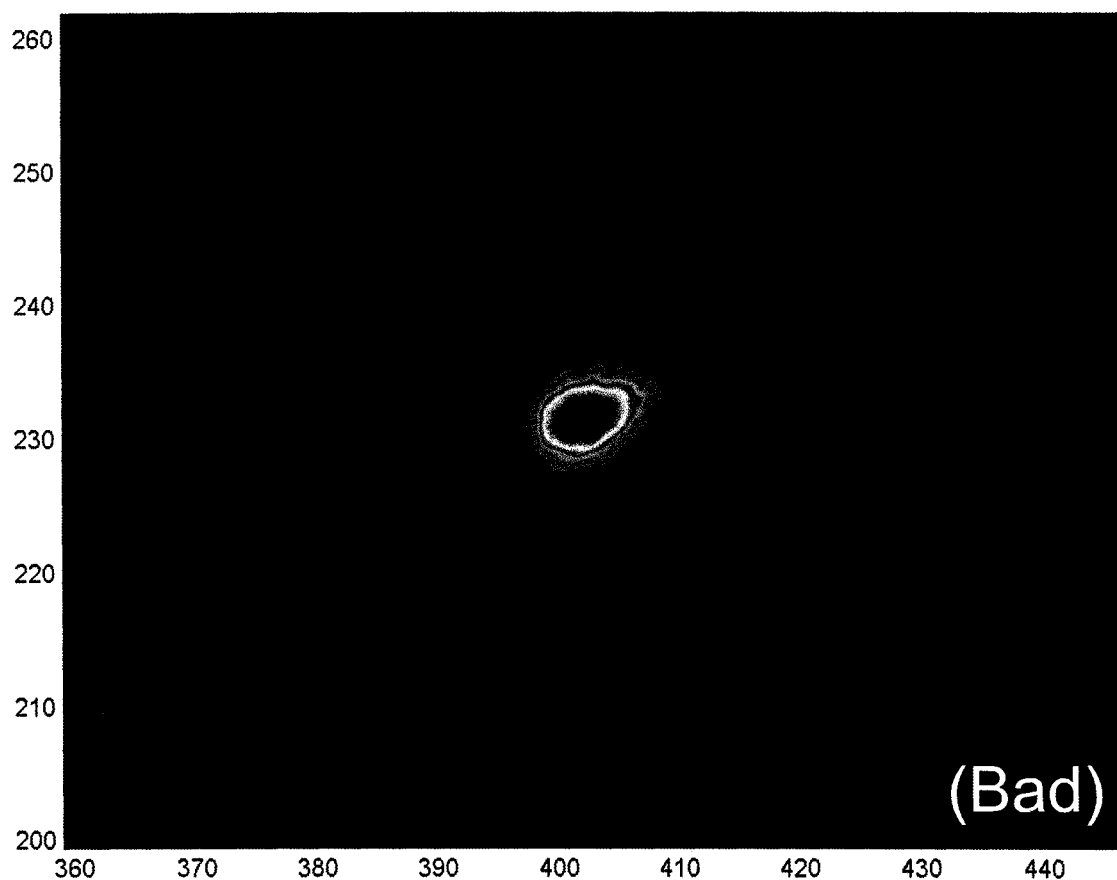


Figure 2.11 This image of the optical trapping beam was acquired prior to final alignment by direct exposure of an Electrim (EDC-1000N) CCD camera. Such images are used to fine tune the alignment of the optical setups, such as those shown in figs. 2.9 and 2.10 (this is of the latter). This image was taken before the focus (~ 1 mm) of the beam and shows an elongation in the horizontal direction that is a typical result of lens centration and tilt errors. The distortion of the beam continues through the focus, as is seen in the next fig. 2.12. For these images, the x and y axis labels refer to pixels, which are $7.4 \mu\text{m}$ square.

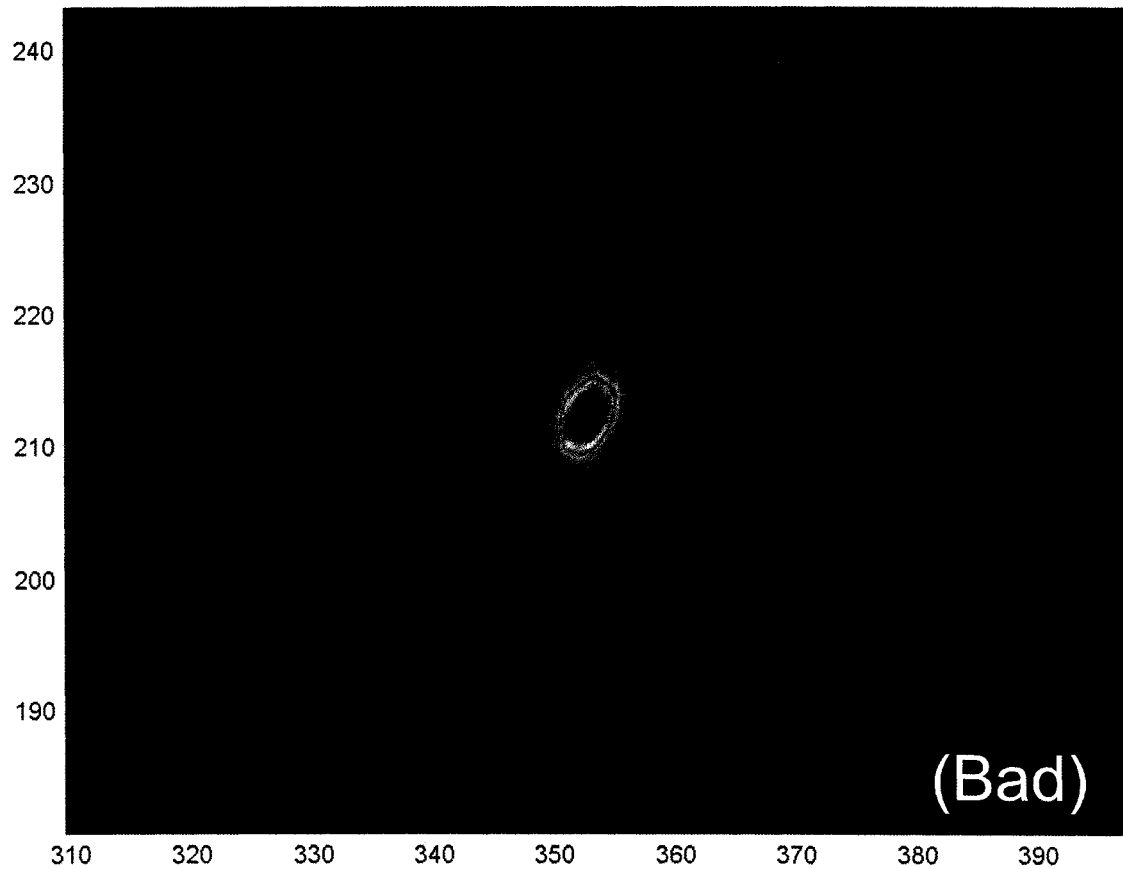


Figure 2.12 This image was taken nearer to the focus of the beam than that in fig. 2.11. The aspect ratio of the beam has now switched, since the dimension with the larger waist initially, now focusses to a smaller waist. The alignment errors that cause distortions such as these are small, however a trapping potential with this shape would prove difficult to accurately characterize. Additionally, the spatial distribution of the trapped atoms are particularly important in the experiments on imbalanced spin mixture presented in Chapter 4, so a more uniform and symmetric potential is required.



Figure 2.13 This is an image taken at the focus of the optical trap after optimization of the alignments of the optical components shown in fig. 2.10 using images such as those of the previous two figures as feedback. This focus is characterized by a symmetric round shape, both at the focus and in the far field. The waist of this beam is determined by a fit to a gaussian such as that shown in fig. 2.14.

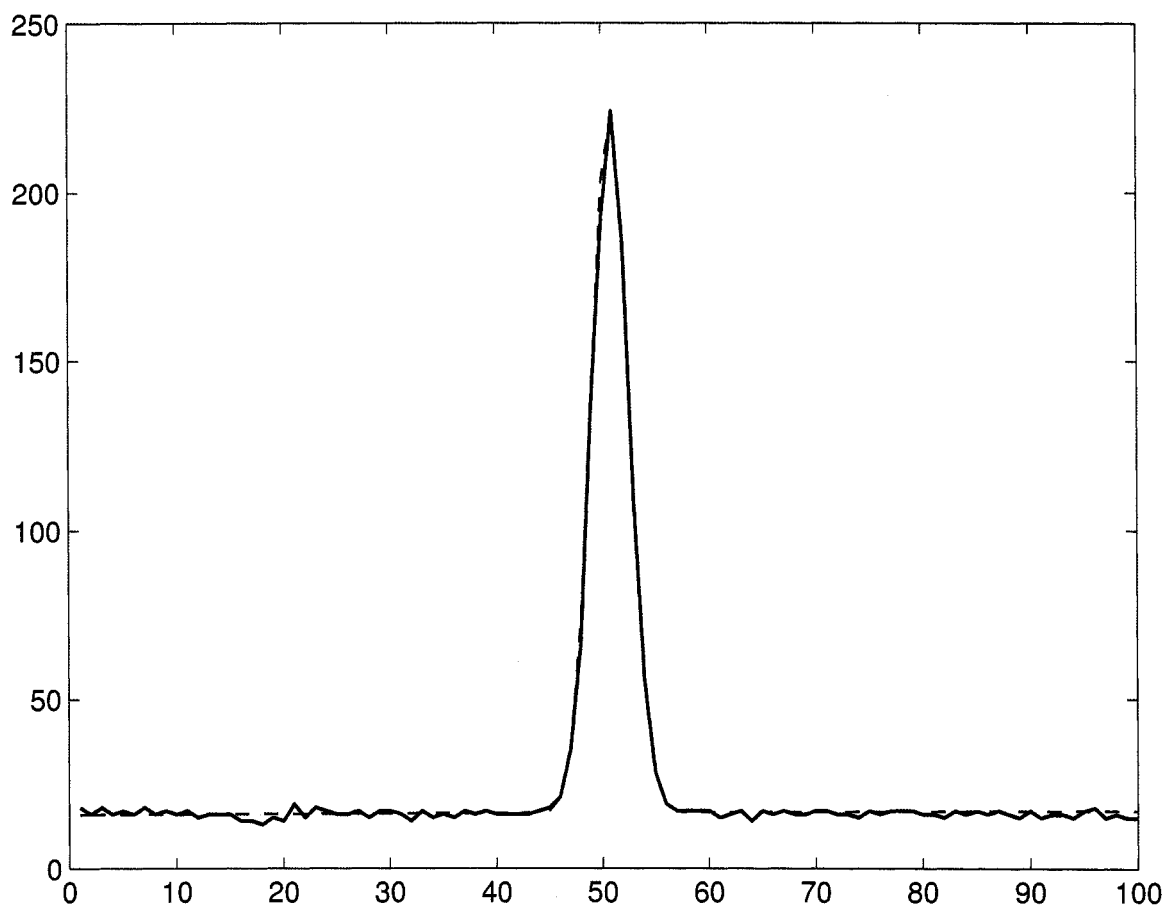


Figure 2.14 The blue line is a cut along one axis of the image in the previous figure (2.13). The red dashed line is the fit used to find the waist of the beam, which gives $26.0 \pm 0.5 \mu\text{m}$. The fitted waist versus focus position is used to determine the M^2 parameter, as in fig. 2.15. Such fits are done in multiple directions along the images to verify a symmetric beam.

beam waist is given by

$$w(z) = w_0 \left(1 + \left(\frac{zM^2\lambda}{\pi w_o^2} \right)^2 \right)^{1/2}, \quad (2.8)$$

where $M^2 = 1$ corresponds to an ideal focus. Were it an ideal gaussian beam, the Rayleigh length, R_L , would be $(\pi w_o^2/\lambda) = 1.97$ mm, for waist $w_o = 26.0$ μm , and $\lambda = 1080$ nm. The effective R_L of a the “real” beam is reduced by a factor of M^2 , since the divergence angle is larger than for the ideal case [33]. Figure 2.15 shows this measurement made for the current optical trap. From this plot, it is determined that the beam is nearly ideal, with $M^2 \leq 1.17$. This measurement places an upper limit on the value of M^2 because the measured waist at the focus approaches the resolution limit of the camera (~ 7 μm pixel size) used, and so it is possible that the measured minimum waist (26 μm) is an overestimate. (We will soon see, however, that measurements of the radial trapping frequencies confirm this value.)

Calculated Trap Frequencies

A parameter that is commonly used to describe trapping potentials is the harmonic oscillation frequency(s) ν_i of an atom in the trap. The frequency of the trap is dependent upon which atom (isotope), as $\nu \propto m^{-1/2}$, where m is the atomic mass. Additionally, since the potential is not harmonic in shape, but instead gaussian, the harmonic frequencies represent an approximation for small atom excursions from the center of the trap.

To calculate the frequencies of the trap, we set the potential given by eq. 2.4 equal to the harmonic oscillator energy,

$$U(r_i) = \frac{\hbar(I(r_i)/I_{sat})\gamma^2}{4\Delta} = \frac{1}{2}m\omega_i^2 r_i^2, \quad (2.9)$$

where r_i is the radial (r) or axial (z) dimension, and ω_i is $(2\pi)\nu_i$.

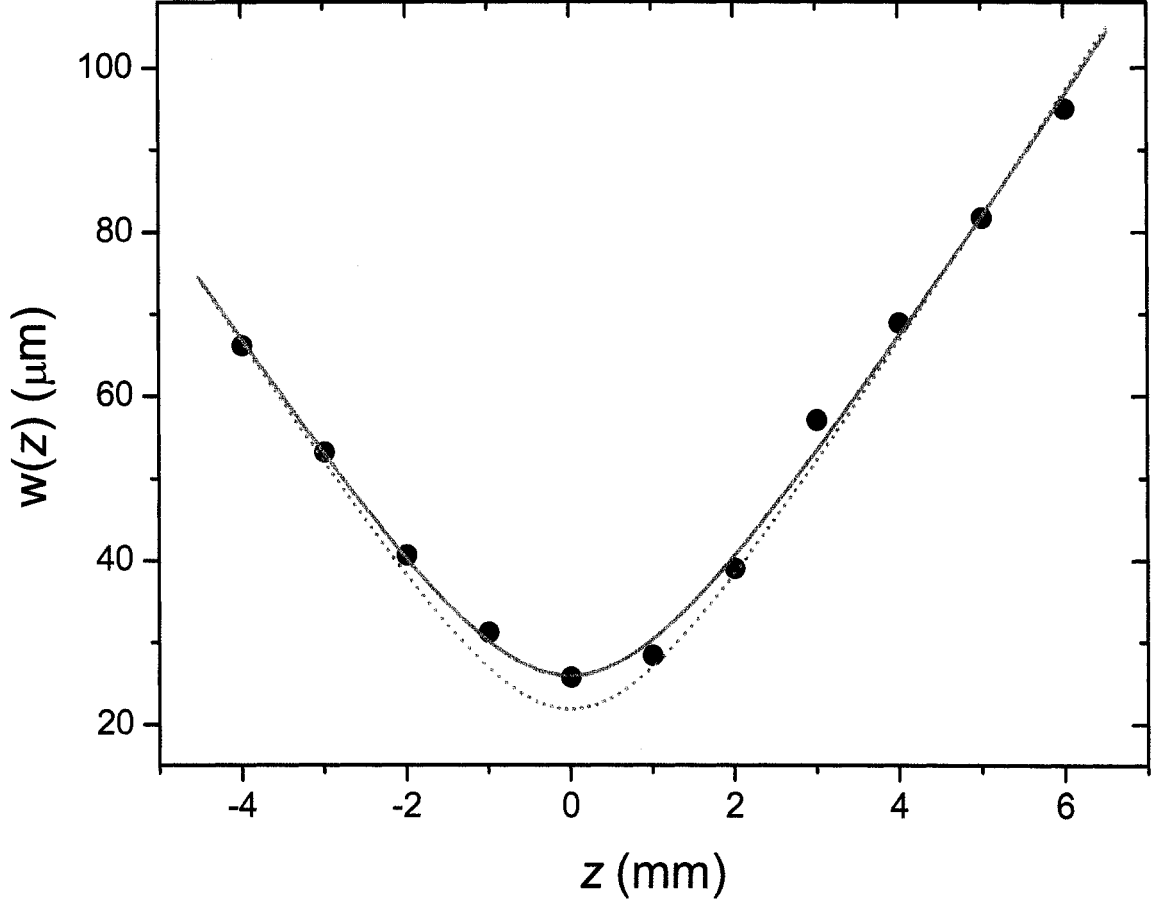


Figure 2.15 This plot of measured beam waist versus position along the beam propagation direction is used to find the M^2 parameter and minimum waist w_o of the optical trap beam. The solid line is a fit to eq. 2.8 and gives $M^2 = 1.17 \pm 0.04$, and $w_o = 26 \pm 1 \mu\text{m}$. The dotted line shows a fit only including the points farther from the focus with the constraint $M^2 = 1$. Though an M^2 value can not be used to completely characterize a given beam, its fit value near 1 along with the inspection of the images of the beam show that the quality of the focus used for this optical trap is high. (By performing this analysis on multiple axes of the beam we have also ruled out any measurable astigmatism.)

The peak radial frequency is determined by setting $z = 0$, so that $w(z) = w_o$. This gives $I(r, z = 0) = I_o e^{-2r^2/w_o^2}$. Expanding this expression for small r , and combining with eq. 2.9 gives

$$U(r, z = 0) = \frac{\hbar(I_o(1 - \frac{2r^2}{w_o^2}))/I_{sat})\gamma^2}{4\Delta} = \frac{1}{2}m\omega_r^2 r^2. \quad (2.10)$$

This can be rearranged such that the radial frequency is given by

$$\omega_r = \frac{\gamma}{w_o} \left(\frac{\hbar I_o}{m|\Delta|I_s} \right)^{1/2}. \quad (2.11)$$

For a gaussian beam, the peak intensity can be written in terms of the optical power, P , and the beam waist as $I_o = (2P)/(\pi w_o^2)$. Inserting this into eq. 2.11 gives the radial frequency in terms of the measurable quantities, power and beam waist:

$$\omega_r = 2\pi\nu_r = \left(\frac{2P\hbar\gamma^2}{\pi m|\Delta|w_o^4 I_s} \right)^{1/2}. \quad (2.12)$$

In a similar fashion, the axial frequency of an ideal beam can be calculated by $U(r = 0, z) = \frac{1}{2}m\omega_z^2 z^2$. This gives, for small z ,

$$\omega_z = 2\pi\nu_z = \frac{\gamma}{R_L} \left(\frac{\hbar I_o}{2m|\Delta|I_s} \right)^{1/2} = \frac{w_o}{\sqrt{2}R_L} \omega_r. \quad (2.13)$$

Now, to plug in some numbers: for a power of 1 W, and $w_o = 26.0 \mu\text{m}$ at 1080 nm, the predicted frequencies for ${}^6\text{Li}$ are

$$\omega_r = (2\pi)3.06 \text{ KHz and } \omega_z = (2\pi)28.6 \text{ Hz}. \quad (2.14)$$

Radial Frequency Measurement

The frequencies calculated from the characterization of the trapping beam should be relatively accurate, however, it is still a good idea to measure the frequencies directly, since our data analysis depends so critically on knowing these frequencies. Measuring the actual frequencies will also provide a check for the value of the beam waist w_o obtained by the direct measurements detailed earlier.

The technique for the measurement of the radial trapping frequency, ν_r , utilizes the heating that occurs in the trapped gas when the radial trap position oscillates with a frequency equal to ν_r . This measurement consists of modulating the position of the trap with a sinusoid of various frequencies, and monitoring the fraction of the gas that remains after some time. Modulation is accomplished by inputting a sine wave function into the FM input of the synthesizer that sets the frequency of the optical trap turn-on AOM*. Variations in the drive frequency of this AOM result in spatial variations in the radial position of the focus.

When the trap is shaken in the radial direction, energy is imparted at a rate given by O'Hara [34]

$$\langle \dot{E} \rangle = \frac{\pi}{2} m \omega_r^4 S_x(\omega_r) \quad (2.15)$$

where S_x is the one sided power spectrum of the position fluctuations. (This is the same heating mechanism that has been problematic on our experiment in the past [21].)

Since, in this case, we are driving the trap with a pure frequency, we expect to observe maximum heating (via loss of atoms from the trap) when the drive frequency coincides with the trap frequency*. That is, $S_x = 0$ for $\omega_{shaking} \neq \omega_r$ and so $S_x > 0$ when the trap is shaken at the trap frequency. Figure 2.16 shows a loss spectrum for ^7Li taken by modulating the position of the trap at various frequencies at a power of 1.00 W. At this power, we predict a radial frequency from eq. 2.12 of 2840 Hz. This value agrees well with the position of the resonance.

We have also performed such measurements for different trap powers. Figure 2.17 shows the central loss frequencies versus the square root of the power. The linear relation verifies the correct dependence of the frequency on power, and confirms the prediction of eq. 2.12. Confirming this dependence also enables us to predict the

*Normally this AOM is controlled by a VCO, but for this measurement a synthesizer is used due to its more predictable modulation behavior.

*We will for now neglect the effects of the anharmonic aspect of the confinement.

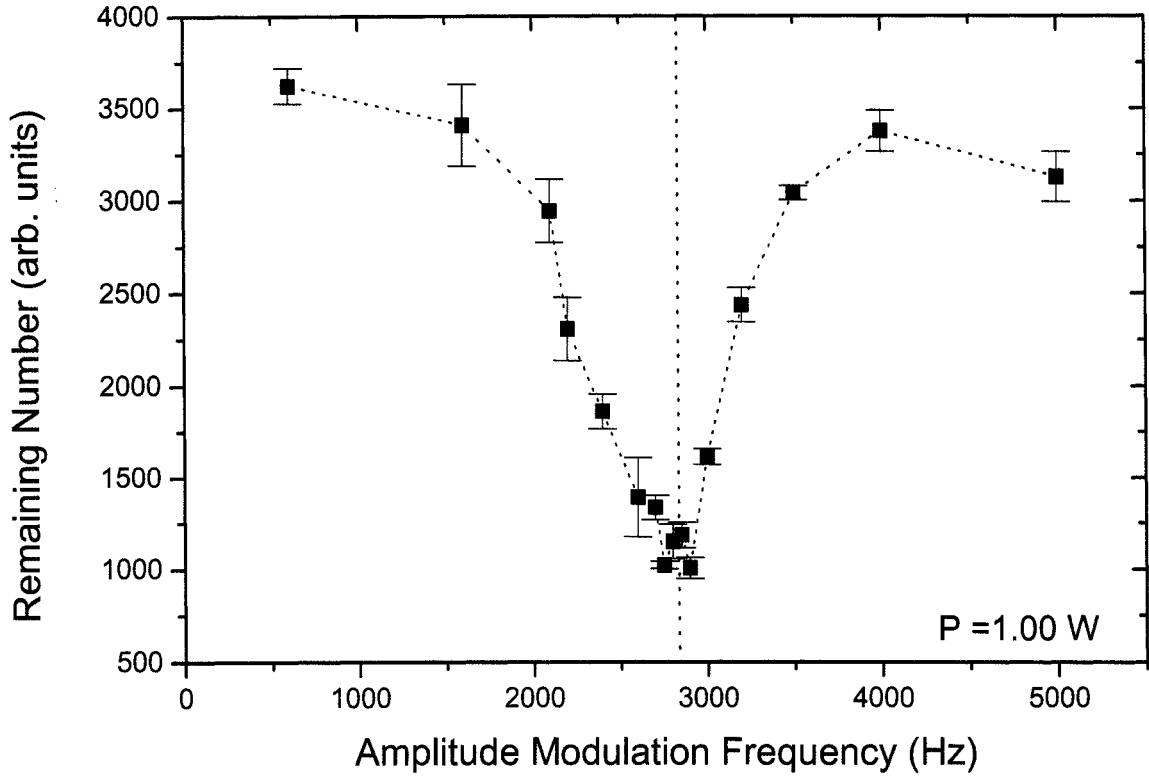


Figure 2.16 The data points correspond to the number of atoms left in the trap after its pointing is modulated at various frequencies for 75 ms. Since the peak heating rate occurs when the trap is modulated at the radial trapping frequency, the frequency of peak loss corresponds to ν_r . The dotted green line corresponds to $\nu_r = 2840 \pm 250$ Hz which is the radial frequency for ^7Li calculated from eq. 2.12, given a beam waist of $26 \pm 0.5 \mu\text{m}$ and an optical power in the trap of 1.0 ± 0.1 W. The asymmetry in the resonance shape results from the gaussian shape of the potential, since atoms sample parts of the trap that are far from the center of the potential, particularly as they are heated. Since, at large r , the gaussian potential is less steep than the corresponding harmonic approximation, this effect tends to weight the distribution towards the low frequency side. For the experiments presented in Chapter 4, it is possible for the Fermi energy of the trapped gas to be comparable to the trap depth (up to $\sim 75\%$). In this case, an effective frequency, corresponding to the center of the resonance (not the peak) obtained from a fit to a symmetric lorentzian function, was used as a first approximation.

radial frequency for any trap depth by measuring the trapping power.

Axial Potential Characterization

The above procedure for measuring the radial waist depends on the strong (4th power) dependence of the heating rate on the trapping frequency (eq. 2.15). Since the axial frequency is predicted to be more than 100 times smaller than the radial frequency (eq. 2.13), this method is no longer practical, since the time required to impart enough heat to cause a signal loss is prohibitively long (as it is, the radial frequency measurements take 50 - 100 ms). In addition, it is more difficult experimentally to modulate the axial position of the focus of the beam. For these reasons, we have adopted another technique for measuring the axial frequency.

The axial frequency is measured by imparting a kick* to a cloud of atoms and imaging at a later time. In order to most accurately represent the conditions that the majority of our data is taken under, this measurement is typically done in the high magnetic bias field using an evaporatively cooled gas of paired ^6Li atoms (discussed in the next section). By repeating and varying the delay time, the axial position of the cloud may be mapped out as a function of time. By fitting a sinusoid to these oscillations, the trapping frequency can be directly measured.

Figure 2.18 shows such an oscillation, taken at a trap power of 13.8 mW. At this trap depth, the axial frequency, predicted from eq. 2.13 is $\nu_z = 3.36$ Hz. The fit to the data, on the other hand, gives $\nu_z = 7.470(7)$ Hz. After some amount of contemplation, we have realized that the discrepancy arises because the “flat” bias field which is applied to access the Feshbach resonance is not completely flat, and in reality, the curvature in this field contributes to the axial potential. Now, in

*The “kick” is provided by quickly turning on a gradient magnetic field midway through the evaporation trajectory to shift the axial position of the trap. This works because, as we shall see shortly, there is a magnetic component to the axial confinement that is offset from the optical potential. By varying the trap depth at which the gradient field turns on (thereby centering the two potentials), we may adjust the initial displacement from the trap center.

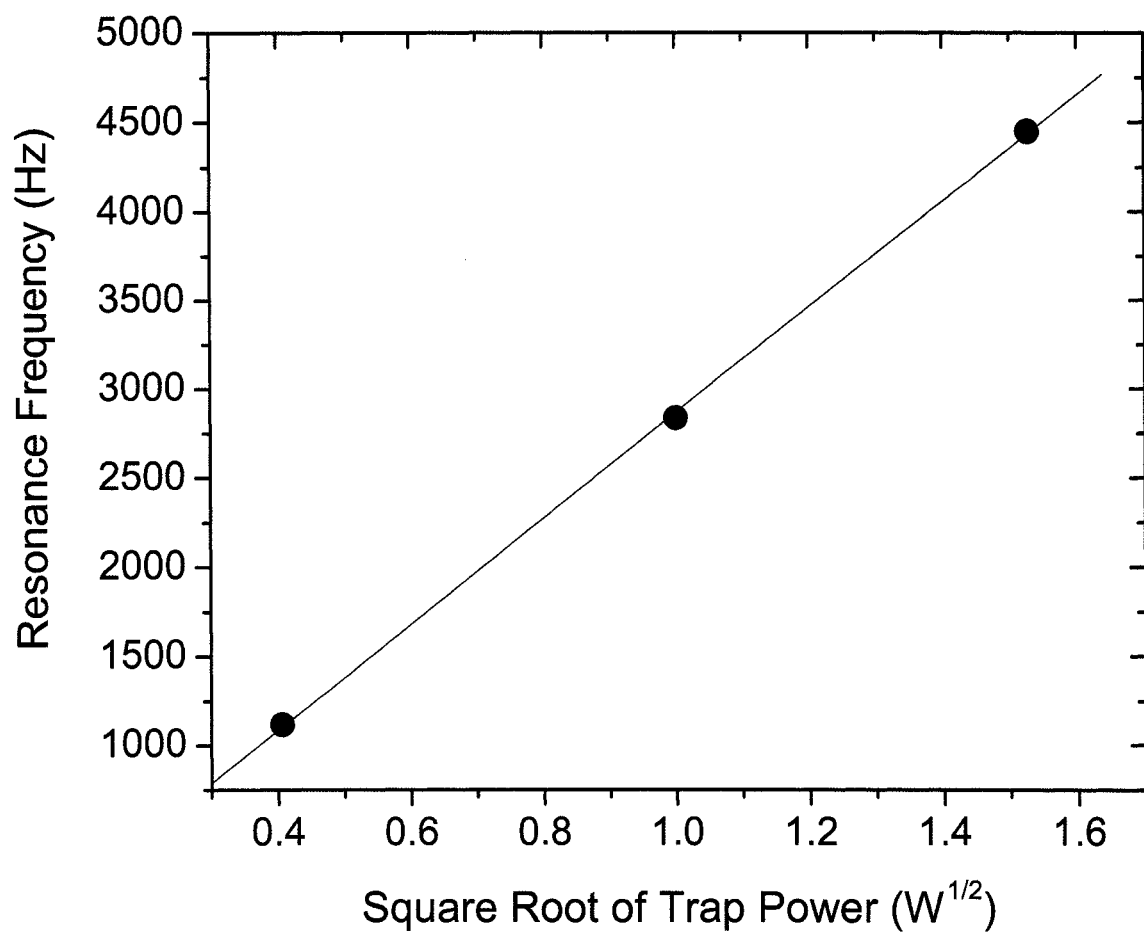


Figure 2.17 The data points correspond to frequencies obtained from resonance plots such as in fig. 2.16 taken at different trap depths. The frequencies are plotted versus the square root of the optical power. The linear fit is consistent with the dependence predicted by eq. 2.12.

order to completely understand the axial potential, it is necessary to characterize this contribution.

By measuring the axial frequency at various trap depths and magnetic fields, the magnetic plus optical potential can be determined. Figure 2.19 shows a schematic showing the axial potential formed from the optical trap as well as a potential formed from magnetic field curvature. Since the centers of these two potentials do not overlap at the same position, a gradient field from a single coil is also applied which serves to move the minimum of the magnetic potential. The optical and magnetic potentials are overlapped at each field by adjusting the strength of the gradient field.

The model which we utilize for this system is a magnetic field with quadratic curvature plus the optical potential. In such a case, the axial frequency would be written as

$$\nu_z = (\nu_{z(opt)}^2 + \alpha B)^{1/2}, \quad (2.16)$$

where $\nu_{z(opt)}$ is the frequency associated with the optical contribution, B is the bias magnetic field, and α is a proportionality constant to be determined. This may be re-arranged so that

$$(\nu_z/\nu_{z(opt)})^2 - 1 = \alpha(B/\nu_{z(opt)}^2). \quad (2.17)$$

Figure 2.20 shows a plot of $(\nu_z/\nu_{z(opt)})^2 - 1$ versus $B/\nu_{z(opt)}^2$ extracted for oscillations, such as that shown in fig. 2.18, taken at magnetic fields ranging from 650 - 920 G. From the slope of this graph, the constant $\alpha = 0.051 \text{ Hz}^2/\text{G}$ is extracted. For all points, the model predicts the measured frequency to within 1-2%.

Since the magnetic field provides a confining potential for the atoms in states $|1\rangle$ and $|2\rangle$, which are high field seekers, we can conclude that there is a magnetic field maximum in the axial direction. There can be no global magnetic field maxima in free space, so the field must spatially be a saddle point. Such a field is anti-confining in the radial direction, though the contribution is negligible compared to the optical radial potential that ranges from a few hundred Hz at the lowest trap depths to a

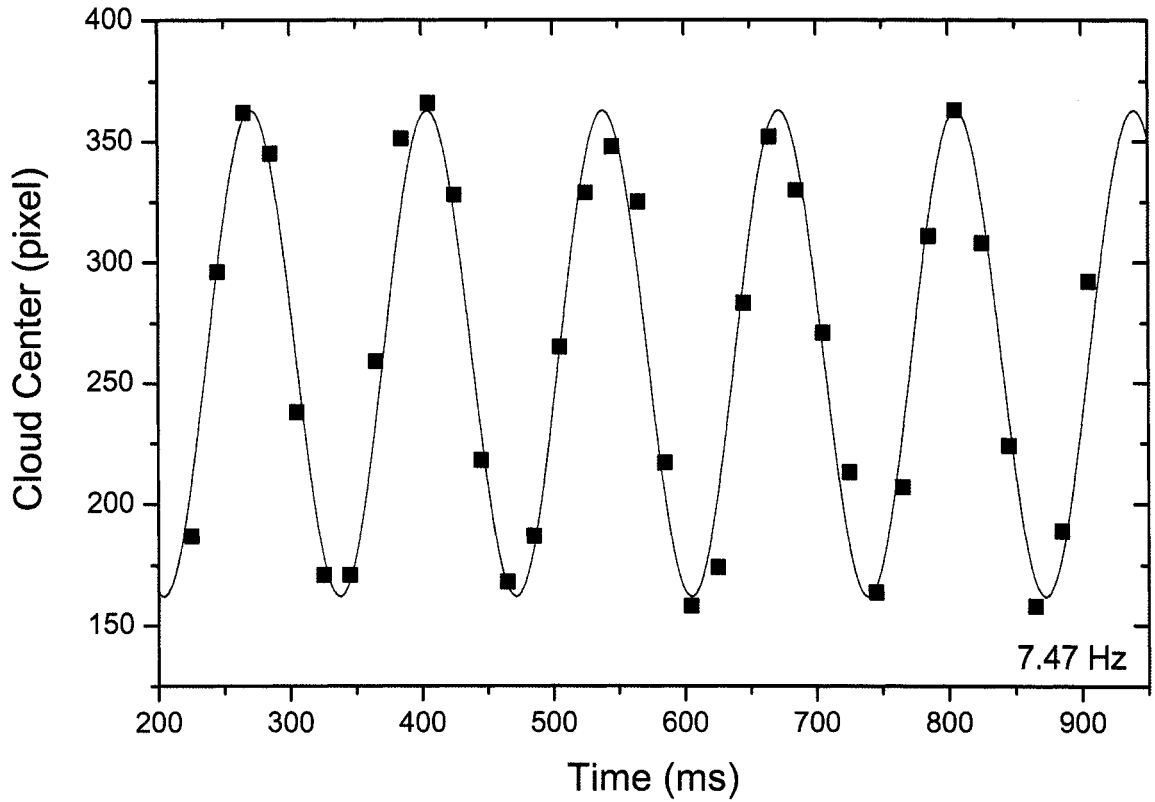


Figure 2.18 The data points show the measured axial position of an evaporatively cooled cloud of ${}^6\text{Li}$ versus time, after it has been kicked using a transient magnetic field gradient (see text). (Each point is a separate experimental run.) The red line is a fit to a sinusoid, and gives an oscillation frequency of $7.470(7)$ Hz. This value is significantly higher than that predicted from the previous analysis of the optical potential (3.36 Hz). This discrepancy is due to additional confinement provided by curvature in the applied magnetic bias field, as discussed in the text. This plot was taken at 834 G, with a trap power of 13.8 mW which corresponds to a trap depth of $0.6 \mu\text{K}$.

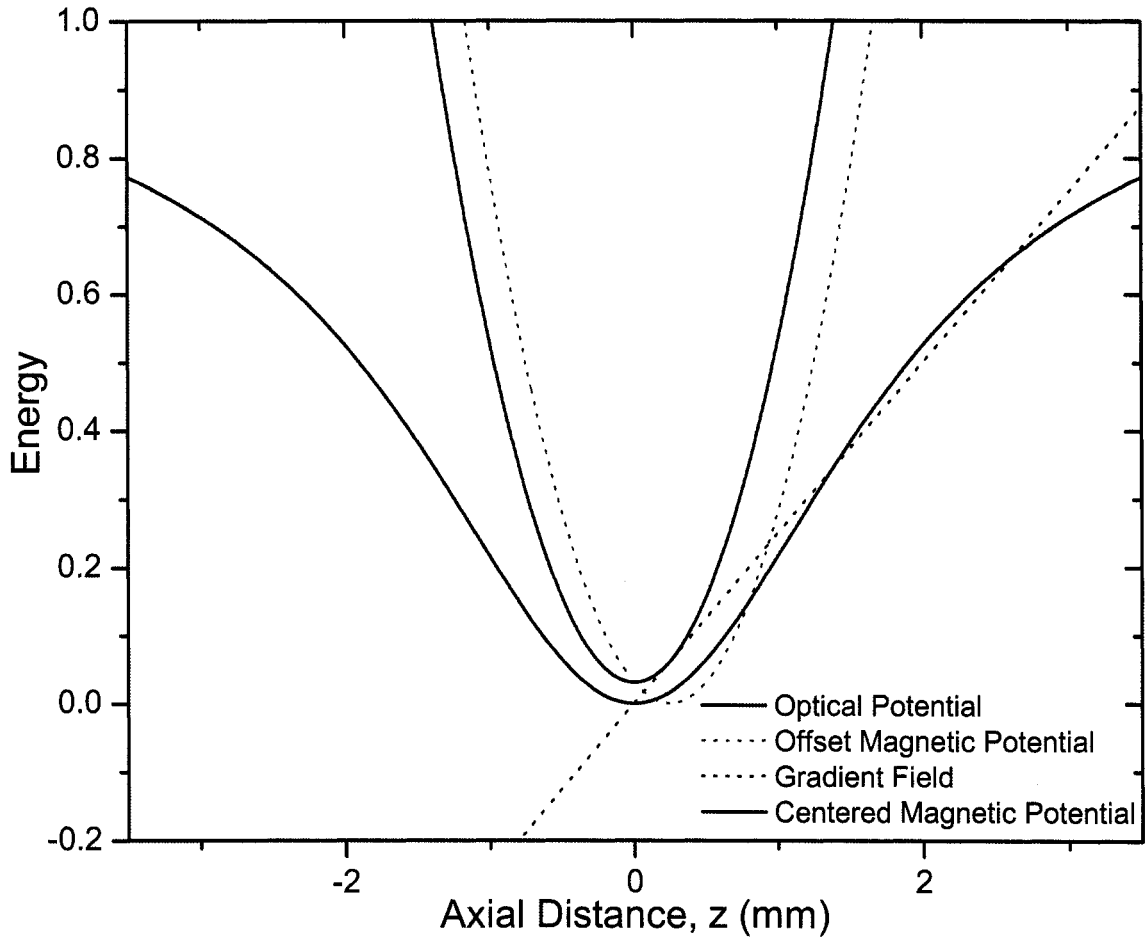


Figure 2.19 Shown are the various contributions to the axial potential. The red curve is the optical potential given by eq. 2.6 ($U(r = 0, z)$). The curved dotted green line is the harmonic contribution from the magnetic field curvature, which does not overlap with the optical potential. The straight black dotted line is the field gradient created from a single coil that is used to move the center position of the harmonic component. Since the coil is far from the center of the trap, the gradient appears linear on this scale. The solid blue line is the sum of the gradient with the magnetic curvature. The gradient field is changed for each high field value so that the harmonic magnetic component is overlapped with the optical potential.

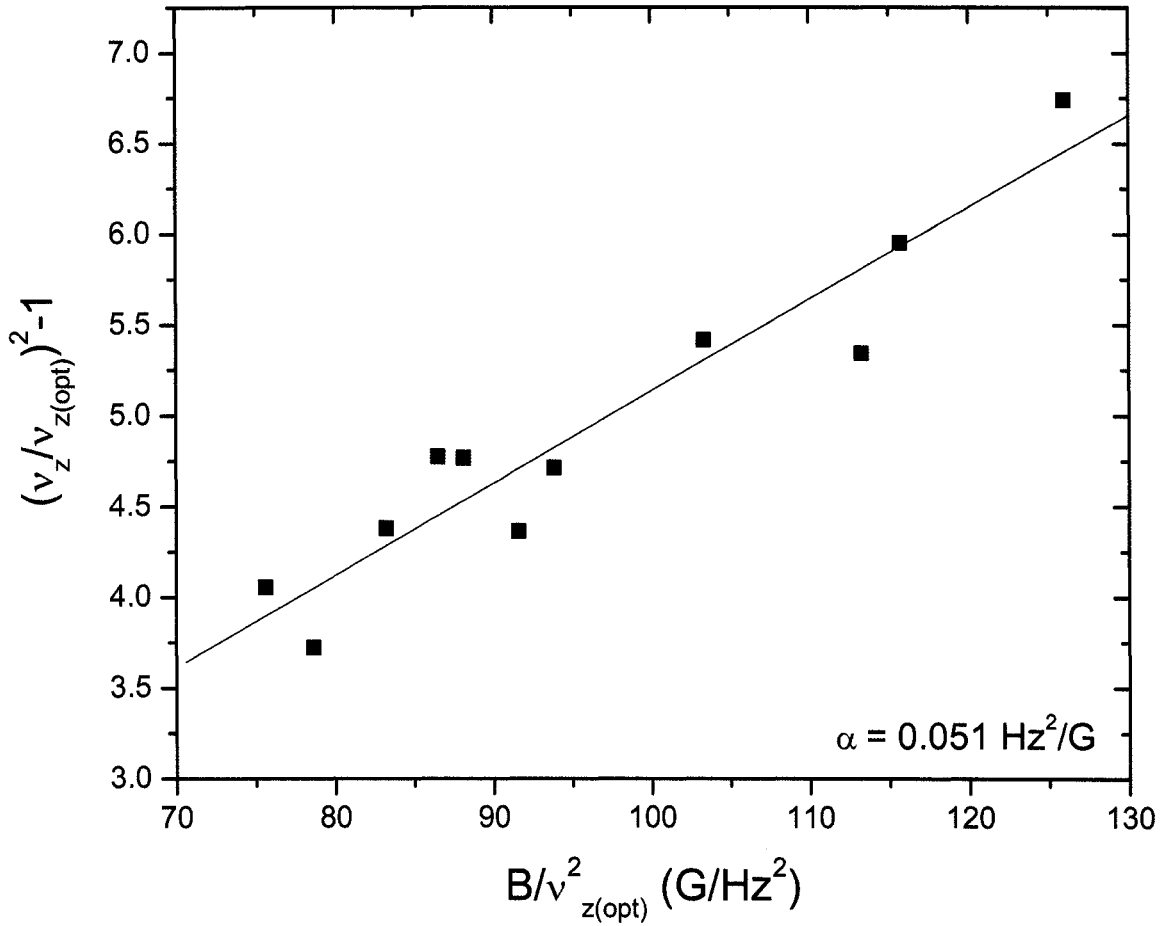


Figure 2.20 This is a plot of $(\nu_z/\nu_{z(opt)})^2 - 1$ versus $B/\nu_{z(opt)}^2$, where ν_z is the measured axial frequency, $\nu_{z(opt)}$ is the predicted optical contribution, and B is the magnetic bias field strength. From this plot, a value of α is extracted so that the axial frequency may be calculated from eq. 2.16 for a known trap depth and bias field. The linear dependence of the data in this plot lends confidence to the model shown in the previous fig. 2.19 and underlying eq. 2.16.

couple of kHz at full trap depth. This field curvature results from slight imperfections in the spacing of the coils used to create the bias field.

Optimal Trap Loading

The transfer of atoms from the magnetic trap to the optical trap is a crucial step in the sequence of events which comprise an experimental run. Atoms are loaded into the optical trap at the end of the magnetic trap evaporation cycle. In the past, when the magnetic and optical traps were well mode matched (i.e. they provided similar trapping frequencies), the transfer took place quickly, with the optical trap ramping up as the magnetic trap turned off in an attempt to make the transfer adiabatic. With this scheme, however, any misalignment of the potentials would cause heating, and furthermore, the transfer efficiency was sensitive to timing variations.

With the current trap, the turn-on is accomplished by slowly ramping on the optical potential over a few hundred milliseconds while the magnetic trap is still on. Since the optical trap provides significantly higher radial trapping frequency than the magnetic trap, the extra squeezing due to the magnetic trap is negligible and so little extra heating is caused by having both on at the same time. Since both traps are on for an extended time, the atoms have a chance to find the optical potential, and so the transfer efficiency achieved with this method is less sensitive to the precise overlap of the optical and magnetic potentials. Similarly, the relatively long time scales involved reduce the susceptibility to inconsistencies resulting from timing variances.

For the current experiments, the trap is loaded from the magnetic trap with $N \sim 10^7$ fermionic ^6Li atoms. These atoms have been cooled to a degeneracy of $T/T_F \sim 0.1$, where T_F is the Fermi temperature in the magnetic trap, given by $T_F = \hbar\bar{\omega}(6N)^{1/3} \sim 7 \mu\text{K}$, where the mean frequency is $\bar{\omega} = (\omega_r^2\omega_z)^{1/3}$ with magnetic trap frequencies $\omega_r = 790 \text{ Hz}$ and $\omega_z = 79 \text{ Hz}$ [21].

Though atoms can be transferred to the trap at higher temperatures, when the gas

is further evaporatively cooled in the optical trap at the Feshbach resonance, highly degenerate clouds are not achieved. We find that it is most efficient to do the maximum amount of cooling possible in the magnetic trap prior to transfer. Additionally, due to off resonant scattering, running the laser at full power results in shorter lifetime and further negates any possible benefit. We have experimentally determined the optimal power for the optical trap by measuring the number of atoms remaining in the trap at some time after transfer as a function of power. Figure 2.21 shows that as power is initially increased, the number in the optical trap also increases. This is not unexpected, since the transfer heating scales as the ratio of mean frequencies of the two traps, $T_{final} = T_{initial}(\bar{\omega}_{final}/\bar{\omega}_{initial})$, where the frequency increases as the square root of the trap depth, U_0 , which is proportional to optical power. The result is that the ratio of U_0 to the temperature will increase with increasing power (as $U_0^{1/2}$). As U_0 is further increased, the number of atoms transferred is seen to plateau. This point corresponds to the transfer of the maximum number of atoms to the optical trap*. Further increase in the optical trap depth beyond this point only results in unnecessary heating. This power, at the cusp of the drop-off, corresponds to the point of best trade-off between transfer efficiency and heating. Given these results, the trap is typically run at a power of 2.4 W, safely away from the dropoff. This power gives $U_0 = 110 \mu\text{K}$.

2.3 High Field

After the optical trap is loaded, a bias magnetic field of up to 1000 G is created using the bias coils of the magnetic trap [21] (note: this is the field that contributes to the axial trapping potential). Once at the selected high field, the atoms may be transferred from the $F = 3/2, m_F = 3/2$ ($|6\rangle$ state) to the $F = 1/2, m_F = 1/2$ ($|1\rangle$ state) using a linear RF sweep. For a 40 ms sweep spanning 4 MHz, centered on the

*For a cloud of $0.5 - 1 \times 10^7$ ^6Li atoms, cooled to $T \sim 0.1 T_F$ in the magnetic trap, we observe the peak transfer efficiency to be around 50%.

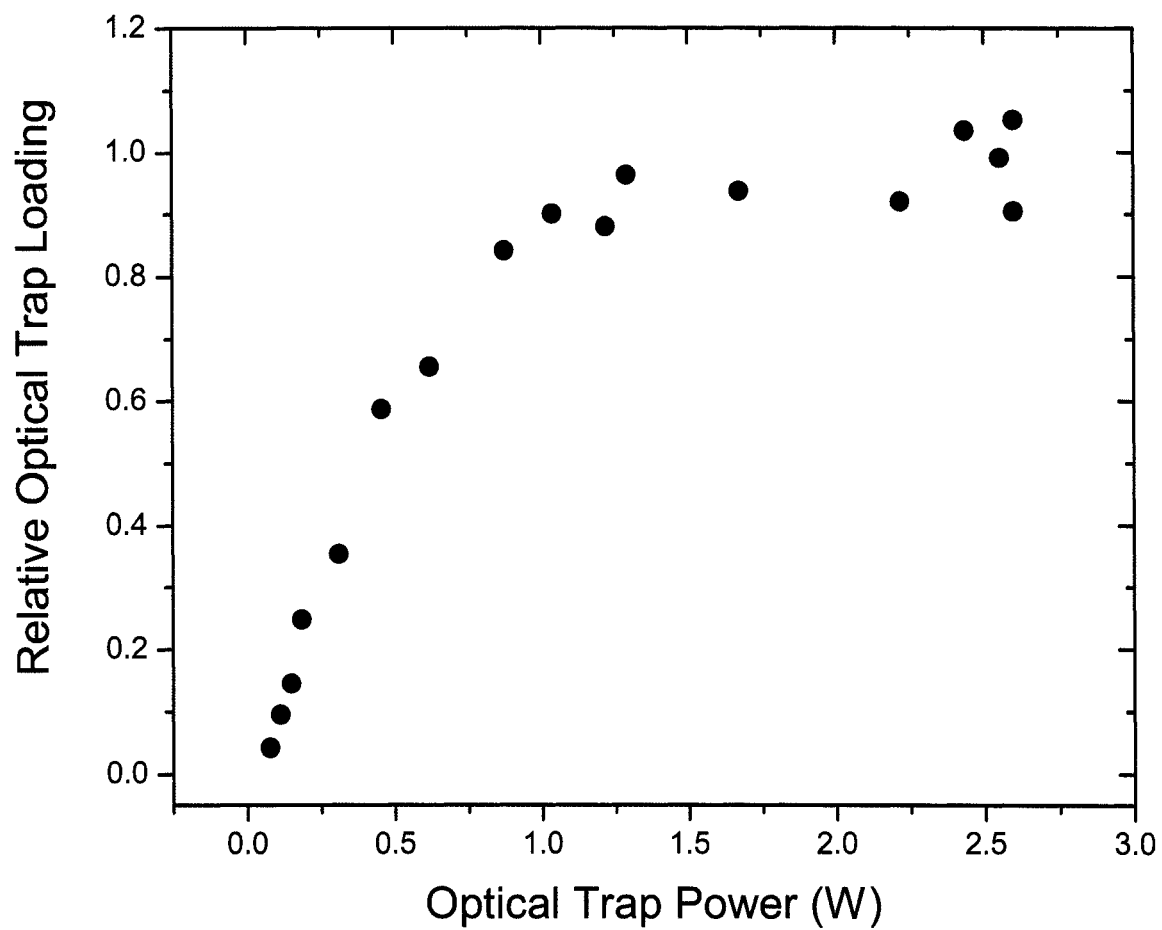


Figure 2.21 This plot shows the loading of the optical trap versus maximum optical trap power, and is used to determine the optimal power.

transition frequency (1-3 GHz, field dependent), nearly all the population may be transferred ($> 95\%$) via rapid adiabatic passage. Such transfers rely on coherence in the system, as will be described in more depth in the next section. We have found that if the inverse sweep time is too slow compared to the axial trapping frequency, coherence is lost and a complete transfer can not occur. Therefore, since the sweep time is limited, the transfer efficiency is ultimately limited by the coupling of the RF power into the chamber. In the current configuration, a piece of conductive copper tape attached to the inner surface of the re-entrant coil form serves as the antenna [21]. We have also experimented with loop antennas mounted on the re-entrant imaging system, but, in addition to perturbing up the imaging system, these designs have proven not to be as effective. For future use, we have also procured a commercially built tuned dipole antenna (RA Mayes, p/n: PD2450, 2450 MHz), which should be a much more efficient radiator at the frequencies of interest. In the current configuration of the apparatus, there is no effective location for placement of this antenna. However, the next time a coil form is extracted from the apparatus, the coil mounting plate will be modified so that the antenna can be placed inside the re-entrant flange, just behind the coil form.

Any small improvement in the $|6\rangle \rightarrow |1\rangle$ transfer efficiency is beneficial, since any atoms left in the $|6\rangle$ state lead to loss via three body inelastic collisions later in the experiment, when a spin mixture of states $|1\rangle$ and $|2\rangle$ ($F = 1/2, m_F = \pm 1/2$) is created. Such three-body losses have been observed in bosonic gases near Feshbach resonances [35–37], but are suppressed in two component fermionic gases due to the fact that two of any three bodies are identical fermions, and are therefore forbidden from interacting [38–40]. When a third unique particle is introduced, however, this suppression is lost. This effect is also shown in Chapter 4, where a third state’s population leads to a measured loss of the other two.

2.3.1 Spin Mixture

Pairing phenomena such as superfluidity requires interactions between fermions. To get interactions between ultracold fermionic atoms, two unique fermionic states are required, since the Pauli exclusion principle forbids s-wave interactions between identical fermions. We create a spin mixture of states $|1\rangle$ and $|2\rangle$ by driving RF transitions between them. Since these states interact via the broad Feshbach resonance that was introduced in the previous chapter, the spin mixture is typically created at a bias field of 650 - 820 G. In the experiment, this means that from the time the fermionic ^6Li atoms are loaded into the optical trap until the time the spin mixture is created, there are no interactions.

When the spin mixture is created, the gas should rapidly gain interactions and thermalize. Note, however, that interactions rely on an incoherent mixture of spin states rather than a coherent superposition of the two spin states. In the latter case, the gas remains non-interacting because each fermionic atom is in the same superposition state, as we have previously observed [19]. We previously demonstrated this coherence in the system by driving coherent Rabi oscillations between the two spin states, as shown in fig. 2.22. These oscillations were observed to persist for several seconds without decay. The onset of coherence can also be detected by monitoring the population of the gas, since interactions facilitate evaporation from the trap and thereby reduce the number. This effect is shown in fig. 2.23.

We believe that the coherence previously observed in this system was a result of an extremely flat bias magnetic field, whereas in their current configuration, our coils produce a slight curvature in addition to the bias field. As the atoms traverse the trapping region (and collide) in the inhomogeneous field, they become irreversibly mixed and therefore become incoherent. Using the current coil set, we are no longer able to observe any signs of coherence on the time scale of the states $|1\rangle$ and $|2\rangle$ mixture pulse.

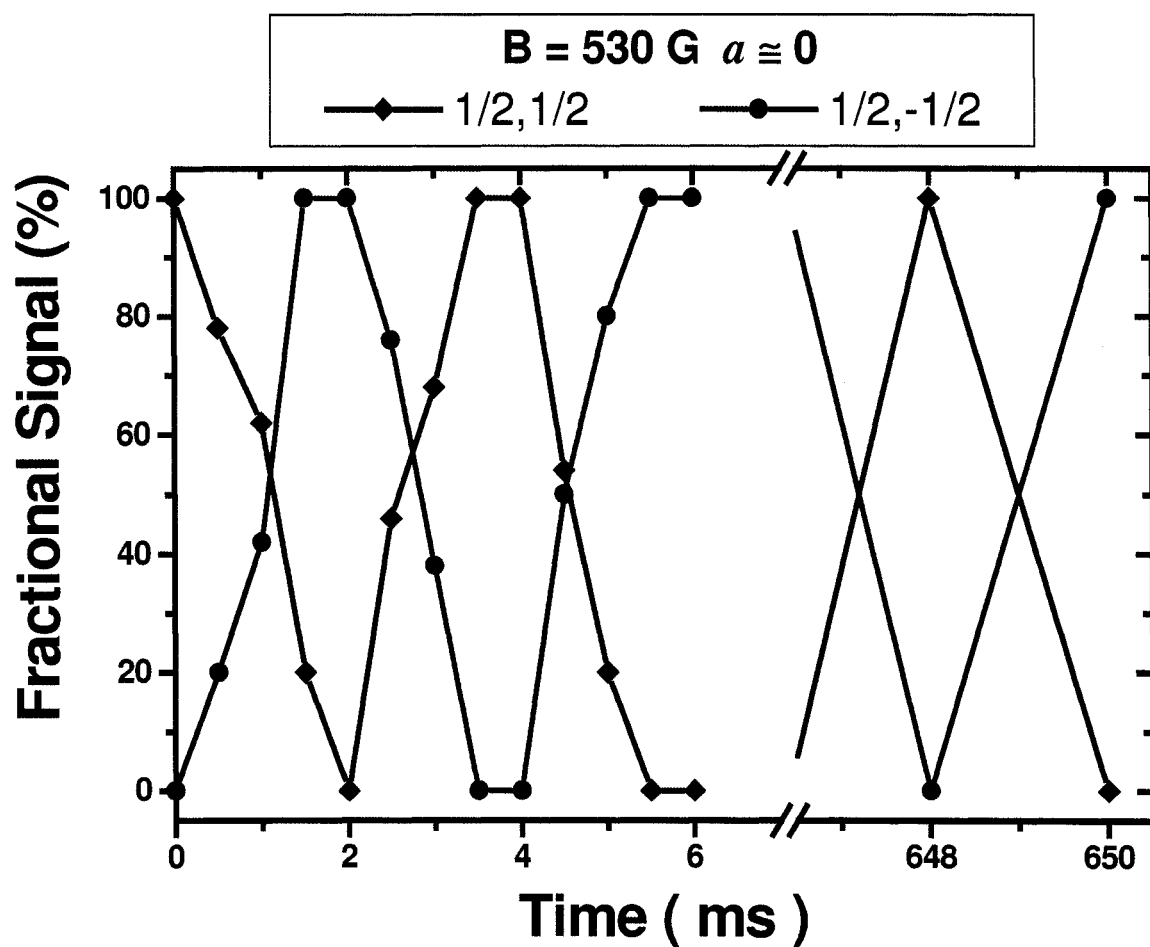


Figure 2.22 Rabi Oscillations driven between the two lowest hyperfine levels of ^6Li at 530 G, where $a \cong 0$. Oscillations were also observed at fields where the predicted interactions were non-zero. This indicates a suppression of the interactions through coherence. In either case, oscillations were observed for > 10 seconds, with no sign of damping.

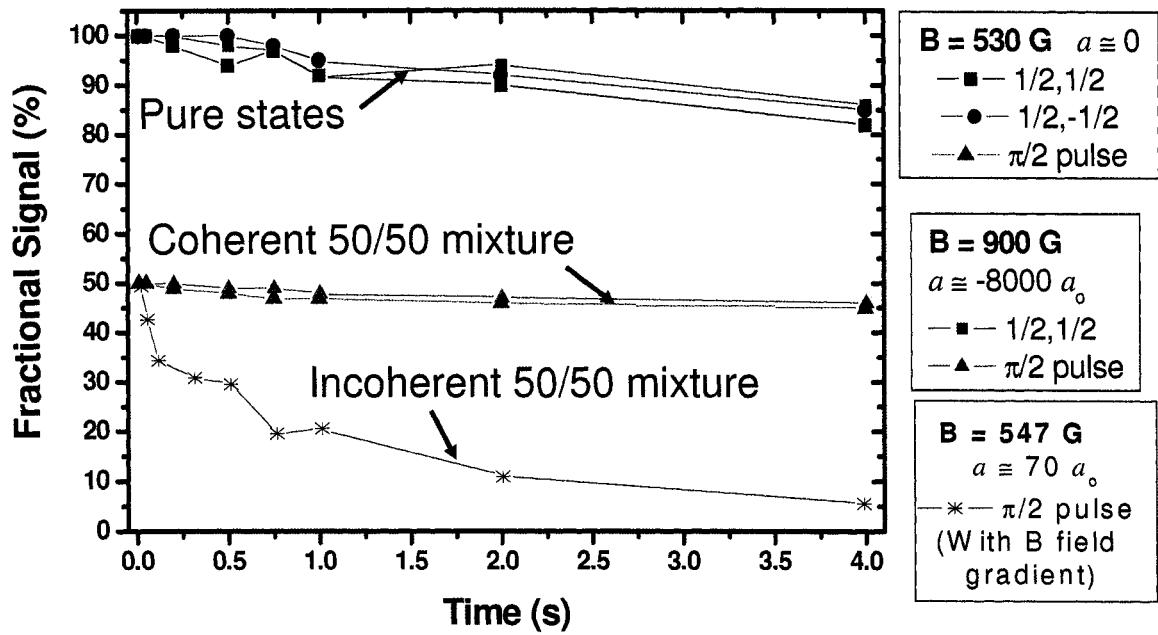


Figure 2.23 The population in the optical trap as a function of time for various pure states and spin mixtures. The pure states give a background lifetime for the trap, since they have no interactions. If the gas were to interact, it would seek a thermal equilibrium through evaporation, which in turn would show up as a loss of atoms. Indeed, the gas which has been incoherently prepared shows a much shorter lifetime, indicating the appearance of interactions. (The mixtures are shown as 50%, since there is half the number in each state.)

For the experiments presented in the next two chapters, it is crucial to have good control over the spin mixture, and in particular to have the ability to create an exactly even mixture (though we will intentionally create mismatched mixtures as well). An even mixture may be created in a number of different ways: one could sweep a weak RF pulse across resonance so that only half of the population is transferred, or one may pulse on a fixed RF frequency and drive a $\pi/2$ pulse. While both these methods could work, their performance depends crucially on the RF coupling strength as well as exact knowledge of the transition frequency (particularly in the latter case). In practice, it is difficult to control such parameters to the precision necessary to ensure an exactly even mixture. In addition, inevitable fluctuations in the measurement of the atom number will further complicate the situation and add to the uncertainty. Instead of using these techniques, we have developed an alternate method that reduces the sensitivity to experimental parameters, and ensures an exactly even mixture can be made.

Our method incorporates many RF sweeps across the transition frequency, each one transferring a relatively small fraction of the population. The effect of many such ramps is to cause the populations of the two states to converge. With this implementation, the final spin mixture is insensitive to the efficiency of each ramp, and since the ramps may be relatively weak, the sweep can be broad so that the exact transition frequency is not crucial. Figure 2.24 shows the effect of many weak ramps on the populations of the two states. From the fig., it is evident that an even mixture is created after 100 ramps, even for single sweep efficiencies of a few percent.

2.3.2 Optical Trap Evaporation Trajectories

Once a spin mixture is created, it must be further cooled in order to perform experiments in the quantum degenerate regime. The gas is cooled by forced evaporation from the optical trap and is accomplished by reducing the trap depth (laser power)

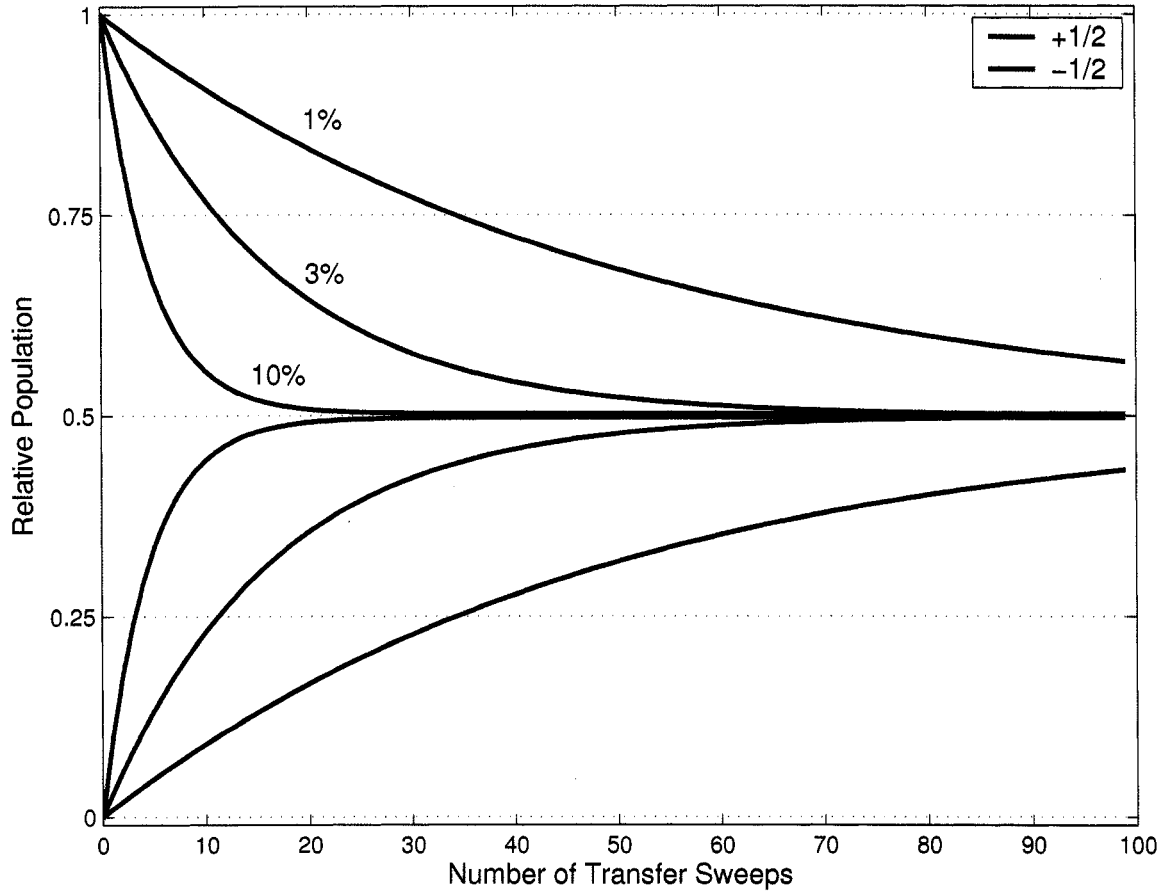


Figure 2.24 These curves show the populations of two spin states of ${}^6\text{Li}$ ($F = 1/2$, $m_F = \pm 1/2$) in the optical trap. During the mixture preparation, a sequence of 100 frequency sweeps, centered on energy separation ~ 76 MHz of the two states, transfers atoms from one state to the other. The three curves for each spin state correspond to the transfer efficiency of a single sweep. Using this method, it is possible to create an even mixture from an initially pure $m_F = +1/2$ state, using sweeps with efficiencies as low as 3%. The 100 sweeps are applied in a saw tooth structure (two sweeps/cycle) over a period of one second to ensure ample time for decoherence of the mixture.

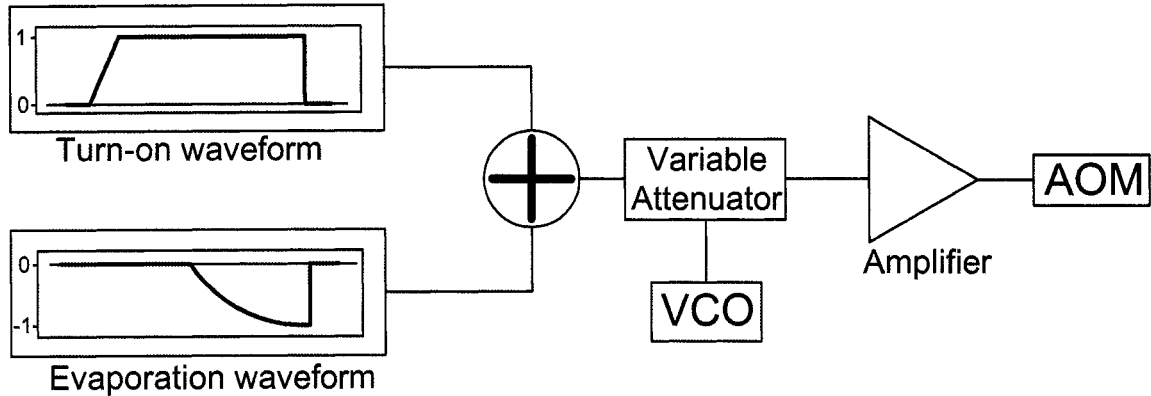


Figure 2.25 The power in the optical trap is controlled by varying the RF power to an AOM (see figs. 2.9, and 2.10). The RF power is controlled by a voltage controlled attenuator (Minicircuits ZMAS-1, which is technically a current based device). The control voltage is provided by the sum of two arbitrary waveform generators (Agilent 33120A). One provides the trap turn-on waveform, and the other provides the evaporation waveform. The final trap depth is fine-tuned by adjusting the amplitude of the evaporation waveform.

in a controlled way.

After experimentation with many different optical trap trajectories, we have determined that an exponential trajectory in time gives the best results (so far). This is not necessarily the optimized trajectory for cooling a strongly interacting Fermi gas [41], however, by increasing the evaporation time, we are able to achieve very effective cooling. Since the optical trap evaporation is on the order of one second out of a ~ 65 second cycle, a slow trajectory does not significantly affect our data output rate, nor are non-evaporative losses significant over this time.

The trap laser intensity is controlled by sending a control voltage to a variable RF attenuator that sets the diffracted power from the switching AOM (fig. 2.25). We use a programmable arbitrary waveform generator to send the voltage waveform. The response of the variable attenuator and AOM used to control the trap depth is not linear with input voltage, so if an exponential voltage waveform is used, the optical intensity will not vary exponentially. Instead, to precisely control the evaporation trajectory, it is necessary to characterize the response of the attenuator and AOM.

Figure 2.26 shows the relative power in the trap versus control voltage. The voltage is negative because it is added to another separate waveform that is used to turn the trap on. This turn-on function is fit to an empirically determined function given by

$$I = \exp[-(\exp[-k(V - V_o)])], \quad (2.18)$$

where I is the intensity and V is the voltage applied to the variable attenuator, and the fit constants are $k = 10.364$ and $V_o = -0.739$. Rearranging this function and writing it as voltage in terms of intensity gives

$$V = -(\ln(-\ln(I))/k) + V_o. \quad (2.19)$$

Now, by simply plugging in the desired intensity sequence, we get the required voltage input. Figure 2.27 shows a demonstration where a linear optical trajectory is created, and fig. 2.28 shows the waveform used for an exponential evaporation.

Finally, fig. 2.29 shows the measured temperature of a spin mixture versus the optical trap depth as it is cooled by the exponential trajectory. This evaporation results in an ultracold two component Fermi gas which means we are finally ready to do some experiments.

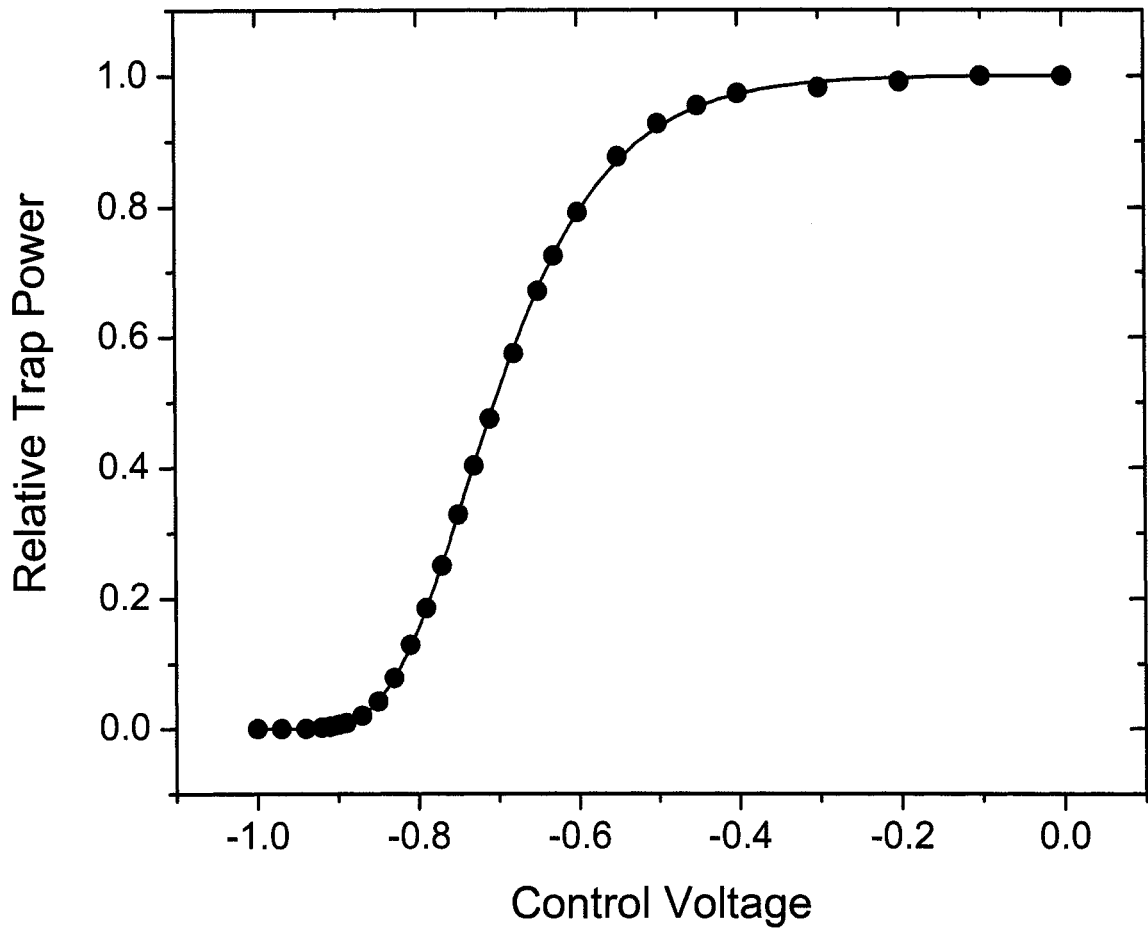


Figure 2.26 This is a convolution of the response of the variable attenuator and the AOM. The data points are measurements of the optical trap power as a function of the control voltage sent to the variable attenuator that controls the RF drive power of the trap AOM (see figs. 2.25 and 2.10). The measured points are fit to the function given by eq. 2.18. This gives an analytical expression for the turn on response of the trap so that arbitrary intensity trajectories can be created.

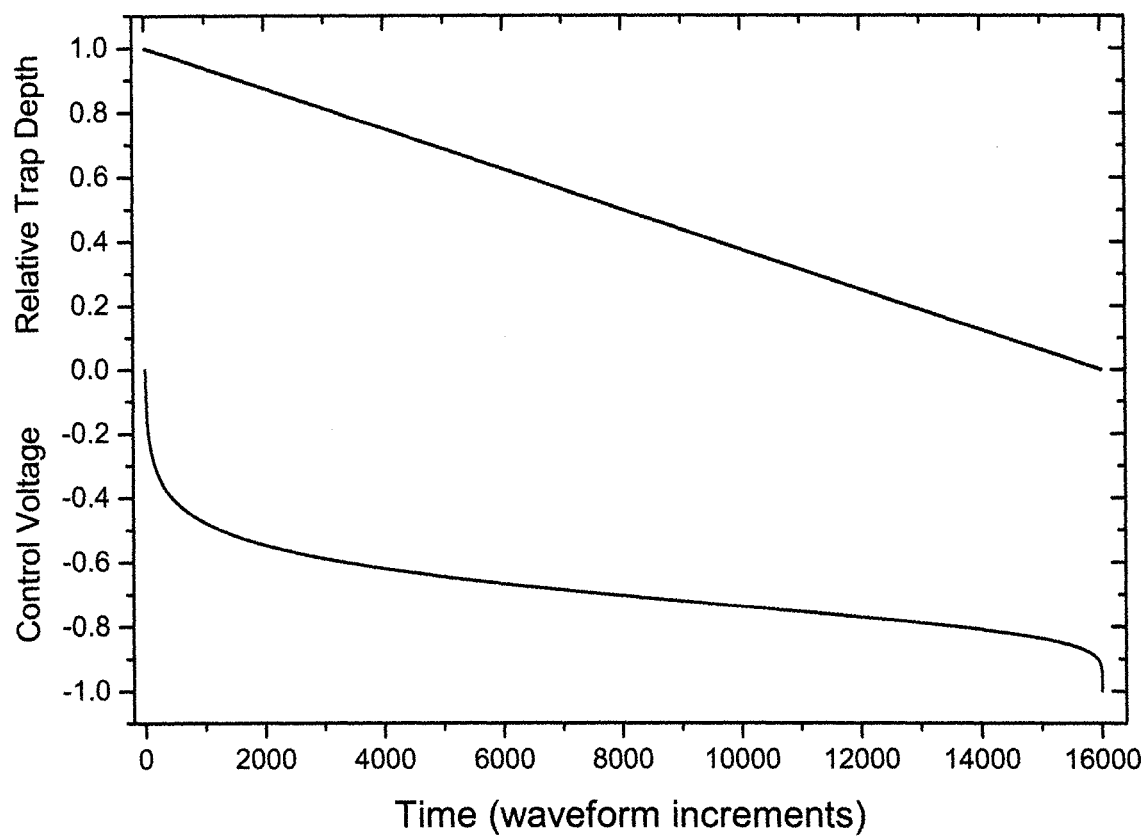


Figure 2.27 This plot shows the control voltage necessary to create linear evaporation trajectory. This trajectory is used on the experiment to verify that the process for creating trajectories is working.

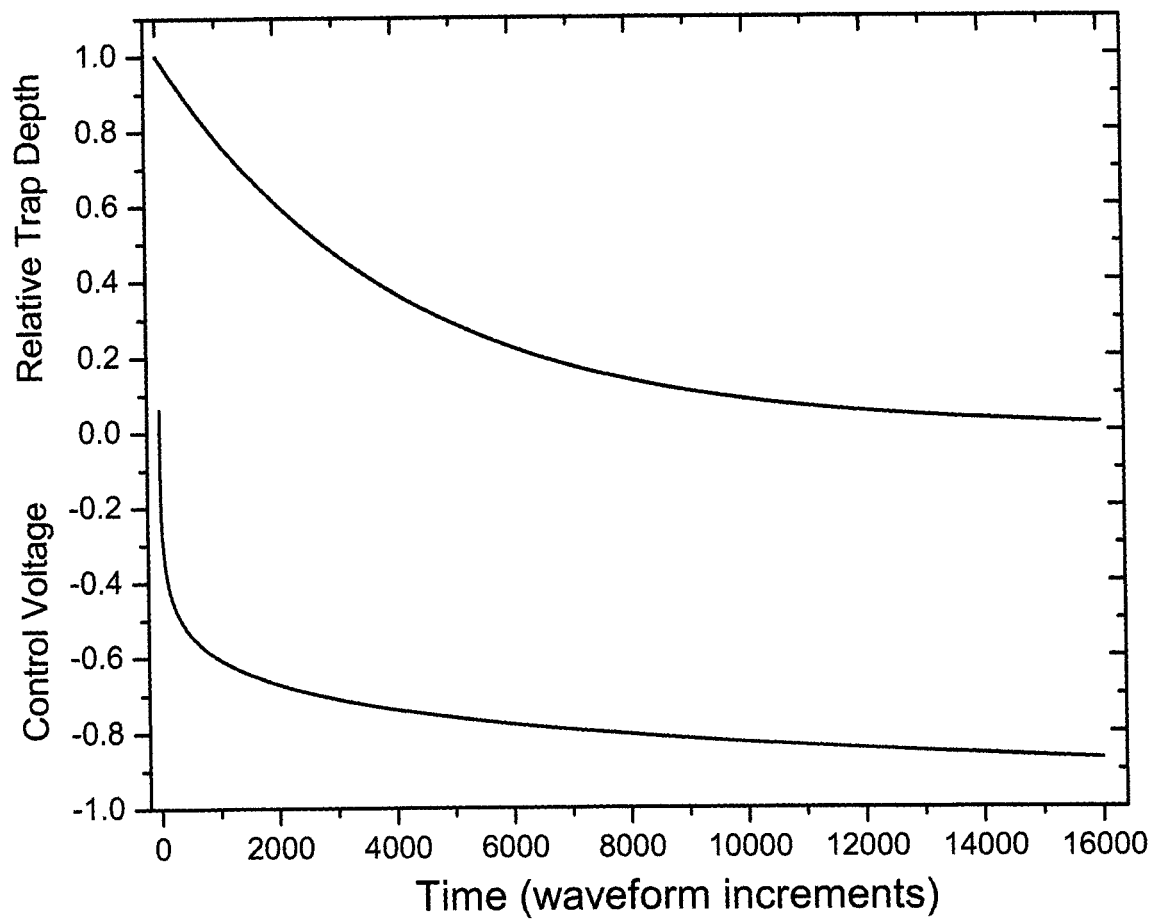


Figure 2.28 This is an exponential trajectory that is used for the experiments in this thesis.

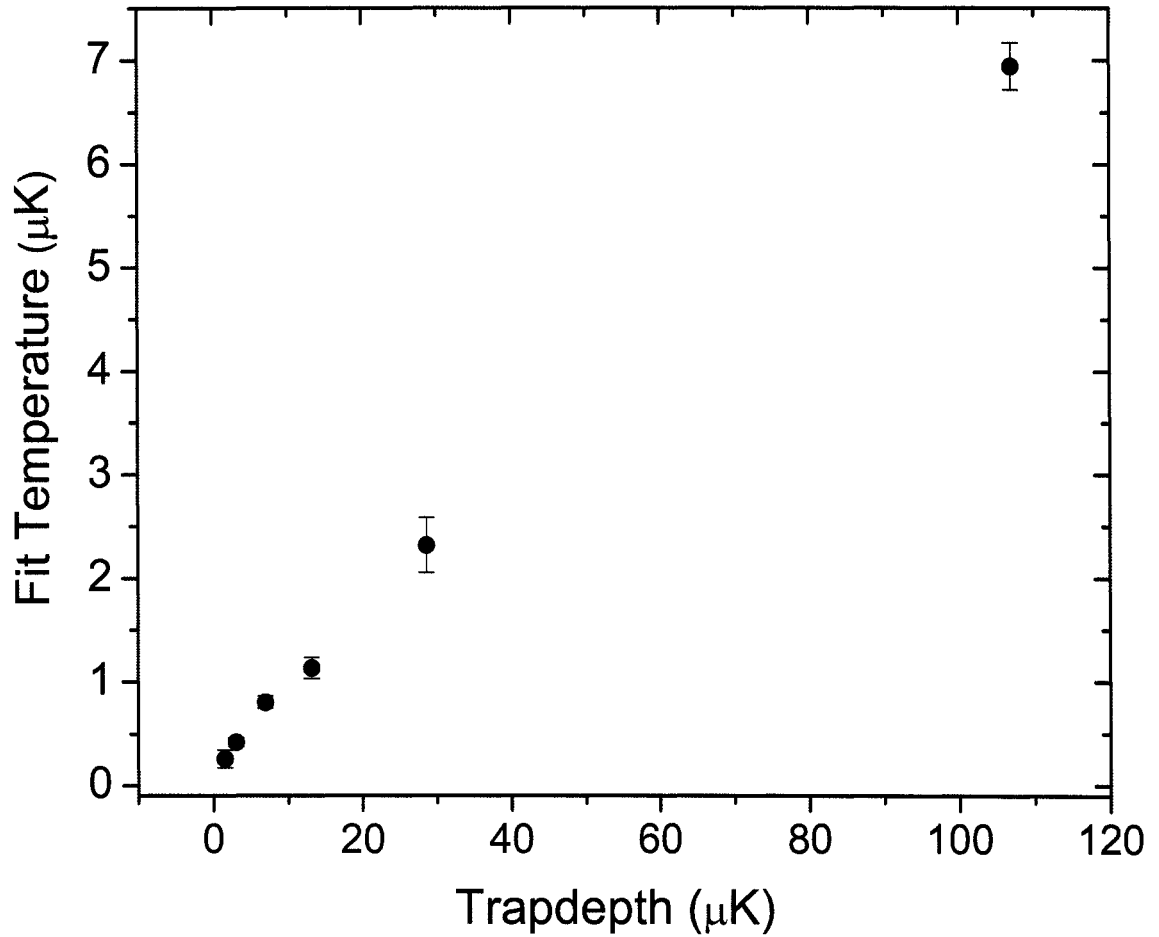


Figure 2.29 This plot shows the fitted temperatures of a strongly interacting spin mixtures of ^6Li , measured after halting the evaporation trajectory at various trap depths. Since accurate temperature determination in fermionic gases becomes difficult for low temperatures, this data was taken deep in the BEC regime (695 G, $k_F a \sim 0.15$) so as to minimize the fermionic character of the gas. When this trajectory reaches a trap depth of $\sim 0.5 - 1\%$ a molecular BEC is formed, as seen in the next chapter. It is worth noting that this relative trap depth for condensation appears to be somewhat constant across different traps.

Chapter 3

Molecular Probe of Pairing

Pairing in fermionic systems underlies the phenomena of superfluid ^3He and superconductivity. In such systems, the interactions between the pairing particles determine the character of the pairs and of the final superfluid or superconducting state. The major advance that has recently enabled experimenters using ultracold atoms access to these exotic systems is the Feshbach resonance, which allows the interactions between pairs of atoms to be tuned by application of a magnetic field. Such resonances allow for the creation of paired superfluid gases of fermionic atoms. In this chapter, I will describe a quantitative measurement of the composition of these pairs, formed in a Feshbach resonance. In addition, this measurement is extended to quantify pairing in the weakly interacting BCS superfluid regime for the first time in an ultracold trapped Fermi gas.

3.1 Molecules, Pairs and a Feshbach Resonance

Feshbach resonances occur when the energy of a pair of colliding atoms is tuned near that of a bound state of a molecular potential of the two atoms, as shown in fig. 3.1 [15]. If only two atoms are present, the effect of being near resonance with a bound state modifies their interaction and affects the s-wave scattering length. Energy and momentum conservation, however, prevent the pair from actually forming a bound molecular state, even when the bound state energy is lower than that of the free atoms. The addition of a third colliding atom, however, provides a mechanism for the excess energy to be removed from the system, thereby allowing two of the colliding atoms to fall into a bound molecular state. Within the resonance, this bound state is actually a quantum mixture of both the free atom state (also called the open channel) and the bound molecular state (the closed channel) that results from the avoided crossing of

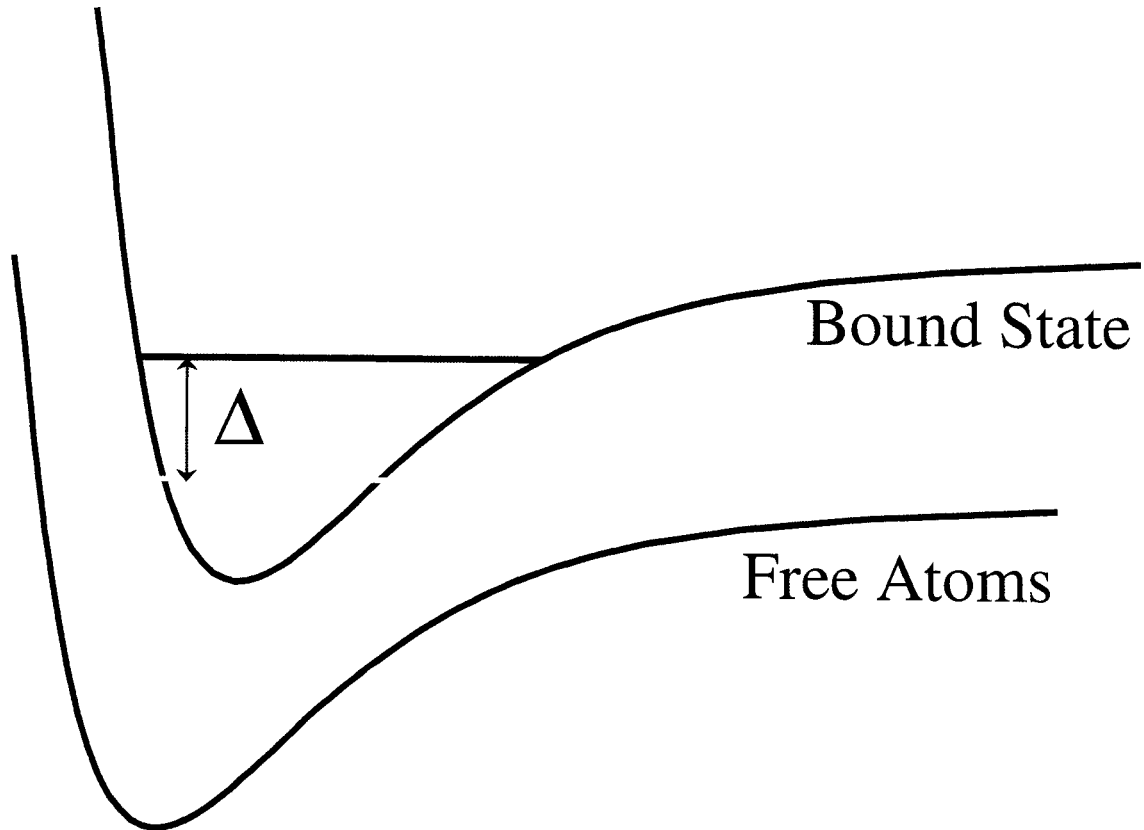


Figure 3.1 A Feshbach resonance arises when the energy of the free atoms is tuned near that of a bound molecular state via a magnetic field. In the case shown, the detuning, Δ , is positive since the bound state energy is above that of the atoms. This case corresponds to the BCS regime, where bound state molecules are energetically unstable. According to two-body theory, it is only when the molecular energy is lower than the atomic energy that bound molecules are possible.

these states [15]. Pairs which occupy this hybrid crossover state, the so-called dressed molecules, are composed of two fermionic atoms, and are therefore bosonic in nature. This results in markedly different behavior from the constituent fermionic atoms. It is possible, for example, to form a Bose-Einstein condensate of dressed molecules even though the underlying constituent atoms are fermionic.

For resonances that are broad compared to the Fermi energy, the closed channel character of the dressed molecules is predicted to be small throughout an experimentally relevant region about the resonance [42–45]. If this is the case, the resonance may be well-described by a single-channel model where the physics is universal, such that the macroscopic properties of the gas are independent of the microscopic physics that underlie the two-body interactions. An accurate and quantitative experimental determination of the composition and molecular character of the composition of the pairs in a broad Feshbach resonance will confirm the universality in the description of pairing in atomic gases. This confirmation will thereby establish the relevance of paired atomic gases to other systems, most notably high-temperature superconductors.

3.1.1 ^6Li Feshbach Resonances

In ^6Li there are two resonances between the $F = 1/2, M_F = \pm 1/2$ Zeeman sublevels which are particularly interesting, shown in fig. 3.2 [46, 47]. For the magnetic fields of interest ($B \geq 600$ G) these states are nearly electronically spin polarized, but differ in their nuclear spin projections.

Though these two resonances are inherently intertwined, slight differences in the mechanisms responsible for their appearance lead to surprisingly different characters. The first resonance, located at around 543 G is narrow, spanning less than 0.2 G. We previously generated bound molecules via an adiabatic magnetic field sweep over this resonance as described in [18]. Whereas the resonance at 543 G is distinguished

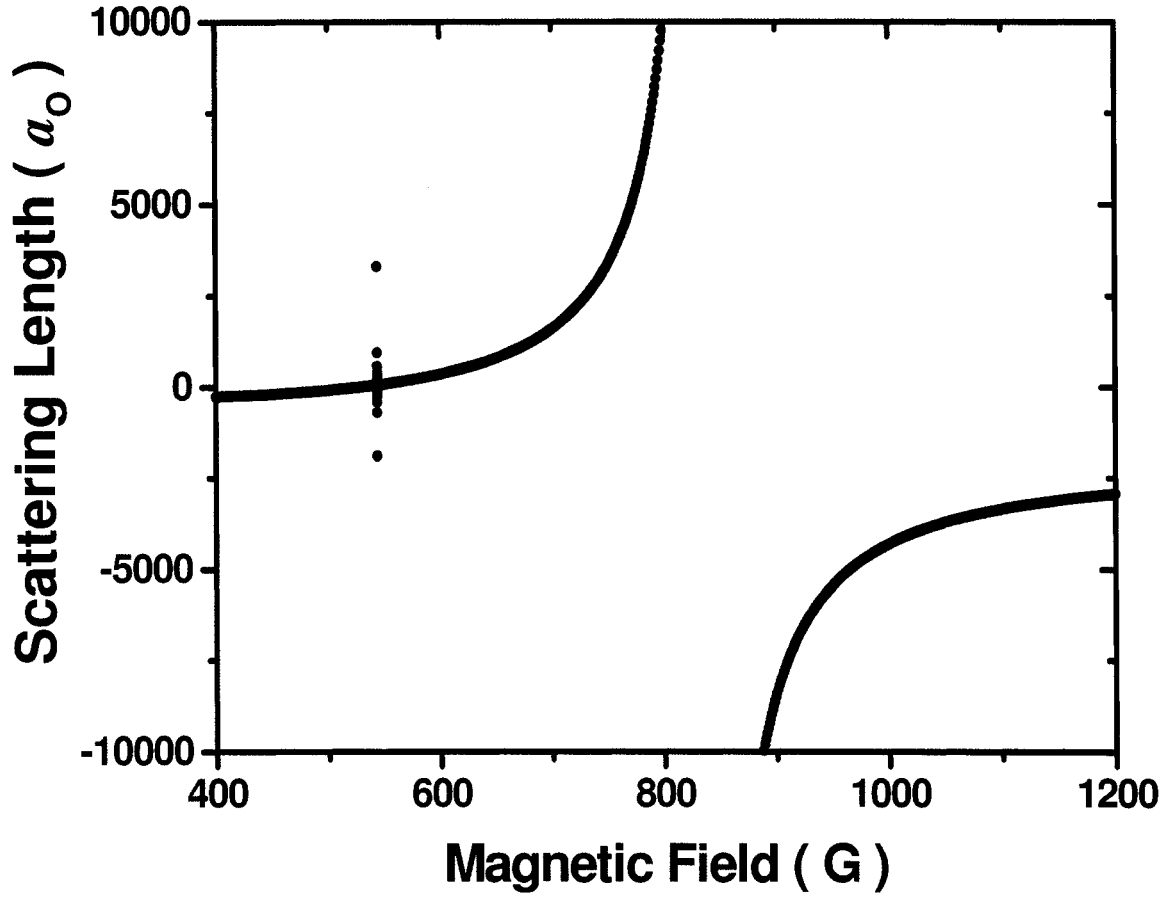


Figure 3.2 This plot shows the results of a coupled-channel calculation of the s-wave scattering length between the $F = 1/2, m_F = \pm 1/2$ levels of ^6Li . Two Feshbach resonances are apparent: a narrow resonance near 543 G and a broad resonance centered at 834 G. The broad resonance is the focus of the current experiment, though the mechanisms that give rise to both are described in the text.

by its narrow extent, the one at 834 G is exceptional for its broad extent, spanning hundreds of Gauss. Figure 3.3 shows the energy of the bound and free atom states versus magnetic field strength. The total spin of the atom pair is given by $S = \vec{s}_1 + \vec{s}_2$, where \vec{s}_i are the electronic spins of the atoms, $|\vec{s}_i| = 1/2$. This gives $S = 0$ or 1 for the pair. $S = 0$ corresponds to a singlet, which does not tune with magnetic field (due to electronic spin), and $S = 1$ is a triplet whose energy tunes as $g_s \mu_B B$, where $g_s \approx 2$ is the Landé g-factor, μ_B is the Bohr magneton, and B is the magnetic field. For sufficiently high fields, where $\mu_B B > \Delta_{HF}$, the hyperfine splitting, the atomic states have $S \approx 1$, since they are nearly spin polarized. In addition, the singlet ($S = 0$) molecular state $^1\Sigma_g^+$, $v = 38$, actually consists of two different channels with differing nuclear spin, $I = 0$ and 2. These states give rise to the broad and narrow resonances, respectively [48]. As these two states are approached by the tuned triplet ($S = 1$) state of the atoms, their behavior diverges. The large variation in width between these two resonances derives from the way in which the associated singlet molecular channels cross the triplet atomic state. The singlet state with $I = 2$ passes through the triplet atomic state at $\sim 540\text{G}$ with little perturbation. This crossing is the origin of the narrow resonance. The $I = 0$ singlet state, on the other hand, strongly couples to the triplet atomic level via a virtual bound state of the free atoms [45, 49]. As a result of this coupling, the states undergoes an avoided crossing which extends up to the position of the broad resonance at 834 G before finally converging. This is not visible on the scale of fig. 3.3, though by zooming in, the gradual nature of the crossing that leads to the extremely broad resonance is apparent, as shown in fig. 3.4.

It is this dressed state of singlet molecules (also called “bare” molecules) and atoms which we will probe using the experiment presented in this chapter.

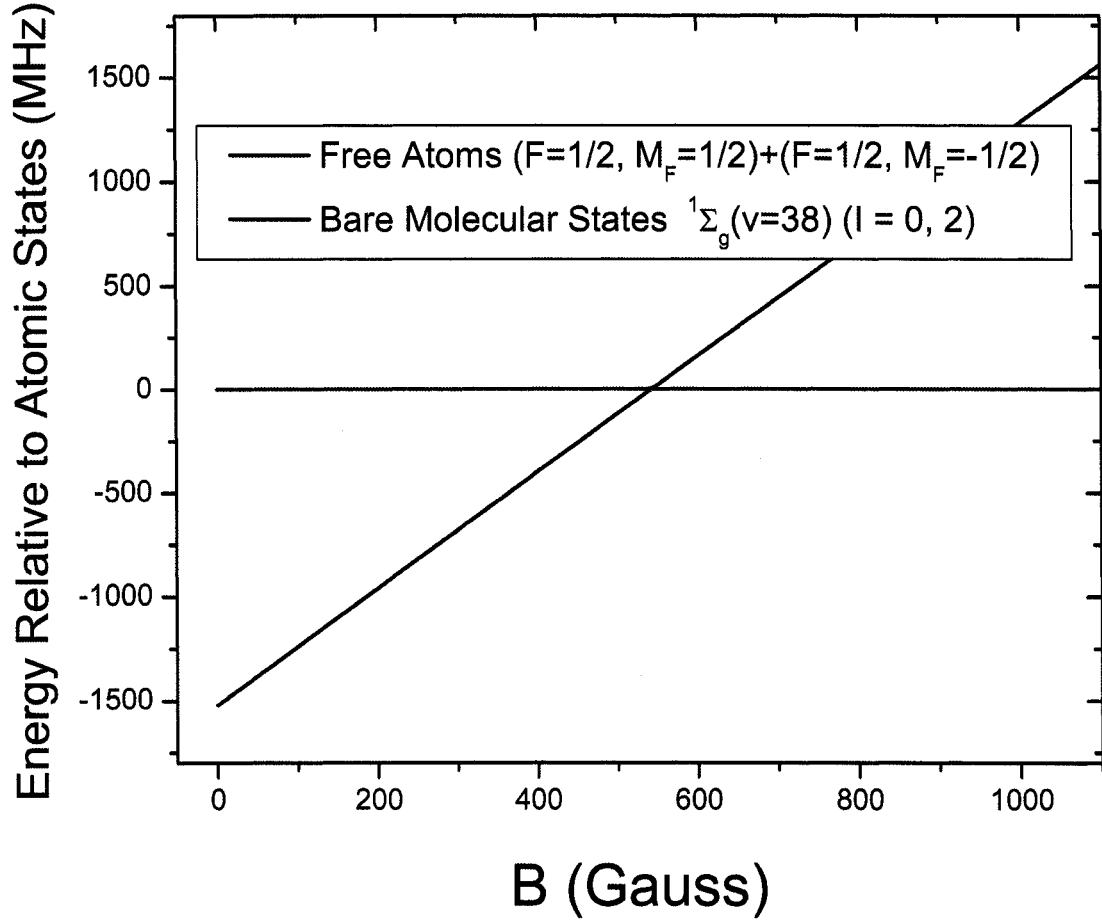


Figure 3.3 This plot shows the magnetic field dependence of the singlet molecular state, $^1\Sigma_g^+$, $v = 38$, and free atomic states, relative to the atomic state energy. (The atomic state is actually tuning, since it is a spin triplet, and the singlet molecular state does not tune.) The ~ 1.6 GHz molecular binding energy is evident at $B = 0$ [50]. From this plot, the crossing that is the origin of the resonance at 543 G is also evident, though the origin of the broad resonance at 834 G can not be discerned on this scale. (see fig. 3.4)

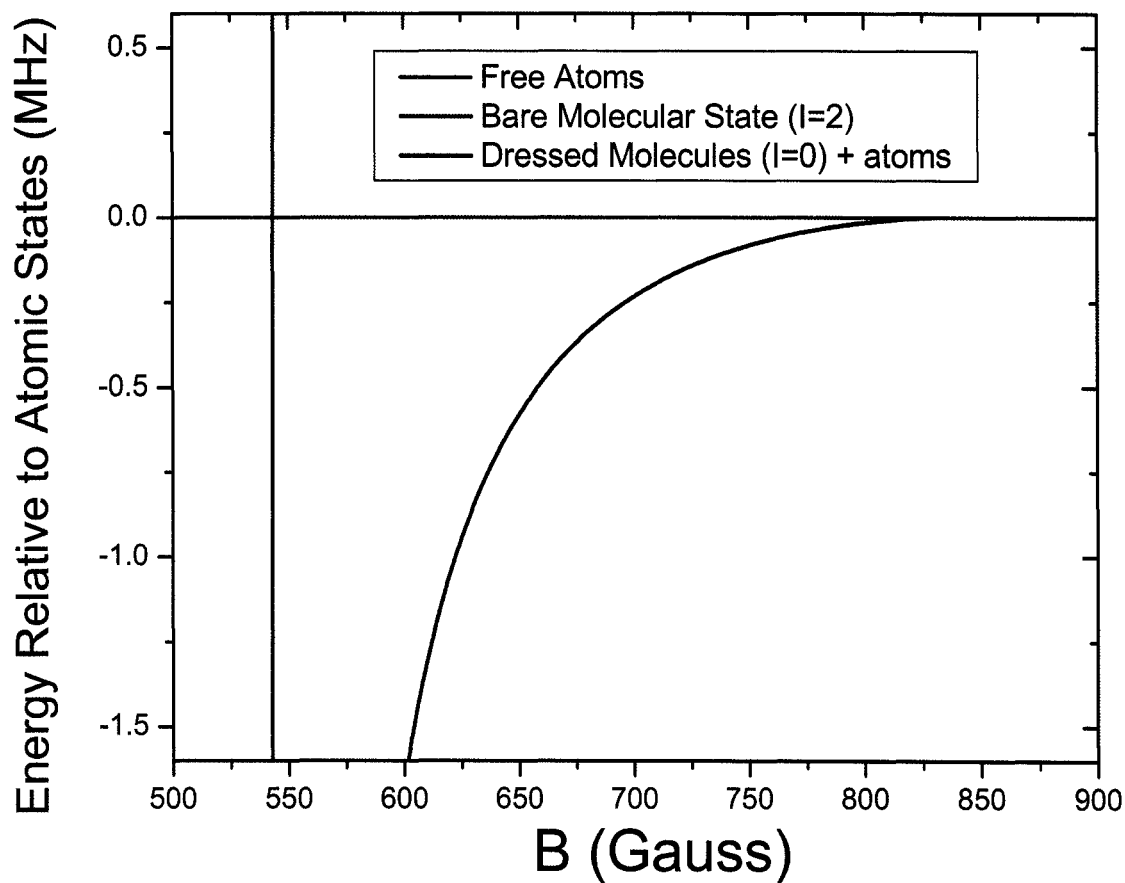


Figure 3.4 A close-up view of the level crossings responsible for the narrow and broad Feshbach resonances, as shown in fig. 3.3. An extended avoided crossing between the $I = 0$ molecular state and the atomic state leads to the extreme width of the 834 G resonance. The mixed atomic/molecular state is labeled dressed molecules. The relative contributions of the bare molecular and atomic states to the dressed molecules is the focus of this chapter.

3.2 The Experiment

In some of our previous experiments using cold atoms and Feshbach resonances, the resonance has been used to tune the interatomic interactions, without much regard or need for the underlying details that result in the modification of the interactions (for example, creating matter wave solitons [17]). The current experiment, on the other hand, works to address the inner workings of the Feshbach resonance, with the goal of developing an accurate picture of the mechanisms at play. As we shall see, such experiments also have the potential to establish the relevance of ultracold atoms in Feshbach resonances to other diverse areas of physics through the concept of universality. In the experiment reported here, a laser is used to project the dressed molecules/atoms onto an excited singlet molecular state. The crux of this measurement is that $\Delta S = 0$ in the optical transition so that the bare molecular (singlet) portion of the dressed wavefunction is driven to the excited state. By starting with an evaporatively cooled gas on the BEC side of the resonance, followed by an adiabatic change in the magnetic field, a nearly zero temperature gas can be probed throughout the BEC-BCS crossover by measuring the rate of the molecular excitation due to the laser. This enables a direct measurement of the closed channel molecular fraction, and for the first time in an atomic gas, provides clear evidence for the presence of pair correlations in the weakly interacting BCS regime where, by two-body theory, bound molecules are not expected to exist [22].

3.2.1 The Setup

Many of the methods used for this experiment have been previously described in Chapter 2 and in the other theses and papers [6, 18–22]. The optical trap is formed from a 1 W Nd:YAG laser at 1064 nm, as described in the previous chapter. In this implementation, the optical trap, at full laser intensity, has a trap depth of 25 μK and radial and axial frequencies of $\nu_r = 2270$ Hz and $\nu_z = 21$ Hz, respectively. Curvature

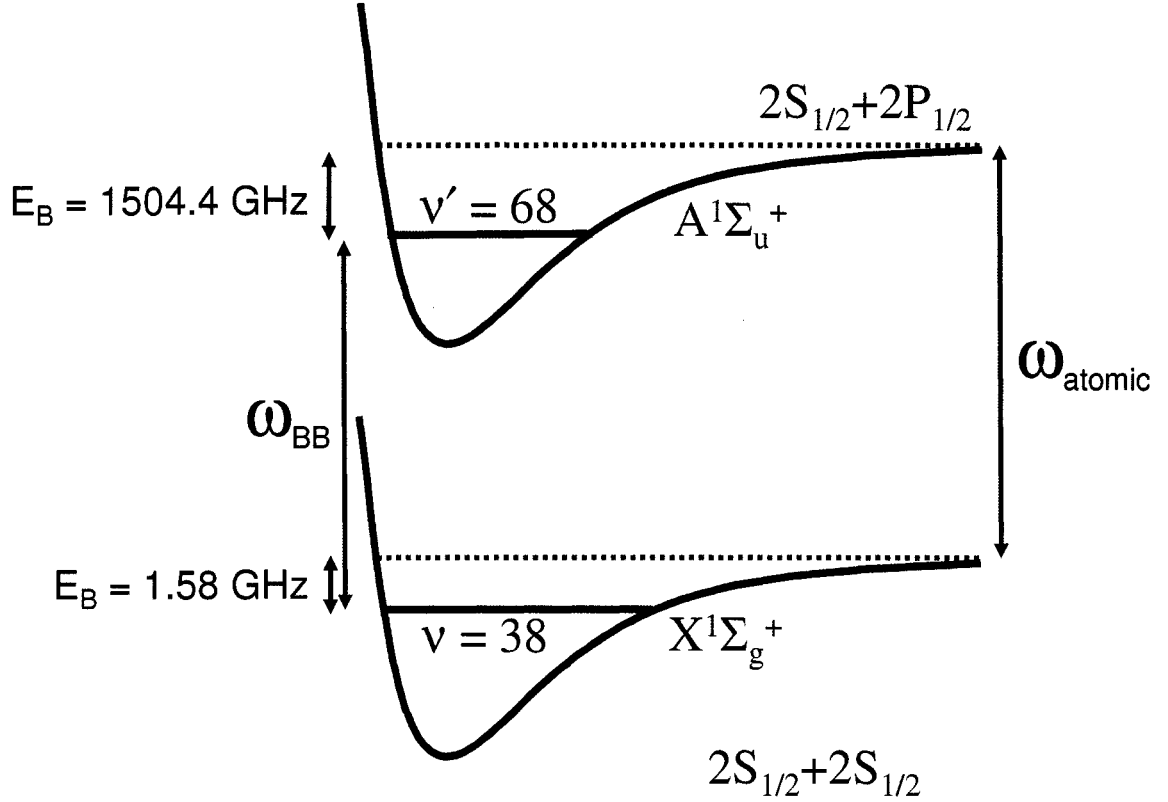


Figure 3.5 Schematic of relevant energy levels taken into consideration for calculation of bound-bound molecular transition frequency (not to scale).

in the magnetic bias field modifies the axial frequency such that $\nu'_z = \sqrt{\nu_z^2 + \lambda B}$, where $\lambda = .029(3)$ Hz²/G.

In addition, we have set up a laser system designed to drive a bound-bound molecular transition, which I shall now describe.

Characterization of Bound-Bound Molecular Transition

In order to drive the bound-bound molecular transition, we must first determine the frequency of the transition. The transition frequency is that of the atomic ⁶Li D1, $2S_{1/2} \rightarrow 2P_{1/2}$ transition, modified by the binding energies of the molecular states, as shown in fig. 3.5. We excite from the least bound vibrational level of the $X^1\Sigma_g^+(v = 38)$ state, which is bound by 1.57709 GHz (calc.)[50], to the $A^1\Sigma_u^+(N =$

1)($v' = 68$) level, which is bound by 1504.375(85) GHz [51]. The wavenumber of the ${}^6\text{Li}$ D1 transition at zero field is 14903.296792(23) cm^{-1} [52]. This gives a frequency of $\nu_{D1} = 4.467895977(7) \times 10^{14}$ Hz for the atomic transition. To find the frequency of the bound-bound transition, we subtract the binding energy of the excited state, and add the binding energy of the ground state to that of the atomic transition. This gives

$$\begin{aligned}\nu_{BB} &= 4.467895977(7) \times 10^{14} - 1504.375(85) \times 10^9 + 1.58 \times 10^9 \text{Hz} \\ &= 4.45286803(85) \times 10^{14} \text{Hz},\end{aligned}\tag{3.1}$$

where the uncertainty comes primarily from the binding energy of the $v' = 68$ bound state. The frequency of the probe laser is set by use of a Michelson wavemeter that references a stabilized He-Ne laser. On our apparatus, we use the D1 atomic transition to provide the repump beams in our ${}^6\text{Li}$ MOT [19], and so it is straightforward to calibrate our wavemeter to the D1 atomic transition. For this transition, referenced to a saturated absorption heat pipe signal, the wavemeter reads 0.943364(1) (This number is the ratio of the HeNe wavelength, ~ 633 nm, to that of the ${}^6\text{Li}$ D1, ~ 671 nm). Using this calibration, we predict a wavemeter reading of 0.940190(1) for the bound-bound transition, where the uncertainty corresponds to the resolution of the wavemeter. The actual transition was found to be within the uncertainty of this prediction. Additionally, depending on magnetic field, small corrections are necessary because for this experiment we actually drive a transition from the dressed state of the singlet molecular ground state and triplet atomic state, as described in the previous section. The measurement of the field dependence will be presented in the following section.

The measurement of the closed channel molecular fraction depends on the ability to relate an observed molecular excitation rate to the applied laser intensity. To do this, we must calculate the effective Rabi frequency as a function of intensity. The

on-resonance Rabi frequency for the molecular transition is given by

$$\Omega_m = \langle \psi_{v'=68}(S=0) | \vec{d}_m \cdot \vec{E}_L | \psi_{v=38}(S=0) \rangle, \quad (3.2)$$

where \vec{d}_m is the molecular transition dipole, \vec{E}_L is the laser field of the molecular probe, $\psi_{v'=68}(S=0)$ and $\psi_{v=38}(S=0)$ are the excited and ground state molecular wavefunctions [22, 53]. In order to quantify Ω_m , we will write it in terms of the corresponding atomic Rabi frequency,

$$\Omega_a = \vec{d}_a \cdot \vec{E}_L. \quad (3.3)$$

Combining and rearranging expressions 3.2 and 3.3 gives

$$\Omega_m = \langle \psi_{v'=68}(S=0) | \psi_{v=38}(S=0) \rangle \frac{\vec{d}_m \cdot \vec{E}_L}{\vec{d}_a \cdot \vec{E}_L} \Omega_a. \quad (3.4)$$

The ratio of the molecular to atomic transition dipole moments $\frac{\vec{d}_m}{\vec{d}_a}$ involves two different considerations. The first arises because the binding energy of the $v' = 68$ energy level is greater than that of the fine splitting and hyperfine interactions [51]. This causes the electronic and nuclear spins to decouple from the probe light, which results in the dipole moment of the molecule \vec{d}_m aligning along the internuclear axis [53]. Since the internuclear axis is randomly oriented in space, \vec{d}_m is reduced by a factor of $\sqrt{1/3}$ from that of the atomic transition. Moreover, the molecular transition dipole moment also depends on the excited state decay rate. Since the molecule has more decay channels available than a single atom, the decay rate γ_m is correspondingly larger than that of the excited state atom γ_a by a factor of two. The effect of this is to increase the effective molecular dipole transition element by a factor of $\sqrt{2}$.

The square of the remaining term, $|\langle \psi_{v'=68}(S=0) | \psi_{v=38}(S=0) \rangle|^2$, is the Frank-Condon overlap between the ground and excited molecular states, and has a computed value of 0.077 [54]. Finally, the atomic Rabi frequency may be written as $\Omega_a = \gamma_a \sqrt{I/I_{sat}}$, where $\gamma_a = (2\pi)5.86$ MHz is the atomic linewidth, $I_{sat} = 5.1$ mW/cm²

is the atomic saturation intensity, and I is the photoassociation laser intensity. We may now plug these values into the expression for the molecular Rabi frequency, eq. 3.4

$$\Omega_m = 2\pi \cdot 0.588 \text{ MHz} \cdot \sqrt{I(\text{mw/cm}^2)}. \quad (3.5)$$

Photo-Association Laser System

The optical frequency of the bound-bound molecular transition differs from that of the atomic transition by ~ 2 nm, which necessitates the use of another laser, tuned specifically to this transition. Additionally, since the molecular transition is far from the atomic transition, there is no reference frequency available from the heat pipe that is used for the optical frequency reference for driving atomic transitions. For this reason, we utilize another scheme to accurately reference and control the resonant frequency of the molecular probe laser.

The system begins with a single mode external cavity diode laser, such as those discussed in my Master's thesis [19], with an output of 5 mW at ~ 673 nm. As shown in fig. 3.6, this laser is stabilized by locking it to a reference Fabry-Perot cavity. The output of this laser is directed through an 80 MHz switching AOM (Crystal Technology, p/n: 3080-151) that is used to pulse on the probe for a controlled duration into a single mode optical fiber that takes a portion of the light to the apparatus table and directs it to the atoms as shown in fig. 3.7. The beam waist, w_o , is measured to be 0.107 cm at the atoms.

For the current experiment, this setup delivers approximately 0.4 mW of optical power to the atoms. This corresponds to a peak intensity of $I_o = (2P)/(\pi w_o^2) \sim 20$ mW/cm² at the center of the beam, and a molecular Rabi frequency of $\sim (2\pi)2.6$ MHz. Since the extent of the cooled atom cloud in the trap (axial waist ~ 200 μm) is significantly smaller than w_o , the peak intensity is a good approximation to the actual intensity the atoms experience. In addition, since the molecular probe beam is fired

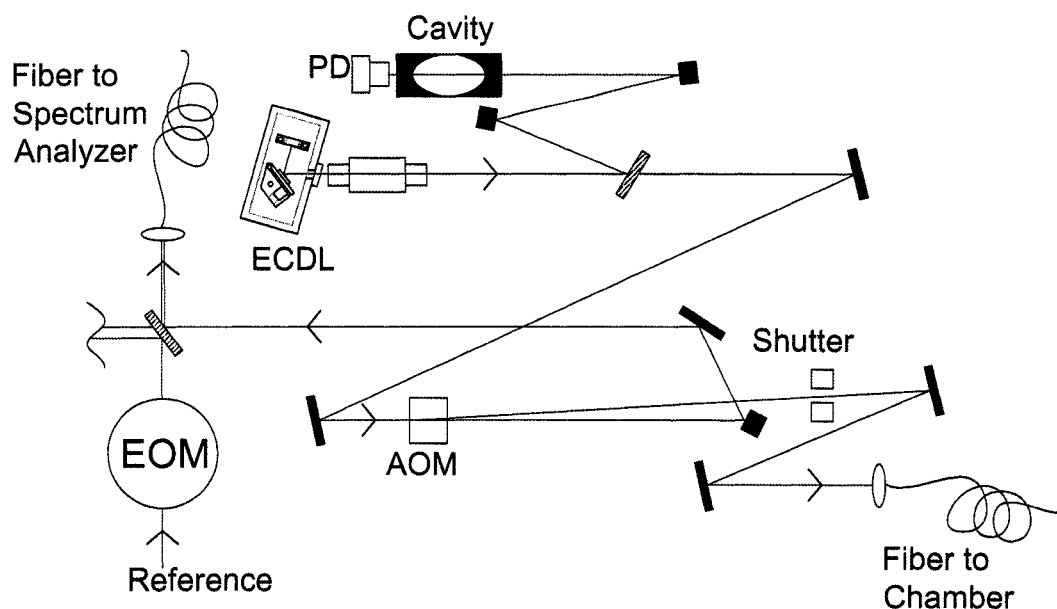


Figure 3.6 Optical system for generating molecular probe light. The extended cavity diode laser (ECDL) is locked to a Fabry-Perot reference cavity. The frequency of the laser is tuned by providing a feed-forward signal to the cavity. The output of the laser is pulsed into a fiber leading to the apparatus table by a switching acousto-optic modulator (AOM). A shutter prevents leakage light. Reference is achieved by overlapping the ECDL with a reference beam, locked to a heat pipe and superimposed in an optical spectrum analyzer. A tunable electro-optic modulator (EOM) gives the reference laser a movable frequency sideband with which the probe laser can be overlapped (see appendix C).

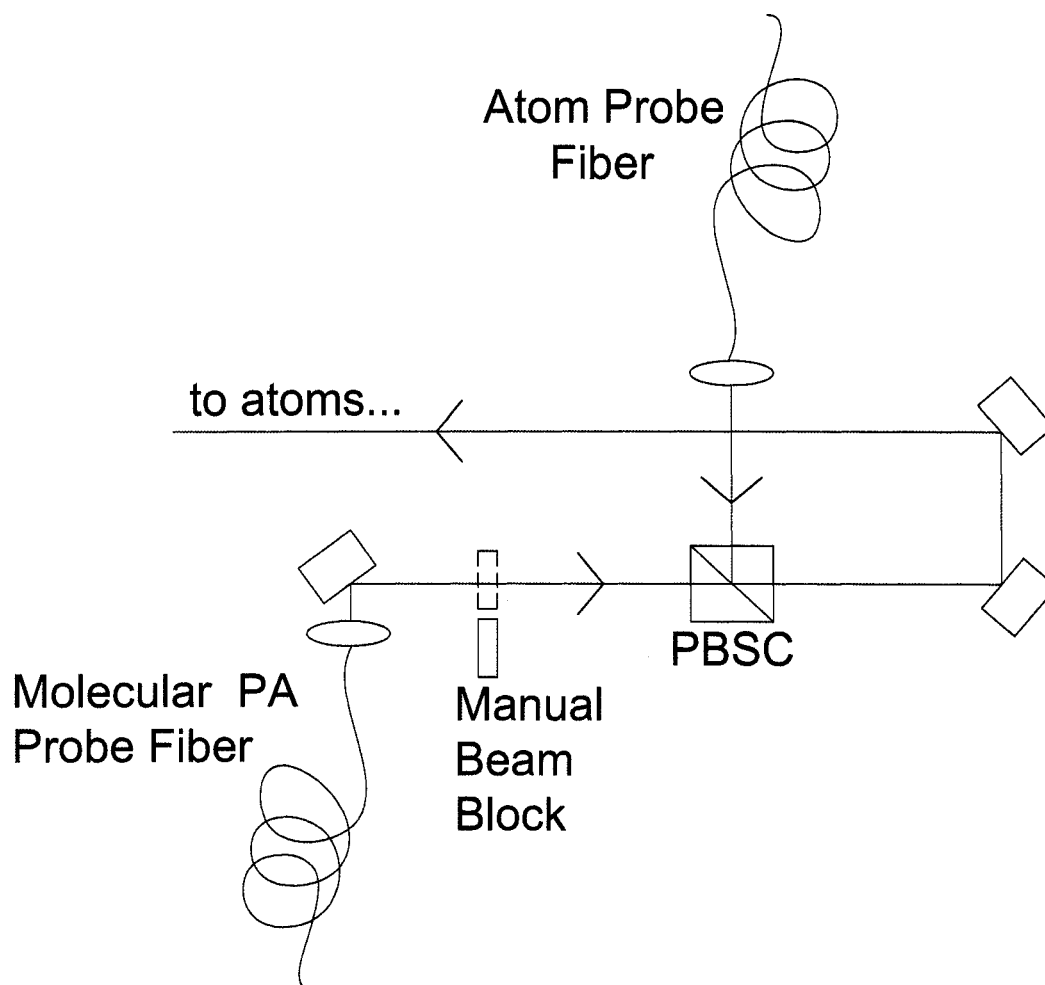


Figure 3.7 Probe combination optics. The output of the molecular probe fiber and the atomic probe fiber are combined on the apparatus table and directed towards the trap. The molecular probe drives the bound-bound transition, and subsequently the remaining atom number is measured using the atomic probe. The loss signal is normalized by repeating the measurement with the molecular probe laser blocked.

along the imaging axis, we capture an image of the beam that is used for each shot. Since the duration of the probe pulse is known, we can measure the intensity from the pixel counts on the CCD, once we have calibrated the response of our camera and imaging system.* This measurement, specific to each shot, allows us to account for shot to shot intensity fluctuations as well as for spatial abnormalities in the beam profile. We therefore are able to make a good measurement of the intensity of the probe each time it is used.

The molecular probe frequency is initially (coarsely: ~ 500 MHz) set around the predicted value by using a Michelson wavemeter at the frequency calculated in the previous section. From this point, the exact frequency is found by monitoring trap loss for long (1-2 s), probe pulses as a function of frequency.* This is most effective at low temperatures in the BEC regime (e.g. 754 G), since the entire trap may be emptied by even a relatively short, weak (or off resonant) pulse. When a trap loss is observed, the resonant frequency is narrowed down by decreasing the sweep width. Once the transition is initially found, it is fairly straightforward to return to the given frequency using the reference system that is described below.

Frequency reference is achieved by overlapping the molecular probe laser with a reference laser and comparing both in the same optical spectrum analyzer. Specifically, the straight through (zeroth order) of the probe pulse AOM is overlapped on a beamsplitter with a weak beam from the Coherent dye laser used for the ^7Li portion of the apparatus. The dye laser is locked to a heat pipe, and provides a stable day to day reference point when both lasers are coupled into a 300 MHz spectrum analyzer (via an optical fiber, used to minimize variations due to pointing differences between the lasers). Before this overlap, the dye laser has passed through a tunable

*Our calibration procedure consists of correlating the total number of counts accumulated on the CCD array to an optical pulse of known power and duration, focussed entirely onto the array. Details are provided in Ramsey Kamar's Masters Thesis [55].

*These pulses may be swept as well to increase the searched frequency space. We used sweeps of several hundred MHz over the course of a second or two.

electro-optic modulator (EOM) (see appendix C) that adds sidebands to the frequency spectrum. Tunability of the resonance frequency of the EOM allows the driving RF frequency to be changed such that a sideband of the dye laser is overlapped with the peak of the probe laser. The tunability of the EOM is sufficient to cover a free spectral range of the spectrum analyzer, so that a reference may be created for any wavelength. This configuration allows for repeatable control of the probe frequency on the scale of a MHz, which is small compared to the linewidth of the molecular transition, $\gamma = (2\pi)11.7$ MHz. Using this system, it is possible to measure the resonance frequency of the transition, as shown in fig. 3.8. Additionally, we have mapped out the magnetic field dependence of this transition so that we may effectively and consistently drive it on resonance. We find that the transition tunes with a slope very nearly equal to $2\mu_B$, as shown in fig. 3.9. This field dependence emphasizes the strong triplet atomic character of the dressed atoms, though it is important to note that the transition strength is greatly enhanced by the small contribution of the bound molecular state.

3.2.2 Starting Point: Molecular Bose-Einstein Condensate

The first step in conducting a measurement of the bare molecular fraction of pairs in the Feshbach resonance is to create a Bose-Einstein condensate of the dressed molecules on the BEC ($a_s > 0$) side of the resonance, as has also been observed by other groups [56–59]. This step is accomplished by preparing an equal incoherent 50/50 spin mixture of the two lowest hyperfine states of ^6Li in the optical trap at a bias field of 754 G. At this field, the broad Feshbach resonance induces the s-wave scattering length to be $a \simeq 3680 a_o$. The atomic scattering length a is determined from a coupled channels calculation [46], where we have adjusted our triplet potential slightly to shift the location of the Feshbach resonance from 837 G to the measured location of 834 G [47]. As outlined earlier, by evaporatively cooling the gas, dressed

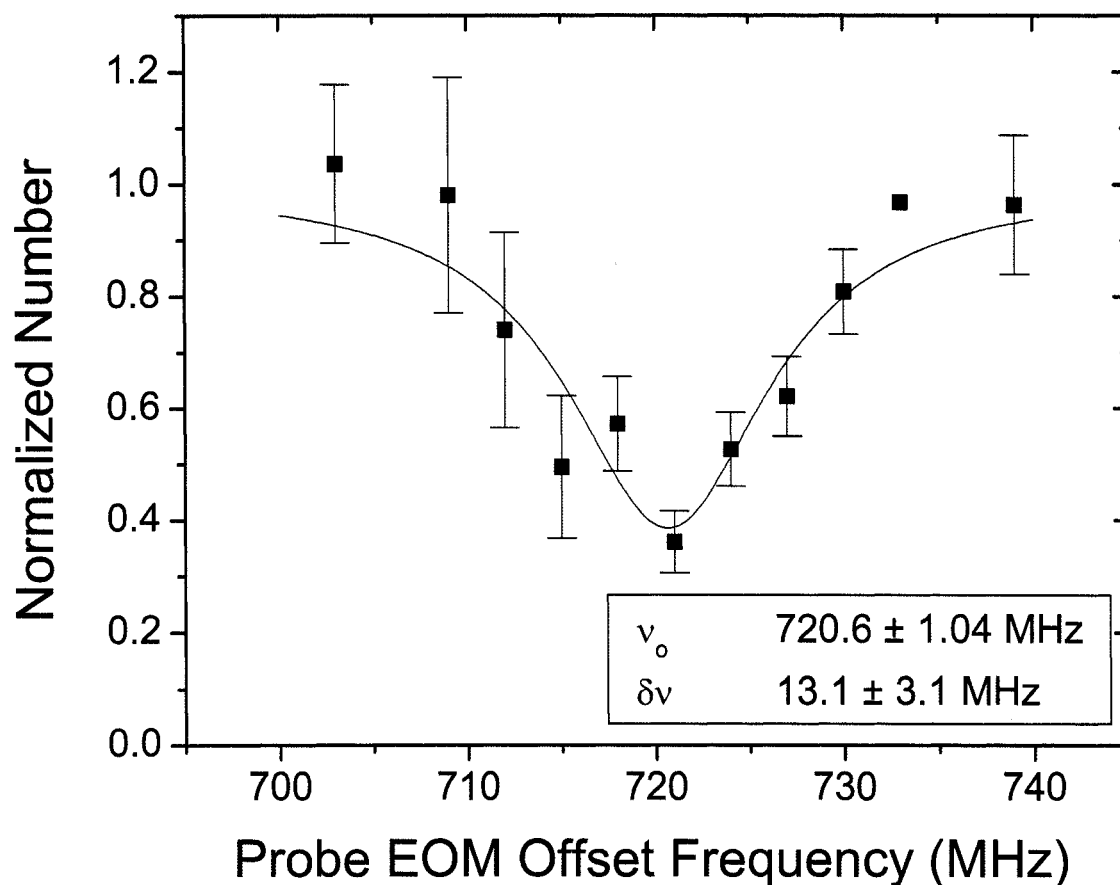


Figure 3.8 A typical molecular resonance, this one taken at 695 G with a probe duration of $100 \mu s$. The signal is the number remaining after a probe pulse, normalized to shots taken with the probe beam blocked. The frequency shown is the drive frequency of the tunable EOM used to create the sideband of the reference laser. The measured width of ~ 13 MHz is consistent with expected width of $\gamma_m/(2\pi) = 11.7$ MHz. Similar resonances were taken at several magnetic fields to produce the plot shown in fig. 3.9.

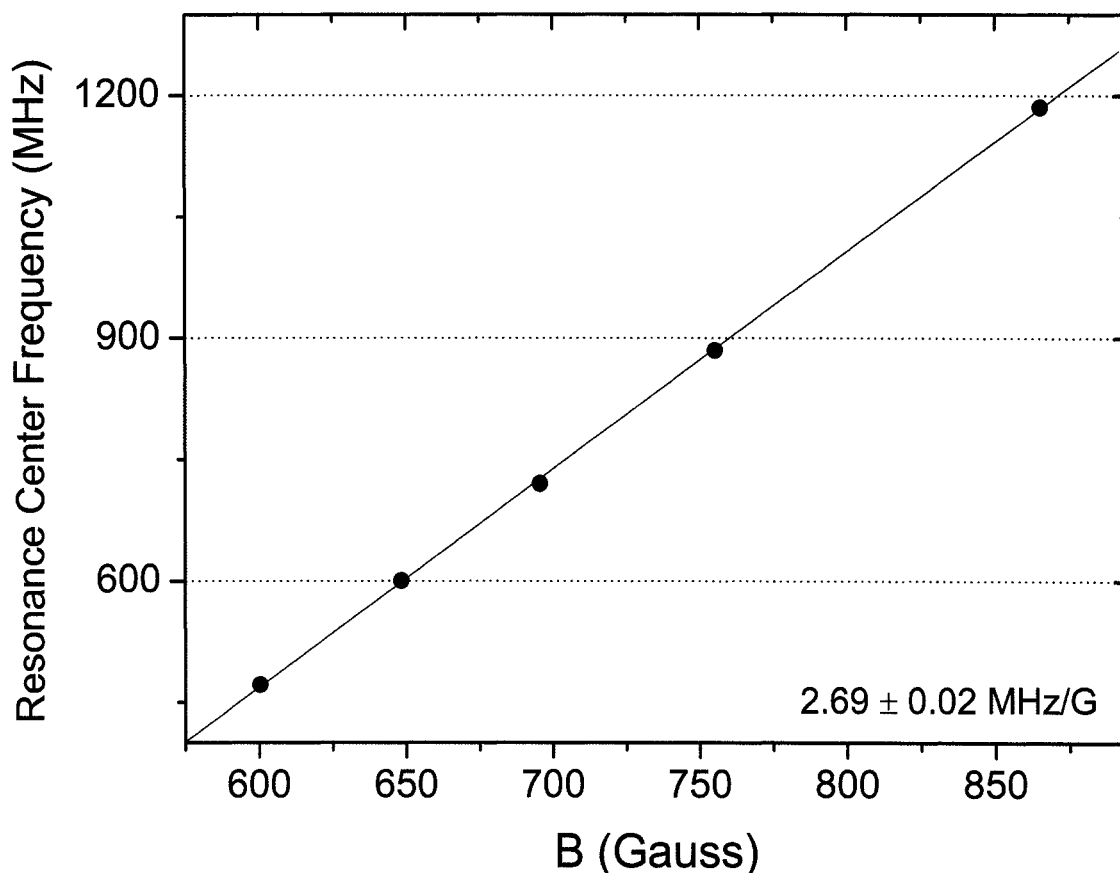


Figure 3.9 Measured transition resonance frequency for dressed molecules versus magnetic field. Since the transition is from a state that consists of small singlet and large triplet contributions, the resonant frequency shifts with field. This behavior reflects the fact that the transition is being driven not from bare molecules, but from dressed molecules that have a significant atomic contribution. From fig. 3.4, it is evident that beyond the 534 G resonance, the dressed molecular state closely follows that of the triplet atoms. This is verified by the slope of the transition frequency, which is very close to $2\mu_B$, the approximate slope at which the atomic energy tunes. Below 534 G, the transition frequency is that calculated earlier in eq. 3.8. The frequency for each field is extracted from a lorentzian fit to a resonance such as that shown in fig. 3.8. The dotted lines mark free spectral ranges of the spectrum analyzer used to measure the frequency.

molecules are formed by three-body recombination, and the large scattering length* allows efficient rethermalization and cooling.

For the current experiment, the optical trap evaporation is accomplished by reducing the light intensity in an approximately exponential trajectory in 750 ms. The details of the optical trap trajectories are provided in the previous chapter. Once the trap intensity reaches its final value, the magnetic field may be ramped to a different value such that the entire BEC-BCS crossover may be explored. In addition, adiabatic (isentropic) field sweeps from low (BEC) to high (towards BCS) fields are predicted to result in additional cooling (see fig. 3.10) [62–64]. We verify adiabaticity by ramping from 754 G to a field above the Feshbach resonance and back. In such a process, we detect no heating upon returning to the original field [65].

The bottom half of fig. 3.11 shows an axial cut of the column density of an *in-situ* absorption image of a nearly pure molecular BEC prepared by the methods described above at a field of 754 G, and subsequently imaged after ramping down to 695 G, where $a \simeq 1510 a_o$. This field, which is deep in the BEC regime ($k_F a \sim 0.15$), is chosen because the smaller scattering length and more deeply bound dressed molecules make the bosonic behavior of the gas, such as a spatially well defined condensate, more obvious. At higher fields, the bosonic nature of the gas is washed out as fermionic attributes become increasingly dominant. Due to the weakly bound nature of the dressed molecules (as shown in fig. 3.4), the atomic probe may be used to simultaneously dissociate and probe the molecules. The lack of any detectible thermal component in this profile (condensed number fraction $N_0/N > 0.90$) places an upper limit of $T/T_c \lesssim 0.5$, where T is the temperature and T_c is the critical

*The molecular (dimer-dimer) scattering length, a_m , is related to the atomic scattering length, a , though the precise relation is still a point of contention. BCS theory gives $a_m = 2a$, though this result is generally regarded as incorrect. A better relation, $a_m = 0.6a$, is given by Petrov et al. [40] when the size of the pairs is small compared to their separation. Astrakharchik et. al [60] obtain the same result through a Monte Carlo simulation. In addition Stajic et al. [61] find an interaction dependent ratio of a_m/a from a many body theory.

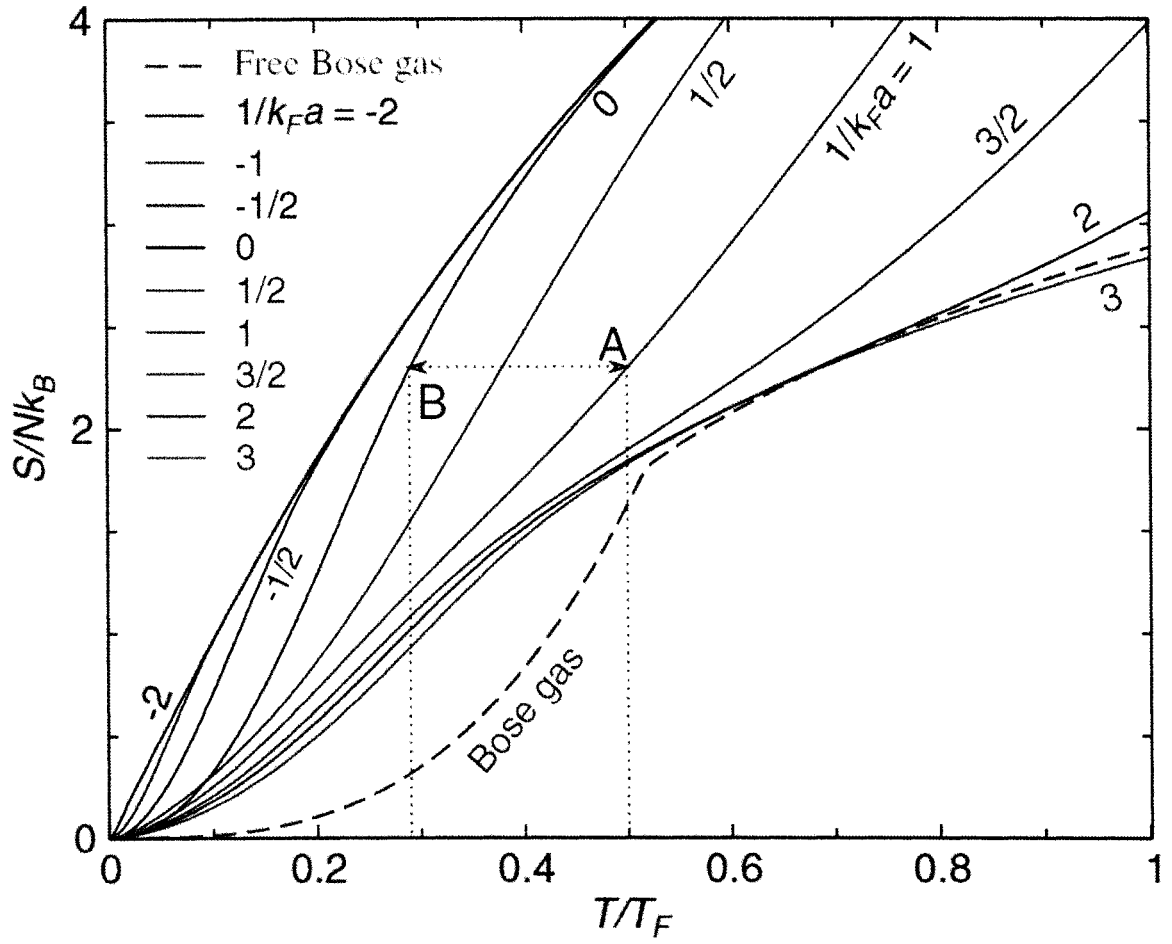


Figure 3.10 Adapted from [63]: “Entropy per atom as a function of T for different values of $1/k_F a$ from BCS to BEC in a harmonic trap. The dotted lines show an isentropic sweep between $1/k_F a = 1$ and unitarity. For comparison, we also plot S for an ideal Bose gas (dashed line).” Magnetic field sweeps in the current experiment originate from 754 G ($1/k_F a \approx 1.5$).

temperature for condensation, since

$$\frac{N_0}{N} = 1 - \left(\frac{T}{T_c}\right)^q \quad (3.6)$$

with $q = D/\alpha = 3$ since $D = 3$ is the dimensionality, and $\alpha = 1$ for a harmonic trap [66, 67].

The final trap depth after evaporation for the bottom panel of fig. 3.11 is $U_o = 0.27 \mu\text{K}$, which corresponds to $\sim 1\%$ of the initial trap depth. This low final trap depth is necessary to produce a pure condensate, with no detectible thermal fraction, since if the trajectory is stopped at a higher value, uncondensed molecules remain. The top panel of fig. 3.11 shows the resulting distribution if the trajectory is stopped at $U_o = 0.5 \mu\text{K}$. In this shot, a component of thermal, uncondensed molecules is distinguishable from the condensed core.

3.2.3 Measuring the Bare Molecular Fraction: Picking out the Pairs

Once a molecular BEC has been created, as above, we may finally get down to making a measurement. As alluded to earlier, the dressed molecules that exist within the Feshbach resonance are a superposition state composed of free atoms and deeply bound bare molecules. In more specific terms, the wavefunction of the dressed molecules can be expressed as a superposition of the $v = 38$ singlet molecules and free atom pairs in the triplet channel [15]:

$$|\psi_p\rangle = Z^{1/2}|\psi_{v=38}(S=0)\rangle + (1-Z)^{1/2}|\phi_a(S=1)\rangle, \quad (3.7)$$

where Z can be identified as the singlet, closed-channel, amplitude of the dressed molecules. It is this quantity, Z , which we wish to measure.

For a given measurement, the magnetic field is set to a value between 600 - 920 G. The lower end of this field range is dictated by the decreasing lifetime of the dressed molecules as the field is moved farther into the BEC limit. In this case, the lifetime of the dressed molecules becomes shorter due to collisional relaxation as the

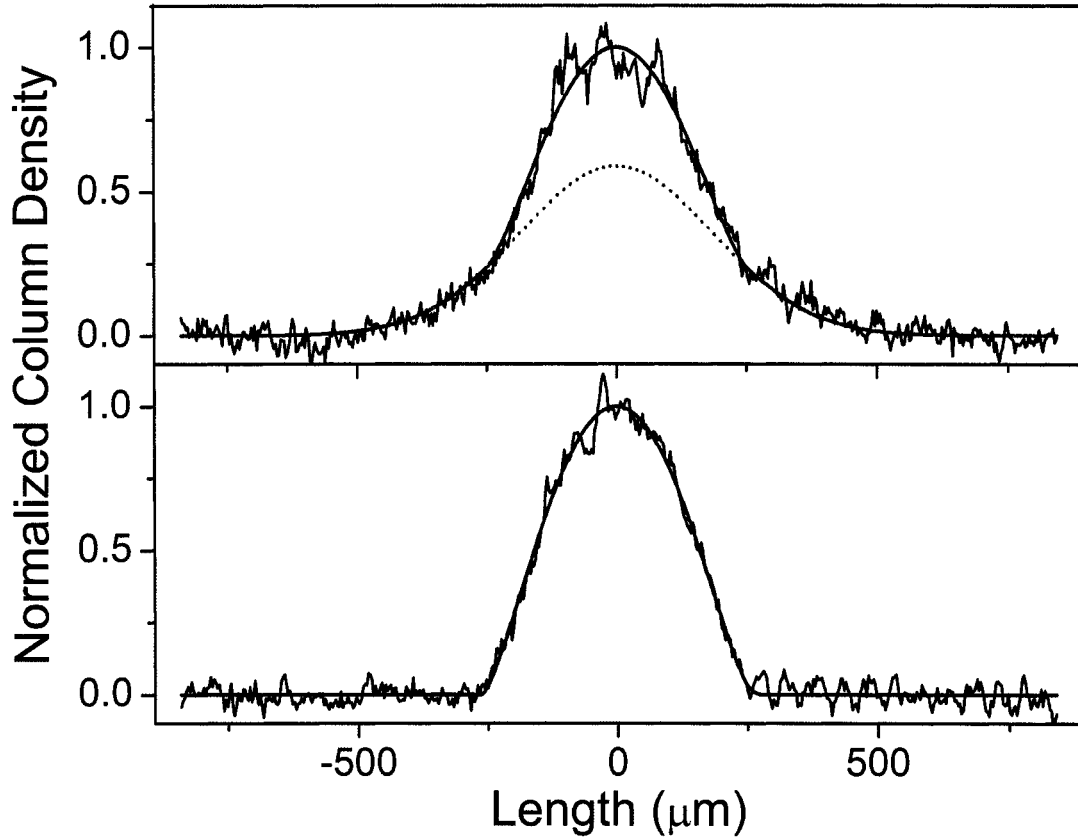


Figure 3.11 *In-situ* absorption image profiles showing a molecular BEC. These images were recorded at a field of 695 G after evaporation at 754 G. For the top panel, the optical trap depth was lowered to 0.5 μK . The solid line is a fit to a Gaussian (dotted line) plus Thomas-Fermi distribution which distinguishes the condensate from residual thermal molecules. For the bottom panel, the trap depth is reduced to 0.27 μK , producing an essentially pure molecular condensate with the number of molecules, $N = 46,000$. We estimate that the condensate fraction is $>90\%$, implying $T/T_c \leq 0.5$, where T_c is the critical temperature for BEC at 695 G. The solid line is a Thomas-Fermi distribution.

molecules acquire more bosonic character [40]. The upper limit is determined by a combination of the capability of our magnetic coils, and the diminishing returns in terms of scattering length versus field (see fig. 3.2), since at this field, the scattering length is not strongly field dependent. This field range is sufficient, however, to span the entire crossover, starting from the BEC limit and pushing beyond the strongly interacting regime, into the BCS limit.

A diagram of the measurement scheme is shown in fig. 3.12. The molecular probe laser is pulsed on for a given period of time, during which it drives the pairs to the excited molecular state at a rate, Γ . Once the pairs are in the excited state, they quickly decay at a rate $\gamma_m = (2\pi)11.7$ MHz, which is twice the atomic decay rate, as discussed earlier. The decay of the excited state molecule results in a gain of kinetic energy that is sufficient to cause the paired atoms to be lost from the trap. This loss rate may be expressed as

$$\Gamma = Z\Omega_m^2/\gamma_m, \quad (3.8)$$

where Ω_m is the on-resonance, intensity dependent, molecular Rabi frequency given by eq. 3.5 [22]. After the molecular probe pulse, the magnetic field is ramped back to 754 G in order to eliminate possible systematic uncertainties associated with probing at different fields. This loss is measured for a given field and pulse length by comparing the number of atoms remaining after the molecular pulse with a cloud for which the pulse is not fired. This measurement is repeated many times for each of several probe durations at each field. From these loss curves, rates are extracted, as described in the following section.

3.2.4 Molecular Loss Rate, BEC Side

Figure 3.13 shows typical loss curves, which are plots of normalized number versus molecular probe duration. The two data sets correspond to two different temperatures: one for a BEC (open circles), and one for a thermal gas at $T/T_F \sim 0.75$

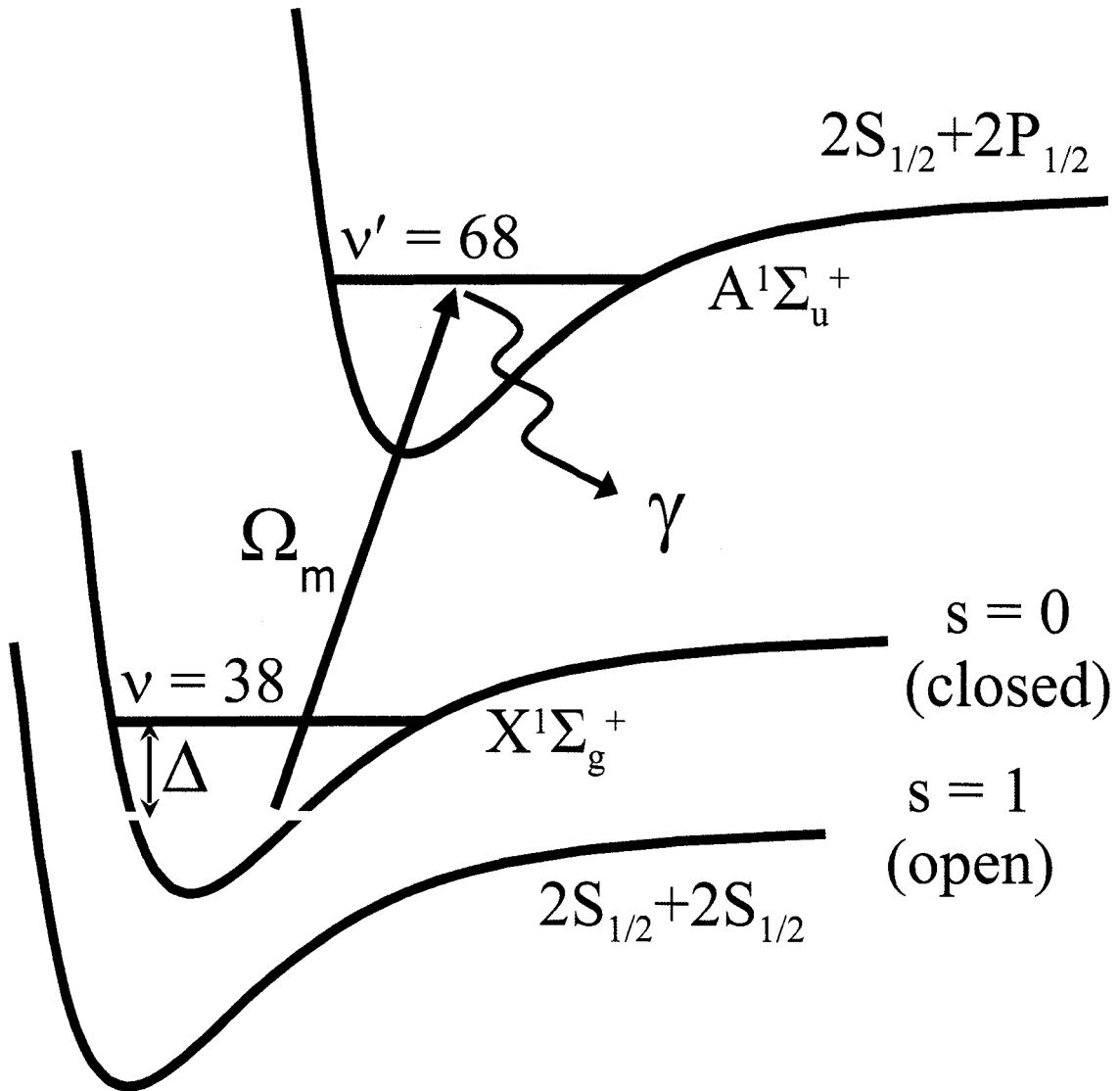


Figure 3.12 This diagram shows the generalized scheme for measuring the bare molecular contribution Z of dressed molecules, as in eq. 3.7, around the broad Feshbach resonance. A bias magnetic field is used to tune the $X^1\Sigma_g^+, v = 38$ bound state (closed channel) near the free atom threshold energy (open channel), to set a detuning $\Delta(B)$. A probe laser drives transitions from the dressed state to the excited molecular state, $A^1\Sigma_u^+, v' = 68$ at a rate Ω_m , given in the text. Once excited, the molecules decay at rate $\gamma \gg \Omega_m$ and are lost from the trap. The loss rate from the trap, Γ , is measured. Z is calculated for each $\Delta(B)$ by rearranging eq. 3.8 such that $Z = (\gamma\Gamma)/\Omega_m^2$.

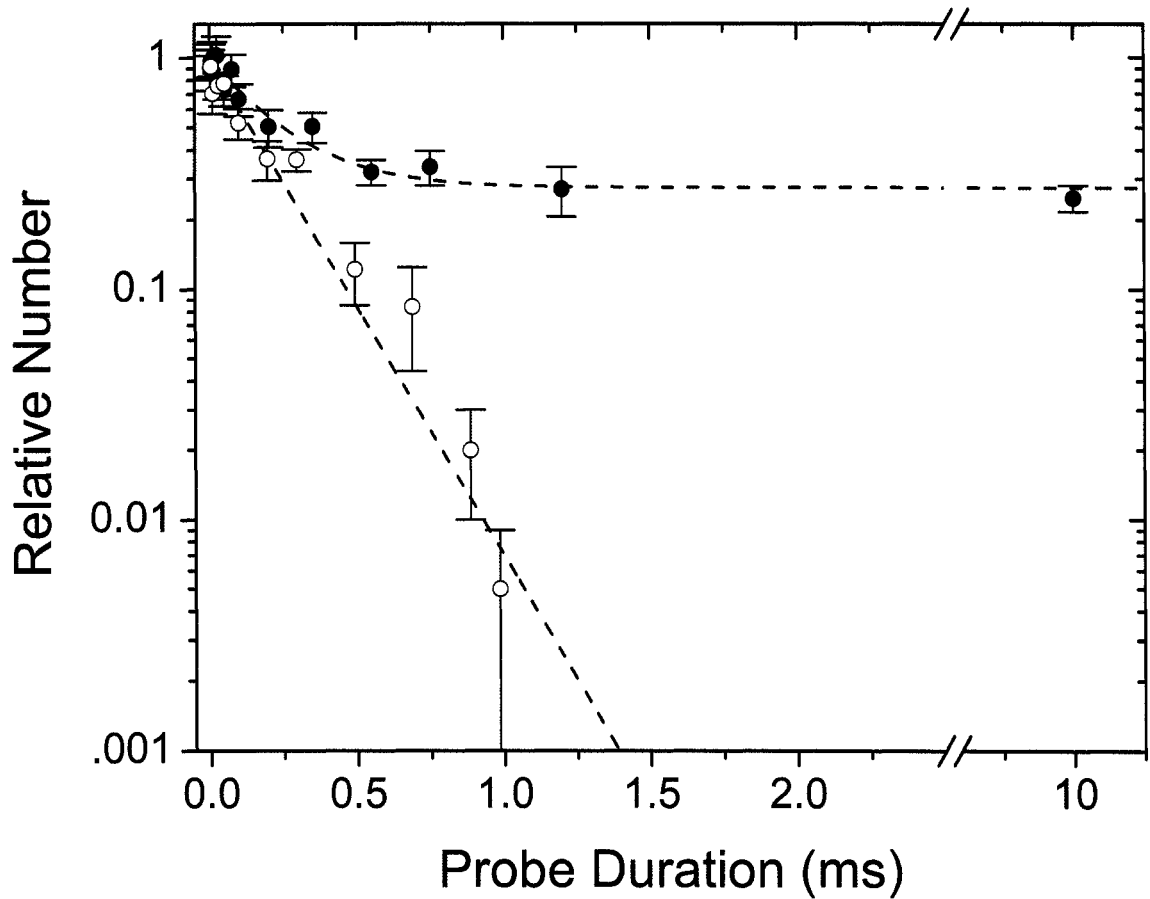


Figure 3.13 Loss of signal vs molecular probe duration at 695 G. The open circles correspond to a gas evaporatively cooled to a nearly pure molecular BEC, while the closed circles correspond to full trap depth, where $T/T_F \simeq 0.75$. The dashed lines are fits to exponentials, with a leftover fraction of 25% in the high temperature case. The time axis for the BEC data was scaled to account for differences in molecular probe laser intensity between the BEC data (30 mW/cm^2) and the high temperature data (15 mW/cm^2). We have verified that the loss rate depends linearly on intensity. The error bars represent the statistical standard deviation from the mean of ~ 10 independent measurements.

(closed circles), obtained without optical trap evaporation. This plot is taken at a magnetic field of 695 G, which is well into the BEC regime, since $a \simeq 1510 a_o$ and $k_F a \simeq 0.15 \ll 1$. As expected in the case of the BEC, the entire trap can be depleted for sufficiently long probe duration. An exponential fit to this data gives the value for the loss rate, Γ , from which, the numerical value of Z is computed by using eq. 3.8, along with the measured probe intensity. It turns out that the bare molecular contribution is quite small, as the measured value of Z from this rate is 0.0018(6). For the higher temperature data, the loss is initially exponential, but 25% of the initial number remain after a long probe duration. The remainder can be understood as thermally dissociated atoms that are only weakly affected by the probe, since they have a relatively small singlet character and excitation occurs only by two-body photoassociation.

Beyond the numerical result gained above, a more subtle understanding of the system may be gleaned from this result. That is, this excitation rate at the lowest temperature tells us that the observed process is a single body process, given the exponential loss curve. This means that even though we are driving a process with two atoms, these two atoms are behaving as a single particle, i.e. a bound molecule (despite the very small Z). In the present case, this is not all that surprising, since bound molecules are energetically stable on the BEC side of the Feshbach resonance, due to their lower energy relative to free atoms (see again fig. 3.4). As we shall soon see, however, this single body loss rate will become very telling as this measurement is extended to the BCS side of the resonance.

3.2.5 Molecular Loss Rate, BCS Side

Figure 3.14 shows the loss of signal vs. probe duration on the BCS side of the resonance at 865 G, where $a \simeq -15600 a_o$, for gases prepared at the same low and high temperatures as in the previous graph (fig. 3.13). At this field, the gas

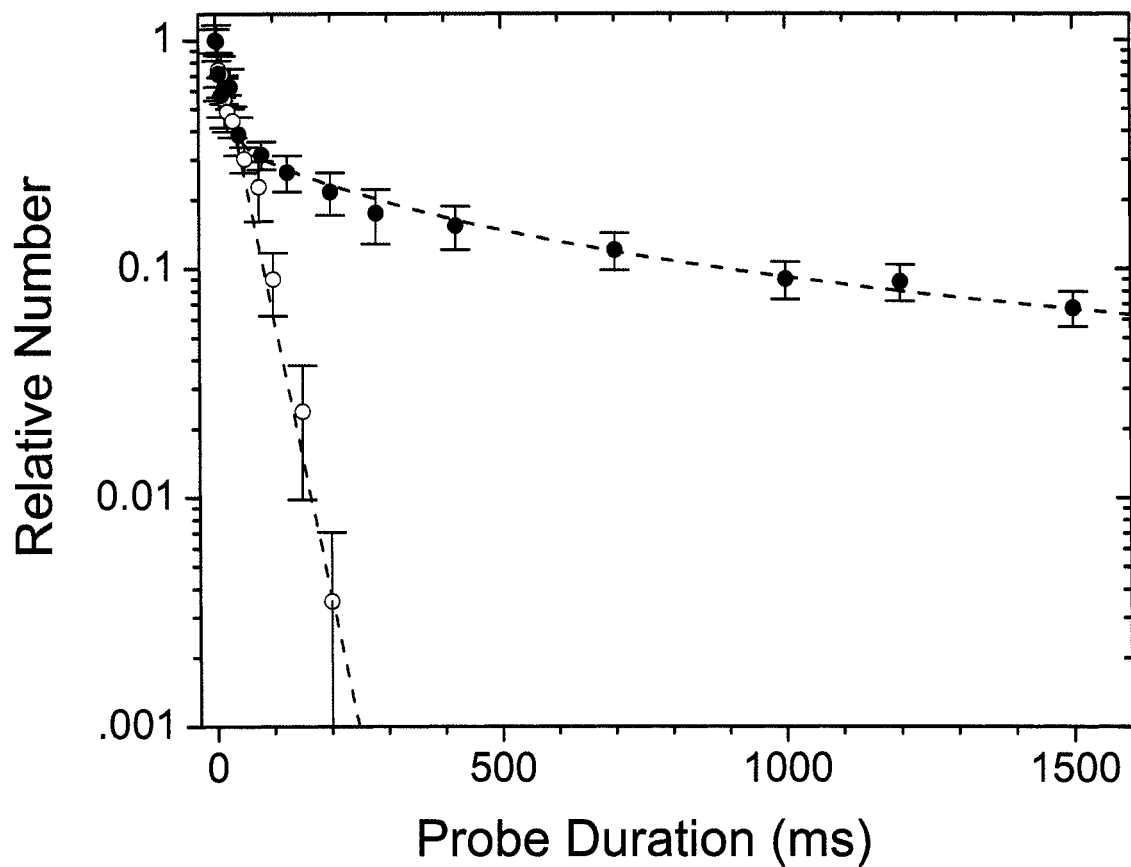


Figure 3.14 Same as for Fig. 3.13, except at 865 G. The dashed line in the case of the full trap depth data (closed circles) is a fit to a “two-fluid” model where one component decays via a rapid one-body loss process and the other via a slower non-linear two-body loss process. Approximately 75% of the gas is lost by the initial fast process.

is in the strongly interacting regime where $k_F|a| > 1$. This plot again shows the exponential dependence on probe duration that indicates a one-body loss process. This is surprising in this case, since, according to two-body physics, there are no bound states above the resonance at 834 G, and probe-induced loss would arise exclusively from two-body photoassociation.

At full trap depth, where the temperature is higher, the decay consists of two parts: an initial exponential decay, followed by a much slower two-body process. As the temperature of the cloud is $T \simeq 0.75 T_F$, this initial fast decay may indicate the presence of uncondensed paired fermions [12] or finite-lifetime molecules. The slower (two-body) process is ascribed to free-bound photoassociation of free atoms, which is supported by the fact that the extracted two-body rate coefficient, $K_2 = 4.9(3.3) \times 10^{-10} \text{ (cm}^3 \text{ s}^{-1})/(\text{W cm}^{-2})$, is reasonably consistent with the calculated value of $9.8(2.6) \times 10^{-10} \text{ (cm}^3 \text{ s}^{-1})/(\text{W cm}^{-2})$ obtained using the expression for K_2 given in ref. [53], where the uncertainties arise mainly from the temperature determination.

3.2.6 Paired Fraction: Molecules and Beyond

Figure 3.15 shows the values of Z extracted from loss rates taken at fields between 600 and 920 G. For fields below the resonance, our results are well modeled by a coupled channels calculation, shown as the curve in fig. 3.15. The quantity obtained from the coupled channels calculation is

$$|\langle \psi_{v'=68}(S=0) | \psi_p(B) \rangle / \langle \psi_{v'=68}(S=0) | \psi_p(B=0) \rangle|^2, \quad (3.9)$$

which represents an exact two-body theory in free space. An analytic expression for Z on the BEC side of the resonance has been given in ref. [68] and is also in good agreement with our result.

Since the size of the dressed molecules diverges at resonance, two-body theory predicts that the overlap with the excited molecules vanishes and Z goes to zero as the resonance is approached. Furthermore, there is no longer an energetically stable

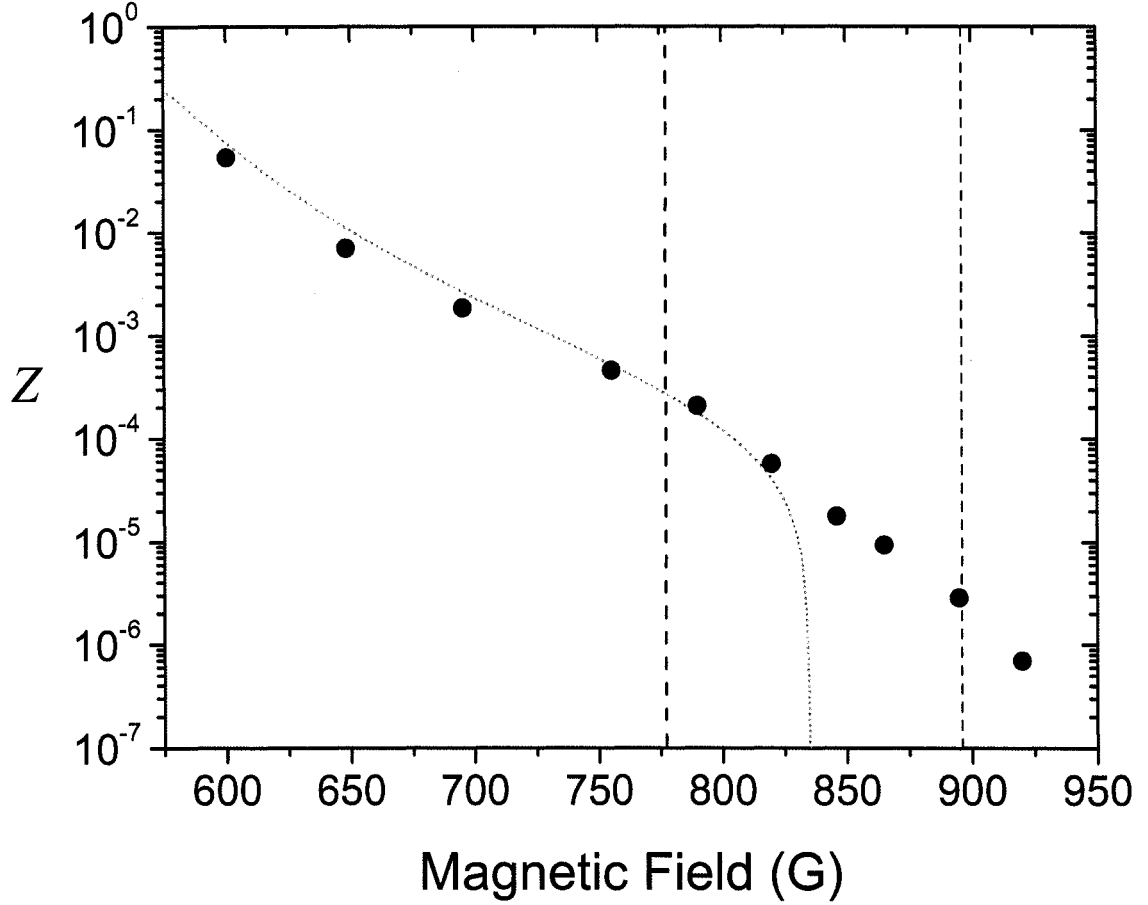


Figure 3.15 Z vs. B . The closed circles represent the value of Z extracted from measured values of Γ . The uncertainty in Z is approximately equal to the size of the closed circles, and is due mainly to uncertainty in the probe laser intensity. The dotted curve shows a comparison with results obtained from a coupled channels calculation that only takes two-body physics into account. The vertical dashed lines represent the boundaries of the strongly-interacting regime, $k_F|a| > 1$, where k_F is evaluated using typical values of N at the low and high field extremes. Although shot-to-shot variations in N are 30%, the average value of N at each field is between 13,000 and 90,000 due to day to day variations. T_F is between 200 and 600 nK due to differences in N as well as the trap frequencies. For all the data, $T < T_c$, and for the points above 850 G, $T < 0.5 T_c$, where T_c refers to the critical temperature at 695 G.

bound state above the resonance, since it has been tuned above the threshold energy of the atomic state. Accordingly, this theory predicts that Z should be zero at and above the resonance. Despite this prediction, however, the measured quantity continues smoothly through resonance, and while the two-body theory fails for fields above resonance, the data compares favorably with more detailed theoretical calculations which span the entire range of interactions and include many body [69, 70] and mean field effects [71].

While two-body (multi-channel) theory does not capture the essential physics above resonance, it is possible to gain intuition by moving to a single channel model. This approach is considered since the magnitude of Z is small, and the Feshbach resonance is broad (compared to the Fermi energy). Under these circumstances, the physics of the crossover should be well described by a single channel model [45]. In this approach, we note that the loss rate Γ is proportional to the local pair correlation function $G_2(r, r) = \langle \hat{\psi}_\downarrow^\dagger(r) \hat{\psi}_\uparrow^\dagger(r) \hat{\psi}_\uparrow(r) \hat{\psi}_\downarrow(r) \rangle$, where $\hat{\psi}_\uparrow$ and $\hat{\psi}_\downarrow$ are the fermionic field operators for atoms in different internal states. In the mean-field approximation G_2 may be factorized as $G_2(r, r) = n^2(r) + \langle \hat{\psi}_\downarrow^\dagger(r) \hat{\psi}_\uparrow^\dagger(r) \rangle \langle \hat{\psi}_\uparrow(r) \hat{\psi}_\downarrow(r) \rangle$, where the first term is the Hartree term with atom density $n(r) = n_\uparrow(r) = n_\downarrow(r)$. This term is linked to the slow two-body photoassociation observed in the high temperature data of fig. 3.14. The second term is non-zero only for correlated pairs and is proportional to $|\Delta|^2$, the square of the order parameter. In the BCS limit, $|\Delta|^2 \propto \epsilon_F^2 e^{-\pi/(k_F a)}$, whereas in the BEC limit, $|\Delta|^2 \propto \epsilon_F^2/(k_F a)$ [72], which is simply proportional to $n(r)$, and produces a rapid one-body loss.

Figure 3.16 shows a plot of the data and the functional form of $|\Delta|^2$ versus $(k_F a)^{-1}$. From this figure it is evident that the data has the correct dependance on $(k_F a)^{-1}$ on the BEC and BCS sides of the resonance, and smoothly links both through the crossover region. Note that non-condensed pairs [12] will give rise to a similar factorization of G_2 but it is not expected to have the same dependence on $k_F a$.

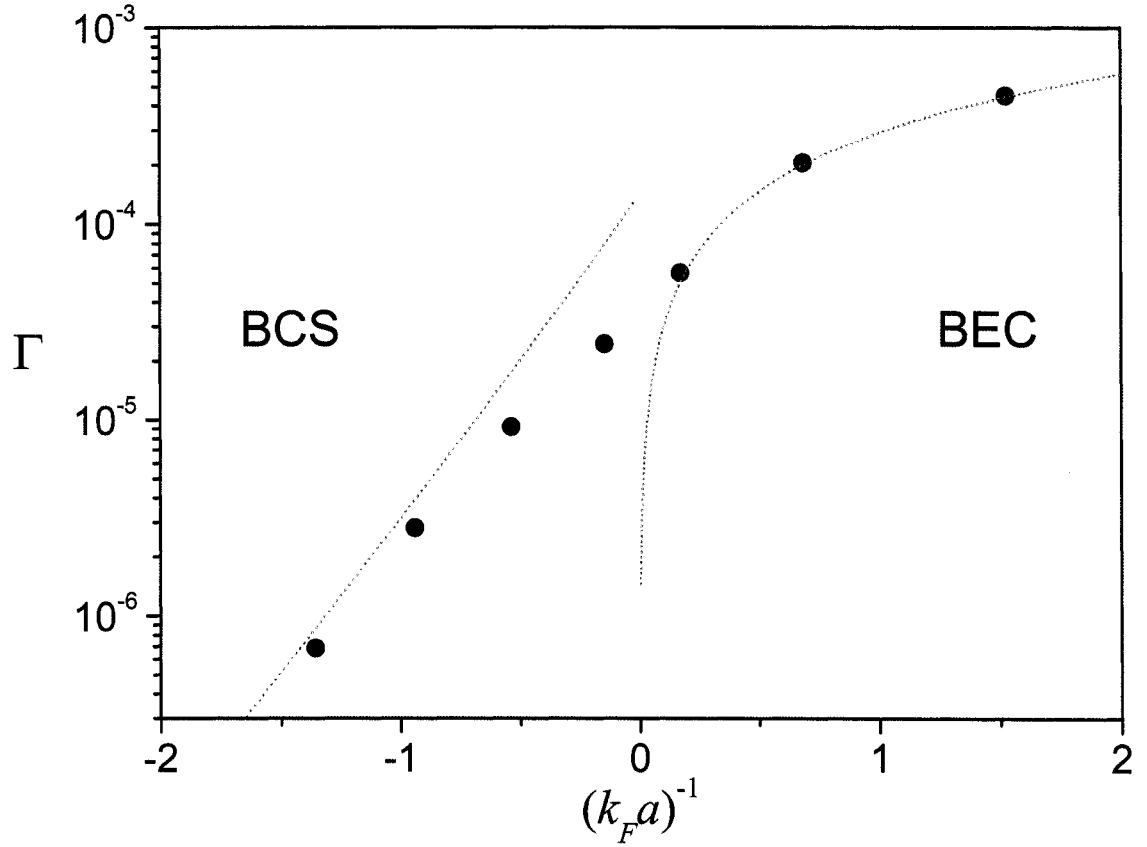


Figure 3.16 Comparison of Γ with $|\Delta|^2$. Γ is expressed in units of Ω^2/γ making it equivalent to Z plotted in Fig. 3.15. The dashed lines correspond to evaluations of $|\Delta|^2$ in the BCS and the BEC limits integrated over a Thomas-Fermi density profile. They have been scaled by the same factor to give the best fit on the BEC side.

3.3 Conclusions

By driving a transition to an electronically excited molecular singlet level, we have measured the paired component of spin mixture of interacting fermionic atoms from the BEC to the BCS limits, as well as in between. This method provides a very accurate measurement of a very small quantity, since although the closed-channel fraction is finite and measurable, its magnitude above resonance is sufficiently small, $\lesssim 10^{-5}$, that the expectation of the number of closed-channel molecules is less than one (since our trap typically contains $\sim 10^5$ atoms). The quantitative nature of this measurement can be used to refine theoretical models of the Feshbach resonance and the associated crossover.

Remarkably, we also find that the pairing amplitude is continuous across the resonance and extends into the weakly interacting BCS regime, where two body physics predicts no such molecular contribution. By adopting a single channel model, we are able to associate the measured loss rate with pair correlations through the order parameter. We find the proper dependence on interaction strength, $k_F a$, for both the BEC and BCS regimes.

This experiment represents a decomposition of the pair wavefunction, and reveals that the singlet closed channel component of the pairs is extremely small, less than 10^{-3} , in the strongly interacting regime. In this regime, the strongly interacting gas may be considered universal, since the scattering length diverges and the physics of the Fermi gas is determined only by the Fermi energy, E_F , and the temperature, T/T_F [73–75]. Moreover, it has been shown that the characteristics and behavior of the gas in the strongly coupled regime, where $|k_F a| > 1$, are accurately described by a single channel model that considers only the open, scattering (fermionic) channel, [45]. Confirmation of this idea strongly supports the contention that spin mixtures of fermionic atoms in a broad Feshbach resonance may be used as a model system for other crossover fermionic systems, such as high T_c superconductors.

We will continue to utilize, as well as verify, this universality in the next chapter where we extend our studies of pairing to characterize phases that result when there are not even numbers of atoms in each state to pair.

Chapter 4

Polarized Fermi Gases

In order to study pairing of fermionic ${}^6\text{Li}$, we have up to this point required a uniform spin mixture of the two spin states needed to access the Feshbach resonance. In this chapter I will present experiments designed to probe the behavior of such a system when the populations of the two spin states are unequal.

4.1 Polarized Fermionic Systems

Pairing in fermionic systems is the key to superconductivity and superfluidity. In an evenly paired superconductor or superfluid, the BCS pairs are formed near the (spherical) Fermi surfaces by particles with equal and opposite momenta, such that $\vec{Q} = \vec{k}_{F\uparrow} + \vec{k}_{F\downarrow} = 0$, where Q is the net pair momentum and $\hbar k_{F\uparrow,\downarrow}$ are the momenta of the two constituent fermionic particles.

While the pairing is facilitated in balanced systems, where there is an overlap between the Fermi surfaces of the two constituents, it is interesting to consider the case in which the two Fermi surfaces do not overlap entirely, as shown in fig. 4.1. This situation may occur when different particles have different masses, such as in cold dense matter at the core of neutron stars [76]. A mismatch may also result from a mismatch of populations of two pairing states. In such instances, it would seem as if superfluidity may not be possible, due to the lack of overlap between particles which are needed to form pairs. Indeed in the BCS limit, pairing and superconductivity break down when the difference in the chemical potentials approaches that of the pairing gap [77]

$$\Delta \lesssim \mu_1 - \mu_2. \quad (4.1)$$

This is known as the Clogston limit, where μ_i are the chemical potentials of the two states, and Δ is the gap, which is small in the weakly interacting BCS regime.

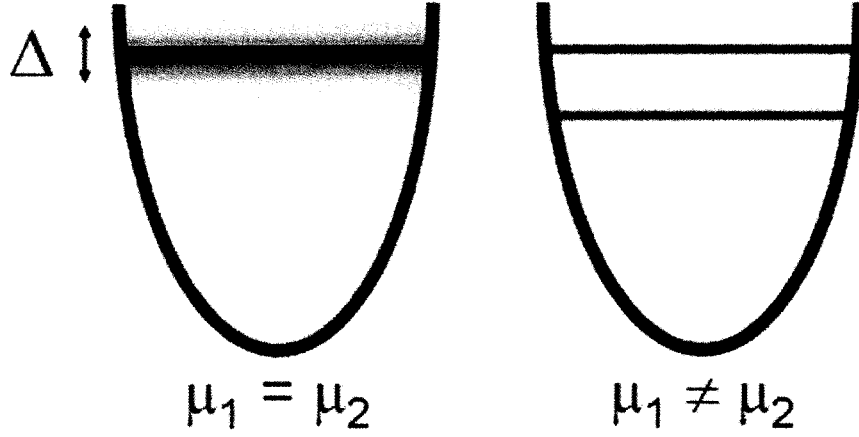


Figure 4.1 When the chemical potentials of two interacting Fermion species overlap, pairing may result. Imbalanced chemical potentials can be caused by differences in mass or number of the two species, and can eliminate the pairing and superfluidity if the difference is too large.

Despite this apparent limit, there are several proposed mechanisms which may allow for a system to remain at least partially superfluid under imbalanced conditions, especially when interaction strength is increased. These proposed mechanisms boil down to different ways for a portion of the system to remain paired while accommodating the excess unpaired particles in some way. They can be classified by the symmetry of the resulting Fermi surfaces for the so called majority (larger) and minority (smaller) Fermi surfaces, and are illustrated in fig. 4.2.

The first imbalanced superfluid is known as the Sarma (or breached pair) phase [78, 79]. This phase is also sometimes referred to as a polarized or magnetized superfluid. In the Sarma phase, pairing occurs at the location of the minority Fermi surface, leaving a shell (in \mathbf{k} -space) of leftover unpaired majority particles. This pairing results in both rotational and translational symmetries being preserved, as in the BCS case. In real space, the pairs and the excess unpaired particles co-exist.

The next mechanism for imbalance accommodation is the deformed Fermi surface (DFS). A DFS state occurs when the Fermi surfaces of the minority and majority states deform in order to maximize their overlap [80, 81]. To first order, the surfaces

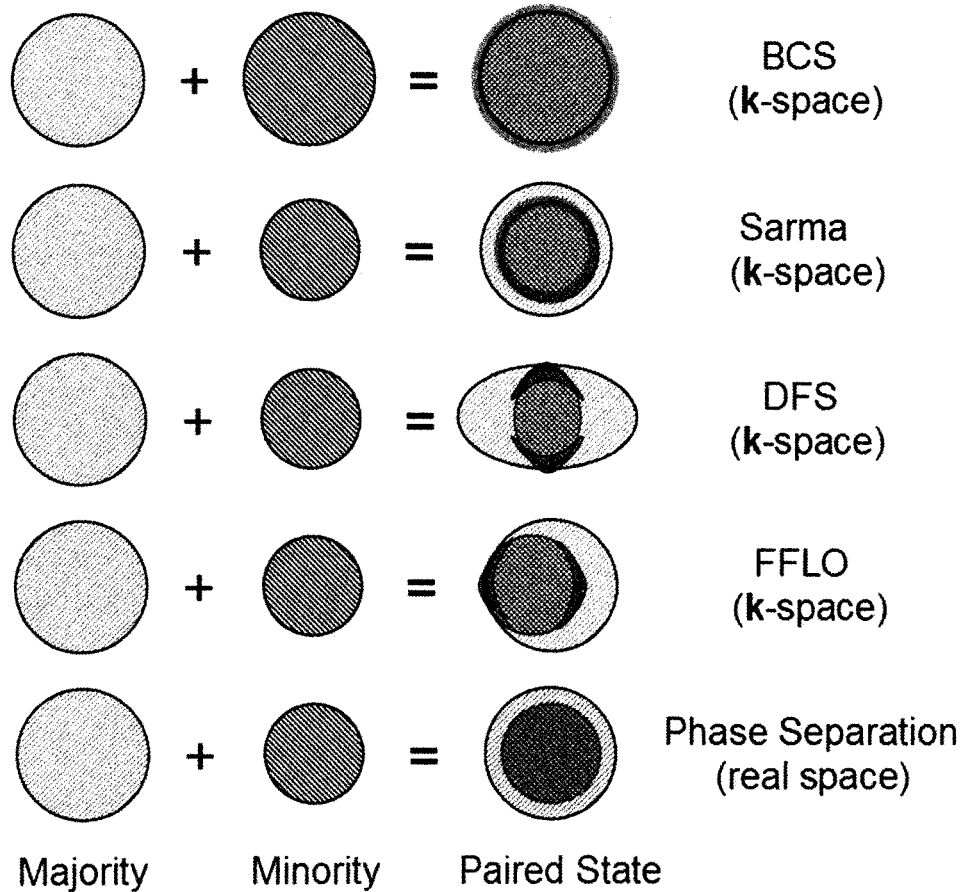


Figure 4.2 Shown are representative Fermi surfaces for a two component mixture. The top row corresponds to the case of a balanced mixture, in which the two Fermi surfaces overlap. In such a situation, pairing and superfluidity may occur. For weak interactions, in the BCS limit (shown) pairs form near the edge of the Fermi surfaces. For sufficiently strong interactions, nearly the entire system may pair. The remainder of the rows shows possible outcomes that may result from an imbalance in the Fermi energies of the two species. In the second row (Sarma), pairing is relocated to a shell at the edge of the minority Fermi surface. Outside this shell, there are unpaired majority atoms. The third row shows the DFS state, where the Fermi surfaces of the majority and minority have deformed so that some overlap is possible. Pairing occurs where they meet. The fourth row shows the FFLO state, where the minority component has shifted relative to the majority so that the Fermi surfaces can be closer. Since the momentum of the two paired constituents are not equal in magnitude, the pairs have nonzero momentum. Finally, in the last row, a phase separation in real space is shown. In this case, the uniformly paired superfluid core separates from the normal unpaired shell.

deform from spherical to become ellipsoidal, with opposite major axes. In the region of overlap, where the deformed surfaces meet, there may be pairing and subsequently, superfluidity. In the DFS state, pairs are still formed from particles with equal and opposite momenta ($Q = q_1 + q_2 = 0$), so they have zero net momentum and translational symmetry. However, this phase is characterized by the breaking of rotational symmetry in momentum space because of the angular dependence of the pairing.

Another proposed mechanism to allow imbalanced pairing is the Fulde-Ferrell-Larkin-Ovchinnikov (FFLO) state [82, 83]. In this phase, the Fermi surfaces of the minority and majority states offset from each other in momentum space in order to maximize their overlap. This offset results in pairing between particles with unequal magnitudes of momentum, $\vec{q}_1 \neq -\vec{q}_2$, and pairs which have a net non-zero momentum $Q = q_1 + q_2 \neq 0$. This state is characterized by the breaking of rotational and translational symmetry.

In addition to the momentum distributions of the majority and minority changing to accommodate an imbalance, the real space distributions may also be modified. One such possibility is for a phase separation to occur between uniformly paired region(s) and the remaining unpaired majority particles [84–88]. In this case, the paired superfluid fraction is effectively isolated from the normal, unpaired phase, and in this way, remains balanced. As we shall see, in many situations (such as in our experiments) a result of this separation is that the other phases above may be preempted, since the effects of the imbalance is effectively negated when the phases separate.

4.2 Experiments

Only recently has there been experimental activity regarding imbalanced superfluids and superconductors. In the field of solid state physics, a newly discovered heavy fermion superconductor, CeCoIn₅, with a quasi-2D electronic structure has allowed

for a series of experiments aimed at searching the phase space of a superconductor in a magnetic field [89–93]. Evidence for an inhomogeneous superconducting state may indicate the stabilization of the FFLO phase under certain conditions, though alternate explanations have also been suggested [94].

Our field of ultracold atomic gases has also recently begun a push to explore the possibilities which may exist for trapped ultracold imbalanced Fermi gases. Shortly on the heels of the demonstration of pairing [22, 95–97], and superfluidity [98–100] in a two-state spin mixture of fermionic atoms, our own experiments [23, 24] and experiments conducted in Wolfgang Ketterle’s lab at MIT [101–103] have demonstrated that the tools at the disposal of an atomic physicist are well suited for this endeavor.

For these experiments, we have developed a system for creating and probing a polarized gas of trapped ultracold fermionic ${}^6\text{Li}$ atoms. By utilizing the controllability and tunability inherent in such a system, we are able to explore many facets of this problem that have previously not been experimentally accessible. Though much of the apparatus used for this experiment is described in previous chapters, there are several additions and modifications specific to creating and probing a polarized gas that must be described.

4.2.1 Experimental Process

In the previous chapters, a spin mixture of two types of interacting fermionic atoms was needed to allow for pairing to take place. For the experiments presented so far, we have used an even mixture of two hyperfine states of ${}^6\text{Li}$ to meet this requirement. In this way, we have seen that it is possible to create superfluid states with paired atoms. In much the same way, we may also study a superfluid with mismatched Fermi surfaces by varying the relative populations of the two spin states.

As in the previous chapter, an ultracold gas of ${}^6\text{Li}$ is transferred from a magnetic trap to an optical trap. The optical trap used for these experiments is formed from

a single focussed infrared laser beam at 1080 nm. At transfer, the trap depth is set to approximately $110 \mu K$, and produces trapping frequencies of 4.8 KHz radially and 45 Hz axially. The details and characterization of this trap are given in Chapter 2.

As before, upon transfer to the optical trap, a bias magnetic field is ramped to a magnetic field within the broad Feshbach resonance. This field is typically either 834 G, the center of the resonance [47, 104], or 754 G, on the BEC side. At this field, the atoms are transferred from state $|6\rangle$ ($F = 3/2$, $m_F = 3/2$) to state $|1\rangle$ ($F = 1/2$, $m_F = 1/2$) by a single RF sweep.

It is at this point in the process where the spin mixture of states $|1\rangle$ and $|2\rangle$ ($F = 1/2$, $m_F = \pm 1/2$) is created that the experiments in this chapter diverge from those described previously.

4.2.2 Uneven Spin Mixture

The most obvious experimental change for these experiments is that we now wish to have a spin mixture that consists of unequal numbers of each state, $|1\rangle$ and $|2\rangle$. As previously described in Chapter 2, we create an even spin mixture by a succession of RF frequency ramps that transfer the gas, initially in state $|1\rangle$, to an even mixture of $|1\rangle$ and $|2\rangle$. After creating this mixture, strong Feshbach mediated s-wave interactions allow for efficient evaporation in the optical trap. At first impression, we believed that it would be relatively straightforward to modify this procedure to create an uneven mixture, and in the end, this proved to be more or less true. However, through the course of developing this procedure, we have experimented with several pathways for creating ultracold unequal spin mixtures.

Constraints

The methods we have available for creating a cold, uneven mixture are subject to two constraints, the first of which is obvious, and the second of which we have identified through experimentation. First, it is necessary to have both spin states

present in the trap during the evaporative cooling cycle. Otherwise, there will be no interactions (identical fermions) and therefore no rethermalization and no cooling may take place. Second, at the lowest temperatures (after evaporation), when states $|1\rangle$ and $|2\rangle$ are paired, any manipulation of either state will perturb the other through their binding or pairing energy. As such, if one atom of the pair is manipulated or removed, the other member of the pair may be heated. For this reason, the spin mixture preparation should take place before the gas is paired. The overall result is that some sort of spin mixture must be prepared prior to evaporation to comply with the first constraint, but the mixture cannot be even, since manipulation of the spin populations after cooling tends to result in loss.

Methods

One method for creating an imbalanced spin mixture is to drive atoms from state $|2\rangle$ to state $|3\rangle$ using RF frequency ramps tuned to the transition frequency (~ 80 MHz), as shown in fig. 4.3. Once a $|2\rangle$ atom is converted to a $|3\rangle$, it immediately (on the time scale of the RF sweeps) partakes in a three body collision with an atom each of states $|1\rangle$ and $|2\rangle$, since the third body negates the suppression of these collisions that applies when only two fermionic species are present. This collision results in the loss of all three atoms from the trap. Figure 4.4 shows the population of the three states as a function of weak RF ramps. Since state $|2\rangle$ atoms are lost faster than those of state $|1\rangle$, an imbalance may be achieved. In the end, though this method successfully produced a polarized gas, it also resulted in an unacceptable loss in total number, so was not pursued further. Along a similar vein, it is also possible to selectively remove atoms of either state via an optical pulse tuned to a transition specific to one state or the other. In this case there are no three body losses to contend with, though this method is again based on removing atoms and so is not optimal.

Instead of starting with an even mixture and making it uneven, as above, we now

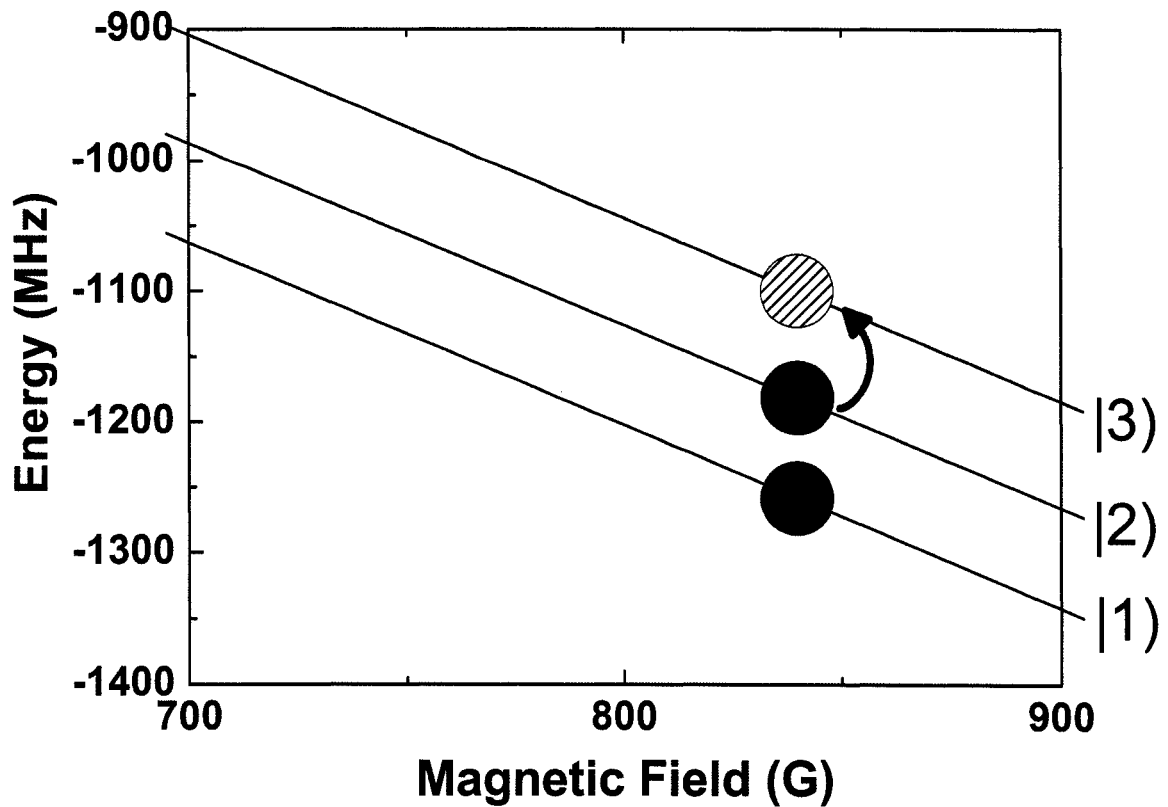


Figure 4.3 An imbalanced spin mixture can be created by driving atoms in an even mixture from state $|2\rangle$ to state $|3\rangle$ by driving weak ramps tuned to the transition frequency of ~ 80 MHz. When this is done within the Feshbach resonance where interactions are strong, three-body loss removes the state $|3\rangle$ atoms as they are converted. This process also removes one each of the $|1\rangle$ and $|2\rangle$ atoms. Though this process will create an imbalance, it does so at the cost of lost atoms as shown in fig. (4.4).

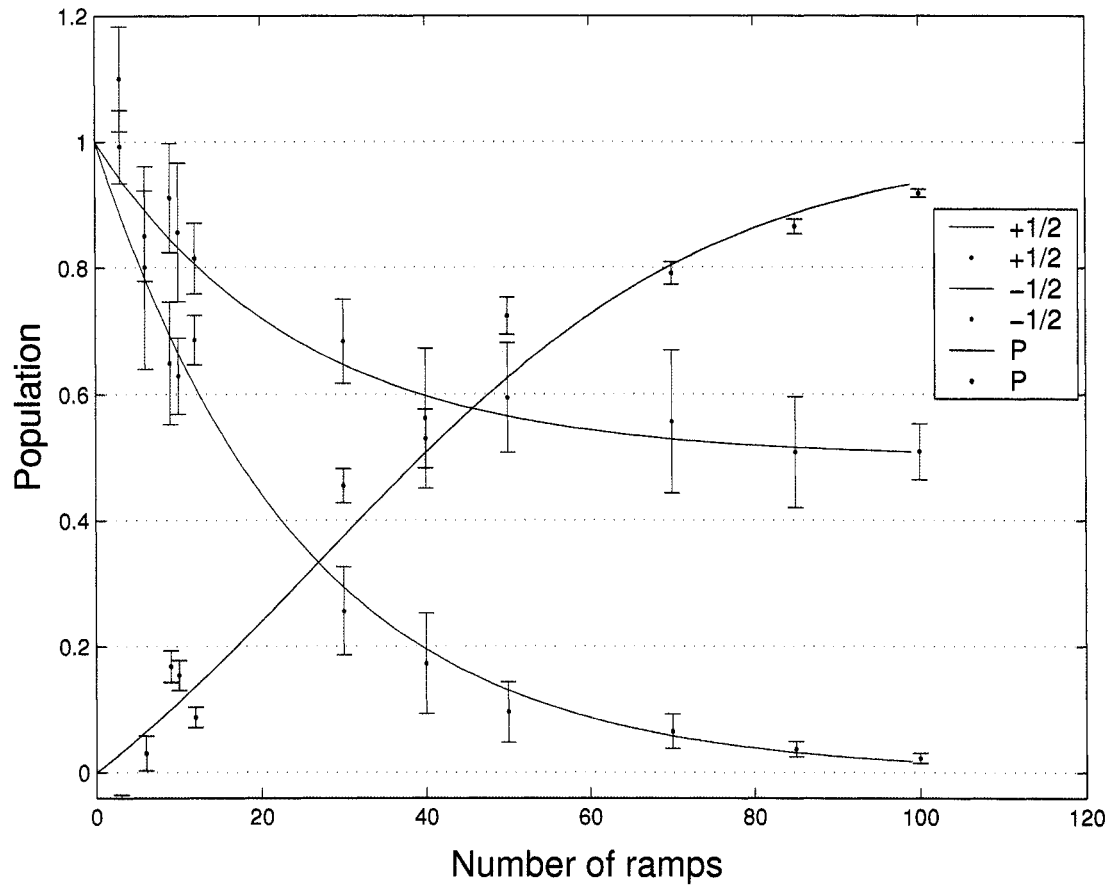


Figure 4.4 This graph shows the result of driving the transitions described in the previous fig. (4.3). The blue (red) data points are the relative population of state $|1\rangle$ ($|2\rangle$). The black points are the polarization P . The solid lines are the result of a simulation for which 2% of the $|2\rangle$ atoms are transferred to state $|3\rangle$ per ramp. Subsequently, each $|3\rangle$ atom removes two atoms, one of each state $|1\rangle$ and $|2\rangle$.

simply stop short of creating an even mixture. The method which proved to be most reliable consisted of reducing the RF power in the multiple ramps used to drive the transition between states $|1\rangle$ and $|2\rangle$, described in Chapter 2. This method was chosen primarily because it produced polarized samples with relatively large majority atom number, and also provided a way to create unpolarized samples as well. In addition, this method allowed for a quick turnaround if a different polarization was desired, since it only necessitated changing a single parameter of the control program.

When using the above method, there is some variation in the final polarization at the end of evaporation for a given mixture ramp RF power.* The variance in prepared P for a given setting is effected by experimental quantities such as atom number, final trap depth and intended polarization range. In general, the scatter in P increases with increasing P . Typically, there is a scatter of $\delta P/P \sim 0.1 - 0.2$ for the range of $0.1 \lesssim P \lesssim 0.8$, with less scatter at lower P and more at the highest values. Variations in polarization arise partly because the optical trap evaporative cooling is quite sensitive to small variations initial conditions, though for the experiments presented in this work, this behavior is not necessarily a limitation, since a distribution of polarizations is desired. Changing the RF power between a few settings which coarsely set the final polarization range of the samples, convolved with shot-to-shot fluctuations, produces a uniform distribution of polarizations.

4.2.3 Rapid Dual Probing

Since our control over the final polarization of the gas is coarse, it is necessary to accurately measure the polarization which is actually produced. With this in mind, and to most accurately characterize the *in-situ* distributions of each state, we have constructed an optical probing system that is capable of independently imaging both states $|1\rangle$ and $|2\rangle$ in rapid succession. From these images, numbers N_1 and N_2 , may

*Intentionally prepared even mixtures are the exception, since they are reliably produced ($\delta P/P = 0$), as previously described in Chapter 2.

be obtained. To quantify the mismatch, we also define the polarization $P = \frac{(N_1 - N_2)}{N_1 + N_2}$.

The function of the dual probe is to rapidly switch the ^6Li probe laser between the two frequencies needed to probe states $|1\rangle$ and $|2\rangle$. In addition, an acquisition system has been developed that is capable of receiving and recording the rapidly produced images of states $|1\rangle$ and $|2\rangle$. Figure 4.5 shows the optical layout of the two-species probe setup (the “dual probe”). The frequency switching is accomplished through the use of an AOM tuned to the frequency difference between the two optical probing transitions (~ 77 MHz).

An acquisition is typically obtained by tuning the probe laser to the proper frequency for probing state $|2\rangle$ during the magnetic trap evaporation, which lasts approximately one minute. After the final polarization state is prepared in the optical trap, the probe sequence fires once to probe state $|2\rangle$. In quick succession, the dual probe system switches the probe frequency and the probe fires again to probe state $|1\rangle$ (see fig. 4.6). For most of the work presented in this chapter, the delay time between pulses is $27\ \mu\text{s}$, though some of the earlier data was taken with a delay of $215\ \mu\text{s}$ * [23]. As a test for systematic uncertainties arising from the probe order, these experiments have been confirmed by repetition with the opposite probe order.

In order to acquire images at a such rapid repetition rates, it is necessary to utilize a specialized CCD camera with the ability to acquire in a mode known as fast kinetics, where the CCD array itself is used as temporary storage memory. This application consists of masking off most of the array so that no light may reach it, thereby leaving a small strip along the top exposed†. After the first absorption image has been exposed on the top of the array, it is transferred down onto the masked

*The limiting factor for the probe repetition rate is the parallel shift rate of the CCD camera. The rate for the later data was improved by upgrading our camera. (Andor iXon DV887, parallel shift rate $\sim 0.5\ \mu\text{s}/\text{row}$.)

†For this data, the exposed region is typically 40-48 rows, out of 512 total. The masking of the array is accomplished by placing a razor blade at the image plane of the imaging system. The camera itself un-modified. The shift speed of the new camera (see previous footnote) of $0.5\ \mu\text{s}/\text{row}$, plus a 3-5 μs exposure, sets the $\sim 27\ \mu\text{s}$ repetition rate.

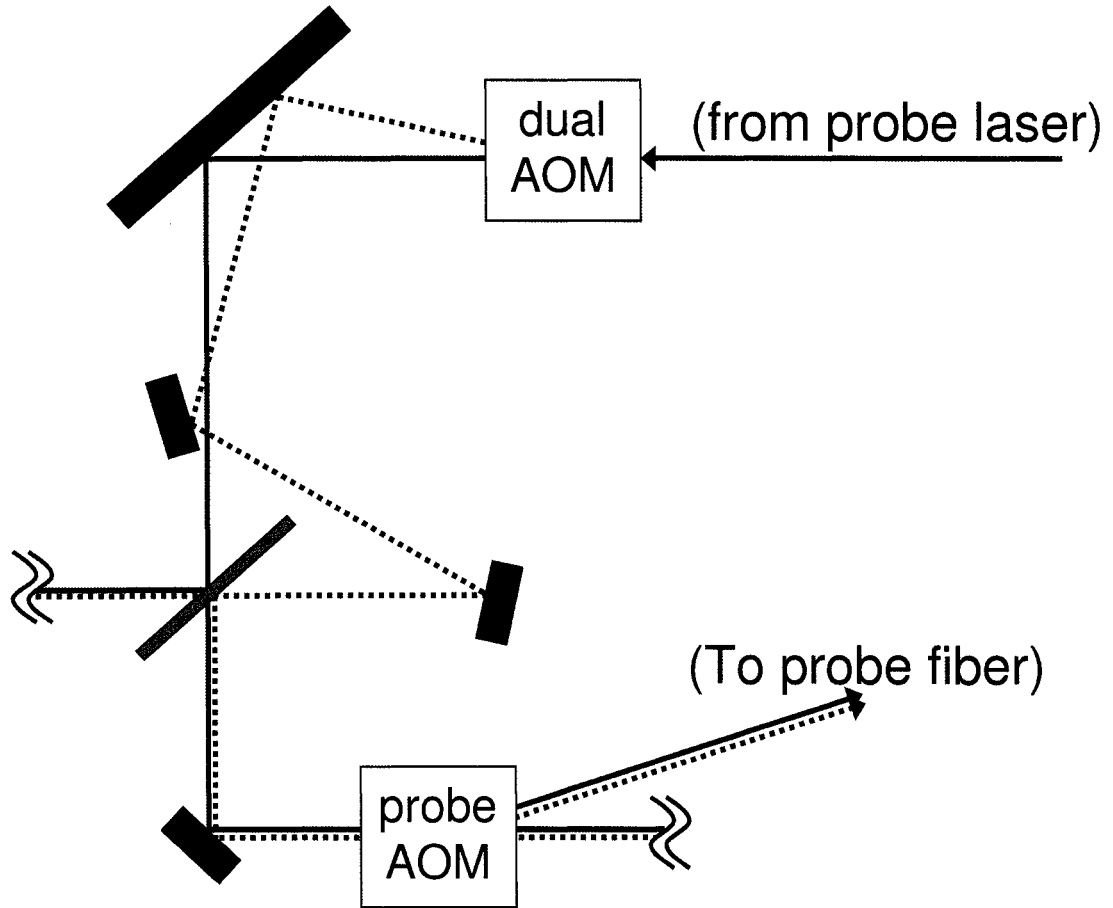


Figure 4.5 The optical probes for both states $|1\rangle$ and $|2\rangle$ are produced from a single beam by this optical setup. To probe both states, a beam tuned to the probing transition of state $|2\rangle$, enters the “dual” AOM. If the AOM is off, the light (solid line) passes through and is directed to the “probe” AOM which pulses it on for the specified probe duration, typically 3 - 5 μs . The pulsed beam is coupled into a single mode optical fiber that takes the light to the atoms, as described in Chapter 2. After the first state ($|2\rangle$) is probed, the dual AOM is pulsed on by a pulse delay circuit so that its first blue sideband is shifted by the drive frequency ~ 77 MHz, the difference in the probe frequencies of the two states. The first order of the dual AOM is also directed into the probe AOM via a beamsplitter, and is pulsed on in the same manner. When the dual AOM is pulsed on, the undefracted beam is reduced to $\sim 10\%$ of its initial power. Moreover, the remaining light is not well coupled through the fiber due to its poor spatial mode (and possibly to transient polarization effects). When the system is properly aligned, leakage of the undefracted beam in the second probe is $\lesssim 1\%$ after the fiber.

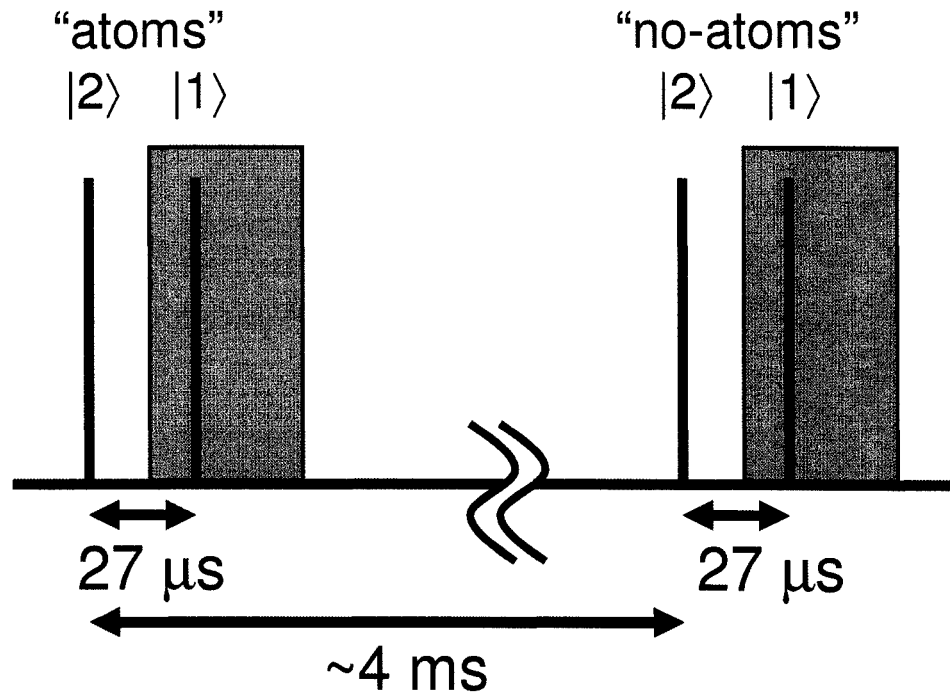


Figure 4.6 The timing diagram of a probe sequence is shown. The probe AOM is shown as black lines and the dual AOM as gray rectangles. The “atoms” shots are the absorption probes, and the “no-atoms” shots are identical images taken after the optical trap is cleared of atoms, and are used for image processing. To reverse the state probe order, the pulse of the dual AOM is shifted to the first shot. The data in this chapter was taken with a $27\ \mu\text{s}$ delay between probe shots, except for the data in figs. 4.32 and 4.33, which had a $215\ \mu\text{s}$ delay. Probe durations were $3\text{--}5\ \mu\text{s}$.

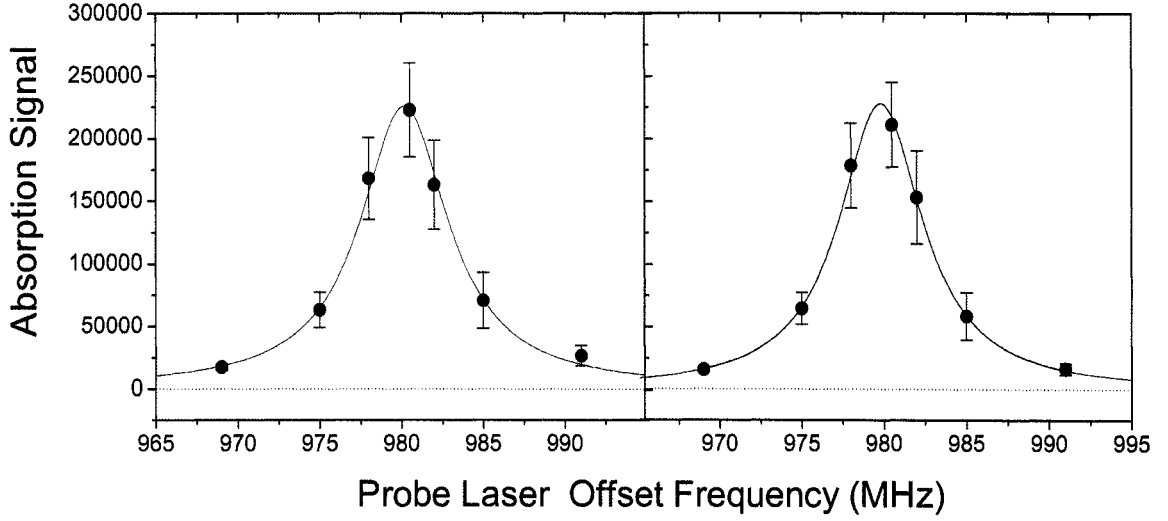


Figure 4.7 These data show the resonance curves for probing states $|1\rangle$ (left) and $|2\rangle$ (right). The scale of the Y-axis is the measured number, assuming on resonance probing, $\Delta = 0$. The error bars are the standard error of 6 measurements. The frequency is that of the detuning of the probe laser from a laser referenced to a heat pipe (see text/footnotes). The red lines are fit to a lorentzian distribution. For state $|1\rangle$ ($|2\rangle$), the fit gives a central frequency of 980.2 ± 0.4 (979.8 ± 0.4) MHz, with a width of 6.5 ± 1.5 (6.2 ± 1.4) MHz, consistent with the linewidth of the transition $\Gamma = 5.9$ MHz. Both resonances are centered on the same frequency since the dual AOM frequency shift is not included in the plot.

portion of the array, and another image is exposed.

Figure 4.7 shows a measurement of the absorption signal versus detuning taken using this dual probe setup. For these resonances, the offset of the probe laser is set by monitoring a beat note formed by overlapping the probe laser with a reference beam on a photodiode.* Both resonances fit to the same central frequency because the laser setpoint is held constant while the dual probe AOM accounts for the frequency difference between the two states. Resonances such as these are used to determine the precise probing frequency, and in addition, verify that both states can be rapidly probed using this method.

When the number of atoms in the first state is measured, those atoms are heated

*The reference laser is locked to the ^6Li D2 crossover feature, though the absolute frequency of the beatnote is modified since both beams pass through various AOM's before being overlapped on the photodiode.

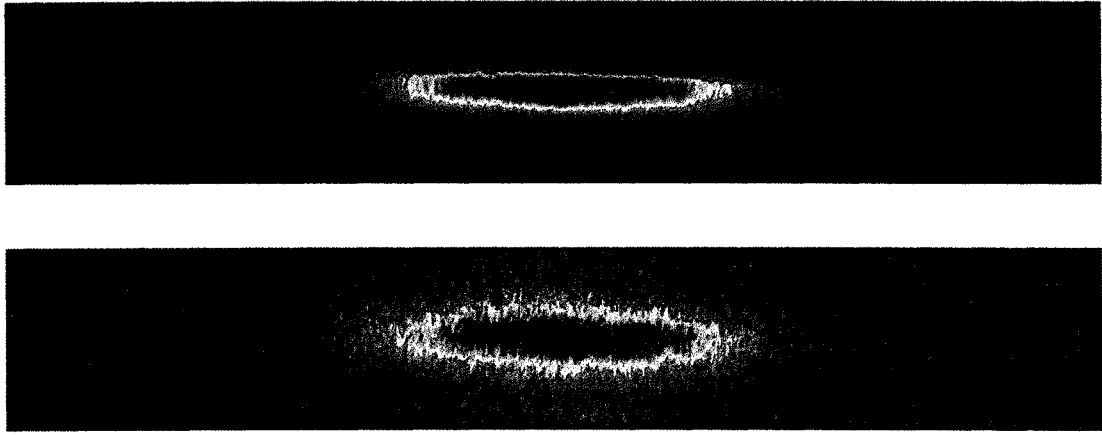


Figure 4.8 Column densities of states $|2\rangle$ (top) and $|1\rangle$ (bottom) in a molecular BEC probed at 754 G with a delay between probes of $215\ \mu\text{s}$ ($P = 0$). The top image is first shot probed, and the bottom is the second. The significant radial expansion in the bottom image is the result of the energy imparted to the atoms through the binding energy by the removal of the first state probed. This image pair represents the worst case, with long delay time and relatively tightly bound pairs.

due to the scattering of photons from the probe beam. If the atoms that are probed are paired with those in the other, unprobed, spin state, energy is coupled between the two via the binding energy. It follows that the more deeply bound the pair, the greater the heating. The effect of this heating can be seen in figs. 4.8 and 4.9, which show the first and second states probed for delay times of $215\ \mu\text{s}$ and $27\ \mu\text{s}$, respectively. In these images the radial extent of the second state probed is larger, due to expansion during the interval between probes. (The extent of the expansion is not appreciable on the scale of the axial size of the cloud, so it manifests itself as a radial broadening.) In order to accentuate the heating effect, these images were taken in the BEC regime (754 G), where the pairs are bound by $\sim 3.5\ \mu\text{K}$. Pairs at unitarity, in the center of the resonance (834 G), are much more weakly coupled, and so the associated heating is also much less. In fact, for the same probe delay as in fig. 4.9 ($27\ \mu\text{s}$) there is nearly no detectable radial expansion.

In addition to the radial broadening associated with breaking of pairs that occurs

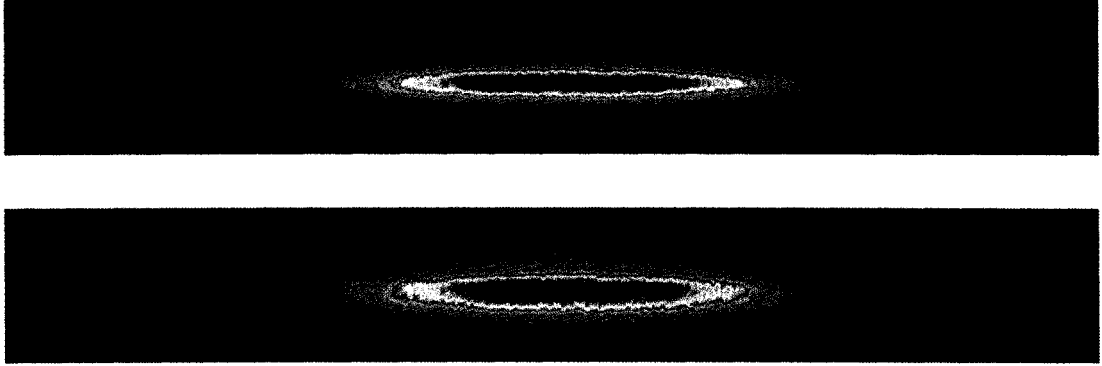


Figure 4.9 Same as the previous fig. (4.8), except with delay between probes reduced to $27 \mu\text{s}$ (again in the BEC regime at 754 G). The radial expansion is significantly improved. Images taken at the center of the resonance (834 G), such as the rest of the data in this chapter, exhibit nearly no expansion due to the weakly bound nature of the pairs.

between probes, we have found that excessive probe intensity or duration results in heating of the atoms that manifests as radial broadening *during* the probe pulse. This broadening is linked to the number of scattered photons, and so depends on probe intensity, detuning and duration. The number of photons scattered from the probe is given by

$$N_{\text{scattered}} = \Gamma \cdot \rho_{ee} \cdot t_{\text{probe}} = \frac{s_0 \Gamma}{1 + 2s_0 + (2\Delta/\Gamma)^2} \cdot t_{\text{probe}}, \quad (4.2)$$

where ρ_{ee} is the excited state population, Γ is the natural linewidth, Δ is the detuning from resonance, and $s_0 = I/I_{\text{sat}}$ is the saturation parameter, with saturation intensity $I_{\text{sat}} = 5.1 \text{ mW/cm}^2$ for the lithium principle transition. The data presented in this chapter were obtained on resonance at typical intensities of $I \sim 0.05 - 0.1 I_{\text{sat}}$ for probe durations, t_{probe} , of 3 - 5 μs , giving 5 - 15 scattered photons.

4.3 Results

4.3.1 Universal Many Body Parameter, β , in an Unpolarized Gas at Unitarity

Before continuing on to the imbalanced systems, it will be useful to describe the measured characteristics of the strongly interacting evenly paired gas at unitarity. In

doing so, we again confirm pairing in the gas and establish a starting point for the later experiments involving imbalanced spin mixtures.

We showed in Chapter 3 that the bare, singlet molecular contribution to the pairing wave function was small within the strongly interacting regime of the broad Feshbach resonance in ^6Li , centered at 834 G. This measurement confirms the expected result for the case that the Fermi energy is much smaller than the energy width of the resonance [42–45], and supports the concept of universality for a spin mixture in a broad Feshbach resonance.

In the following, we will show that this universal behavior can also be observed through the effects of interatomic interactions. We will see that for sufficiently strong interactions, the behavior of the system does not depend on the underlying microscopic details of the interaction. Instead, the interaction strength reaches a maximum value which is determined only by the fermionic character of the gas, and in this way, the system is said to be universal, since this limiting behavior is common to all strongly interacting Fermi systems.

To start, we will consider the equation of state of a non-interacting Fermi gas in a potential [105],

$$\mu = \epsilon_F(r) + U(r), \quad (4.3)$$

where μ is the global chemical potential, $\epsilon_F(r) = \hbar^2 k_F^2(r)/2m$ is the local Fermi Energy, with local Fermi wave vector $k_F(r)$, and $U(r)$ is the trapping potential.

With the addition of interactions, the chemical potential is modified by the mean field energy, so that

$$\mu^* = \epsilon_F(r) + U(r) + U_{mf}, \quad (4.4)$$

where μ^* is the global chemical potential modified by interactions, $U_{mf} \propto a_{eff} n(r)$ is the mean field energy with effective atomic scattering length a_{eff} and density $n(r)$. For weak interactions, $a_{eff} = a_s$, the s-wave scattering length. As a_s is increased, however, such as in the Feshbach resonance where $a_s \rightarrow \infty$, it is not physical for the

interaction strength to also become infinite. Instead, a_{eff} , reaches a limit that is set by the inter-particle separation, which in a Fermi gas is given by the inverse of the Fermi wave vector, k_F^{-1} . This limit is the means by which the universality of the system arises, since when the scattering length between particles exceeds their separation, the interactions no longer depend on the microscopic details of the scattering potential.

In addition, the density is also proportional to the Fermi wave vector, $n(r) \propto k_F^3(r)$ [105], which allows the interaction energy term to be written as $U_{mf} \propto a_{eff}n(r) \propto k_F^2(r)$. Since this term shares the same dependence on $k_F(r)$ as the local Fermi energy $\epsilon_F(r)$, we may combine terms so that 4.4 becomes

$$\mu^* = (1 + \beta)\epsilon_F(r) + U(r), \quad (4.5)$$

where β is a dimensionless constant which relates the interaction energy and the local Fermi energy.

To make better sense of expression, we will substitute an effective particle mass $m^* = m/(1 + \beta)$ and rewrite eq. 4.5 as

$$\mu^* = \epsilon_F^*(r) + U(r), \quad (4.6)$$

where the local Fermi energy now includes the effective mass $\epsilon_F^*(r) = \hbar^2 k_F^2(r)/2m^*$. We now see that eq. 4.6 for a unitary gas is simply that of a non-interacting gas (eq. 4.3) with the substitution of the effective mass, $m \rightarrow m^*$.

Now, for a harmonically trapped non-interacting Fermi gas,

$$\mu = \epsilon_F = \hbar\bar{\omega}(6N)^{1/3}, \quad (4.7)$$

where ϵ_F is the Fermi energy at the center of the trap, N is the atom number and $\bar{\omega} = (\omega_x\omega_y\omega_z)^{1/3}$ is the geometric mean trapping frequency. Since the oscillation frequency in the trap is proportional to the inverse of the square root of the mass, $\bar{\omega} \propto \sqrt{1/m}$, we may write eq. 4.7 for the interacting case,

$$\mu^* = \epsilon_F^* = \hbar\bar{\omega}^*(6N)^{1/3} = \epsilon_F(m/m^*)^{1/2}. \quad (4.8)$$

Using the definition of the effective mass, we now write for strongly interacting fermions in a harmonic trap in the unitarity limit,

$$\epsilon_F^* = \epsilon_F(1 + \beta)^{1/2}, \quad (4.9)$$

[65, 106, 107]. We now write eq. 4.9,

$$\begin{aligned} \epsilon_F^* &= \epsilon_F(1 + \beta)^{1/2} \\ \frac{1}{2}m\omega_z^2 R_z^2 &= \frac{1}{2}m\omega_z^2 R_{TF}^2(1 + \beta)^{1/2} \\ \frac{R_z}{R_{TF}} &= (1 + \beta)^{1/4} \end{aligned} \quad (4.10)$$

in terms of the axial Thomas-Fermi radius calculated for a non-interacting Fermi distribution,

$$R_{TF} = \left(\frac{2\epsilon_F}{m\omega_z^2} \right)^{1/2}, \quad (4.11)$$

and the axial radius in the strongly interacting limit, R_z .

Since $\beta < 0$ [73], its effect is to reduce the chemical potential, which in turn results in a reduction in size of the trapped gas [108] as shown in fig. 4.10. By comparing the measured (smaller) axial size, R_z , of a gas to that predicted for a non-interacting Fermi gas, R_{TF} , β can be determined from rearranging 4.10 to give

$$\beta = (R_z/R_{TF})^4 - 1. \quad (4.12)$$

To obtain R_z , we first integrate the column density images along the remaining radial direction, and then fit the integrated profile to a non-interacting integrated Thomas-Fermi distribution,

$$n(z) = A\left(1 - \frac{z^2}{R_z^2}\right)^{5/2}, \quad (4.13)$$

where both A and R_z are adjustable fitting parameters.

Figure 4.11 shows an integrated axial profile for a gas with temperature $T \lesssim 0.1T_F$, prepared at unitarity within the resonance, along with the fit used to determine R_z ,

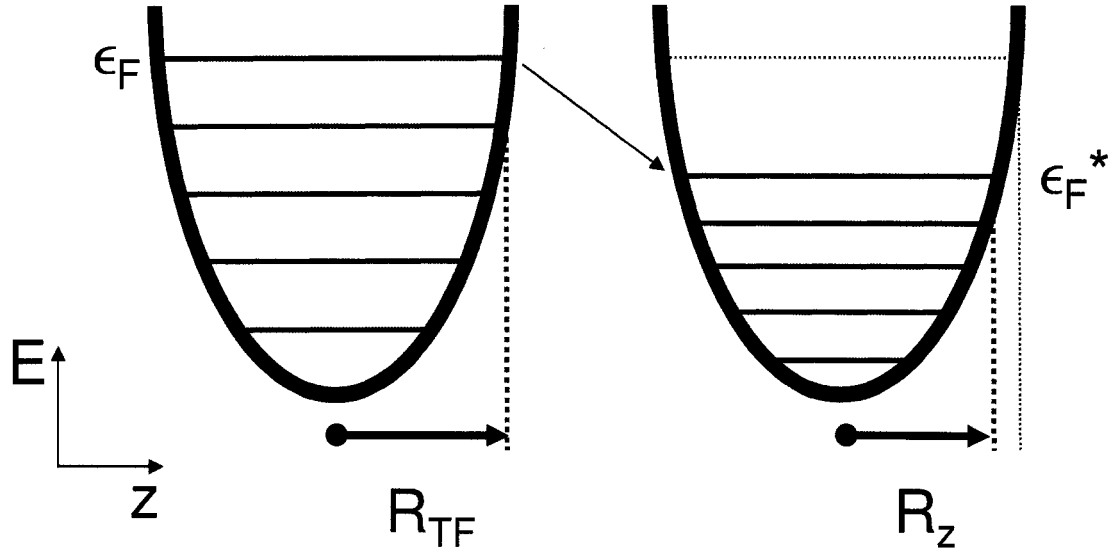


Figure 4.10 On the left is a schematic of a $T = 0$ non-interacting Fermi gas in a harmonic trap. On the right is the same with unitarity limited interactions. The effect of the interactions is to lower the Fermi energy ϵ_F by the factor of $\sqrt{1 + \beta}$ as in eq. 4.9. Due to the dependence $R_z \propto \epsilon_F^{1/2}$, the size of the gas is reduced by $(1 + \beta)^{1/4}$ (eq. 4.10). A measurement of R_z can therefore be used to find β .

and the predicted Thomas-Fermi profile of a non-interacting Fermi gas. Figure 4.12 shows results of measurements of R/R_{TF} . Using Eq.(4.12) and the measured value $R/R_{TF} = 0.825 \pm 0.02$, we determine

$$\beta = -0.54 \pm 0.05, \quad (4.14)$$

where the uncertainty is derived from the systematic uncertainties of the measured parameters (see appendix A).

This value for β agrees well with that of theoretical prediction ($\beta = -0.545$) [107], numerical Monte Carlo simulations ($\beta = -0.58 \pm 0.01$) [60, 86, 109] and other experimental measurements using ^6Li [59, 65, 108, 110] and ^{40}K [111]. Not surprisingly, our measurement does not agree well with that predicted by BCS mean-field theory, $\beta = -0.41$ [107].

The agreement with the last measurement using ^{40}K ($\beta = -0.54^{+0.05}_{-0.12}$) is particularly revealing, since it provides further evidence that trapped alkali gases within

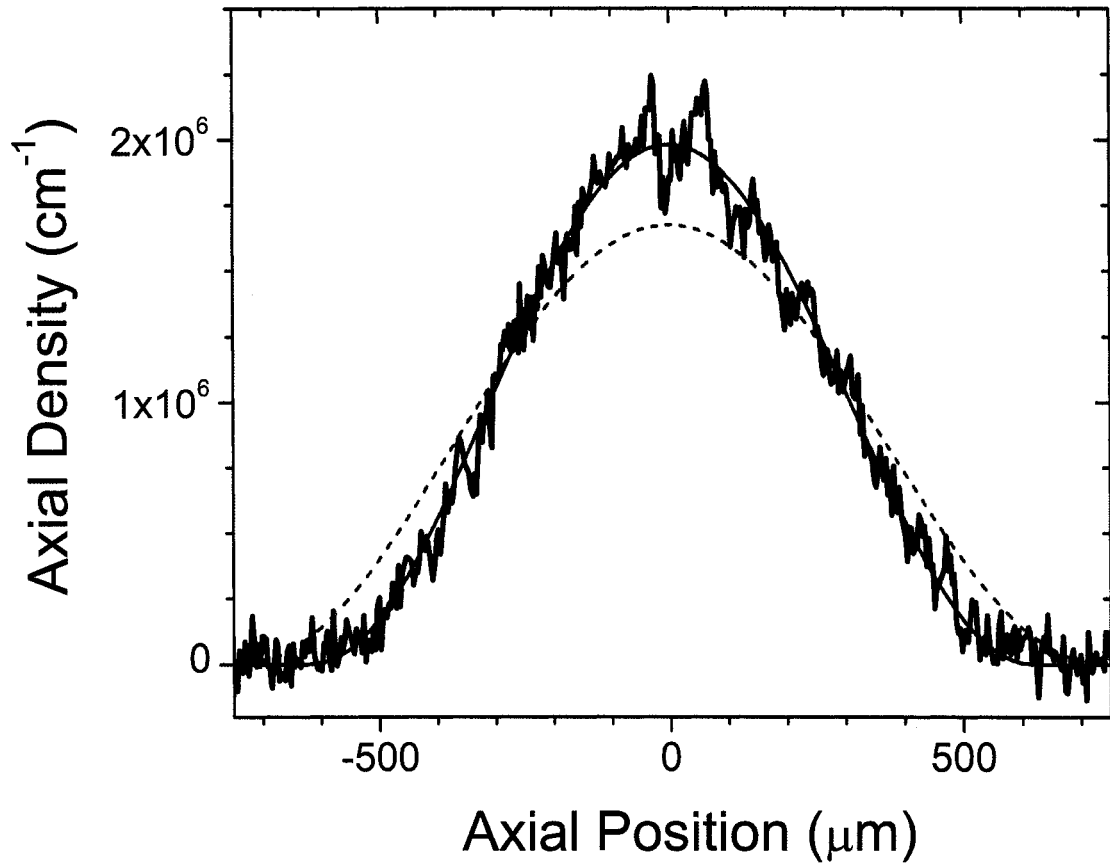


Figure 4.11 Black jagged line is an integrated axial profile of state $|1\rangle$ taken at 834 G with an unpolarized mixture. The red curve is a fit to a $T = 0$ Thomas-Fermi distribution, given in the text by eq. 4.13, and the green dashed line is the theoretical integrated axial $T = 0$ T-F profile for a non-interacting gas, given by $n(z) = \frac{8N}{5\pi R_{TF}} \left(1 - \frac{z^2}{R_{TF}^2}\right)^{5/2}$. The ratio of the measured waist to the non-interacting waist is used to measure β .

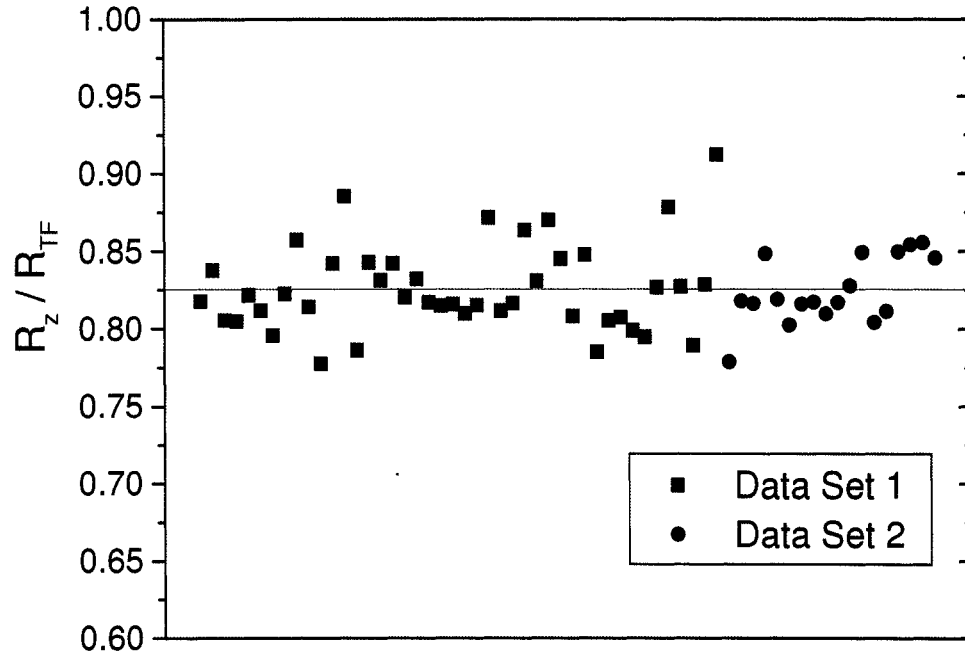


Figure 4.12 Sample of measurements of ratio of measured axial waist, R_z , to non-interacting waist, R_{TF} taken at 834 G with an unpolarized spin mixture.

broad Feshbach resonances are controlled by universal physical properties that are independent of the microscopic details of the system (such as the type of atom, in this case).

4.3.2 Phase Separation

We have now shown, both through the direct measurement of pairs, and through the observation of the universal interaction energy, that the evaporatively cooled gas is paired when there are equal numbers of the majority and minority atoms, $|1\rangle$ and $|2\rangle$. In addition, several experiments have shown that such a gas is in fact superfluid [98–100]. We will now investigate the behavior of such a gas when the mixture of the constituent states is imbalanced.

When a spin polarized gas is evaporatively cooled to degeneracy and imaged, the resultant column density distributions indicate that something unusual is occurring. Figure 4.13 shows *in-situ* absorption images, acquired as described previously, of a

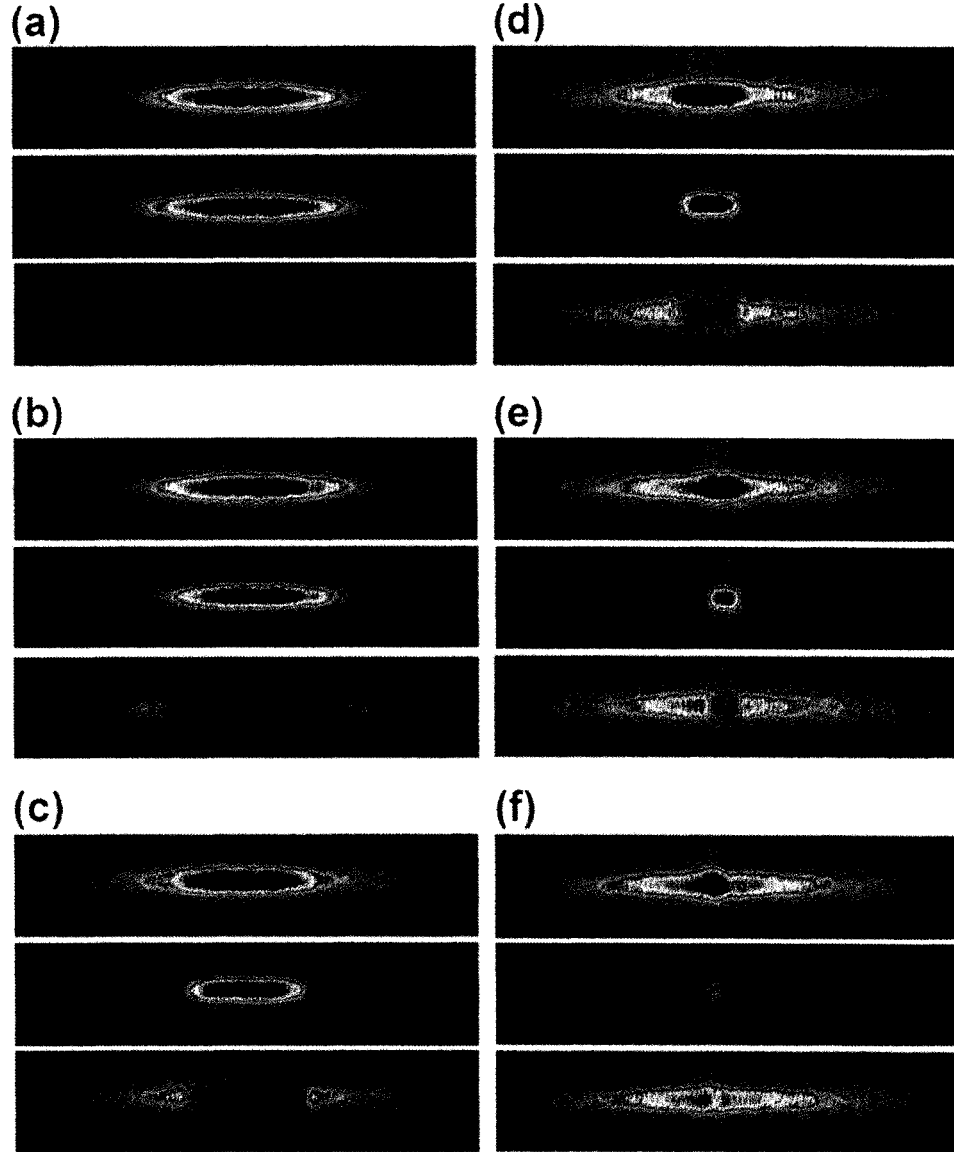


Figure 4.13 *In-situ* absorption images of a polarized Fermi gas. The top image of each sequence corresponds to the column density of majority state ($|1\rangle$), the middle to the minority state ($|2\rangle$), and the bottom to the difference of the two ($|1\rangle - |2\rangle$). In these images, the spatial distribution of the minority component corresponds to that of the evenly paired core, while that of the difference corresponds to the excess, unpaired majority atoms. The polarizations are (a), $P = 0$, (b), $P = 0.18$, (c), $P = 0.37$, (d), $P = 0.60$, (e), $P = 0.79$, and (f), $P = 0.95$. In each sequence, state $|2\rangle$ was imaged first, followed by state $|1\rangle$. The field of view for these images is $1654 \mu\text{m}$ by $81 \mu\text{m}$. The displayed aspect ratio was reduced by a factor of 4.4 for clarity. Note that the apparent inversion of aspect ratio of the minority state in (f) is a result of this scaling.

spin polarized gas of ${}^6\text{Li}$. For each polarization, three images are shown: the top image is of the majority spin state; the middle is the minority; and the bottom is the difference of the two. In these images, the spatial distribution of the minority component corresponds to that of the evenly paired core, while that of the difference corresponds to the excess, unpaired majority atoms. The first images correspond to an even spin mixture. As expected, the images of the two states are the same, and the difference image is blank. This case corresponds to a completely paired gas. With increasing polarization, however, the distributions of the majority and minority become increasingly different. Despite this, a central uniformly paired region persists up to the highest values of polarization, as evidenced by the complete subtraction of the two states. A similar experiment at MIT has shown that while it is evenly paired, the core is also superfluid [101]. As I will show in the following sections, our measurements also show that the gas is superfluid.

These images suggest that in order to accommodate the mismatched populations, the excess majority atoms have been expelled from a uniformly paired core. It appears that in this way, through a phase separation, that the superfluid state is able to accommodate the excess unpaired atoms. Alternately, such a phase separation may be explained in the BEC regime [112] where atoms and paired molecules are thought to have strong repulsive interactions [40]. This may be ruled out however, since as a result the pair-pair interactions would also be repulsive [40], in contrast to the negative interactions observed through the measurement of β . Instead, we attribute the redistribution as a result of the energy cost of including an unpaired atom into the paired core [84–88]. This interpretation will be more quantitatively tested in the coming sections.

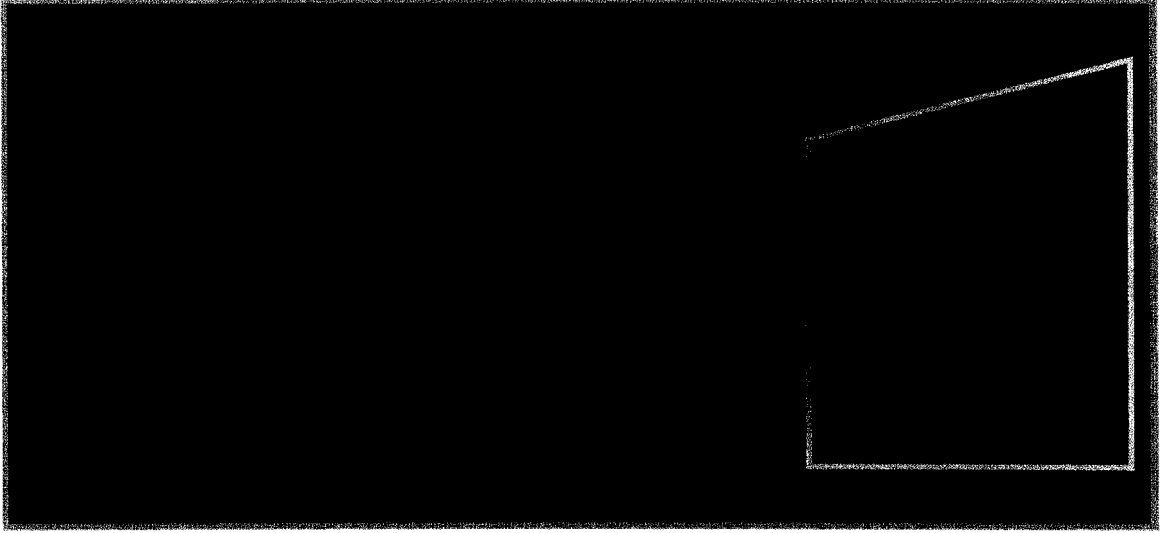


Figure 4.14 The atomic probe (propagating left to right) integrates the atomic density distribution as it passes through it, and the shadow of the cloud is recorded onto a CCD array. Due to cylindrical symmetry of the cloud, the resultant column density can be transformed to reconstruct the true density distribution via an inverse Abel transformation [113].

4.3.3 Uniform Central Pairing

The difference images in fig. 4.13, show a central hole, which we ascribe to a uniformly paired region. However, since the 2-dimensional images represent an integration along the radial direction of the true 3-dimensional density distribution of the atoms, as shown in fig. 4.14, the contribution to the column density of excess majority atoms in a radial shell can not be differentiated from that of paired majority atoms in the trap center. Though it is apparent from the images shown in fig. 4.13 that there is very little accumulation of excess unpaired majority atoms in the radial direction (thereby minimizing this effect), a quantitative determination of the true polarization at the center of the gas can not be precisely measured by simple inspection of the 2-dimensional images. Instead, we must reconstruct the true 3-dimensional density distribution from these images in order to measure the true central polarization.

Cylindrical symmetry of the trap allows the use of an inverse Abel transformation

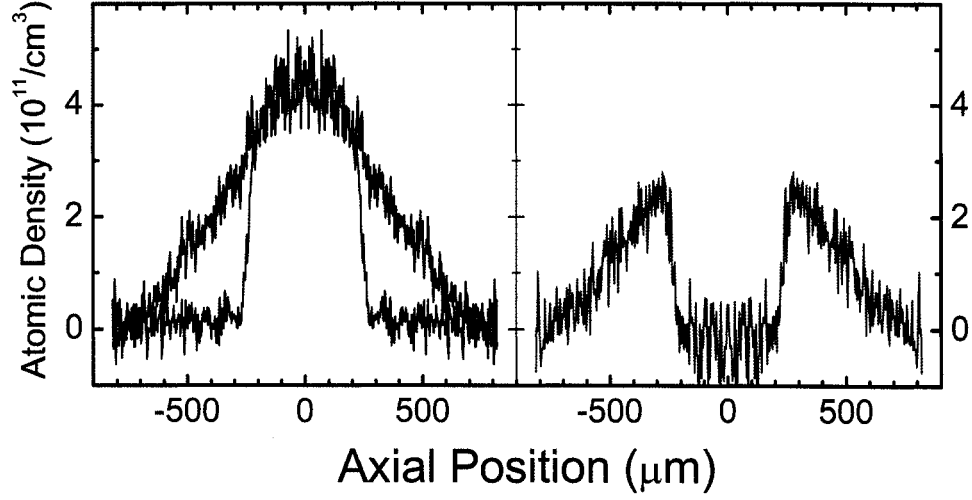


Figure 4.15 Center-line axial cut of the reconstructed 3D densities. The black lines correspond to state $|1\rangle$, the red to state $|2\rangle$, and the green to their difference, for $P = 0.35$ and $N_1 = 175$ k. The signal to noise was improved by reflecting and averaging the column density images about both the $r = 0$ and the $z = 0$ planes before reconstruction. These profiles show even pairing in the center of the trap, and sharp boundaries between regions of completely paired and unpaired atoms.

[113] for reconstruction of the true 3-dimensional atomic density distribution of the minority and majority states from their 2-dimensional projections obtained through absorption imaging. A cut along the long axis of the density distribution, $n(r = 0, z)$, that results from this transformation is shown in fig 4.15. From this 3-dimensional reconstruction, the true atomic density at the center of the trap, $n(r = 0, z = 0)$, is obtained for each state. In the case that a uniformly paired core exists, both the central densities will be equal, while the ratio of central densities of two non-interacting gases is given by $(\frac{1+P}{1-P})^{1/2}$.^{*} Shown in fig 4.16 are the measured ratios of central densities for clouds of varying P . These measurements show that the ratio of

^{*}

$$\frac{n_1}{n_2} = \frac{N_1/V_1}{N_2/V_2} = \frac{N_1/R_1^3}{N_2/R_2^3} \quad (4.15)$$

where the Thomas-Fermi radius $R \propto T_F^{1/2} \propto N^{1/6}$, so

$$\frac{n_1}{n_2} = \frac{N_1/N_1^{1/2}}{N_2/N_2^{1/2}} = \left(\frac{N_1}{N_2}\right)^{1/2}. \quad (4.16)$$

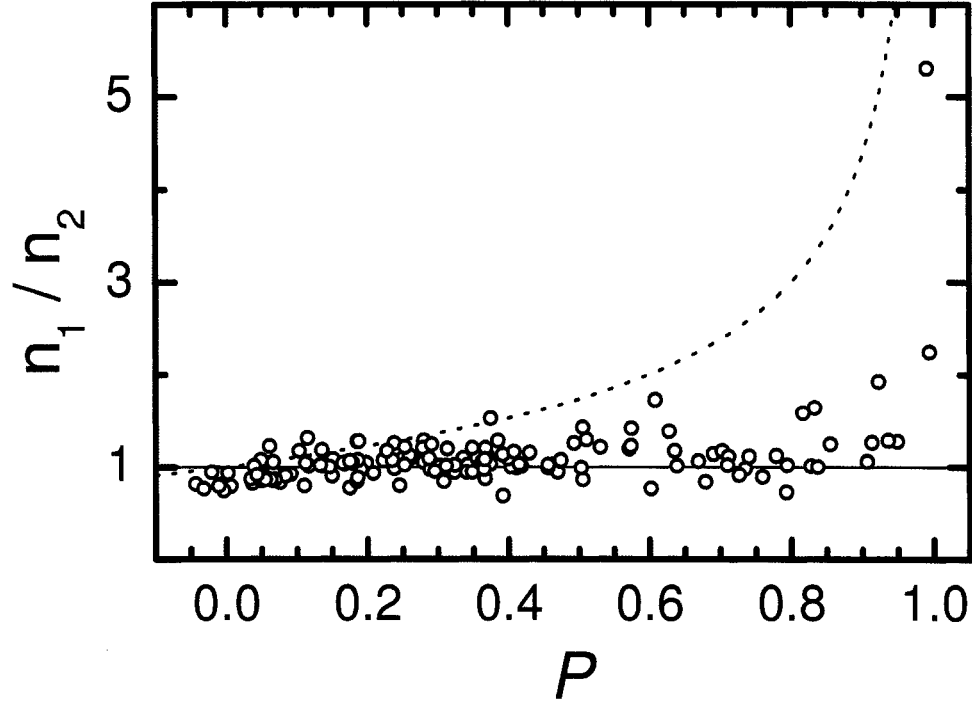


Figure 4.16 Ratio of the central densities vs. polarization for polarized gases prepared at $\bar{T} \leq 0.05$. The dotted lines correspond to $[(1+P)/(1-P)]^{1/2}$, the expected central density ratio for a harmonically confined, non-interacting gas at $T = 0$. The solid line indicates equal central densities. The increase in $n_1(0,0)/n_2(0,0)$ for $P > 0.9$ may be explained by slightly higher temperatures for these data that are the result of reduced efficiency in evaporative cooling at very high P . This inefficiency arises due to the decreasing rethermalization efficiency associated with the diminishing population of state $|2\rangle$.

$n_1(r=0, z=0)/n_2(r=0, z=0)$ remains constant and equal to unity for all but the highest polarizations. This result is consistent with the predicted behavior of a phase separated gas [114].

From fig. 4.16, we verify that the pairing in the center of the trap is indeed complete, as was suggested by the *in-situ* images. This uniformly paired core is a necessary, but not sufficient, condition for phase separation, however, since a polarized

With $N_1/N_2 = (1+P)/(1-P)$,

$$\frac{n_1}{n_2} = \left(\frac{1+P}{1-P} \right)^{1/2}. \quad (4.17)$$

superfluid state that possesses a uniformly paired core without phase separation has also been predicted (see for example [115]).* Such a polarized superfluid exhibits a gradual change in local polarization in the transition region from the uniformly paired core to the unpaired shell, while for the case of phase separation, the boundary between phases is expected to correspond to a first order transition characterized by a sudden jump in local polarization. In order to differentiate between these cases, it is necessary to further characterize the gas, and in particular the boundary between the paired core and the excess unpaired atoms. Along these lines, fig. 4.15 shows that the change from fully paired to fully polarized is quite sudden, with no appreciable transition region. This behavior suggests that a phase separation, characterized by a first order transition between phases, has occurred. This interpretation will be further strengthened in the following sections.

4.3.4 Deformations and Aspect Ratio

In addition to the persistence of a uniformly paired core with sharp boundaries, several other phenomena are hinted at by a simple inspection of the images shown in fig. 4.13. It is clear, for example, that while the axial size of the minority state decreases with increasing P , the radial size remains nearly constant, and matches that of the majority. This behavior is also evidenced through the preferential accumulation of the excess majority atoms at large axial extent, and their relative deficit in the radial direction. In order to quantify this deformation, we measure the aspect ratio (AR) of the density distribution of each component, defined as the axial size divided by the radial size, and plot it versus polarization, P .

The radial size of the component clouds is determined by fitting the column density to a non interacting Thomas-Fermi distribution (for fermions) $A(1 - \frac{z^2}{R^2})^2$, where both

*However, as previously mentioned, the evenly paired core at high P strongly suggest phase separation [114].

A and R are adjustable fitting parameters.* While this functional form provides a good fit and a useful measure of the radial size for the majority and minority states, the same is not true for the axial dimension. Shown in fig. 4.17 is the Thomas-Fermi fit applied to the axial distributions of the minority and majority. From the poor fits, it is clear that this function is not optimal for finding the axial size of the gas. This also indicates that the pairing induced deformation more strongly affects the gas in the axial direction. To more accurately represent the data in this case, it is advantageous to determine the axial sizes of the deformed profiles through an edge finding routine that extrapolates the profiles and determines the axial extent at which the distributions go to zero. These fits are also shown in fig. 4.17.

Figure 4.18 shows the AR of the minority and majority clouds as a function of P . From this plot we can see that while the AR of the majority remains nearly constant (and equal to that of the trapping potential), that of the minority steadily decreases with increasing P , and continues for all P . In fact, over the entire polarization range, the AR of the minority distribution decreases by an order of magnitude.

This deformation also manifests through the difference of the integrated axial profiles. Figure 4.19 shows the integrated axial distributions for both the minority and majority states, as well as their difference. From this figure, it is evident that the spatial deformations in the profiles of the minority and majority states lead to the observed double peaked structure of the difference profile. While, in general, this deformation is not a criterion for phase separation, for all our measurements, we observe that the deformations and characteristic double peaked profiles always accompany phase separation, as identified by the central density ratios and sharp boundaries.

Despite providing a useful signature for phase separation, the observed deforma-

*The functional form of the T-F distribution for fermions is determined from the integral of the 3-dimensional density distribution of the atoms, which has an exponent equal to $3/2$. The single integration to get column density increases the exponent to 2, and a second integration gives $5/2$ power. See also appendix B.

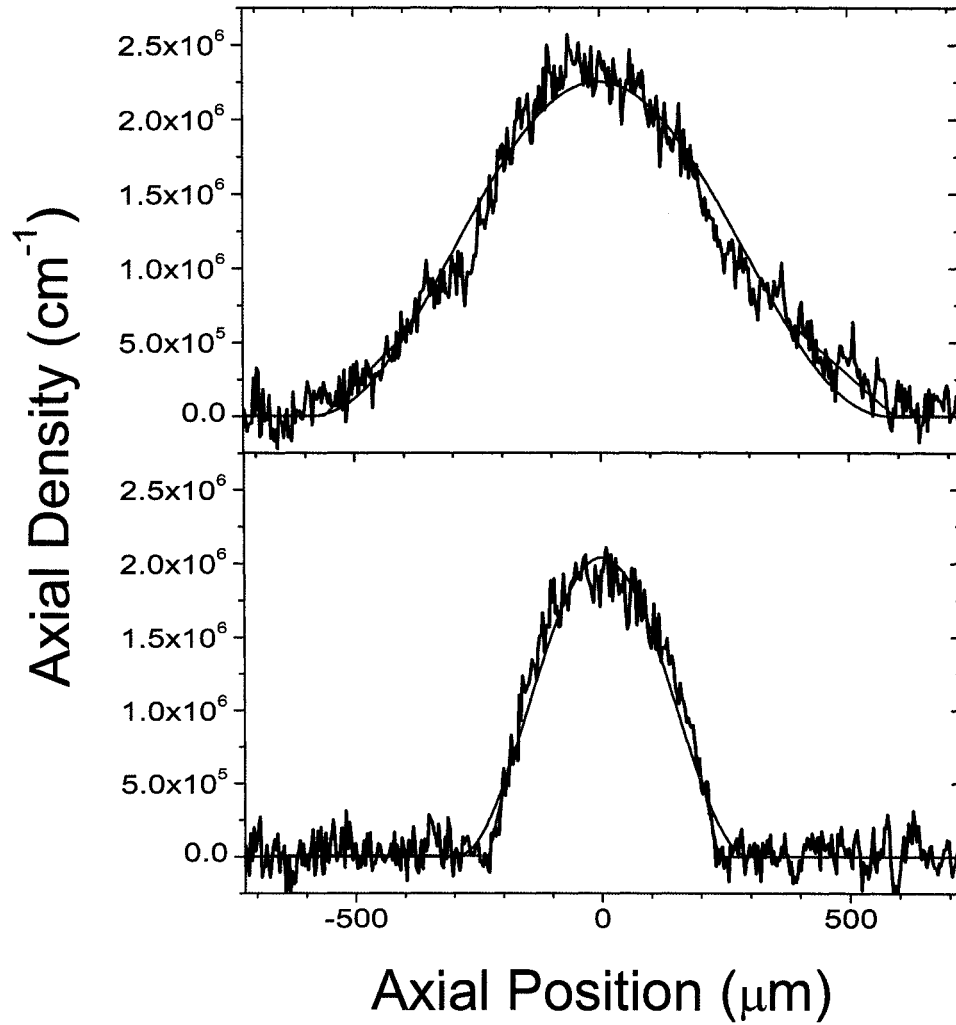


Figure 4.17 Integrated axial distributions for the majority ($|1\rangle$, top) and minority ($|2\rangle$, bottom) states in a phase separated polarized cloud with $P = 0.43$ and $N_1 = 1.35 \times 10^5$. The $T = 0$ T-F fits (red) no longer provide a good fit, due to deformation of both the minority and majority. To find the extent of the clouds, an edge finding algorithm is used instead (green line).

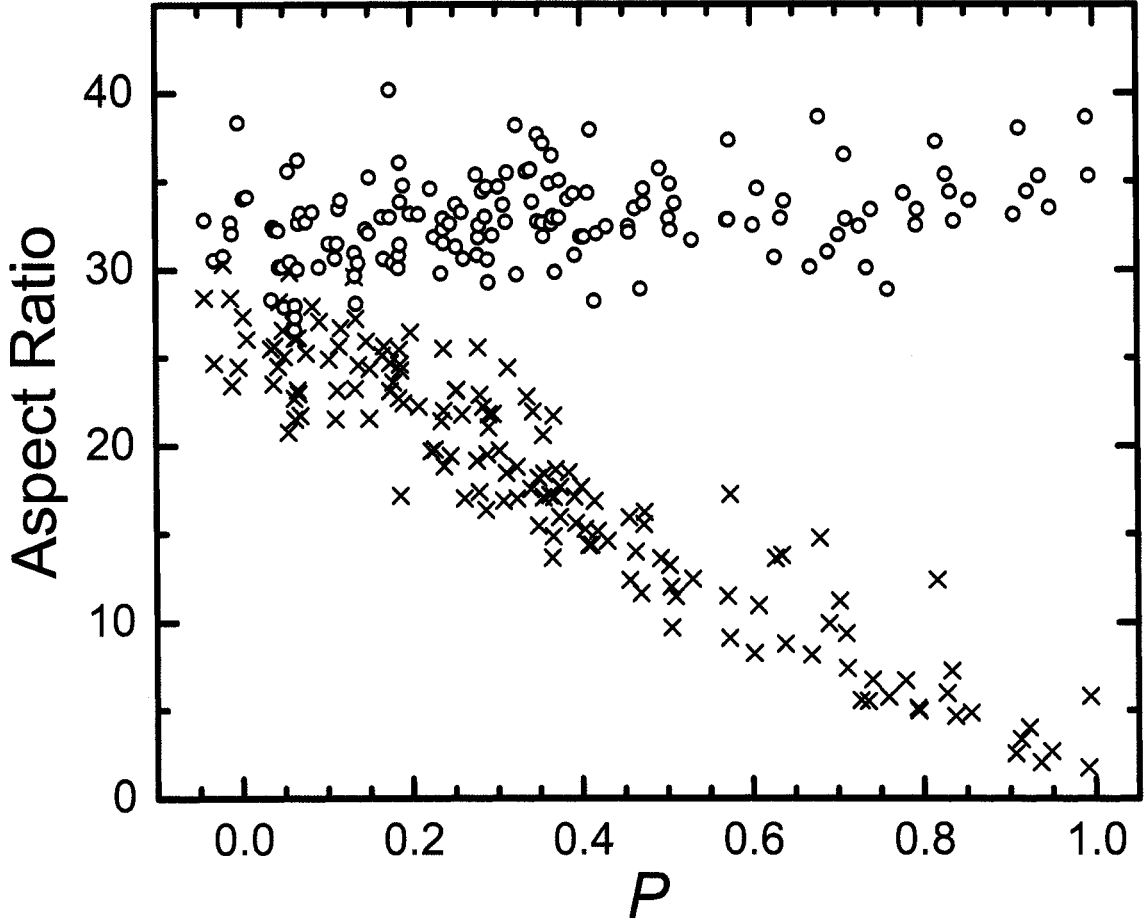


Figure 4.18 Aspect ratio vs. polarization. The ratio of the axial to the radial dimensions, R_z/R_r , is shown for state $|1\rangle$ by the black circles and for state $|2\rangle$ by the red crosses. The radii R_r for both states are determined by fitting the column density profiles to zero-temperature, fermionic Thomas-Fermi distributions. The axial distributions are distinctly non-Thomas-Fermi-like, so R_z is found by a simple linear extrapolation of the column density to zero. An aspect ratio of 36 is the expected value for a non-interacting gas with anharmonic corrections, in reasonable agreement with the observations. The uncertainty in P is 0.04, which is the standard deviation of polarization measurements deliberately prepared as $P = 0$. There are shot to shot variations in N_1 and a small systematic variation towards larger N_1 at smaller P . For $P < 0.40$, $N_1 = 170 \text{ k} \pm 40 \text{ k}$, and for $P > 0.40$, $N_1 = 135 \text{ k} \pm 25 \text{ k}$, where the uncertainty is the standard deviation of the measurements. The corresponding average Fermi temperature is $T_F \approx 430 \text{ nK}$, where we define $T_F = \hbar(\omega_r^2\omega_z)^{1/3}(6N_1)^{1/3}/k_B$.

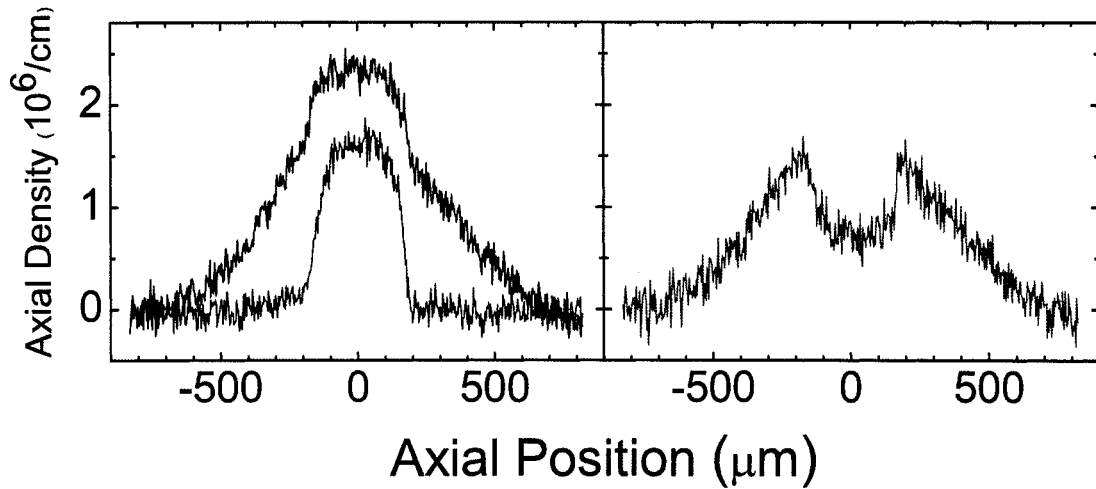


Figure 4.19 The integrated axial density distributions of the majority ($|1\rangle$, black) and minority ($|2\rangle$, red) of a phase separated imbalanced gas ($P = 0.50$, $N_1 = 1.46 \times 10^5$) are shown on the left along with their difference (green) on the right. Deformations of the integrated profiles leads to the central dip evident in their difference. The central bulge in the state $|1\rangle$ profile is indicative of strong attraction between atoms in the core region.

tions are still unexpected. In fact, they are practically forbidden, since they indicate a violation of the local density approximation (LDA) [116]. Simply speaking, the LDA is a tool used to adapt calculations for systems such as these in such a way as to incorporate the effects of a trapping potential. The LDA works by relating a spatially dependent chemical potential $\mu(\vec{r})$ to the trapping potential $U_{trap}(\vec{r})$, as in

$$\mu(\vec{r}) = \mu_o - U_{trap}(\vec{r}). \quad (4.18)$$

(This is essentially the Thomas-Fermi approximation.) As such, the boundaries of trapped atom clouds should follow the trap equipotential surfaces, which are ellipsoids in harmonic traps.

Following our initial observation [23], the expected density distributions for a phase separation in a harmonic trap were calculated under the assumption of the LDA [117–121]. It was pointed out that the difference of the integrated axial profiles of a gas with a uniformly paired core should be flat-topped [116, 122], such as is shown

in fig. 4.20, whereas we observe the double peaked difference distributions (fig. 4.19).

The LDA is generally valid for fermions when there are no size scales smaller than the inverse Fermi momentum, k_F^{-1} [123]. The smallest dimension of our clouds is the radial size, typically 10 - 20 μm , which is much larger than the typical value of $k_F^{-1} \approx 0.3 \mu\text{m}$ [24], so the violation is surprising.

In addition to providing a signature for phase separation, the deformations also provides a signature of a violation of the LDA. While these two seem to go hand in hand in our experiments, no LDA violations were observed in a similar experiment which also utilized *in-situ* imaging of an imbalanced Fermi gas [103]. We will return to this point later, after discussing some possible mechanisms for explaining the deformations.

4.3.5 Mechanisms for Deformation

Here we will compare possible causes for the unexpected spatial deformation of the imbalanced gas in our experiment.*

Role of Anharmonicities in the Optical Trap

The calculated axial density profiles shown in fig. 4.20 assume a harmonic trapping potential and the LDA. As presented in Chapter 2, the trap used for these experiments is formed from a focussed laser beam with a gaussian intensity profile that forms a corresponding gaussian potential. Since the observed density profiles (fig. 4.19) deviate from those predicted to occur in a harmonic trap under the LDA, we must rule out the non-harmonic aspect of the trap as the cause of the deformations in order to confirm a violation of the LDA.

As previously described, the optical trap potential is augmented with a magnetic saddle point that provides additional confinement in the axial direction. The overall

*Imambekov *et al.* have investigated such deformations in the BEC limit [124], though since we are currently working in the strongly interacting regime, this work is only mentioned here.

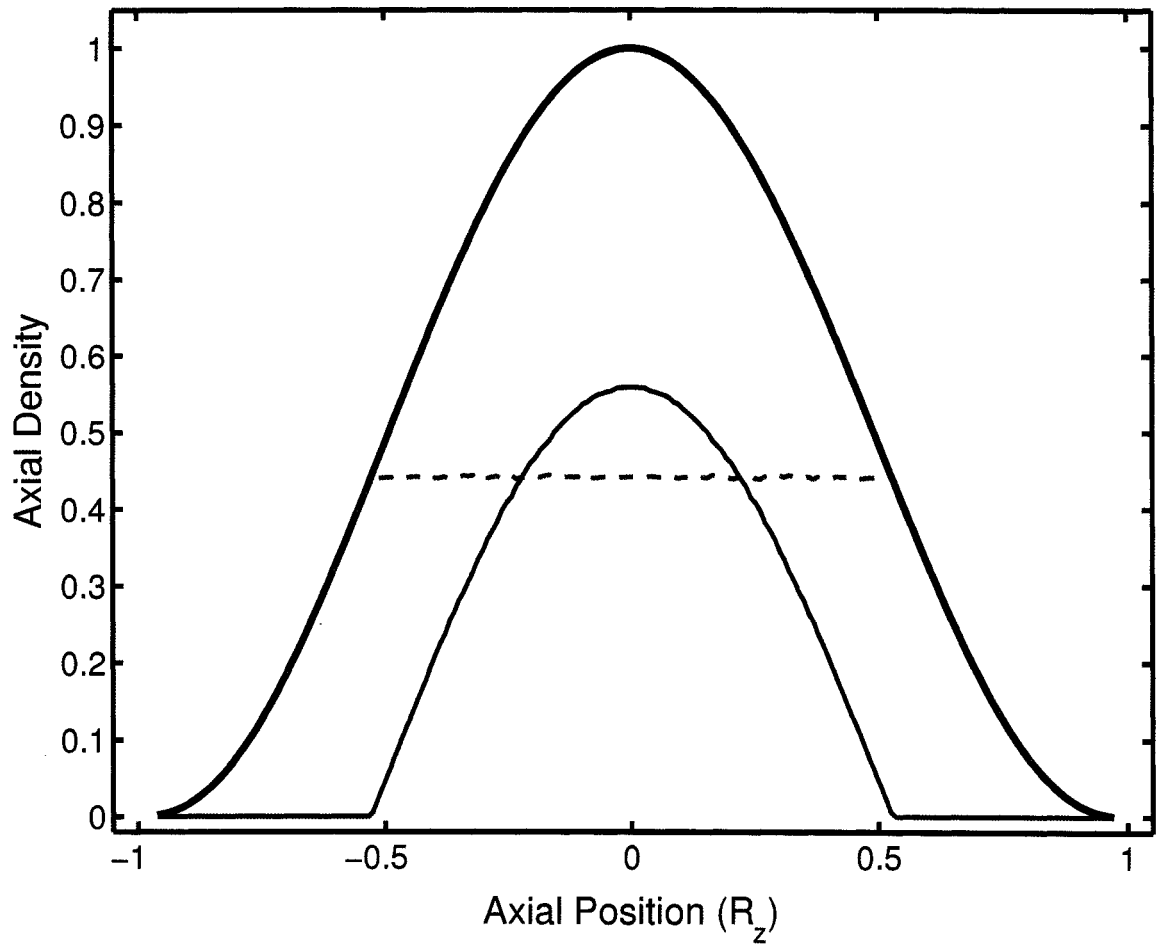


Figure 4.20 Calculation of $T = 0$ doubly-integrated T-F density distributions of a polarized Fermi gas with a uniformly paired core ($P = 0.45$), consistent with the LDA in a harmonic trap. Shown are the majority (black) and minority (red) states, as well as their difference (green dashed). The doubly integrated shell of unpaired atoms leads to a flat-topped difference distribution, whereas our data exhibits a sharp dip (see fig. 4.19).

potential has the form

$$U(r, z) = \frac{1}{2}m\omega_B^2 z^2 + U_o \left(1 - \frac{w_o^2}{w^2(z)} e^{-\frac{2r^2}{w^2(z)}} \right), \quad (4.19)$$

where $\omega_B = (2\pi) \ 6.5 \text{ Hz}$ (at 834 G), $w_o = 26 \ \mu\text{m}$, $w(z) = w_o (1 + (z/z_o)^2)^{1/2}$, $z_o = R_L/M^2 = 1.68 \text{ mm}$, with $R_L = 1.97 \text{ mm}$, $M^2 = 1.17$, and peak trapdepth, $U_o = U(r = z = 0)$, defined in Chapter 2 (2.2.2). Also in Chapter 2, we calculated this trap's oscillation frequencies from a harmonic approximation to the gaussian potential. While this approximation is valid for small excursions of the atoms from the center of the trap, larger excursions lead the necessity for inclusion of additional terms in the approximation. Since the size of a trapped Fermi gas is determined by its Fermi energy, rather than by its temperature, such a gas can having a relatively large extent, even at low temperatures. This may be the case in our experiments, so to quantify the effect of the extended size of the trapped gas, we expand U from eq. 4.19 in terms of r^2 and z^2 .

$$U(r, z) = \left(\frac{1}{2}m\omega_B^2 + \frac{U_o M^4}{z_o^2} \right) z^2 + \left(\frac{2U_o}{w_o^2} \right) \left(1 - \frac{r^2}{w_o^2} - 2 \frac{z^2 M^4}{z_o^2} \right) r^2. \quad (4.20)$$

In the case of the low optical trap intensities used for these experiments, the dominant contribution to the axial potential is the harmonic magnetic confinement, since

$$\frac{\frac{1}{2}m\omega_B^2}{\left(\frac{U_o M^4}{z_o^2} \right)} \approx 2.4. \quad (4.21)$$

For this reason, we omit factors of z^4 in the expansion.

For these experiments, the radial and axial sizes (radii) are typically $R_r \lesssim 18 \mu\text{m}$, and $R_z \lesssim 600 \mu\text{m}$. These numbers give an upper limit for the relative strength of the quartic, r^4 , term to the quadratic r^2 term of $(R_r/w_o)^2 \approx 0.48$, which is not insignificant. In addition, the $z^2 r^2$ cross term modifies the radial harmonic frequency with axial position, z , and vice versa. In the first case, the the radial confinement is reduced at maximum $z = R_z$ by a factor with a relative strength of $2(R_z/z_o)^2 M^4 \approx$

0.25 of the quadratic term. In the second case, the optical component of the axial confinement is actually inverted at maximum $r = R_r$, since $4(R_r^2/w_o^2) > 1$.

This expansion indicates that the non-harmonic terms are not necessarily negligible, so we will now further characterize the effects of the anharmonicities by a simulation of the trapped gas in the *full* potential $U(r, z)$ given in eq. 4.19 (not the expansion). To model the two spin components, two atomic distributions are generated in the 3-dimensional potential, $U(r, z)$. The density distribution of the majority gas is determined from the LDA by eq. 4.18, and so takes the same form as the potential. The minority density distribution is set equal to the majority density within some equipotential surface, and set to zero elsewhere. This situation models a phase separated two component gas that consists of a uniformly paired core and an unpaired, single component, shell.

Figures 4.21 and 4.22 show the integrated axial and radial distributions of the simulated density distributions under the conditions of the the data in this chapter. These profiles differ from that shown for the case of a harmonic trap in such a way that the difference profile of the axial (radial) integrated density has a peak (dip). These features can be understood as a result of the extra majority atoms that spread into the weaker gaussian “wings” of the radial potential and add to the integrated axial profile. This occurs to a lesser extent for the minority atoms, which are lower in the potential and therefore more harmonically confined. This spilling over of the majority state in the radial direction is mediated by the nearly harmonic confinement that remains in the axial direction.

To further characterize the effects upon the density distributions of the filling of the non-harmonic portions of the trap, we now increase filling to the maximum possible. Figures 4.23 and 4.24 again show integrated axial and radial distributions, though in this case, the chemical potential of the atoms is set to completely fill the

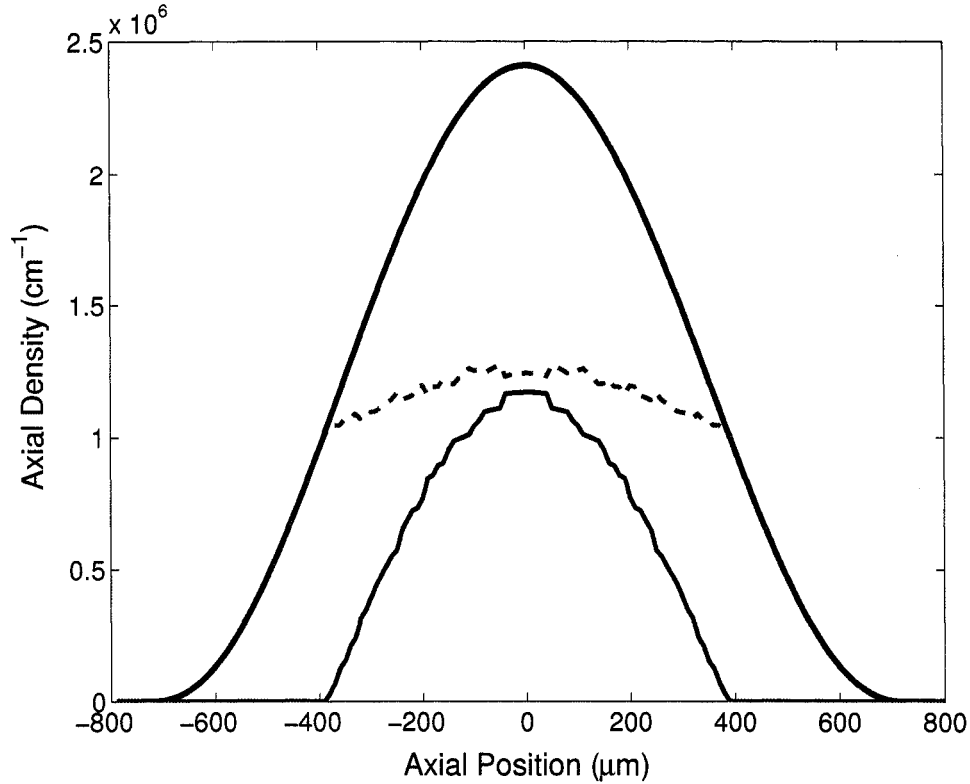


Figure 4.21 Calculation of $T = 0$ doubly-integrated T-F density distributions of a polarized Fermi gas with a uniformly paired core, consistent with the LDA in the trap described by eq. 4.19. Shown are the majority (black) and minority (red) states, as well as their difference (green dashed). In this case, trapping parameters and atom numbers are representative of the data presented in this chapter: $U_o \sim 0.5 \mu\text{K}$, $N_1 = 170k$, $P = 0.5$, $\mu_1/U_o = 0.77$, $\mu_1^{\text{harmonic}}/U_o = 0.85$, $M^2 = 1.17$, and $B = 834 \text{ G}$. μ_1 and μ_1^{harmonic} are the true and calculated chemical potentials for the majority state. (See text and footnote.)

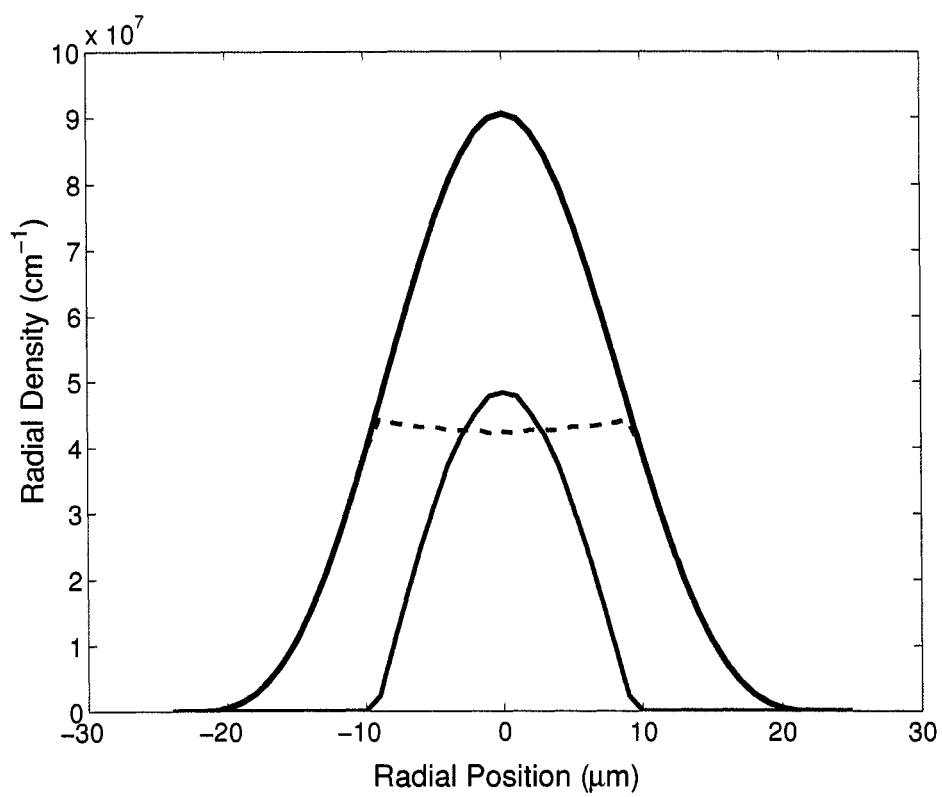


Figure 4.22 Same as previous figure (4.21), radial direction.

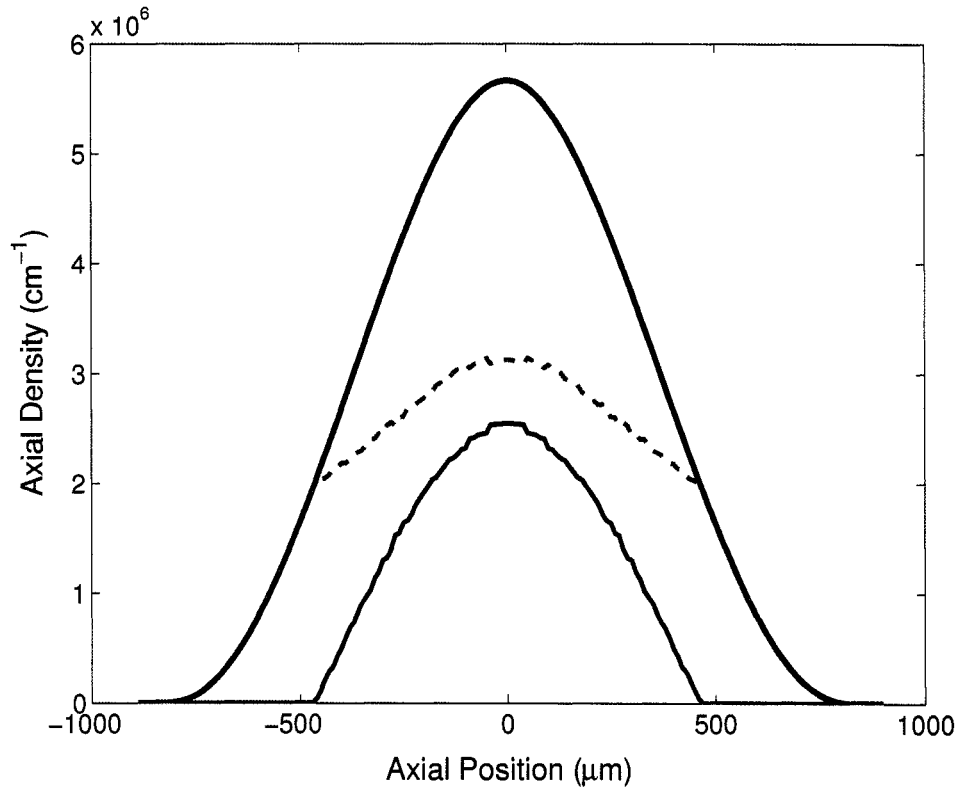


Figure 4.23 Same as fig. 4.21, except with completely filled potential ($\mu_1 = U_o$). Again, trapping parameters are representative of the data presented in this chapter, but number is increased: $U_o \sim 0.5 \mu\text{K}$, $N_1 = 440k$, $P = 0.5$, $\mu_1/U_o = 1.0$, $\mu_1^{\text{harmonic}}/U_o = 1.17$, $M^2 = 1.17$, and $B = 834 \text{ G}$.

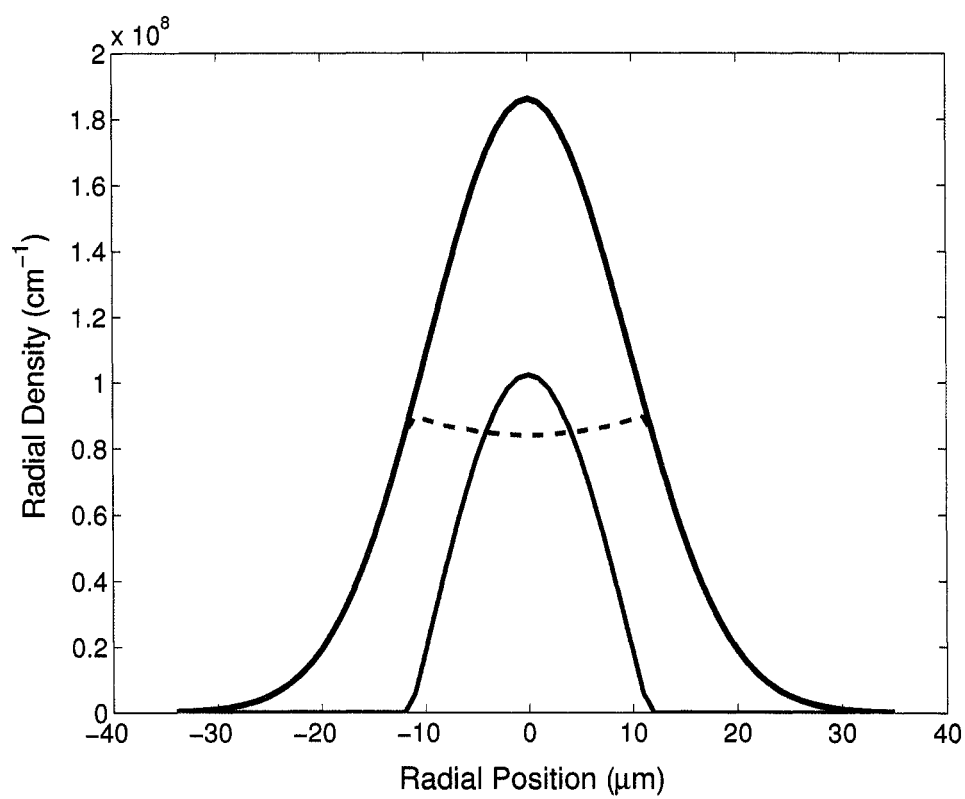


Figure 4.24 Same as previous figure (4.23), radial direction.

trap, $\mu_1 = U_o$, where μ_1 is the chemical potential of the majority ($|1\rangle$) state.* These distributions are similar to those shown previously, save for their increased size and the enhanced peak/dip of the their difference.

Finally, we will calculate the effects that the gaussian beam propagation parameter M^2 has on the density distributions. While, in Chapter 2, we measured this parameter to be $M^2 \leq 1.17$ for our trap ($M^2 = 1$ for an ideal beam), it is still instructive to investigate the sensitivity of the density distributions to this parameter. M^2 enters into the potential through the z^2 coefficient (as M^4), where, by decreasing the effective Rayleigh length, z_o , of the trapping beam (see eq.'s 4.19, and 4.20), an increased M^2 increases the steepness of the axial potential. In addition, M^2 determines the strength of the $r^2 z^2$ cross term in eq. 4.20 (again, as M^4). Figures 4.25 and 4.26 show that by sufficiently increasing M^2 (in this case, $M^2 = 5$), a small dip in the axial distribution can be realized under the (remaining) conditions of these experiments. Even given this extremely large M^2 value that overestimates its effects by a factor of $1.17^2/5^2 \approx 18$, the predicted profiles do not closely resemble those of the data. For the case of no magnetic contribution to the potential, this dip may arise at lower values of M^2 , though it is accompanied by a significant deviation (from ellipsoidal) of the majority state's density distribution.

From this study, we may conclude that although some deviation from the predicted profiles for a harmonic trap should be expected, these deviations, and in particular, the bulge in the axial difference profile in fig. 4.21, are actually contrary to those observed in the data. In addition, the magnitude of the these deviations, even with exaggerated anharmonicities, are slight compared to those observed.

*Note that μ_1 is the actual chemical potential of the majority state and not that calculated using the atom number and approximated harmonic frequencies ($\mu_1^{harmonic} = \epsilon_F = \hbar\bar{\omega}(6N_1)^{1/3}$). Such a calculation can give a quantity that is actually greater than the trap depth, as in figs. 4.23 and 4.24.

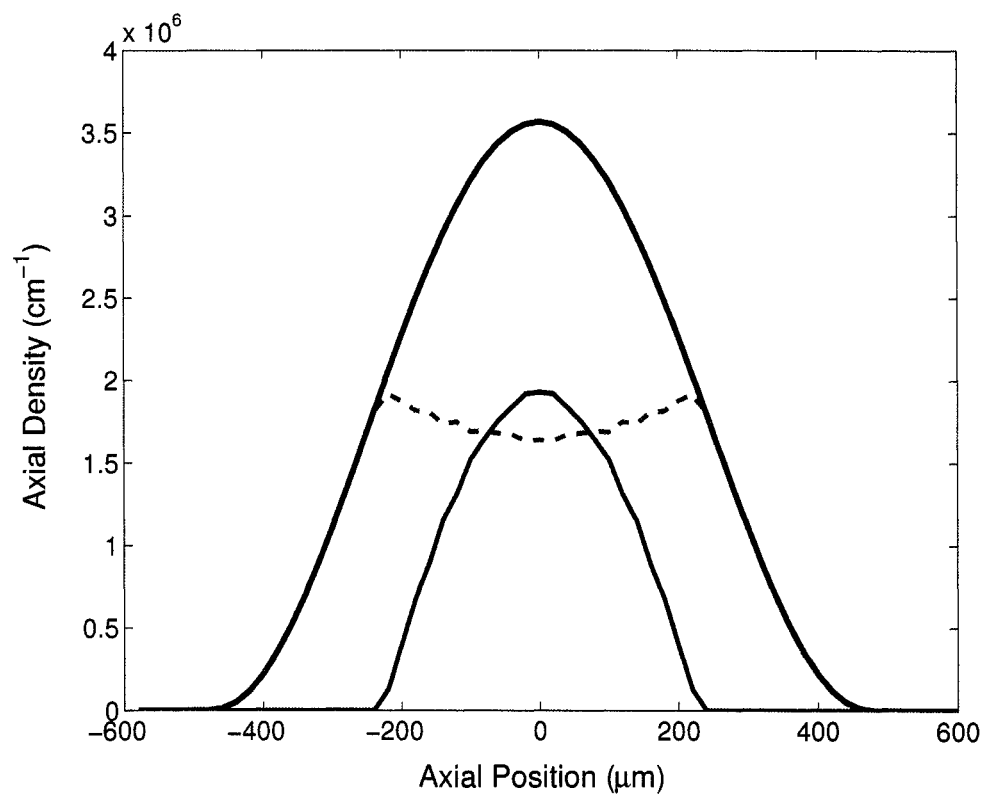


Figure 4.25 Same as fig. 4.21, except with $M^2 = 5$. $U_o \sim 0.5$ μ K, $N_1 = 172k$, $P = 0.5$, $\mu_1/U_o = 0.875$, $\mu_1^{harmonic}/U_o = 1.12$, $M^2 = 5$, and $B = 834$ G.

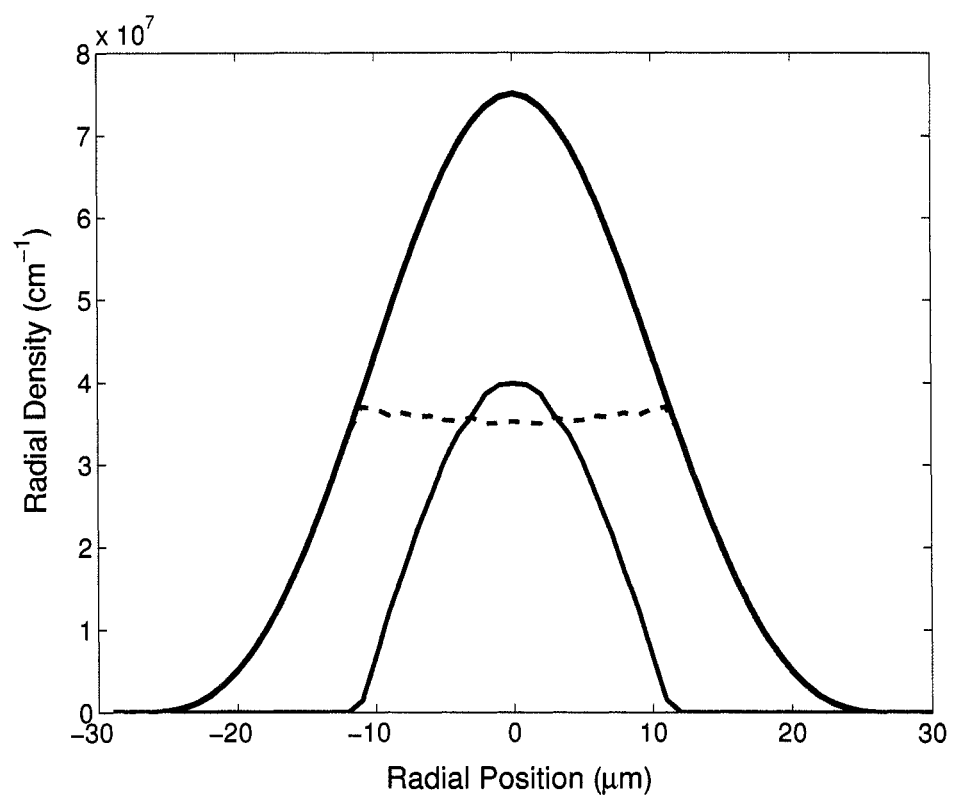


Figure 4.26 Same as previous figure (4.25), radial direction.

Surface Tension

Surface tension is a familiar phenomenon that arises in many situations. For example, it is the mechanism responsible for the beading of water on a waxed surface, and the formation of the meniscus at the top of a liquid filled beaker. This tension also gives the a water bug the ability to walk on water without breaking through the surface. In these situations, surface tension occurs at the boundary of a liquid with another solid, liquid or gas (or vacuum). In these instances, surface tension arises because of the affinity that the molecules in the liquid have for one another compared to that for the surface they are interfacing with. In the cases for which there are attractive interactions between particles in a liquid (as is the case for water molecules), the particles in the interior of the system feel attractive forces in all directions, such that these forces cancel. Surface tension arises when particles at the edge of the system only feel attraction from one side (the inside), since they are not attracted to the other substance, be it a liquid, solid or vacuum. In such an instance, the resulting lowest energy state of the system is that with minimum surface area. This is, for example, why a falling droplet of water becomes a sphere: the shape of minimum surface area for a given volume.

It has been proposed by DeSilva and Mueller that, in a similar fashion as the examples above, surface tension exists between the superfluid core and the normal unpaired majority atoms [125]. Furthermore, it is predicted that in a high aspect ratio trapping potential such as ours, this surface tension may lead to deformations such as those observed in the experiments. In this case, the deformations provide a means to minimize the surface area of the interface between the superfluid paired phase and the unpaired normal phase.

Figure 4.27 shows axial difference profiles predicted by a calculation that takes into account the effects of surface tension. Also shown in this figure are our experimental profiles, which agree well with the calculation. This work also predicts that the effects

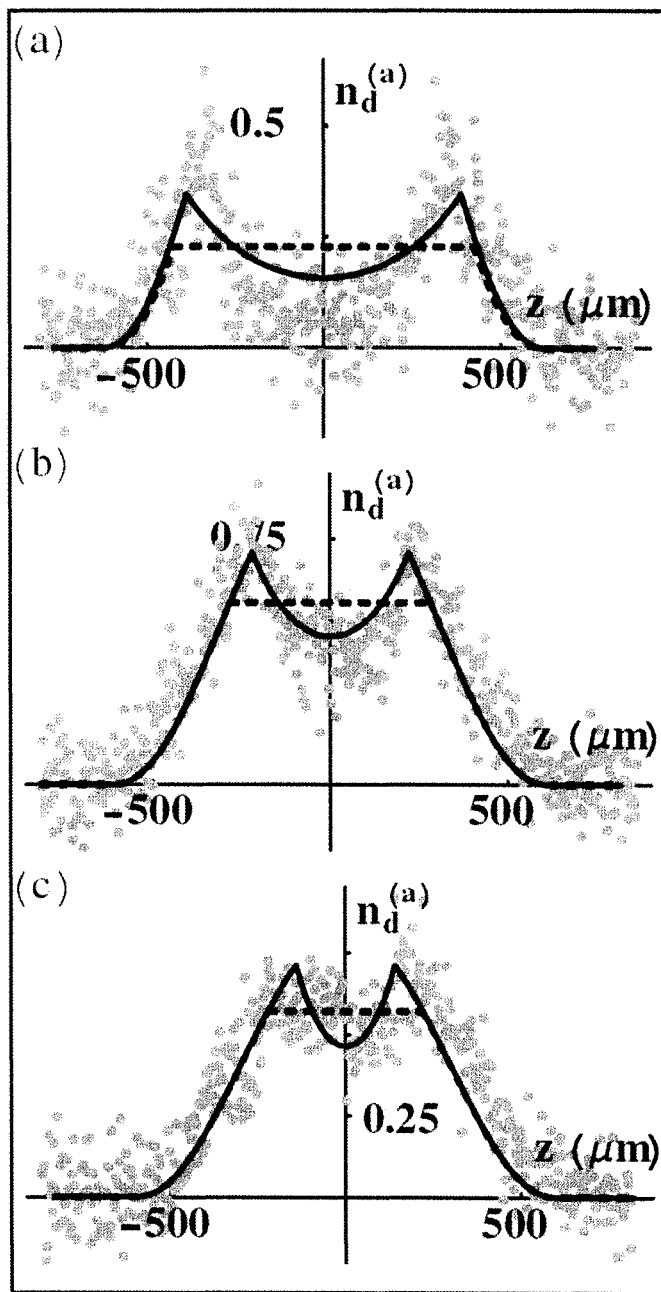


Figure 4.27 (Adapted from reference [125].) Axial density difference profiles of zero temperature harmonically trapped unitary Fermi gas in units of 10^6 cm^{-1} . (a), (b), and (c) represent polarization $P = 0.14$, 0.53 , and 0.72 , respectively. The gray points are our experimental data [23]. The dashed line shows the predicted zero surface tension density difference, while the solid line model includes surface tension between phases.

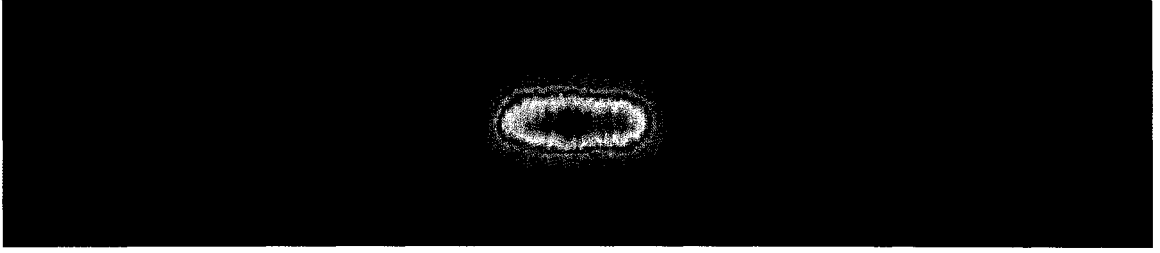


Figure 4.28 The minority ($|2\rangle$) column density of a phase separated gas with $N_2 = 0.39 \times 10^5$, and $P = 0.72$. The spatial distribution, which corresponds to that of the paired core, is noticeably non-ellipsoidal. This deformation is attributed to the surface interaction energy between the superfluid paired core and the normal unpaired majority atoms. A formalism has been developed to facilitate analysis of such misshapen clouds, and is described in the text.

of surface tension will have less of an effect on the spatial distribution as the aspect ratio of the trap is lowered. This may also be the first clue as to why no deformations were reported in a similar experiment performed at MIT, as their trap has a lower aspect ratio, ~ 5.6 [103], compared to ours, ~ 35 [24]. On the other hand, more recent work [126] has indicated that the surface tension effects, though small, should still be measurable in their case.

Figure 4.28 shows an absorption image of the minority state from a polarized gas. Aside from having a reduced aspect ratio, as already discussed, the cloud appears non-elliptical and exhibits a somewhat cylindrical shape which is abruptly capped off at the ends.

Motivated in part by this observation, Stoof and Haque have developed a method for analyzing data such as ours through an extension of the LDA which allows for a directional dependence of the local Fermi surface [126]. Using this anisotropic formalization allows for clouds with arbitrary, non-ellipsoidal geometries to be explicitly represented (figs. 4.29 and 4.30). In the context of surface tension, this has allowed for an analysis of the details of the distortion and the surface that causes it.

In the unitarity limit, the surface energy involves just one universal constant, η_s [125, 126]. By using the value of the universal surface energy constant η_s determined

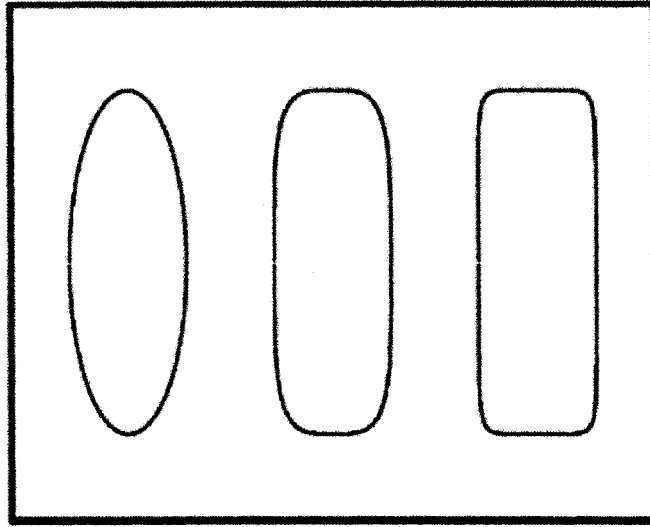


Figure 4.29 (Adapted from [126]) Generalized shapes used to describe the deformed core surface. Boundaries are defined by $(r/R)^\gamma + (z/Z)^\gamma = 1$, where $\gamma = 2$ gives an ellipsoid, and $\gamma = \infty$ gives a cylinder. Shown are profiles for $\gamma = 2, 4$, and 9 .

from the deformation of our data, the expected deformations in similar systems can be predicted as a function of atom number and trap aspect ratio, as shown in fig. 4.31. Curiously, the authors of ref. [126] find that given experimental parameters reported by Shin *et al.* [103], surface tension resulting from a phase separation should have produced small, though measurable, deviations from the LDA (deformations), however none were reported.

4.4 Critical Polarization

In our first experiments on imbalanced Fermi gases, we found that phase separation, and the accompanying deformations, were only present beyond a critical polarization, $P_c \approx 0.1$ [23]. This result is in contrast to the later data, where the gas is observed to phase separate for any non-zero value of polarization [24]. The onset of the critical polarization is shown in fig. 4.32, where the axial profiles of the minority and majority states, as well as their difference at varying degrees of polarization are shown. Part a) in this figure are profiles of an even spin mixture, and fit well to the

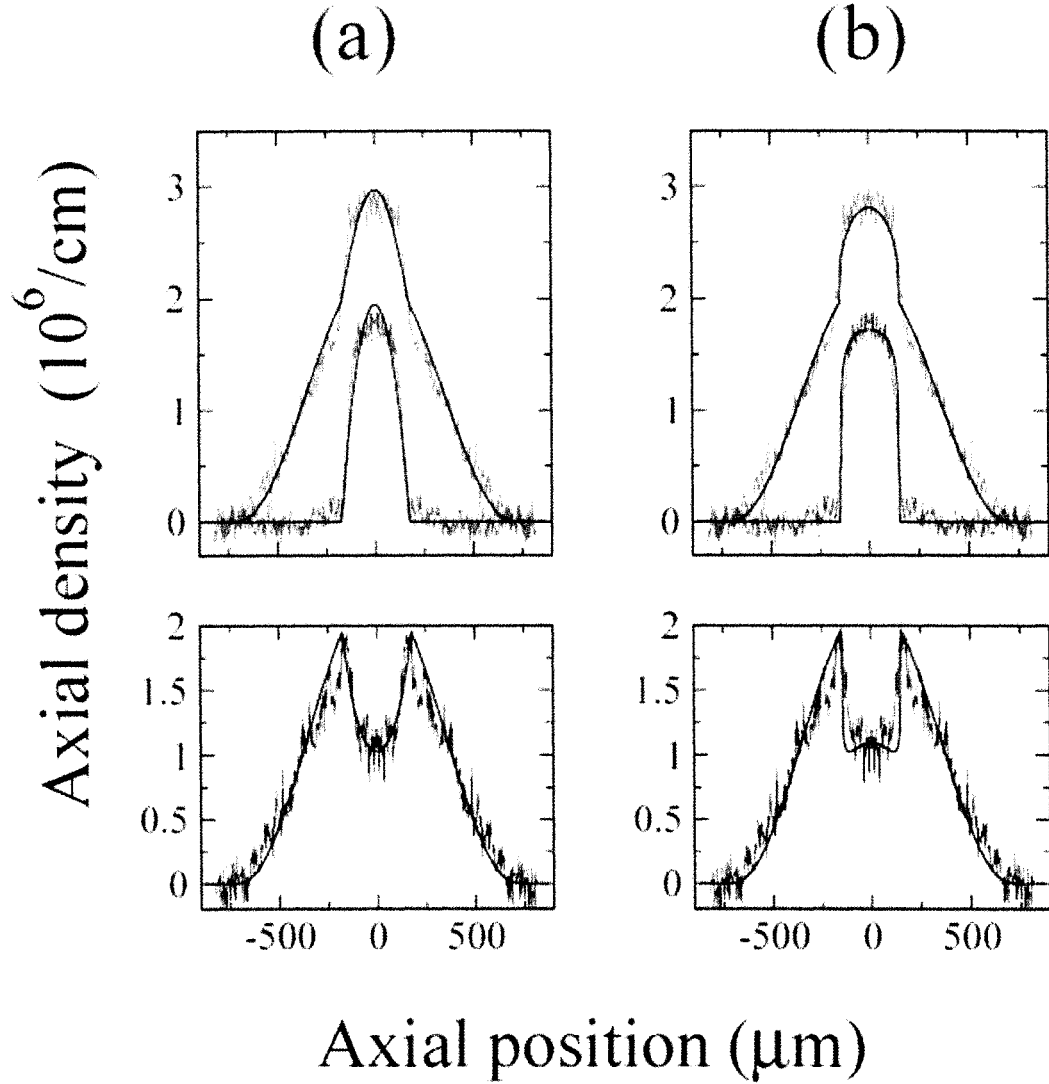


Figure 4.30 (Adapted from [126]) Fits to majority, minority and difference axial density distributions, taken from our data, using deformed core shapes, as shown in fig. 4.29. (a) shows the fit for $\gamma = 2$, and (b) shows $\gamma = 8$. In the fits of (a), the sharp features of the density distributions are missed, whereas in (b) they are overemphasized. The authors of ref. [126] find that values of γ between 3 and 6 best reproduce the data. (Note that these fits also include the effects of surface tension.)

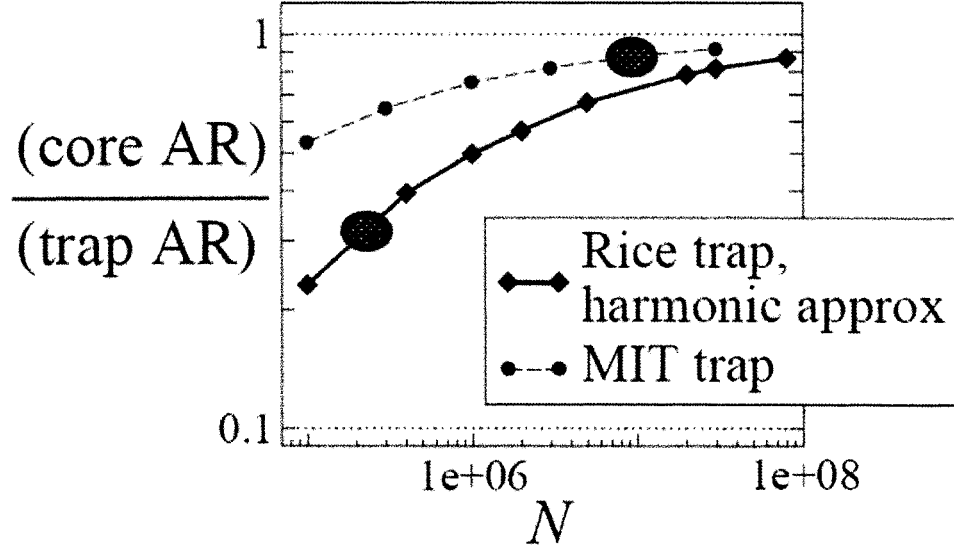


Figure 4.31 (Adapted from [126]) This plot shows the expected magnitude of deformation due to surface tension effects for different trapping geometries and atom number ranges for a fixed polarization $P = 0.49$. This calculation uses the universal (at unitarity) surface tension constant determined from our data. The green spots show the regions where the two groups working in this field operate. (Rice trap, this work; MIT trap, refs. [101–103].)

non-interacting Thomas-Fermi distributions, also shown. Part b) corresponds to a polarized gas that has a polarization less than P_c . The profiles of this polarized gas fit well to the Thomas-Fermi distributions as well, where the increasing polarization leads to a larger amplitude for the majority. As a result, for this polarization, taking the difference of the two profiles leads to a monotonic profile with a central maximum, and not the twin peaked structure that indicates deformation. As the polarization is increased beyond P_c , however, the twin peaked distribution abruptly appears, as is shown in part c). We should also note that the onset of the deformations may also be discerned from the distinctly non-Thomas-Fermi-like distribution that the minority assumes, as evidenced by the poor fit. Above the critical polarization, the wings of the distribution become truncated and sharply go to zero, while the central peak height is enhanced. As higher polarizations are attained, the height of the integrated minority distribution begins to shrink, though the deformations remain.

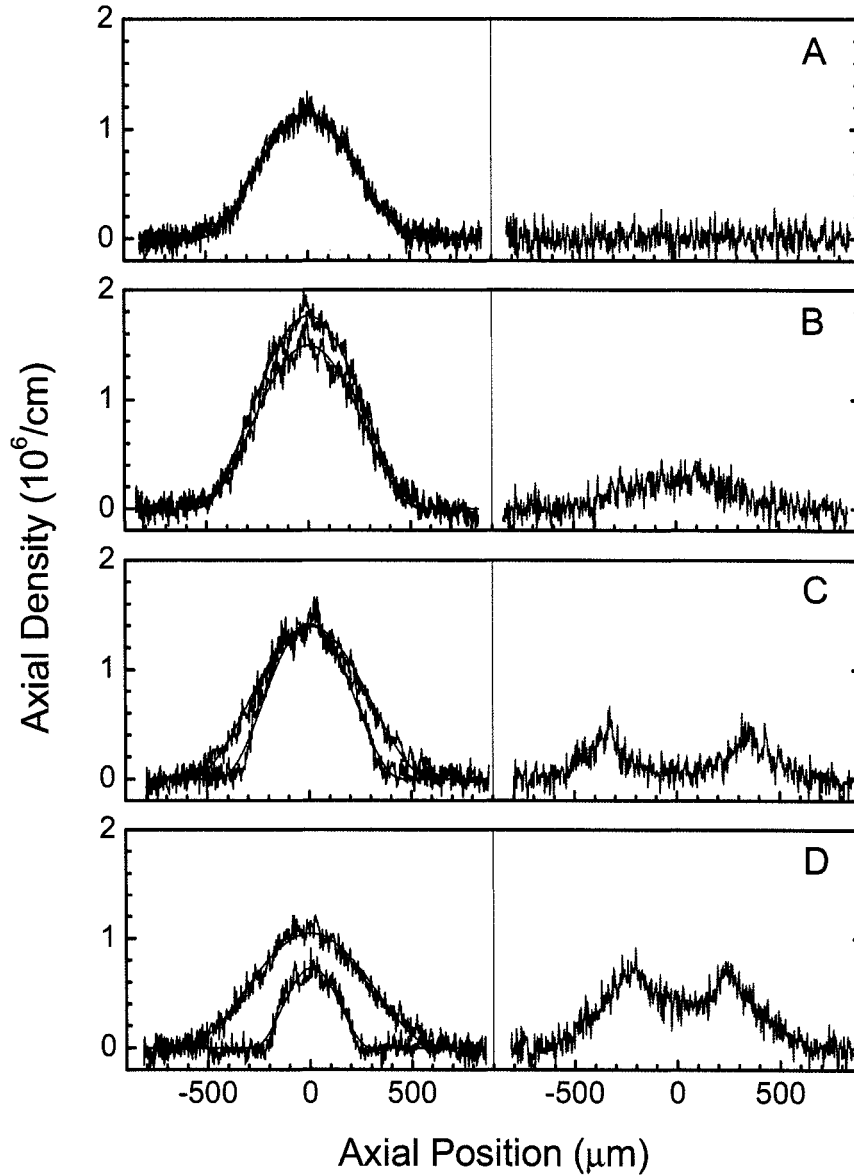


Figure 4.32 Axial density profiles at 830 G. For the curves on the left, the blue (red) data correspond to state $|1\rangle(|2\rangle)$, while the green curves on the right show the difference distributions, $|1\rangle - |2\rangle$. The axial density measurements are absolute and without separate normalization for the two states. The solid lines on the left curves are fits to a Thomas-Fermi distribution for fermions, as described in the text, where the fitted parameters are A and R . (A) $P = 0.01$, $N_1 = 6.4 \times 10^4$; (B) $P = 0.09$, $N_1 = 1.0 \times 10^5$; (C) $P = 0.14$, $N_1 = 8.6 \times 10^4$; (D) $P = 0.53$, $N_1 = 6.8 \times 10^4$. The state $|2\rangle$ distributions reflect the distribution of pairs, while the difference distributions show the unpaired atoms. Phase separation is evident in (C) and (D).

In fig. 4.32 the axial size of the gas for the minority state is seen to decrease once the critical polarization is past. We may better quantify this effect by plotting the fit Thomas-Fermi radius, normalized by the radius calculated for a non-interacting Fermi gas with given number and trap frequencies, as a function of P . (Note that while the Thomas-Fermi profiles do not provide a great fit for the axial distributions of polarized gases, they still provide a reasonable estimate of the cloud size.)

From the plot shown in fig. 4.33, we see that at low polarization, the axial sizes of both the majority and minority species are reduced from that expected for a noninteracting Fermi gas. Recall that this reduced axial size (of evenly paired shots) was used previously in Sec. 4.3.1 to determine the universal interaction energy constant β . At a polarization of around 0.1, corresponding to P_c , the normalized axial sizes of the minority and majority suddenly diverge. While the majority size approaches that of a non-interacting Fermi gas, that of the minority steadily decreases up to the highest measured polarizations.

The seeming inconsistency associated with the presence [23] and subsequent absence [24] of a critical polarization, may in fact offer a clue as to the bigger picture of what is going on with this system. As we shall see shortly, the sudden transition from the polarized homogeneous gas to the deformed, phase separated gas is consistent with crossing a phase boundary between a polarized superfluid (i.e. Sarma or breached pair), and a phase-separated gas [78, 79, 127] at non-zero temperature.

4.5 Temperature Dependence

Since the above behavior suggests the possibility of a temperature dependent phase diagram, we must adopt a method to measure the temperatures of the gases that we create.

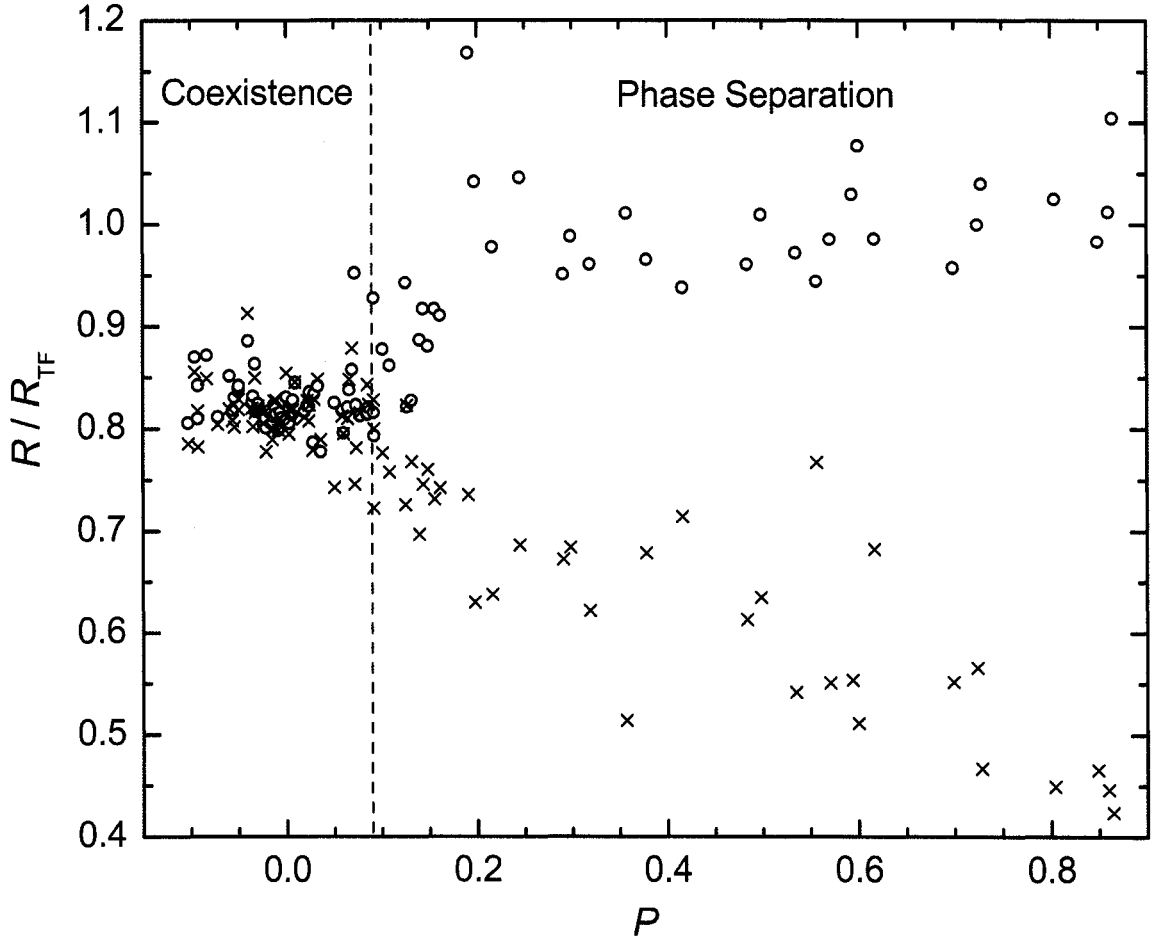


Figure 4.33 R/R_{TF} vs. P . The ratio of the measured axial radius to that of a non-interacting Thomas-Fermi distribution are shown as blue open circles for state $|1\rangle$, and red crosses for state $|2\rangle$. The data combine 92 independent shots. The dashed line corresponds to the estimated critical polarization, $P_c = 0.09$, for the phase transition from coexisting to separated phases. The images are of sufficient quality that the assignment of phase separation is ambiguous in only two of the shots represented in this figure. Our contention for a phase transition at P_c is based on statistical evidence: none of the 31 shots deliberately prepared as $P = 0$ and only one with a measured $P < 0.07$ are phase separated, while all but two shots with $P > 0.11$ are. The width of this transition region is consistent with our statistical uncertainty in the measurement of P . Although fluctuations in absolute probe detuning lead to 15% uncertainty in total number, the difference in the two probe frequencies is precisely controlled, resulting in lower uncertainty in P . We estimate the uncertainty in a single measurement of P to be 5%, which is the standard deviation of measurements of P for distributions prepared as $P = 0$. Also from these distributions, we find no significant systematic shift in detection of relative number. The uncertainty in the ratio R/R_{TF} is estimated to be 2.5%, due mainly to the uncertainty in measuring ν_z . The uncertainty in R/R_{TF} for state $|2\rangle$ grows with increasing P due to greater uncertainty in the fitted value of R with decreasing N_2 .

4.5.1 Temperature determination

In many situations, the temperature of a trapped atomic gas can be determined from a measurement of the size of the gas and knowledge of the confining potential. In general, for a thermal gas in a curved (i.e. not box shaped) potential, higher temperatures lead to larger atom clouds, since the kinetic energy associated with the temperature allow the atoms to sample more of the potential. By their very nature, however, highly degenerate trapped Fermi gases are difficult to accurately characterize in terms of temperature. This is due to the fact that when a gas of identical fermions is cooled, Fermi statistics require the atoms only fall to the lowest unoccupied level. This characteristic means that as temperature is decreased, the spatial distribution of the Fermi gas is determined more by the Fermi energy, and less by the temperature.

This stabilization of size by the “Fermi pressure” is exemplified in fig. 4.34 [6], the first such observation in a trapped gas of fermionic atoms. For this data, the temperature of the Fermi gas was determined from that of a coexisting Bose gas of ^7Li . This technique was used since the sizes of trapped bosonic gases are typically much more dependent on temperature than comparable gases of fermions (unless interatomic interactions are very strong, which they are not in this case). Unfortunately, it is not possible to use such a technique for the current experiments since the introduction of a third species, such as a gas of bosonic ^7Li , to the spin mixture within the Feshbach resonance results in a three-body loss (see fig. 4.4). Instead, we estimate the temperature of our samples using a couple of independent methods.

The first method that is used to estimate the temperature of our fermionic atoms requires turning them into bosons. This is done to take advantage of the more striking dependence on temperature the bosonic particles exhibit. In the BCS limit, as well as in the crossover, the fermionic nature of the atoms dominates their behavior, and no obvious signatures appear when the pairs condense (at least in the case of an even mixture [102]). By virtue of the broad Feshbach resonance, we may continuously tune

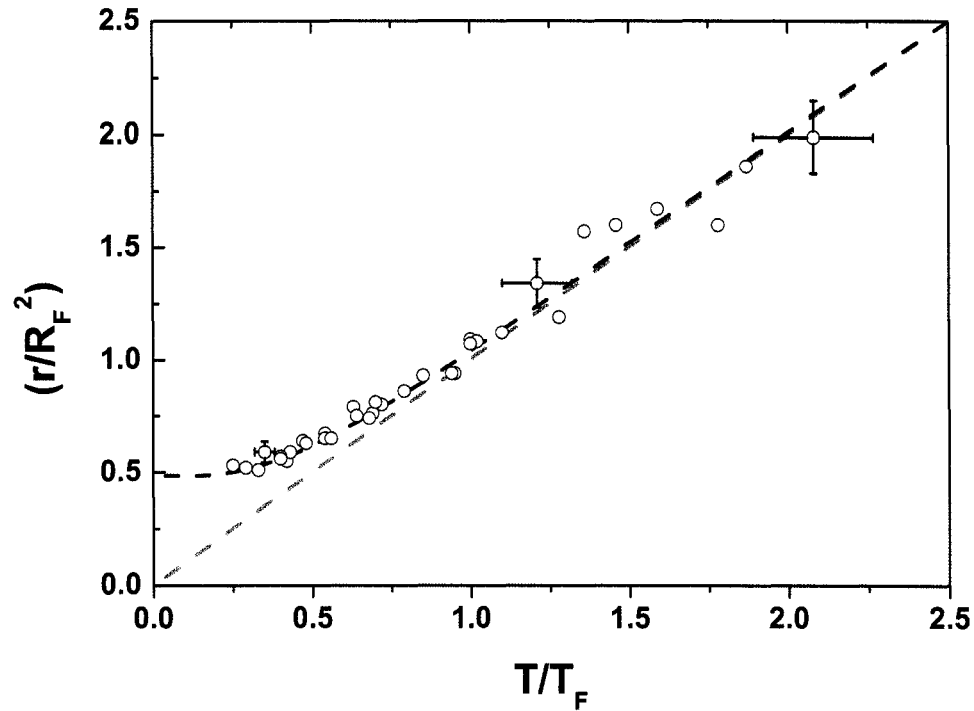


Figure 4.34 Demonstration of Fermi pressure: At higher temperatures, the size of the gas behaves classically (black dashed line), however, at lower temperatures, Fermi degeneracy prevents the size of the gas from continuing to shrink. Plotted is the square of the $1/e$ axial radius, r , of the ${}^6\text{Li}$ clouds versus T/T_F . The radius is normalized by the Fermi radius. The solid line is the prediction for an ideal Fermi gas, whereas the dashed line is calculated assuming classical statistics. Several representative error bars are shown. These result from the uncertainties in number, temperature and measured radius. (Figure taken from ref. [6].)

our pairs of atoms from weakly bound Cooper pairs to deeply bound bosonic molecules as was exemplified in Chapter 3. When the interactions are tuned to the BEC regime, the bosonic nature of the pairs becomes appreciable. As such, the spatial distribution can be observed to progress from that of a classical gas at higher temperatures, to the bimodal distribution of a partially condensed gas at lower temperatures. At this stage, the temperature may still be determined by a fit to the thermal portion of the cloud.

In addition, as already discussed in Chapter 3, T/T_c may be estimated from the measured condensate fraction N_0/N since

$$\frac{N_0}{N} = 1 - \left(\frac{T}{T_c}\right)^q; \quad (4.22)$$

with $q = D/\alpha = 3$ since $D = 3$ is the dimensionality, and $\alpha = 1$ for a harmonic trap [66, 67].

At the lowest temperatures, a nearly pure condensate emerges, and no measurable non-condensed fraction remains. As done in Chapter 3, we can place a lower limit on the condensate fraction of ~ 0.9 which gives $T/T_c \lesssim 0.5$. This measurement, when made in the BEC limit, gives an upper limit on the temperature of $T \lesssim 0.26 T_F$, since

$$\frac{T}{T_F} \lesssim \left(\frac{T}{T_c}\right) \left(\frac{T_c}{T_F}\right) = 0.5 \left(\frac{\hbar\bar{\omega}(N/1.2)^{1/3}}{\hbar\bar{\omega}(6N)^{1/3}}\right) = 0.26 \quad (4.23)$$

At unitarity ($1/k_F a = 0$), the temperature would be estimated to be $T \lesssim 0.15 T_F$, since $T_c/T_F \approx 0.3$ [12, 128–131]. The temperature of a pure molecular BEC observed at 754 G ($1/k_F a \sim 1.5$), near the field limit where the condensate is still distinguishable from thermal atoms, should fall somewhere within these limits. In addition, as discussed in Chapter 3 (3.2.2), adiabatic sweeps from BEC to unitarity result in additional cooling.

While the above method sets a constraint for the upper limit of the temperature, it becomes insensitive at lower temperatures since no visible thermal fraction remains,

and the condensate distribution is no longer affected by temperature. In order to measure lower temperatures, a new method must be adopted. Ideally, such a method would allow for a determination of the temperature directly from the data of interest, taken at arbitrary interaction, and not rely on a calibration taken at a different field, such as above. At a minimum, this would reduce the chances of a systematic error in temperature determination due to effects of ramping the magnetic field. Analysis in the unitary regime of strong interactions, however, further complicates the prospects of directly determining temperature. This is due to in part to the complex make-up of such a gases at finite temperatures (condensed pairs + non-condensed pairs + unpaired atoms [132]), combined with the lingering insensitivity of the distribution of the gas to temperature variations.

Despite these difficulties, it is still possible to determine an effective temperature by fitting a profile of the trapped gas to a finite temperature Thomas-Fermi distribution. Our method is comparable to that previously developed in a collaboration between the Levin and Thomas groups [110, 132]. Details regarding the specifics of our fitting analysis are provided in Appendix B.

The result of this method is a dimensionless effective temperature parameter, \tilde{T} , which at a minimum, allows us to compare the temperatures of our various data. In addition, \tilde{T} has been calibrated to the actual temperature, T/T_F [110]. This calibration is approximately given by

$$\tilde{T} \approx \frac{T}{T_F \sqrt{1 + \beta}}, \quad (4.24)$$

where $\beta = -0.54$ is the universal many body parameter we measured in sec. 4.3.1. A more refined calibration is given in Appendix B.

4.5.2 Temperature Results

As discussed earlier, the polarized ($P \neq 0$) shots do not fit well to Thomas-Fermi distributions. To circumvent this effect, fits to the non-interacting wings of polar-

ized gases (in time of flight) have been used to find temperatures [102]. It has been pointed out, however, that the expansion dynamics of a partially paired gas may add uncertainty to the results obtained by this method [115] since the strongly interacting superfluid core should expand hydrodynamically, whereas the non-interacting unpaired atoms should expand ballistically.

Even though our data is taken *in-situ* (in the trap), and so should not be susceptible to this effect, fitting the wings of the distributions has still proven problematic. Difficulties arise because the deformations of the core also affect the unpaired atoms, since they tend to pile up against the hard wall potential formed by the uniformly paired core. As a result, we assign the temperature for a given data set by fitting temperatures to shots which have been intentionally prepared as unpolarized ($P = 0$).

We find that the fit temperature of the data that exhibits P_c [23] is $\tilde{T} \sim 0.1$, while the data that exhibits phase separation at any non-zero polarization [24] is found to have a significantly lower temperature of $\tilde{T} \leq 0.05$.

4.6 Raise the Temperature

The temperature dependent behavior of the polarized gas, specifically the presence or absence of a critical polarization, hints at a more rich system than initially anticipated. In order to further characterize this system, we have also produced data with fit temperatures $\tilde{T} \sim 0.2$ by intentionally halting the optical trap evaporation at a higher final trap depth.

Figure 4.35 shows column density images, along with integrated axial densities and their difference, for both the lower ($\tilde{T} \leq 0.05$) and higher ($\tilde{T} \sim 0.2$) temperature data. While the difference axial profile of the colder data shows the double peaked structure that indicates deformations, such features are absent in the warmer data, which shows the flat-topped difference profile predicted under the LDA. It is immediately evident from these images that the deformations present in the colder data are significantly

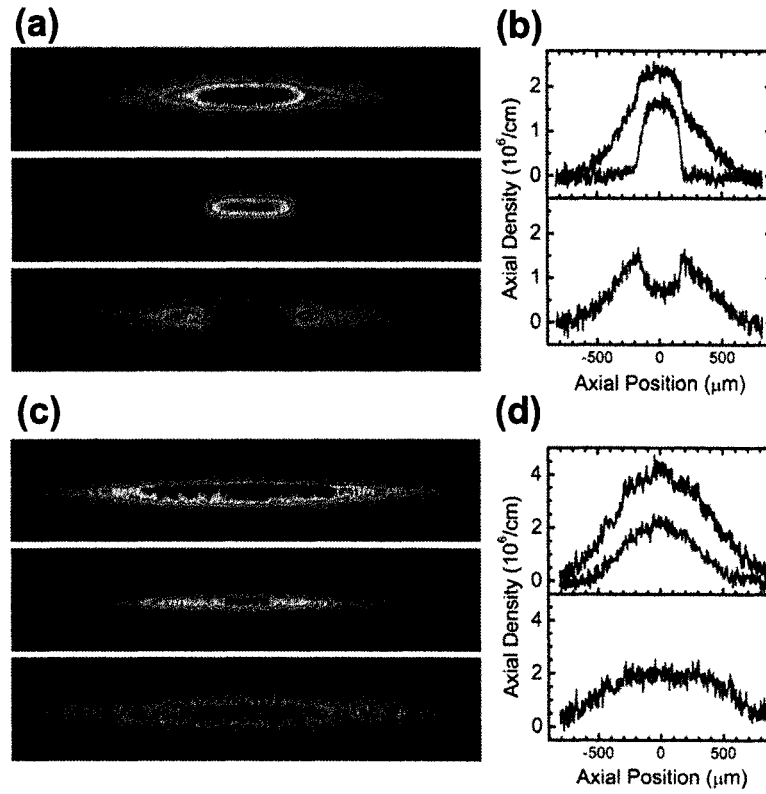


Figure 4.35 *In-situ* absorption images and integrated profiles. To the left are absorption images, while the plots to the right are the corresponding axial density distributions. (a),(b): $P = 0.50$, $N_1 = 146$ k, with $\tilde{T} \leq 0.05$; (c),(d): $P = 0.45$, $N_1 = 374$ k, with $\tilde{T} \approx 0.2$.

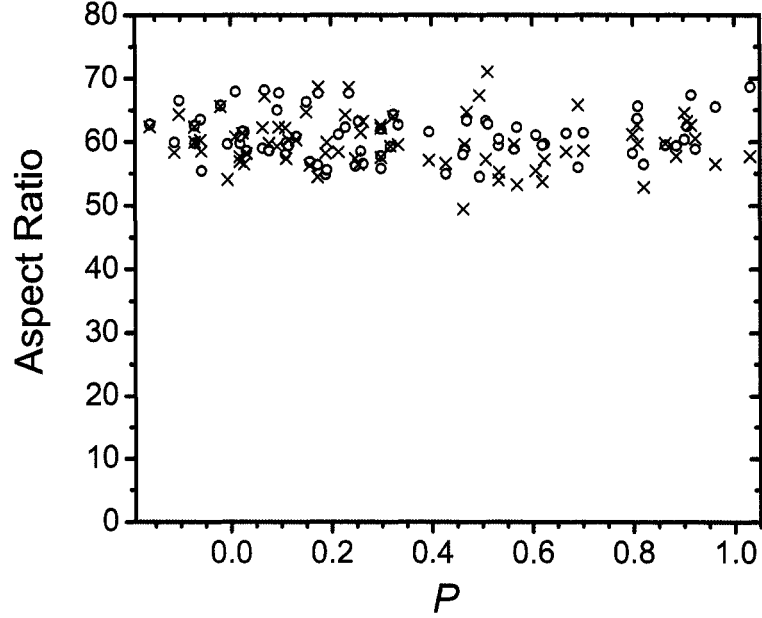


Figure 4.36 Measured aspect ratio R_z/R_r of states $|1\rangle$ (black circles) and $|2\rangle$ (red crosses), extracted from data taken at higher temperature ($\tilde{T} \sim 0.2$). Both the axial and radial sizes are measured by fitting column density profiles to zero-temperature, fermionic Thomas-Fermi distributions. In contrast to the colder data shown in fig. 4.18 ($\tilde{T} \leq 0.05$), the aspect ratios of the two states are equal for all measured P . The constant aspect ratio shows the absence of deformations in the data taken at higher temperature. The measured values are in good agreement with that predicted from the ratio of the radial to the axial frequencies $\nu_r/\nu_z = 62$.

reduced, if not completely gone in the higher temperature data. In fact, a plot of aspect ratio versus P shows that the shapes of both the majority and minority clouds remain the same (fig. 4.36).

Despite the lack of deformations, a reconstruction of the true 3-dimensional atomic density distributions reveals that even up to moderate polarizations, a uniformly paired core remains for the higher temperature data. Figure 4.37 shows that the central densities of the majority and minority remain equal up to a polarization of $P \sim 0.6 - 0.7$. Beyond this point, the core becomes polarized. This behavior contrasts with that of the lower temperature spin mixtures, where the core remains evenly paired up to a polarization of $P \sim 0.9$ (fig. 4.16), but is in better agreement

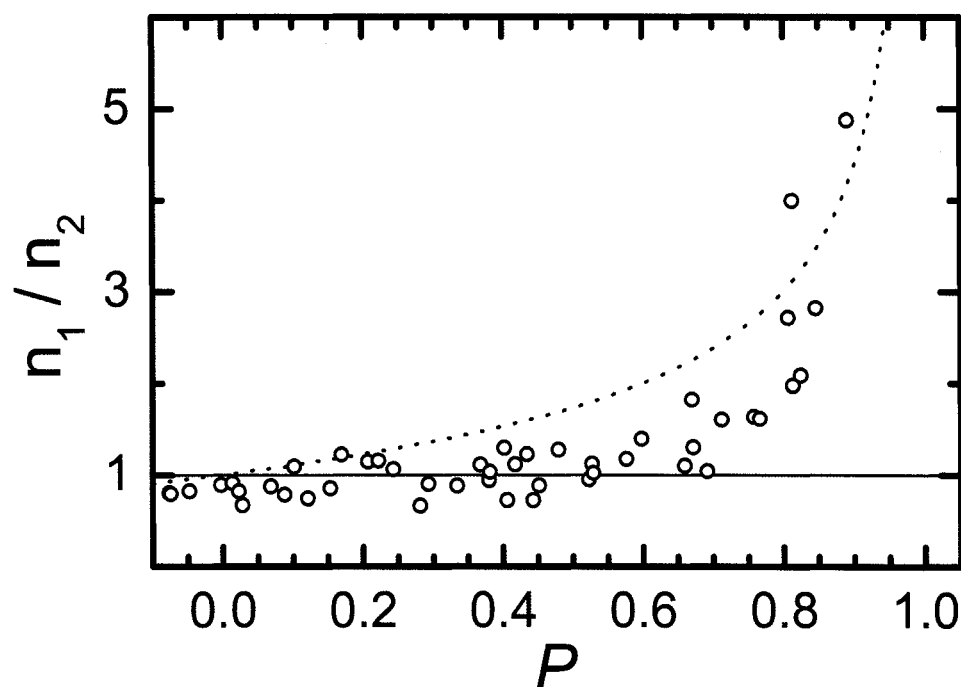


Figure 4.37 Ratio of the central densities vs. polarization for polarized gases prepared at $T \approx 0.2$, with average $N_1 = 500$ k. The dotted lines correspond to $[(1+P)/(1-P)]^{1/2}$, the expected central density ratio for a harmonically confined, non-interacting gas at $T = 0$. The solid line indicates equal central densities.

with the results reported by Shin *et al.* who found that uniform pairing ceased at $P \sim 0.75$ [103].

In addition, the reconstructed density profiles show that there is a region of gradually increasing polarization between the unpolarized central region and the unpaired atoms. This partially polarized region is strikingly different from the sharp transition region observed in the colder, deformed gases. This difference is also apparent in the integrated profiles shown in fig. 4.35.

4.7 The Big(ger) Picture

Hopefully now, with the additional clues gleaned by characterizing the behavior of the polarized Fermi gas at various temperatures, we may begin to form a unifying picture of the underlying system.

Here is what we know so far:

At the lowest temperatures ($\tilde{T} \leq 0.05$), we see LDA violating deformations which are likely a result of surface tension, even central pairing for nearly all P , and sharp phase boundaries between paired and unpaired regions.

At slightly higher temperatures ($\tilde{T} \sim 0.1$), the phase separated clouds maintain the above characteristics, but a critical polarization develops, below which a homogeneous polarized gas exists.

At even higher temperatures ($\tilde{T} \sim 0.2$), the deformations disappear, as do the sharp boundaries. These are replaced by LDA conforming distributions, with gradual boundaries and an extended partially polarized region. Despite this, even central densities persist for some range of P .

At this stage, we are getting close to being able to figure out what exactly is going on with this very rich system. What is missing from all this is a model which incorporates all these inputs and formulates a self consistent picture. Fortunately, several theoretical studies have been undertaken for the imbalanced Fermi gas system

[81, 114, 115, 119, 133–136]

4.7.1 Phase Diagrams

Several of the theoretical works mentioned above include phase diagrams that share many of the same characteristics. Specifically, the diagrams proposed by Parish [134] for the homogenous case, and those of Gubbels [115] and Chien [114] for the trapped case, are composed of the same three phases, connected by a tri-critical point. At lower temperature, below the tri-critical point, a phase separated state is stable. As temperature is raised toward the tri-critical point, a polarized superfluid becomes stable for low polarizations, and a normal state appears for higher polarizations. For these temperatures below the tri-critical point, the phase transition from the phase separated state to the normal state is of first order. When the tri-critical temperature is surpassed, the phase separated state is no longer stable, and what remains is a polarized superfluid, at low P and a normal gas at higher T . In this case, the boundary between these two phases becomes second order.

Figure 4.38, where we have added lines to illustrate the approximate location of our data, illustrates how the structure of these phase diagrams captures the overall observed properties. The blue (long-dashed) line corresponds to the data taken at the lowest temperatures $\tilde{T} \leq 0.05$. We see that this line enters directly into the phase separated regime for any non-zero P as long as the temperature is sufficiently low, just as the data exhibits phase separation for arbitrarily low values of P . In addition, this phase separated state is maintained for nearly the full range of polarization, a prediction that is also consistent with the experimental data. There is further agreement with this diagram when the order of the phase transition from the phase separated state to the normal state is considered. Since this temperature is below the tri-critical point, there is a predicted first order transition between these two phases. Indeed, the sharp boundaries between the unpolarized superfluid core and the normal

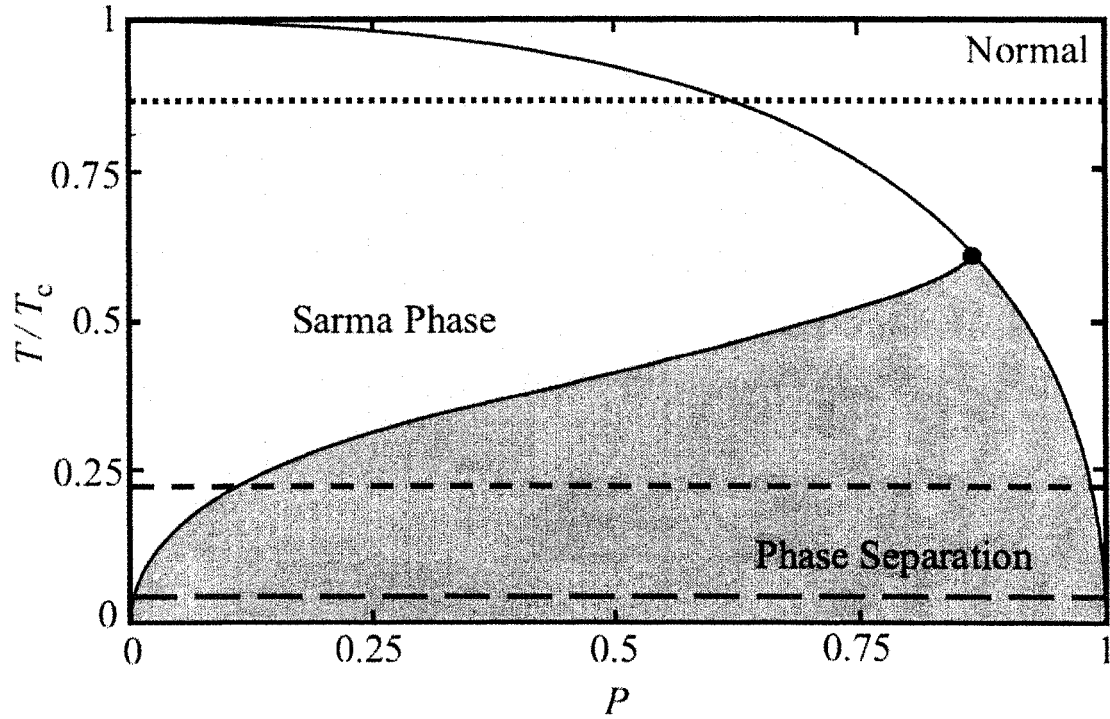


Figure 4.38 Phase Diagram of a polarized Fermi gas at unitarity, adapted from Gubbels *et. al* to illustrate the proposed placement of the data. The phase diagrams of Parish and [134] and Chien [114] show the same basic structure. For temperatures below the tri-critical point, three phases are stable, depending on polarization. At low P and $T \neq 0$, a Sarma (or breached pair, or polarized superfluid) phase, is optimal, while at higher P (or lower T) phase separation is preferred. At high P , except for at the very lowest temperatures, the phase separation breaks down and the gas becomes normal via a first order transition. Above the tricritical point, the gas goes directly from the Sarma phase to normal via a second order transition. Lines have been added (by us) to show the temperature regimes of interest that are consistent with our observations. The blue (long-dashed) line corresponds to the lowest temperature data, which shows phase separation as soon as $P \neq 0$, and remains phase separated for nearly all P . The orange line (dashed) shows intermediate temperature, where the gas is initially in the homogeneously paired Sarma phase, and undergoes a transition to phase separated at $P \sim 0.1$. Finally, the red (short-dashed) line represents the highest temperature data, where the gas is in the Sarma phase until going normal via a second order transition. The temperature scale shown may not be absolute since fluctuations (un-condensed pairs), which are not included in this calculation, will tend to bring down the absolute temperatures [115]. (Note that these fluctuations are included in other work [114].)

atoms exhibited in the data reflects this first order transition. The deformations also indicate a first order transition, since the surface tension that underlies them requires a first order interface to provide direct contact between the superfluid and normal components.

The orange (dashed) line, drawn at a higher temperature, though still below the tri-critical point, corresponds to our data prepared at $\tilde{T} \sim 0.1$. These data are characterized by the existence of a critical polarization, below which the gas does not exhibit deformations or phase separation. If we follow the line shown in the figure, we see that critical polarization observed for phase separation in the data [23] is consistent with passing across the boundary between a polarized superfluid, at low P , and a phase separated state at higher P . The persistence of deformations in this data also indicate the continued presence of a first order transition to the normal state, and further confirm the placement of this data below the tri-critical point.

The red (short-dashed) line, drawn above the tri-critical point, represents the highest temperature data, prepared at $\tilde{T} \sim 0.2$. This data is never in the phase separated region, and instead goes directly to the polarized superfluid state at non-zero P . Such a state is characterized by the continuous reduction in local polarization from a uniformly paired core (at lower values of P). This smooth transition, along with the lack of deformation inducing surface tension, reflects the second order nature of the superfluid to normal boundary. The loss of a uniformly paired core occurs in the data at a polarization of $P \sim 0.5 - 0.7$. This is consistent with crossing the boundary to a normal state at a temperature dependent value of P , since the onset of the polarized core has been linked to the disappearance of superfluidity by the observation of the quenching of vortices in such a polarized gas [101].

Current State of Affairs

From the start, this project with imbalanced spin mixtures has not been without some confusion and controversy. This is partly because the initial observations of our group [23] and the Ketterle group at MIT [101] (both published in the same issue of *Science*) were somewhat contradictory. Moreover, our observations were not all explainable by the current theories (i.e. the critical polarization, P_c , and deformations). As the work of both groups has progressed, and as theories have caught up (surface tension, non-zero temperature phases), however, some of the inconsistencies between the experiments have become explainable.

By looking at our data in the context of the above phase diagrams, we seem to have arrived at a consistent picture of what is going on. The last sticking point is that while this interpretation works well for our data, some features of the MIT results [101–103], such as lack of observed surface tension and loss of even central pairing at $P \approx 0.7$, make the placement of their data less straightforward in this context. Furthermore, direct comparisons of the results of the two experiments are complicated by the different trap aspect ratios and different methods used for temperature determination. It has been suggested that the MIT data may be above the tri-critical point, and therefore in the Sarma phase [115, 126], though the reported temperatures for the work at MIT are comparable to the coldest temperatures we report, so this interpretation remains uncertain.

Chapter 5

Conclusions

In this thesis, I have presented the work that I have engaged in during my time in the lab. While the specific progression of research was not explicitly planned from the beginning, it happens that the sequence of experiments here fit together quite well. As a new student in the lab, I was fortunate to have the opportunity to work with Andrew and Kevin on the Fermi pressure experiment [6] which helped to get the ball rolling, both for our apparatus, and to some extent, for the broader field. The next experiment, the observation of matter wave solitons [17] may seem like a bit of a diversion from the apparently Fermi-heavy research plan we have followed, but in fact this experiment served as an introduction (at least for me) to the potential that magnetic Feshbach resonances offered. Likewise, the formation of bosonic molecules of fermionic ${}^6\text{Li}$ atoms by an adiabatic sweep across the narrow Feshbach resonance [18] got us going on the current studies of fermionic pairing. The long lifetime we measured for the molecules suggested that it would be possible to use such resonances in ways that were not possible for bosonic species, where the Feshbach resonances lead to rapid loss of atoms by enhancing inelastic loss processes [137].

After this sequence of experiments, I became the lead student on our apparatus. I used this opportunity to put to use the lessons learned from the previous experiments by continuing the push into uncharted territory. The first experiment performed under my watch was the molecular probe measurement [22]. This work provided the first quantitative characterization of the pairs formed in a degenerate spin mixture of fermions throughout the broad Feshbach resonance, and provided the first evidence of pairing in the BCS regime. The small magnitude measured for the closed channel fraction in the resonance established the universality of the broad resonance toward other fermionic systems, and therein helped set the framework for our future

experiments.

The final chapter of my research as a student (and of my thesis) was the study of imbalanced superfluid states formed from uneven spin mixtures. In addition to combining all our previous knowledge and experience in areas such as pairing, molecular BEC's, and experimental techniques, this work challenged us to learn and characterize a new and unique system for which we had little intuition about at the onset. Through countless data sets, as well as through valuable collaboration and input from theorists, however, we have begun to form an understanding of this rich system.

5.0.2 Outlook

The study of degenerate Fermi gases represents a recent addition to a young and fast moving field. As a result, experiments in this field progress rapidly, and are governed by a mix of theory and the constant feedback of the latest results. There is always an underlying (and not unjustified) feeling that if we don't get our experiments done as quickly as possible, someone else will do them for us. This kind of environment is beneficial for the field in that the competitive atmosphere drives progress, however, the downside is that in order to be competitive, one is often forced to focus on a singular goal, such that on occasion, interesting side roads must be bypassed and saved for later.

Nearly every aspect of the work I have undertaken here has presented opportunities for further study. In choosing our particular path, we have had to decide which of these opportunities to follow, and which to make note of, and then move on. It would have been interesting, for example to study collisions between the matter wave solitons. The molecule sweep experiment also presented a couple of questions, such as whether the 50% conversion efficiency is fundamental in origin, or simply a coincidence. The long lifetime of the deeply bound molecules also suggests that something interesting is occurring, since the lifetime of molecules prepared in the

broad resonance do not have long lifetimes outside of the resonance.

Given the sensitivity of the molecular probe for characterizing the atom pairs, it would be advantageous to extend this technique towards other measurements. For example, by driving a molecular transition quickly compared to the pair formation rate, one could measure the paired fraction of a superfluid gas. This measurement would potentially contribute to the understanding of pre-formed pairs in the strongly interacting regime; a system that is believed to play a role in high T_c superconductors.

The work with imbalanced mixtures, which at the start was thought to be a relatively straightforward extension of our previous work, has revealed a much richer system than previously expected. There are several possibilities as to the direction this research should take next. It would be informative to fill in the phase diagram at unitarity, or to investigate further the role of the geometry of the trapping potential, for example. The addition of varied interaction strength adds yet another parameter to the phase space of this system to be studied. This is all possible even without mention of an optical lattice, which would further increase the possibilities in all these systems.

With all this being said, the appeal of this field for me is that we don't yet know what the next big discovery will be, or what future experiments have in store. All we really have to do set up the experiments according to our best understanding, and remember to expect the unexpected.

Appendix A

Estimation of Uncertainty in Measurement of β

Since the value β (see Sec. 4.3.1) depends strongly upon the measured quantity R_z/R_{TF} , it is necessary to account for all the mechanisms that contribute to the uncertainty in measuring this quantity. In this way, we may also identify the leading contributors to the uncertainty and focus specifically on improving their measurements. We will primarily focus on systematic uncertainties, since due to the large number of measurements used to determine β , the contribution of statistical uncertainties is greatly reduced, and in the end will be inferred through the scatter of these measurements.

A.0.3 Measured Radius, R_z

R_z is determined by a two-parameter fit to the integrated column density, and is subject to fitting and magnification uncertainties. Uncertainties in fitting due to image noise are statistical in nature, and tend to average out for large data sets. Our imaging magnification is directly measured by relating a known displacement of the optical trap to the measured displacement of atoms imaged in the trap (this procedure is documented in Ramsey Kamar's Masters thesis [55]). From this measurement, we obtain a magnification $M = 3.94$, with $(\delta M/M) = (0.04/3.94) \approx 1\%$, so the systematic uncertainty of measured R_z (from the magnification) is $(\frac{\delta R_z}{R_z}) = 1\%$.

A.0.4 Calculated Radius, R_{TF}

The Thomas-Fermi radius for a non-interacting fermi gas is given by

$$R_{TF} = \left(\frac{2\epsilon_F}{m\omega_z^2} \right)^{1/2}, \quad (\text{A.1})$$

where m is the atomic mass, ω_z is the axial trap frequency, $\epsilon_F = \hbar\bar{\omega}(6N)^{1/3}$, with mean frequency $\bar{\omega} = (\omega_z\omega_r^2)^{1/3}$, where ω_r is the radial frequency. The fractional

uncertainty for R_{TF} is

$$\left(\frac{\delta R_{TF}}{R_{TF}}\right) = \sqrt{\frac{1}{9}\left(\frac{\delta\omega_r}{\omega_r}\right)^2 + \frac{25}{36}\left(\frac{\delta\omega_z}{\omega_z}\right)^2 + \frac{1}{36}\left(\frac{\delta N}{N}\right)^2}, \quad (\text{A.2})$$

The radial frequency for this optical trap was measured by modulation of the radial position of the trap beam. Modulation at frequencies which correspond to trapping frequencies result in resonant heating, and a measurable loss from the trap. At an optical power (at the atoms) of 1.00 W, the radial frequency for ^7Li was measured to be $\omega_r/2\pi = 2860 \pm 40$ Hz. The radial frequency for a given shot is calculated by measuring the power, P , in the optical trap and scaling the measured frequency:

$$\omega_r = 2\pi(7/6)^{1/2} \cdot 2860 \left(\frac{P}{1.00}\right)^{1/2}, \quad (\text{A.3})$$

where the $(7/6)^{1/2}$ term accounts for the ratio of masses of ^6Li and ^7Li . Systematic uncertainties in power cancel, since the measurement is relative, and so the only remaining systematic uncertainty is that of the measured frequency. This gives $\left(\frac{\delta\omega_r}{\omega_r}\right) = 40/2860 = 1.4\%$.

The axial frequency of oscillation could, in principle, be calculated given ω_r and the geometry of the optical trap beam. However, due to a contribution from curvature in the magnetic bias field, the axial frequency is modified. As a result, a direct measurement of ω_z is necessary. This is accomplished by “kicking” the atomic cloud with a transient magnetic field and observing the subsequent oscillations. For the trap depth at which the this particular data was obtained, the measured frequency is $\omega_z/2\pi = 7.18 \pm 0.1$ Hz, so $\left(\frac{\delta\omega_z}{\omega_z}\right) = 1.4\%$.

Atom number, N , is obtained by summing the optical density of the cloud. N is given by

$$N = \frac{2l^2}{\sigma_o} \frac{I_o}{I_s} \Sigma_{x,z} (1 - e^{-OD(x,z)}) + \frac{l^2}{\sigma_o} \left(1 + 4\left(\frac{\Delta}{\Gamma}\right)^2\right) \Sigma_{x,z} OD(x,z), \quad (\text{A.4})$$

where l is the pixel size, I_o is the probe intensity, I_s is saturation intensity, Δ is the probe detuning from resonance, σ_o is the peak absorption cross section, Γ is the natural line width and OD is the measured optical density.

The uncertainty of the number δN is dominated by the uncertainty in N from $\delta\Delta$, which is denoted as δN_Δ , and the uncertainty in N from δI_0 , which is denoted as δN_{I_0} . These can be estimated as follows:

$$\delta N_\Delta = \frac{\partial N}{\partial \Delta} \delta \Delta = \left(\sum_{x,z} OD(x,z) \right) \frac{\ell^2}{\sigma_0} 8|\Delta| \delta \Delta, \quad (\text{A.5})$$

and,

$$\delta N_{I_0} = \frac{\partial N}{\partial I_0} \delta I_0 = \frac{2\ell^2}{\sigma_0} \frac{\delta I_0}{I_s} \sum_{x,z} (1 - e^{-OD(x,z)}). \quad (\text{A.6})$$

Since we nominally probe at $\Delta = 0$, and δN_Δ from Eq.(A.5) depends linearly on Δ , we vary Δ in Eq.(A.4) by its systematic uncertainty $\delta\Delta = 0.5 \text{ MHz} = 0.085 \text{ } \Gamma$. Changing Δ by this amount in the number counting results in a change in N of 1.7%, so $(\frac{\delta N_\Delta}{N}) = 1.7\%$. The typical systematic uncertainty of N from I_0 is $(\frac{\delta N_{I_0}}{N}) = 4.5\%$. In addition, the pixel size ℓ has the uncertainty $(\frac{\delta \ell}{\ell}) = 1\%$ due to the uncertainty of the magnification M . With this contribution included, the overall systematic uncertainty in the number,

$$\frac{\delta N}{N} = \sqrt{4\left(\frac{\delta \ell}{\ell}\right)^2 + \left(\frac{\delta N_\Delta}{N}\right)^2 + \left(\frac{\delta N_{I_0}}{N}\right)^2}, \quad (\text{A.7})$$

is 5.2%.

From the uncertainties of N , ω_z , and ω_r , the uncertainty of calculated Thomas-Fermi radius R_{TF} , is calculated from Eq.(A.2) to be 1.52%.

With the uncertainties of R_z and R_{TF} , the systematic uncertainty of the measurement of R_z/R_{TF} , given by

$$\frac{\delta(R_z/R_{TF})}{R_z/R_{TF}} = \sqrt{\left(\frac{\delta R_z}{R_z}\right)^2 + \left(\frac{\delta R_{TF}}{R_{TF}}\right)^2}, \quad (\text{A.8})$$

is 1.82%. The statistical uncertainty of R_z/R_{TF} , taken from the standard error of all measurements, is 0.4%, and is added to the calculated systematic uncertainty. This gives an overall uncertainty in R_z/R_{TF}

$$\frac{\delta(R_z/R_{TF})}{R_z/R_{TF}} = 0.023 \quad (\text{A.9})$$

From Eq.(4.12), the uncertainty of measured β

$$\frac{\delta\beta}{\delta(R_z/R_{TF})} = 4(R_z/R_{TF})^3, \quad (\text{A.10})$$

so

$$\delta\beta = 4(R_z/R_{TF})^3\delta(R_z/R_{TF}) = 4(R_z/R_{TF})^4\frac{\delta(R_z/R_{TF})}{(R_z/R_{TF})} \quad (\text{A.11})$$

Given the measured value $R_z/R_{TF} = 0.825$, and $\frac{\delta(R_z/R_{TF})}{R_z/R_{TF}} = 0.023$ from A.9,

$$\delta\beta = 4 \times 0.825^4 \times 0.023 = 0.043. \quad (\text{A.12})$$

Appendix B

Temperature Determination of Strongly interacting Fermi Gas

The first step in our approach for obtaining the temperature of the strongly interacting paired Fermi gas will be to forget that it is interacting, and proceed to fit the profile to that of a non-interacting finite temperature Thomas-Fermi profile. We will address the interactions later. The presumption built in to this approach is that the profile of a strongly interacting Fermi gas has the same functional form as that of a non-interacting gas. While this fact is not obvious, given the general uncertainty as to the composition of these gases which may have regions of condensed and uncondensed pairs, as well as unpaired atoms, depending on temperature, our data, along with that of other similar experiments [23, 108, 110] have shown this to be the case. Theoretical analysis suggests that it is the uncondensed pairs that “fill in” the distribution and wash out the bimodality [132] that would otherwise be present in a partially condensed gas.

To get a real space Thomas-Fermi density distribution, we integrate the phase space density distribution [105]

$$w(\vec{r}, \vec{p}) = \frac{1}{(2\pi\hbar)^3} \frac{1}{Z^{-1} e^{\frac{H(\vec{r}, \vec{p})}{k_B T'}} + 1}, \quad (\text{B.1})$$

where \vec{r} and \vec{p} are the position and momentum coordinates, $Z = e^{\mu/k_B T'}$ is the fugacity, and $H(\vec{r}, \vec{p}) = \frac{\vec{p}^2}{2M} + \frac{m\omega_z^2}{2}(x^2 + y^2 + \lambda z^2)$ is the hamiltonian for a particle in a harmonic potential, and T' is an effective temperature which will be calibrated once interactions are included, over momentum, to give

$$n(\vec{\rho}) = - \left(\frac{mk_B T'}{2\pi} \right)^{3/2} \left(\frac{1}{\hbar^3} \right) Li_{3/2}[-Z e^{-\frac{m\omega_z^2 \rho^2}{2k_B T'}}], \quad (\text{B.2})$$

where $\rho^2 = x^2 + y^2 + \lambda z^2 = r^2 + \lambda z^2$ and Li_n is the Poly-Logarithmic function of order n .

This density is integrated over one radial direction to give the column density,

$$n(\vec{x}, \vec{z}) = -\frac{m(k_B T')^2}{2\pi\hbar^3\omega_r} Li_2[-Ze^{-\frac{m\omega_z^2}{2k_B T'}(x^2+\lambda^2 z^2)}]. \quad (B.3)$$

Another integral over the remaining radial direction produces the axial density,

$$n(\vec{z}) = -\left(\frac{m}{2\pi}\right)^{1/2} \frac{(k_B T')^{5/2}}{\hbar^3\omega_r^2} Li_{5/2}[-Ze^{-\frac{m\omega_z^2 z^2}{2k_B T'}}] \quad (B.4)$$

When fitting data, we most commonly fit the $x = 0$ cut of the column density distributions, since this happens to be less computationally demanding (due to the integer subscript in Li_2), however, we also fit integrated axial profiles and have not observed any systematic differences.

For fitting column density, we multiply the top and bottom of expression B.3 by $n(\vec{x} = 0, \vec{z} = 0)$ so that we may write it in terms of the peak value,

$$n(\vec{x}, \vec{z}) = n(\vec{x} = 0, \vec{z} = 0) \frac{Li_2[-Ze^{-\frac{m\omega_z^2}{2k_B T'}(x^2+\lambda^2 z^2)}]}{Li_2[-Z]}. \quad (B.5)$$

This function B.5 is then fit to the data using Mathematica, which has built in Poly-Logarithm capabilities. Before fitting, we set $x = 0$ and rearrange some of the terms to facilitate fitting, such that

$$e^{-\frac{m\omega_z^2 z^2}{2k_B T'}} = e^{-\frac{m\omega_z^2 z^2}{2k_B T'} \left(\frac{\mu(T')}{\mu(T')}\right)} = e^{-\frac{z^2}{R_z^2} \ln(Z)} = Z^{-\frac{z^2}{R_z^2}} \quad (B.6)$$

where $R_z^2 = \frac{2\mu(T')}{m\omega_z^2}$. Now B.5 is written

$$n(\vec{x}, \vec{z}) = n(\vec{x} = 0, \vec{z} = 0) \frac{Li_2[-Z^{1-\frac{z^2}{R_z^2}}]}{Li_2[-Z]}. \quad (B.7)$$

For each distribution, the fit to the data outputs the amplitude, $n(\vec{x} = 0, \vec{z} = 0)$, the Thomas-Fermi radius, R_z , and the fugacity, Z (and a center coordinate). From Z , we can find the temperature, since

$$Z = e^{\frac{\mu(T')}{k_B T'}} \Rightarrow T' = \frac{\mu(T')}{\ln(Z)k_B} \quad (B.8)$$

where $\mu(T') = \frac{1}{2}m\omega_z^2 R_z^2$. (See the figures at the end of the section for example fits.)

This temperature may be divided by the ideal Fermi temperature, $T_F = \frac{\hbar\bar{\omega}(6N)^{1/3}}{k_B}$ to give a more general, dimensionless temperature parameter $\tilde{T} \equiv T'/T_F$.

Now we must consider the effects of interactions. To first order, this measured effective temperature \tilde{T} can be scaled to get the actual temperature by

$$\tilde{T}\sqrt{1+\beta} = \frac{T}{T_F} \quad (\text{B.9})$$

where $\beta = -0.54$ is the universal interaction energy parameter measured in Chapter 4. Model-dependent corrections to this approximation have been performed on J. Thomas' ^6Li experiment at Duke by applying such a fitting routine to theoretical profiles generated for a known temperature (such as those predicted in ref. [132]). In this way, it is possible to establish a one to one correspondence between actual and fitted temperature [110]. The result of their calibration is shown in fig. B.1. A power law fit to this data yields [138]

$$\tilde{T}\sqrt{1+\beta} = 1.8 \left(\frac{T}{T_F} \right)^{1.49}, \text{ for } \tilde{T} < 0.42. \quad (\text{B.10})$$

For lower temperature data, $\tilde{T} < 0.42$, it may be preferable to use this expression, as opposed to eq. B.9, to predict the “true” temperature.

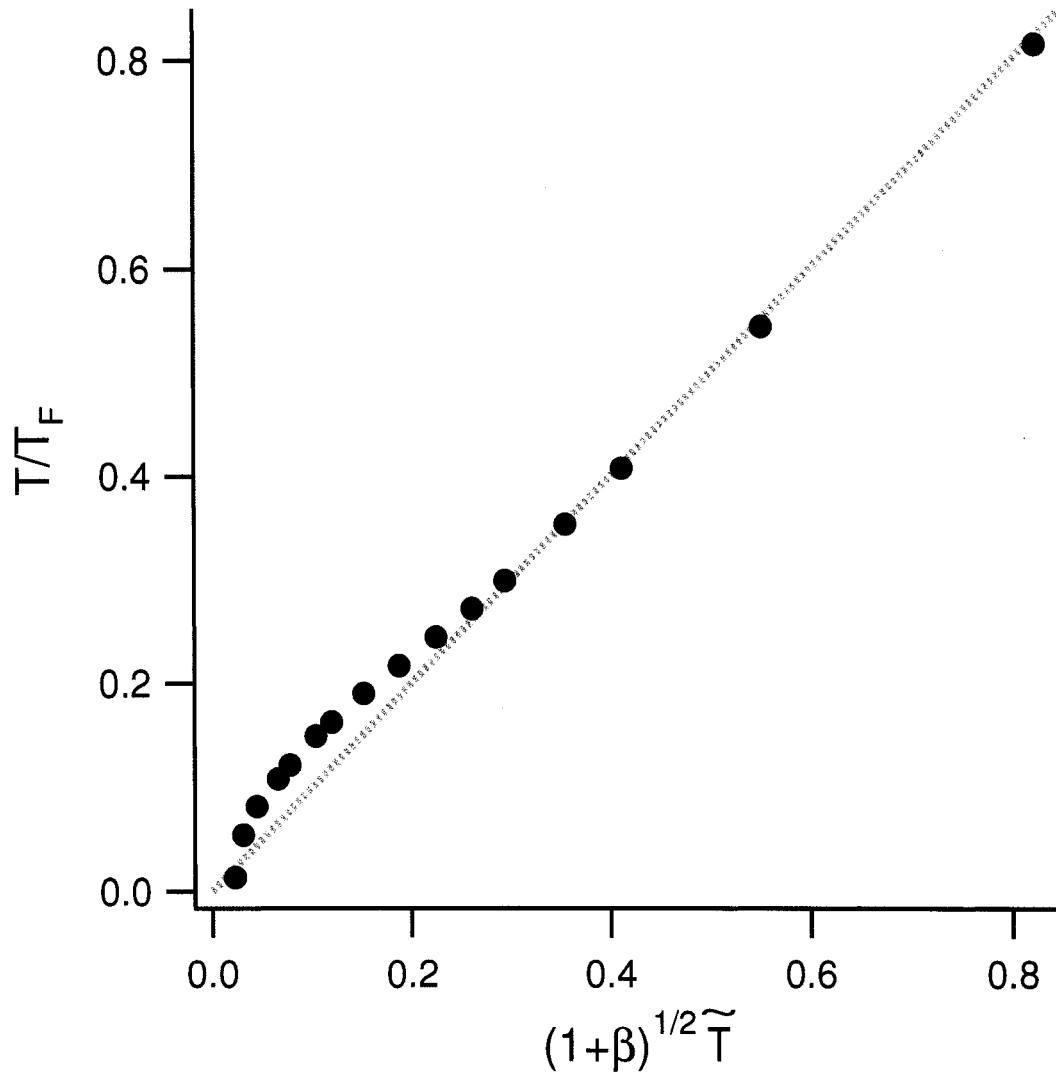


Figure B.1 Figure reprinted from ref. [138]. This plot shows the true temperature, T/T_F , plotted versus the measured empirical temperature \tilde{T} , scaled by $\sqrt{1+\beta}$, as measured by the Duke group in the strongly interacting regime. The diagonal line represents the approximation made in eq. B.9, and the points are the measured calibration, approximated by eq. B.10. The deviation from the straight line is thought to arise from systematic fitting effects due to the emergence of condensed pairs.

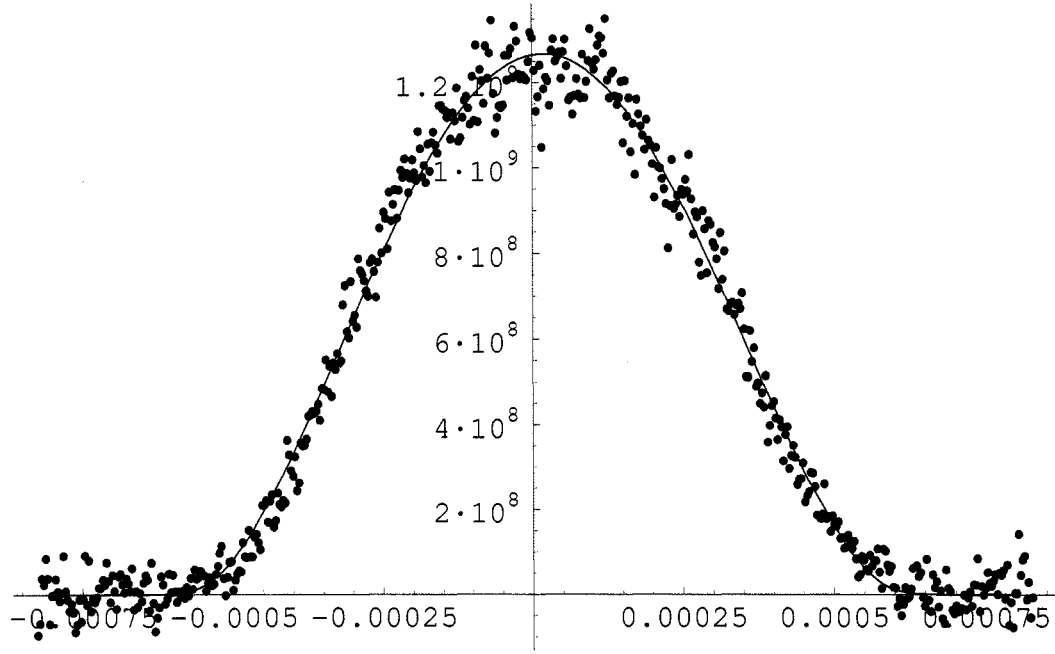


Figure B.2 Axial cut along $x = 0$ of the column density distribution (points, cm^{-2}), fit to the finite temperature T-F distribution given by eq. B.7 (line). For this shot, $N = 165$ k, $T' = 1.5 \times 10^{-8}$ K, $\tilde{T} = T'/T_F = 0.035$. This measured temperature gives $T/T_F = 0.055$ by eq. B.10. (x axis in meters)

B.1 Example Fits

Here I will show typical data which we have fit according to the procedure outlined above. Figure B.2 shows the finite T fit to an evenly paired, unpolarized cloud representative of the coldest data (column density).

Figure B.3 shows both the best fit finite and $T = 0$ functions for the data in the previous figure (B.2). It is clear that at such low temperatures there is very little difference between these two profiles. For this reason, this method can only establish an upper limit for the temperature of the coldest data (i.e $\tilde{T} \lesssim 0.05$).

Figure B.4 shows the finite temperature fit to a slightly less degenerate cloud (column density), and fig. B.5 shows the finite and $T = 0$ fitting functions that are generated by the fit to the (less cold) data in fig. (B.4). Though the difference

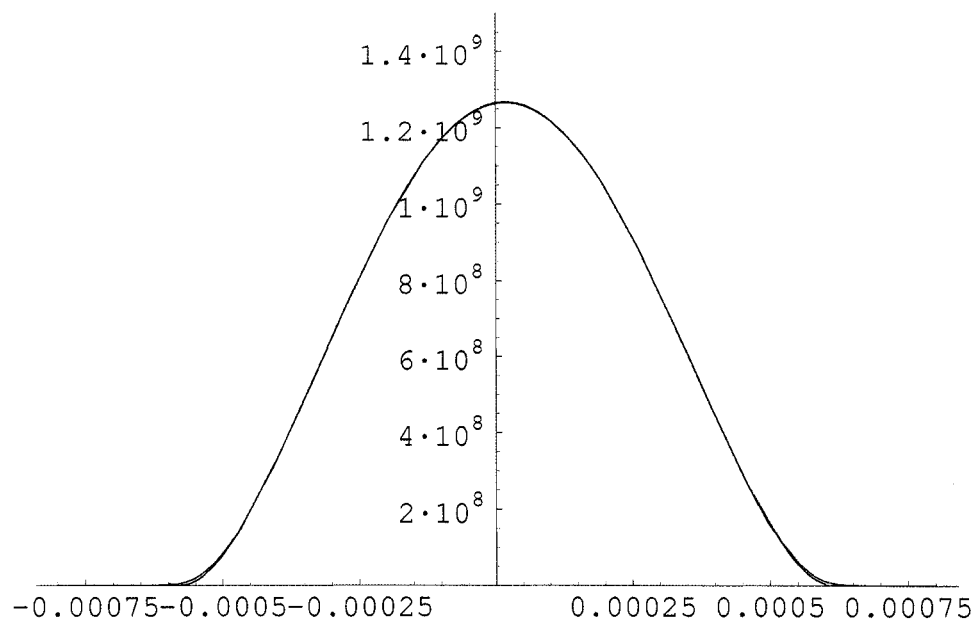


Figure B.3 Finite T (green) and $T = 0$ (red) fermionic Thomas Fermi distributions fit to data in the previous figure (B.2). The effects of finite T are barely perceptible in the wings of the distributions at such low temperatures ($\tilde{T} = 0.035$).

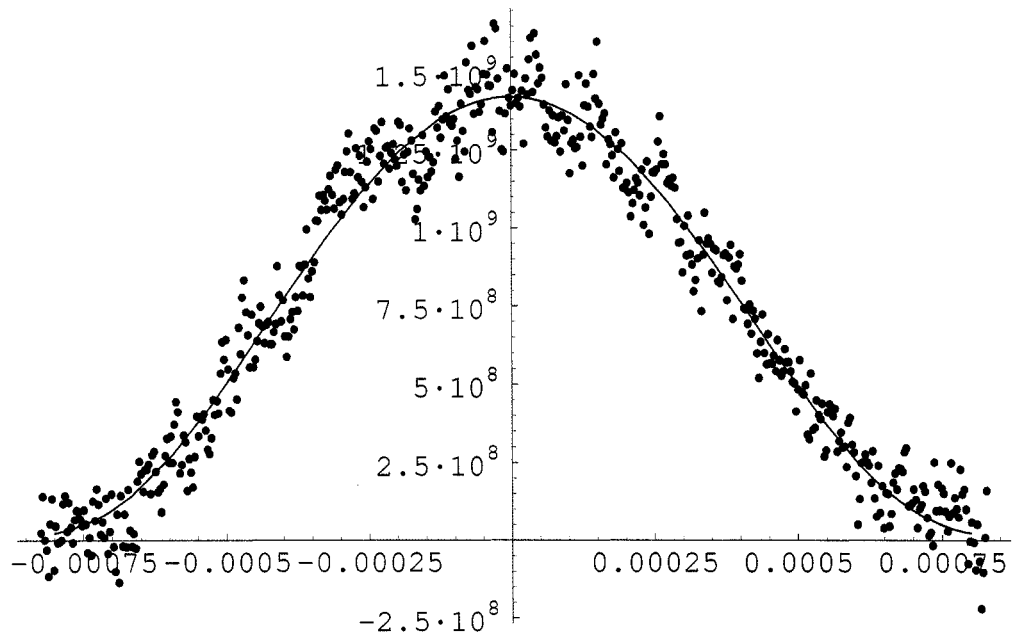


Figure B.4 Axial cut along $x = 0$ of the column density distribution (points, cm^{-2}), fit to the finite temperature T-F distribution given by eq. B.7 (line). For this shot, $N = 335$ k, $T' = 8.2 \times 10^{-8}$ K, $\tilde{T} = T'/T_F = 0.11$. This measured temperature gives $T/T_F = 0.12$ by eq. B.10. (x axis in meters)

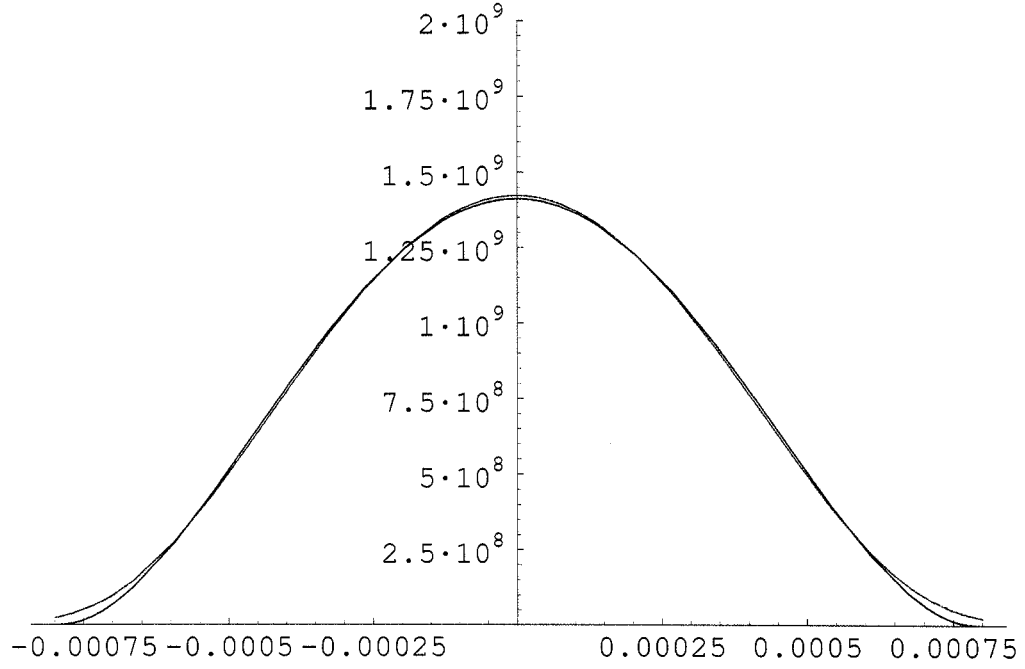


Figure B.5 Finite T (green) and $T = 0$ (red) fermionic Thomas Fermi distributions fit to data in the previous figure (B.4). The effects of finite T are now becoming more perceptible in the wings of the distributions. The small change in shape is enough to distinguish between clouds of differing temperatures. ($\tilde{T} = 0.11$).

between the profiles is still subtle, it is sufficient to provide a reasonable estimate of the temperature.

Appendix C

Tunable Standing wave EOM

The frequency of the molecular probe laser used in Chapter 3 is monitored by the position of its peak in an optical spectrum analyzer, relative to that of a reference laser that is locked to an atomic saturated absorption signal. The reference laser is modulated to produce sidebands, the positions of which in the spectrum analyzer can be tuned by varying the frequency of modulation. In this way, the sideband can be placed at the desired spectral position for the molecular probe, and the two features can be overlapped. This situation allows for maximized accuracy in maintaining the frequency of the probe laser ($\delta\nu < 1$ MHz). In addition, frequency tuning of the laser can be accomplished by tuning the frequency of modulation. This allows relative frequency shifts to be measured via a microwave counter, so that they are not dependent upon knowledge of the free spectral range (FSR) of the spectrum analyzer cavity.

We have designed a tunable electro-optic modulator (EOM) to add the sideband to the reference laser. This design consists of a resonant toroidal cavity with rectangular cross section. The height of the cavity, and thereby its resonant frequency, is tuned by a threaded movable ring (see fig. C.1). A LiTaO₃ electro-optical crystal is placed within the cavity. When the laser is sent through the crystal, its phase is modulated by the frequency of the electric field in the crystal, and, equivalently, sidebands appear in its frequency spectrum [139]. The resonant frequency is given by

$$\nu_0 = \frac{1}{2\pi} \sqrt{\frac{1}{L(h)C}}, \quad (\text{C.1})$$

where C is the total capacitance and $L(h)$ is the cavity inductance as a function of cavity height, h . The inductance of a toroid with rectangular cross section is given

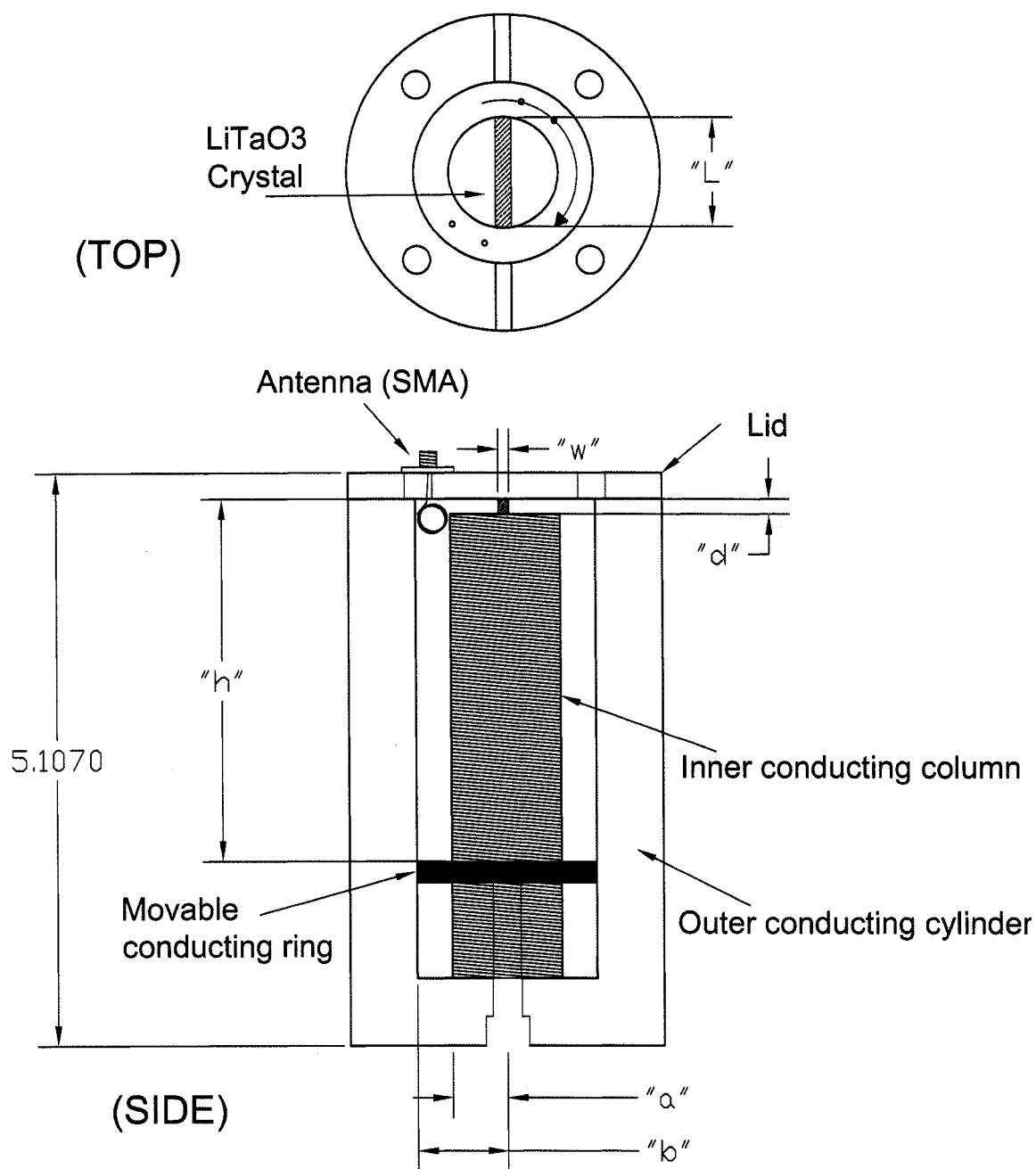


Figure C.1 Tunable EOM. A threaded ring travels up and down on threaded center post (108 threads/in) to adjust the resonant frequency. The LiTaO₃ crystal measures: $d = 3.5$ mm, $w = 2.5$ mm, and $L = 25$ mm (MTI Corporation, “optical grade”, $\langle Y \rangle$ oriented cut, AR coated ends). Also, $a = 0.0125$ m, $b = 0.0205$ m, and $0.01 \leq h \leq 0.100$ m. A static antenna is used in this instance, though efficiency may be further increased through the addition of a tunable antenna. Material: OFHC copper (electroplated). The overall height measurement is given in inches.

by

$$L = \mu \left(\frac{h}{2\pi} \right) \ln \left(\frac{b}{a} \right), \quad (\text{C.2})$$

where $\mu = \mu_o$ is the permeability of free space, h is the (tunable) height of the cavity, and a (b) is the inner (outer) radius of the cavity (see for example, [140]).

The capacitance is calculated for the crystal and the gap above the central post, and is given (for the case that the crystal length, L , equals the diameter of the post, $2a$.) by

$$C = \epsilon_0 \left(\pi \frac{a^2}{d} \right) \left(1 + \frac{2w\Delta\epsilon}{\pi a} \right), \quad (\text{C.3})$$

where ϵ_0 is the permittivity of free space, $\Delta\epsilon = (\epsilon' - \epsilon_0)/\epsilon_0$, where $\epsilon' = 47\epsilon_0$ is the dielectric constant of LiTaO₃, a is the post radius, which in this case is also half the crystal length, w is the crystal width, and d is the crystal height, equal to the gap between the lid and the post. For our crystal, eq. C.3 gives $C = 8.51$ pF.

Figure C.2 shows a plot of the resonant frequency, ν_0 , given by eq. C.1, versus cavity height, $10 \leq h \leq 100$ mm, for the entire tunable range.

We achieved typical modulation efficiencies, defined as the ratio of the power in each of the first order sidebands to the input power, of $\sim 25\%$ for frequencies in the range of 550 - 1200 MHz, using 3 W of RF drive power. At higher frequencies, the modulation diminished since the RF drive power was reduced due to the frequency range of the amplifier used. This range was more than sufficient for our purposes, however, as it easily spanned the 300 MHz FSR of the spectrum analyzer.

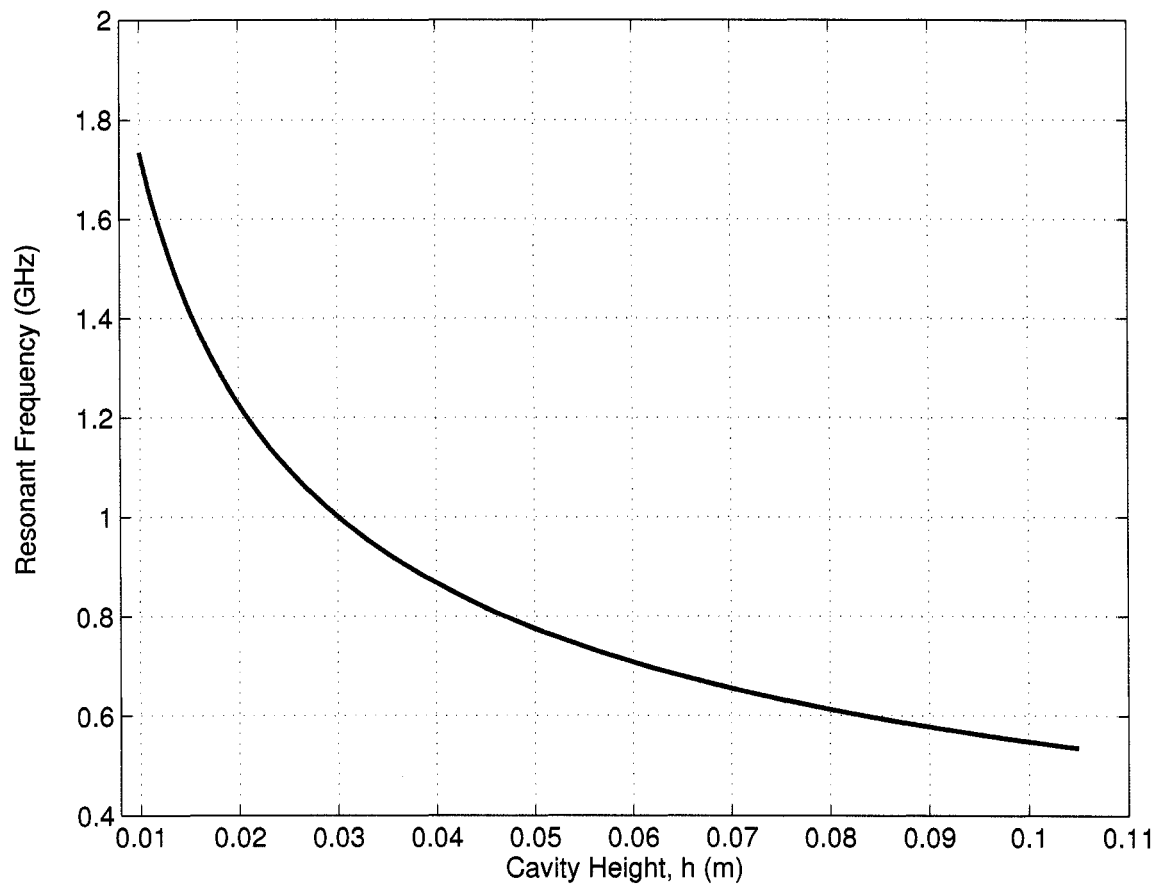


Figure C.2 The calculated tunability of the resonance frequency of the EOM (eq. C.2), for the design shown in fig. C.1.

Appendix D

Experimental Benchmarks

In the following table I have included benchmarks for basic operation of the apparatus. I have tried to include real numbers where possible, however some of the measurements are expressed in “lab” units specific to this apparatus. The “minimum” column represents the threshold at which some types of data, such as trap calibrations or probing resonances, which do not require extremely cold samples, may be produced. These levels will most likely not suffice for taking data such as in Chapter 4, where highly degenerate samples are needed. For this type of data, the apparatus should be very near the “ideal” settings. While it is not possible to include every possible sub-system in such a table, a measured deficit in one of the following parameters should help to narrow down the source of many problems, thereby facilitating more detailed troubleshooting. Moreover, many of the benchmarks of crucial sub-systems are somewhat subjective, such as fine tuning MOT and optical pumping beam alignment. In order to effectively adjust these “unmeasurable” parameters, it is necessary to have all the “measurables” listed below where they should be.

I have also included an updated summary table of the various diode lasers used for trapping ${}^6\text{Li}$, as well as some other random notes, at the end.

Device	Parameter	Minimum	Ideal	Notes
Chamber/Vacuum	Lifetime	120 s	>200 s	^6Li has stricter requirement than ^7Li
Coherent Laser	Power	800 mW	>900 mW	Dye lasts ~ 40 run days (1-1.5 mo's)
Spectra Laser	Power	300 mW	>400 mW	Dye lasts ~ 3 mo's
^7Li Zeeman Beam	Power	150 mW	~ 190 mW	AOM is maximized
^7Li MOT AOM	Efficiency	80%	85%	(rated 85% at 2W RF)
^7Li MOT Fiber In	Power	225 mW	>250 mW	Ophir Meter
^7Li MOT Fiber Out	Power	120 mW	>150 mW	Ophir Meter, Max eff. $\sim 60\%$
^7Li Optical Pump AOM	Power	140 mW	>160 mW	Ophir Meter
^7Li MOT (w/o ^6Li)	Fluorescence	2.5 V	>4 V	Should load in a few seconds
^7Li Mag. Trap (non-evap.)	Fluorescence	1×10^8	2×10^8	Summed array (see notes)
^6Li MOT Fiber In	Power	225 mW	~ 300 mW	Ophir Meter
^6Li MOT Fiber Out	Power	120 mW	>160 mW	Ophir Meter, Max eff. $\sim 60\%$
^6Li Optical Pump Fiber In	Power	80 mW	~ 100 mW	Ophir Meter
^6Li Optical Pump Fiber Out	Power	25 mW	>40 mW	Ophir Meter
^6Li MOT Trap/Repump	Power(s)	25 / 8 mW	35 / 11 mW	Measured at beam expanding lens pair
^6Li MOT (w/o ^7Li)	Fluorescence	100 mV	>160 mV	Should load in a few seconds
^6Li Mag. Trap (evaporated)	Σ "signal" (P.C.)	$\sim 10,000$	$\sim 20,000$	$\sim \text{trapbot} + 0.75 \text{ MHz}$, $\Delta \sim 5\Gamma$, $N \sim 10^7$
^6Li Opt. Trap (non-evap.) $ 6\rangle$	Σ "signal" (abs.)	~ 25	~ 45	High B, $\Delta = 0$, $N \sim 5 \times 10^6$, saturated
^6Li $ 6\rangle \rightarrow 1\rangle$	Efficiency	90%	>95%	40 ms, 4 MHz sweep, max RF ($\sim 3.5 \text{ W}$)
^6Li Spin Mix (evap) $ 1\rangle + 2\rangle$	Σ "signal" (abs.)	~ 10 (each)	>15 (each)	High B, $\Delta = 0$, $N \sim 3 \times 10^5$

Table D.1 Experimental Benchmarks.

More Notes on Table D.1

- The MOT fluorescence levels refer to the voltage of the photodiode mounted on the apparatus (w/ maximized alignment), and are given for either isotope alone. The addition of the ^6Li to the ^7Li MOT reduces the overall fluorescence by $\sim 10\%$. The presence of the ^7Li reduces the ^6Li fluorescence by $\sim 30 - 50\%$. Measure the latter by blocking the ^7Li MOT light and quickly measuring the remaining ^6Li fluorescence.

- ^7Li magnetic trap fluorescence levels refer to the summed fluorescence acquired on the ANDOR camera (use `lifetime.pgm`), while running the apparatus in fluorescence imaging mode, EMACKFR (see also ref. [21]). (Use this imaging method to take background lifetimes as well.)

Conditions:

The imaging system should be zoomed out completely.

Fluorescence pulse is $100\ \mu\text{s}$ ($q3 = 100$), with $\sim 110\ \text{mW}$ total power in MOT beams.

Detuning is $\sim 40\ \text{MHz}$. ($\text{fdetune} = 0.44$)

- Σ “signal” refers to the integrated image for phase contrast with the phase spot (P.C.) or absorption (abs.) images taken with the Andor CCD using processing in the script “`fast_40_iXon_062006_40by512.pgm`”.*

*The image processing in this script is fairly simple, since it is used mainly for real-time monitoring of the experiment. For the phase contrast image, $\text{Image}_{P.C.} = ((A - NA)/NA) \cdot 100$, where A and NA are “atoms” (trap populated) and “no-atoms” (trap empty) shots with reference shots subtracted and NA probe intensity normalized to that of A (the $\cdot 100$ is an historic relic).
For the absorption image: $\text{Image}_{abs.} = \ln(NA/A)$.

Laser-Type	Purpose	use/max/rated	Collimation	Lock(s)	$\sim^{\circ}\text{C}$	Manufacturer
M1-ECDL	D2 trap	7/7/20	elliptical	Cavity+SAL	15	Phillips
M2-ECDL	D1 repump	3/3/10	elliptical	M1, Dig. PLL	15	???
S1-Slave	shift, amp. M1	15/17/20	elliptical	M1, 2pass AOM	15	Phillips
S2-Slave	amplify M2	15/17/20	APP circular	M2	15	Phillips
S3-Slave	amplify S2	20/40/50	APP circular	S2	40	Mitsubishi
Z1-ECDL	Zeeman	10/15/40	elliptical	S1, Cable Delay	35	Mitsubishi
Z3-Slave	amplify Z1	30/40/50	CL circular	Z1	40	Blue Sky

Table D.2 This table gives information about the various diode lasers used for the ^6Li MOT. “Type” specifies either grating stabilized (ECDL) or injection locked (slave). “Purpose” is the light produced or function served. The “use” in the “use/max/rated” column refers to the power, in mW, at which we run the laser, measured after all collimation optics and optical isolators. “Max” represents the maximum attainable power after collimation, grating feedback, isolators and such (i.e, the “max” of “use”). “Rated” is the maximum power rating for the diode device itself. “Collimation” refers to the beam shape and/or the means to produce it: “APP circular” means that an anamorphic prism pair is used with a Melles Griot 06GLC001 lens; “CL circular” means the diode is pre-circularized (a “Circulaser”) and may be circularly collimated with a smaller Thorlabs C140TM-B lens; “Elliptical” means that the ellipticity is not corrected, however the beam waist is small enough to pass the aperture of an optical isolator, since the small Thorlabs lenses have been used. “Lock(s)” specify what the laser is locked to and how (SAL = saturated absorption lock, PLL = phase lock loop). “ $^{\circ}\text{C}$ ” is the approximate operating temperature.

Other Notes

- In many instances of poor apparatus performance, the trouble is often due to one of the following (assuming adequate pressure/background lifetime):

1. Poor optical pumping (especially ^7Li , power, power balance and/or alignment).
2. Problems with the ^7Li heatpipe lock (i.e. not sweeping correctly due to improper alignment or gain settings).
3. MOT beam alignment (“perfectly” overlapped alignment doesn’t work well).

So, when in doubt, these parameters should probably be checked first.

- The ^6Li magnetic trap evaporation performance is more sensitive to the background pressure lifetime and the magnetic trap field minimum. If the ^7Li seems to be working fine (mag. trap signal), while the ^6Li is not, try increasing the bias field ($B_o > 1.5\text{ G}$) or checking lifetime.

References

1. M. H. Anderson, J. R. Ensher, M. R. Matthews, C. E. Wieman, and E. A. Cornell. "Observation of Bose-Einstein Condensation in a Dilute Atomic Vapor." *Science* **269** 198 (1995).
2. K. B. Davis, M.-O. Mewes, M. R. Andrews, N. J. van Druten, D. S. Durfee, D. M. Kurn, and W. Ketterle. "Bose-Einstein Condensation in a Gas of Sodium Atoms." *Phys. Rev. Lett.* **75** 3969 (1995).
3. C. C. Bradley, C. A. Sackett, J. J. Tollett, and R. G. Hulet. "Evidence of Bose-Einstein condensation in an atomic gas with attractive interactions." *Phys. Rev. Lett.* **75** 1687–1690 (1995).
4. C. C. Bradley, C. A. Sackett, and R. G. Hulet. "Bose-Einstein condensation of lithium: observation of limited condensate number." *Phys. Rev. Lett.* **78**(6) 985–989 (1997).
5. B. DeMarco and D. S. Jin. "Onset of Fermi degeneracy in a trapped atomic gas." *Science* **285** 1703 (1999).
6. A. G. Truscott, K. E. Strecker, William I. McAlexander, G. B. Partridge, and R. G. Hulet. "Observation of Fermi Pressure in a Gas of Trapped Atoms." *Science* **291** 2570–2572 (2001).
7. S.L. Shapiro and S.A. Teukolsky. *Black Holes, White Dwarfs, and Neutron Stars, The Physics of Compact Objects*. John Wiley and Sons Inc., New York (1983).
8. H. Kamerlingh Onnes. "The Disappearance of the Resistance of Mercury." *Communications from the Physical Laboratory at the University of Leiden* **122b** 13–15 (1911).

9. J. Bardeen, L. N. Cooper, and J. R. Schrieffer. “Theory of superconductivity.” *Phys. Rev.* **108** 1175 (1957).
10. S. N. Bose. “Plancks Gesetz und Lichtquantenhypothese.” *Zeitschrift fur Physik* **26** 178–181 (1924).
11. A. Einstein. “Quantentheorie des einatomigen idealen Gases.” *Sitzungsber. der Preuss. Akad. der Wissen., Physik.-Mathem. Klasse* 3–16 (1925).
12. Q. Chen, J. Stajic, S. Tan, and K. Levin. “BCS-BEC Crossover: From High Temperature Superconductors to Ultracold Superfluids.” *Phys. Rep.* **412** 1 (2005).
13. D. M. Eagles. “Possible Pairing without Superconductivity at Low Carrier Concentrations in Bulk and Thin-Film Superconducting Semiconductors.” *Phys. Rev.* **186**(2) 456–463 (1969).
14. A. J. Leggett, Editor. *Modern Trends in the Theory of Condensed Matter*. Springer-Verlag, Berlin (1980).
15. R. A. Duine and H. T. C. Stoof. “Atom-molecule coherence in Bose gases.” *Phys. Rep.* **396** 115–195 (2004).
16. A. J. Moerdijk, B. J. Verhaar, and A. Axelsson. “Resonances in ultracold collisions of ^6Li , ^7Li , and ^{23}Na .” *Phys. Rev. A* **51**(6) 4852–4861 (1995).
17. K. E. Strecker, G. B. Partridge, A. G. Truscott, and R. G. Hulet. “Formation and Propagation of Matter Wave Soliton Trains.” *Nature* **417** 150–153 (2002).
18. K. E. Strecker, G. B. Partridge, and R. G. Hulet. “Conversion of an Atomic Fermi Gas to a Long-Lived Molecular Bose Gas.” *Phys. Rev. Lett.* **91**(8) 080406 (2003).

19. G. B. Partridge. *An Improved System for Creating Ultracold Fermi Gases of ^6Li* . Master's Thesis, Rice University (2003).
20. K. E. Strecker. *Sympathetic Cooling of a Bose/Fermi Mixture of Lithium to Quantum Degeneracy*. Master's Thesis, Rice University (2002).
21. K. E. Strecker. *Tunable Interactions in Quantum Degenerate Lithium*. Ph.D Thesis, Rice University (2004).
22. G. B. Partridge, K. E. Strecker, R.I. Kamar, M.W. Jack, and R. G. Hulet. "Molecular Probe of Pairing in the BEC-BCS Crossover." *Phys. Rev. Lett.* **95**(2) 020404–1–4 (2005).
23. G. B. Partridge, Wenhui Li, R. I. Kamar, Y. A. Liao, and R. G. Hulet. "Pairing and Phase Separation in a Polarized Fermi Gas." *Science* **311** 503–5 (2006).
24. G. B. Partridge, Wenhui Li, Y. A. Liao, R. G. Hulet, M. Haque, and H. T. C. Stoof. "Deformation of a Trapped Fermi Gas with Unequal Spin Populations." *Phys. Rev. Lett.* **97**(19) 190407 (2006).
25. B. Baysinger. *Semiconductor Laser System for Magneto-Optical Trapping of Fermionic ^6Li* .
26. J. Walls, R. Ashby, J.J. Clarke, B. Lu, and W.A. van Wijngaarden. "Measurement of Isotope Shifts, Fine and Hyperfine Structure Splittings of the Lithium D Lines." *Eur. Phys. J. D* **22**(2) 159–162 (2003).
27. W. I. McAlexander, E. R. I. Abraham, and R. G. Hulet. "Radiative Lifetime of the 2P State of Lithium." *Phys. Rev. A* **54**(1) R5 – R8 (1996).
28. M.-O. Mewes, M. R. Andrews, N. J. van Druten, D. M. Kurn, D. S. Durfee, and W. Ketterle. "Bose-Einstein Condensation in a Tightly Confining dc Magnetic Trap." *Phys. Rev. Lett.* **77**(3) 416–419 (1996).

29. C. Cohen-Tannoudji. *Cargese Lectures in Physics*. Gordon and Breach, London (1968).
30. J. Dalibard and C. Cohen-Tannoudji. “Dressed-atom approach to atomic motion in laser light: the dipole force revisited.” *J. Opt. Soc. Am. B* **2**(11) 1707–1720 (1985).
31. S. Reynaud and C. Cohen-Tannoudji. “Dressed-atom description of resonance fluorescence and absorption spectra of a multi-level atom in an intense laser beam.” *Journal of Physics B: Atomic and Molecular Physics* **10**(3) 1707–1720 (1977).
32. L. Khaykovich, F. Schreck, G. Ferrari, T. Bourdel, J. Cubizolles, L. D. Carr, Y. Castin, and C. Salomon. “Formation of a Matter-Wave Bright Soliton.” *Science* **296** 1290–1293 (2002).
33. M. W. Sasnett and T. J. Johnston. “Beam characterization and measurement of propagation attributes.” *Proc. SPIE, Laser Beam Diagnostics, Robert N. Hindy; Youssef Kohanzadeh; Eds.* **1414** 21 – 32 (1991).
34. K. M. O’Hara, S. R. Granade, M. E. Gehm, T. A. Savard, S. Bali, C. Freed, and J. E. Thomas. “Ultrastable CO₂ Laser Trapping of Lithium Fermions.” *Phys. Rev. Lett.* **81**(21) 4204 (1999).
35. J. Stenger, S. Inouye, M. R. Andrews, H.-J. Miesner, D. M. Stamper-Kurn, and W. Ketterle. “Strongly Enhanced Inelastic Collisions in a Bose-Einstein Condensate near Feshbach Resonances.” *Phys. Rev. Lett.* **82**(12) 2422–2425 (1999).
36. J. L. Roberts, N. R. Claussen, S. L. Cornish, and C. E. Wieman. “Magnetic Field Dependence of Ultracold Inelastic Collisions near a Feshbach Resonance.” *Phys. Rev. Lett.* **85**(4) 728–731 (2000).

37. T. Weber, J. Herbig, M. Mark, H-C. Nägerl, and R. Grimm. “Three-Body Recombination at Large Scattering Lengths in an Ultracold Atomic Gas.” *Phys. Rev. Lett.* **91**(12) 123201 (2003).
38. B. D. Esry, C. H. Greene, and H. Suno. “Threshold Laws for Three-body Recombination.” *Phys. Rev. A* **65**(1) 010705 (2001).
39. D. S. Petrov. “Three-body problem in Fermi gases with short-range interparticle interaction.” *Phys. Rev. A* **67**(1) 010703 (2003).
40. D. S. Petrov, C. Salomon, and G. V. Shlyapnikov. “Weakly Bound Dimers of Fermionic Atoms.” *Phys. Rev. Lett.* **93**(9) 090404–1–4 (2004).
41. L Luo, B Clancy, J Joseph, J Kinast, A Turlapov, and J E Thomas. “Evaporative cooling of unitary Fermi gas mixtures in optical traps.” *New J. Phys.* **8**(9) 213 (2006).
42. G. M. Bruun. “Universality of a two-component Fermi gas with a resonant interaction.” *Phys. Rev. A* **70** 053602–1–5 (2004).
43. S. De Palo, M. L. Chiofalo, M. J. Holland, and S. J. J. M. F. Kokkelmans. “Resonance effects on the crossover of bosonic to fermionic superfluidity.” *Phys. Lett. A* **327** 490–499 (2004).
44. R. B. Diener and T-L. Ho. “The Condition for Universality at Resonance and Direct Measurement of Pair Wavefunctions Using rf Spectroscopy.” *cond-mat/0405174* (2004).
45. S. Simonucci, P. Pieri, and G. C. Strinati. “Broad versus narrow Fano-Feshbach resonances in the BCS-BEC crossover with trapped Fermi atoms.” *Europhys. Lett.* **69**(5) 713–718 (2005).

- 46. M. Houbiers, H. T. C. Stoof, W. I. McAlexander, and R. G. Hulet. “Elastic and inelastic collisions of ^6Li atoms in magnetic and optical traps.” *Phys. Rev. A* **57**(3) R1497–1500 (1998).
- 47. M. Bartenstein, A. Altmeyer, S. Riedl, R. Geursen, S. Jochim, C. Chin, J. Hecker Denschlag, and R. Grimm. “Precise Determination of ^6Li Cold Collision Parameters by Radio-Frequency Spectroscopy of Weakly Bound Molecules.” *Phys. Rev. Lett.* **94**(10) 103201–1–4 (2005).
- 48. P. Julienne. Personal Communication w/ R. Hulet.
- 49. B. Marcelis, E. G. M. Van Kempen, B. J. Verhaar, and S. J. J. M. F. Kokkelmans. “Feshbach resonances with large background scattering length: Interplay with open-channel resonances.” *Phys. Rev. A* **70** 012701 (2004).
- 50. W. I. McAlexander. *Collisional Interaction in an Ultracold Lithium Gas*. Ph.d., Rice University (2000).
- 51. Eric R. I. Abraham, Nicholas W. M. Ritchie, W. Ian McAlexander, and R. G. Hulet. “Photoassociative Spectroscopy of Long-range States of Ultracold $^6\text{Li}_2$ and $^7\text{Li}_2$.” *J. of Chem. Phys.* **103**(18) 7773–7778 (1995).
- 52. C. J. Sansonetti, B. Richou, R. Engleman, and L. J. Radziemski. “Measurements of the resonance lines of ^6Li and ^7Li by Doppler-free frequency-modulation spectroscopy.” *Phys. Rev. A* **52** 2682 (1995).
- 53. I. D. Prodan, M. Pichler, M. Junker, and R. G. Hulet. “Intensity Dependence of Photoassociation in a Quantum Degenerate Atomic Gas.” *Phys. Rev. Lett.* **91**(8) 080402 (2003).
- 54. W. I. McAlexander. *Low Energy Collisional Interactions in Magnetically Trapped Lithium*. Ph.d., Rice University (2000).

55. R. I. Kamar. *Measurement of the Interactions in a Paired Zero Temperature ^6Li Gas Throughout the BEC-BCS Crossover*. Master's Thesis, Rice University (2006).
56. S. Jochim, M. Bartenstein, A. Altmeyer, G. Hendl, S. Riedl, C. Chin, J. Hecker Denschlag, and R. Grimm. "Bose-Einstein Condensation of Molecules." *Science* **302** 2101 (2003).
57. M. Greiner, C. A. Regal, and D. S. Jin. "Emergence of a Molecular Bose Einstein Condensate from a Fermi Gas." *Nature* **426** 537 (2003).
58. M. W. Zwierlein, C. A. Stan, C. H. Schunck, S. M. F. Raupach, S. Gupta, Z. Hadzibabic, and W. Ketterle. "Observation of Bose-Einstein Condensation of Molecules." *Phys. Rev. Lett.* **91**(25) 250401–1–4 (2003).
59. T. Bourdel, L. Khaykovich, J. Cubizolles, J. Zhang, F. Chevy, M. Teichmann, L. Tarruell, S. J. J. M. F. Kokkelmans, and C. Salomon. "Experimental Study of the BEC-BCS Crossover Region in Lithium 6." *Phys. Rev. Lett.* **93**(5) 050401–1 (2004).
60. G. E. Astrakharchik, J. Boronat, J. Casulleras, and S. Giorgini. "Equation of State of a Fermi Gas in the BEC-BCS Crossover: A Quantum Monte Carlo Study." *Phys. Rev. Lett.* **93**(20) 200404–1–4 (2004).
61. J. Stajic, Q. Chen, and K. Levin. "Particle density distributions in Fermi gas superfluids: Differences between one- and two-channel models in the Bose-Einstein-condensation limit." *Phys. Rev. A* **71**(3) 033601 (2005).
62. L. D. Carr, G. V. Shlyapnikov, and Y. Castin. "Achieving a BCS Transition in an Atomic Fermi Gas." *Phys. Rev. Lett.* **92**(15) 150404 (2004).

- 63. Q. Chen, J. Stajic, and K. Levin. “Thermodynamics of Interacting Fermions in Atomic Traps.” *Phys. Rev. Lett.* **95**(26) 260405 (2005).
- 64. J. E. Williams, N. Nygaard, and C. W. Clark. “Phase Diagrams for an Ideal Gas Mixture of Fermionic Atoms and Bosonic Molecules.” *New J. of Phys.* **6** 123 (2004).
- 65. M. Bartenstein, A. Altmeyer, S. Riedl, S. Jochim, C. Chin, J. Hecker Denschlag, and R. Grimm. “Crossover from a Molecular Bose-Einstein Condensate to a Degenerate Fermi Gas.” *Phys. Rev. Lett.* **92**(12) 120401–1–4 (2004).
- 66. V. Bagnato, D. E. Pritchard, and D. Kleppner. “Bose-Einstein Condensation in an External Potential.” *Phys. Rev. A* **35**(10) 4354–4358 (1987).
- 67. S. R. de Groot, G. J. Hooyman, and C. A. ten Seldam. “On the Bose-Einstein Condensation.” *Proceedings of the Royal Society of London. Series A, Mathematical and Physical Sciences* **203**(1073) 266 – 286 (1950).
- 68. G. M. Falco and H. T. C. Stoof. “Atom-molecule theory of broad Feshbach resonances.” *Phys. Rev. A* **71**(6) 063614 (2005).
- 69. Q. Chen and K. Levin. “Population of Closed-Channel Molecules in Trapped Fermi Gases with Broad Feshbach Resonances.” *Phys. Rev. Lett.* **95** 260406–1–4 (2005).
- 70. M. W. J. Romans and H. T. C. Stoof. “Dressed Feshbach Molecules in the BEC-BCS Crossover.” *Phys. Rev. Lett.* **95** 260407 (2005).
- 71. J. Javanainen, M. Kostrun, M. Mackie, and A. Carmichael. “Simple Mean-Field Theory for a Zero-Temperature Fermionic Gas at a Feshbach Resonance.” *Phys. Rev. Lett.* **95**(11) 110408 (2005).

72. J. R. Engelbrecht, M. Randeria, and C. A. R. S de Melo. “BCS to Bose crossover: Broken-symmetry state.” *Phys. Rev. B* **55**(22) 153–154 (1997).
73. H. Heiselberg. “Fermi systems with long scattering lengths.” *Phys. Rev. A* **63**(4) 043606 (2001).
74. G. A. Baker. “Neutron Matter Model.” *Phys. Rev. C* **60**(5) 054311 (1999).
75. Tin-Lun Ho. “Universal Thermodynamics of Degenerate Quantum Gases in the Unitarity Limit.” *Phys. Rev. Lett.* **92**(9) 090402 (2004).
76. R. Casalbuoni and G. Nardulli. “Inhomogeneous superconductivity in condensed matter and QCD.” *Rev. Mod. Phys.* **76**(1) 263–320 (2004).
77. A. M. Clogston. “Upper Limit for the Critical Field in Hard Superconductors.” *Phys. Rev. Lett.* **9**(6) 266–267 (1962).
78. G. Sarma. “On the Influence of a Uniform Exchange Field Acting on the Spins of the Conduction Electrons in a Superconductor.” *J. of Phys. Chem. Solids* **24** 1029–1032 (1963).
79. W. Vincent Liu and Frank Wilczek. “Interior Gap Superfluidity.” *Phys. Rev. Lett.* **90**(4) 047002–1–4 (2003).
80. H. Müther and A. Sedrakian. “Spontaneous Breaking of Rotational Symmetry in Superconductors.” *Phys. Rev. Lett.* **88**(25) 252503 (2002).
81. A. Sedrakian, J. Mur-Petit, A. Polls, and H. Müther. “Pairing in a two-component ultracold Fermi gas: Phases with broken-space symmetries.” *Phys. Rev. A* **72**(1) 013613–1–8 (2005).
82. P. Fulde and R A. Ferrell. “Superconductivity in a Strong Spin-Exchange Field.” *Phys. Rev.* **135** A550–A563 (1964).

83. A. I Larkin and Yu. N. Ovchinnikov. "Inhomogeneous State of Superconductors." *Soviet Physics JETP* **20**(3) 762–769 (1965).
84. P. F. Bedaque, H. Caldas, and G. Rupak. "Phase Separation in Asymmetrical Fermion Superfluids." *Phys. Rev. Lett.* **91**(24) 247002–1–4 (2003).
85. H. Caldas. "Cold Asymmetrical Fermion Superfluids." *Phys. Rev. A* **69**(6) 063602–1–12 (2004).
86. J. Carlson and S. Reddy. "Asymmetric Two-Component Fermion Systems in Strong Coupling." *Phys. Rev. Lett.* **95**(6) 060401–1–4 (2005).
87. Z-C. Gu, G. Warner, and F. Zhou. "Fermion pairing with population imbalance: energy landscape and phase separation in a constrained Hilbert subspace." *cond-mat/0603091* (2006).
88. Hui Hu and Xia-Ji Liu. "Mean-field phase diagrams of imbalanced Fermi gases near a Feshbach resonance." *Phys. Rev. A* **73**(5) 051603(R) (2006).
89. H. A. Radovan, N. A. Fortune, T. P. Murphy, S. T. Hannahs, E. C. Palm, S. W. Tozer, and D. Hall. "Magnetic enhancement of superconductivity from electron spin domains." *Nature* **425** 51–55 (2003).
90. K. Kakuyanagi, M. Saitoh, K. Kumagai, S. Takashima, M. Nohara, H. Takagi, and Y. Matsuda. "Texture in the Superconducting Order Parameter of CeCoIn₅ Revealed by Nuclear Magnetic Resonance." *Phys. Rev. Lett.* **94**(4) 047602–1–4 (2005).
91. A. Bianchi, R. Movshovich, C. Capan, P. G. Pagliuso, and J. L. Sarrao. "Possible Fulde-Ferrell-Larkin-Ovchinnikov Superconducting State in CeCoIn₅." *Phys. Rev. Lett.* **91**(18) 187004 (2003).

92. H. Won, K. Maki, S. Haas, N. Oeschler, F. Weickert, and P. Gegenwart. “Upper critical field and Fulde-Ferrell-Larkin-Ovchinnikov state in CeCoIn_5 .” *Phys. Rev. B* **69**(18) 180504 (2004).
93. V. F. Mitrovic, M. Horvatic, C. Berthier, G. Knebel, G. Lapertot, and J. Flouquet. “Observation of Spin Susceptibility Enhancement in the Possible Fulde-Ferrell-Larkin-Ovchinnikov State of CeCoIn_5 .” *Phys. Rev. Lett.* **97**(11) 117002 (2006).
94. B. L. Young, R. R. Urbano, N. J. Curro, J. D. Thompson, J. L. Sarrao, A. B. Vorontsov, and M. J. Graf. “Microscopic evidence for field-induced magnetism in CeCoIn_5 .” *Phys. Rev. Lett.* **98** 036402 (2007).
95. C. A. Regal, M. Greiner, and D. S. Jin. “Observation of Resonance Condensation of Fermionic Atom Pairs.” *Phys. Rev. Lett.* **92**(4) 040403–1–4 (2004).
96. M. W. Zwierlein, C. A. Stan, C. H. Schunck, S. M. F. Raupach, A. J. Kerman, and W. Ketterle. “Condensation of Pairs of Fermionic Atoms near a Feshbach Resonance.” *Phys. Rev. Lett.* **92**(12) 120403–1–4 (2004).
97. C. Chin, M. Bartenstein, A. Altmeyer, S. Riedl, S. Jochim, J. Hecker Denschlag, and R. Grimm. “Observation of the Pairing Gap in a Strongly Interacting Fermi Gas.” *Science* **305** 1128–1130 (2004).
98. J. Kinast, S. L. Hemmer, M. E. Gehm, A. Turlapov, and J. E. Thomas. “Evidence for Superfluidity in a Resonantly Interacting Fermi Gas.” *Phys. Rev. Lett.* **92**(15) 150402–1–4 (2004).
99. M. Bartenstein, A. Altmeyer, S. Riedl, S. Jochim, C. Chin, J. Hecker Denschlag, and R. Grimm. “Collective Excitations of a Degenerate Gas at the BEC-BCS Crossover.” *Phys. Rev. Lett.* **92**(30) 203201–1–4 (2004).

100. M. W. Zwierlein, J. R. Abo-Shaeer, A. Schirotzek, C. H. Schunck, and W. Ketterle. "Vortices and superfluidity in a strongly interacting Fermi gas." *Nature* **435** 1047–1051 (2005).
101. M. W. Zwierlein, A. Schirotzek, C. H. Schunck, and W. Ketterle. "Fermionic Superfluidity with Imbalanced Spin Populations." *Science* **311** 492 (2006).
102. M. W. Zwierlein, C. H. Schunck, A. Schirotzek, and W. Ketterle. "Direct Observation of the Superfluid Phase Transition in Ultracold Fermi Gases." *Nature* **442**(7098) 54–58 (2006).
103. Y. Shin, M. W. Zwierlein, C. H. Schunck, A. Schirotzek, and W. Ketterle. "Observation of Phase Separation in a Strongly-Interacting Imbalanced Fermi Gas." *Phys. Rev. Lett.* **97** 030401–1–4 (2006).
104. M. Houbiers, H. T. C. Stoof, W. I. McAlexander, and R. G. Hulet. "Elastic and inelastic collisions of ^6Li atoms in magnetic and optical traps." *Phys. Rev. A* **57**(3) R1497–1500 (1998).
105. D. A. Butts and D. S. Rokhsar. "Trapped Fermi gases." *Phys. Rev. A* **55**(6) 4346 (1997).
106. M. E. Gehm, S. L. Hemmer, S. R. Granade, K. M. O'Hara, and J. E. Thomas. "Mechanical stability of a strongly interacting Fermi gas of atoms." *Phys. Rev. A* **68**(1) 011401–1–4 (2003).
107. A. Perali, P. Pieri, and G. C. Strinati. "Quantitative Comparison between Theoretical Predictions and Experimental Results for the BCS-BEC Crossover." *Phys. Rev. Lett.* **93**(10) 100404–1–4 (2004).
108. K. M. O'Hara, S. L. Hemmer, M. E. Gehm, S. R. Granade, and J. E. Thomas.

- “Observation of a Strongly Interacting Degenerate Fermi Gas of Atoms.” *Science* **298** 2179–2182 (2002).
109. J. Carlson, S.-Y. Chang, V. R. Pandharipande, and K. E. Schmidt. “Superfluid Fermi Gases with Large Scattering Length.” *Phys. Rev. Lett.* **91**(5) 050401–1–4 (2003).
 110. J. Kinast, A. Turlapov, J. E. Thomas, Q. Chen, J. Stajic, and K. Levin. “Heat Capacity of a Strongly Interacting Fermi Gas.” *Science* **307** 1296–1299 (2005).
 111. J. T. Stewart, J. P. Gaebler, C. A. Regal, and D. S. Jin. “Potential Energy of a ^{40}K Fermi Gas in the BCS-BEC Crossover.” *Phys. Rev. Lett.* **97**(22) 220406 (2006).
 112. L. Viverit, C. J. Pethick, and H. Smith. “Zero-temperature phase diagram of binary boson-fermion mixtures.” *Phys. Rev. A* **61**(5) 053605–1–8 (2000).
 113. L. Montgomery Smith, D. R. Keefer, and S. I. Sudharsanan. “Abel Inversion Using Transform Techniques.” *J. Quant. Spectrosc. Radiat. Transfer* **39**(5) 367–373 (1988).
 114. C-C. Chien, Q. Chen, Y. He, and K. Levin. “Superfluid Phase Diagrams of Trapped Fermi Gases with Population Imbalance.” *cond-mat/0612103* (2006).
 115. K. B. Gubbels, M. W. J. Romans, and H. T. C. Stoof. “Sarma Phase in Trapped Unbalanced Fermi Gases.” *cond-mat/0606330* (2006).
 116. T. N. De Silva and E. J. Mueller. “Profiles of near-resonant population-imbalanced trapped Fermi gases.” *Phys. Rev. A* **73**(5) 051602(R) (2006).
 117. P. Pieri and G. C. Strinati. “Trapped Fermions with Density Imbalance in the Bose-Einstein Condensate Limit.” *Phys. Rev. Lett.* **96**(15) 150404–1–4 (2006).

118. W. Yi and L.-M. Duan. "Trapped fermions across a Feshbach resonance with population imbalance." *Phys. Rev. A* **73** 031604(R) (2006).
119. F. Chevy. "Density Profile of a Trapped Strongly Interacting Fermi Gas with Unbalanced Spin Populations." *Phys. Rev. Lett.* **96**(13) 130401–1–4 (2006).
120. C.-H. Pao and S.-K. Yip. "Asymmetric Fermi superfluid in a harmonic trap." *J. Phys.: Condens. Matter* **18**(23) 5567–5577 (2006).
121. C.-C. Chien, Q. Chen, Y. He, and K. Levin. "Finite Temperature Effects in Trapped Fermi Gases with Population Imbalance." *Phys. Rev. A* **74** 021602(R) (2006).
122. M. Haque and H. T. C. Stoof. "Pairing of a trapped resonantly-interacting fermion mixture with unequal spin populations." *Phys. Rev. A* **74** 011602(R) (2006).
123. C. J. Pethick and H. Smith. *BoseEinstein Condensation in Dilute Gases*. Cambridge University Press, Cambridge (2002).
124. A. Imambekov, C. J. Bolech, M. Lukin, and E. Demler. "Breakdown of the Local Density Approximation in Interacting Systems of Cold Fermions in Strongly Anisotropic Traps." *cond-mat/0604423* (2006).
125. T. N. De Silva and E. J. Mueller. "Surface tension in population imbalanced unitary Fermi gases." *Phys Rev Lett* **97** 070402 (2006).
126. M. Haque and H. T. C. Stoof. "Spatial Distortion of Trapped Fermi Gases." *cond-mat/0701464* (2007).
127. M. Houbiers, R. Ferwerda, H. T. C. Stoof, W. I. McAlexander, C. A. Sackett, and R. G. Hulet. "The Superfluid State of Atomic ^6Li in a Magnetic Trap." *Phys. Rev. A* **56**(6) 4864–4878 (1997).

128. G. M. Falco and H. T. C. Stoof. “Crossover Temperature of Bose-Einstein Condensation in an Atomic Fermi Gas.” *Phys. Rev. Lett.* **92**(13) 130401–1–4 (2004).
129. A. Bulgac, J. E. Drut, and P. Magierski. “Spin 1/2 Fermions in the Unitary Regime: A Superfluid of a New Type.” *Phys. Rev. Lett.* **96**(9) 090404 (2006).
130. E. Burovski, N. Prokof’ev, B. Svistunov, and M. Troyer. “Critical Temperature and Thermodynamics of Attractive Fermions at Unitarity.” *Phys. Rev. Lett.* **96**(16) 160402 (2006).
131. L. Luo, B. Clancy, J. Joseph, J. Kinast, and J. E. Thomas. “Measurement of the Entropy and Critical Temperature of a Strongly Interacting Fermi Gas.” *Phys. Rev. Lett.* **98**(8) 080402 (2007).
132. J. Stajic, Q. Chen, and K. Levin. “Density Profiles of Strongly Interacting Trapped Fermi Gases.” *Phys. Rev. Lett.* **94**(6) 060401 (2005).
133. R. Combescot and C. Mora. “The low-temperature Fulde-Ferrell-Larkin-Ovchinnikov phases in 3 dimensions.” *Europhys. Letters* **68**(1) 79–85 (2004).
134. M. M. Parish, F. M. Marchetti, A. Lamacraft, and B. D. Simons. “Finite temperature phase diagram of a polarised Fermi condensate.” *cond-mat/0605744* (2006).
135. K. Machida, T. Mizushima, and M. Ichioka. “Generic Phase Diagram of Fermion Superfluids with Population Imbalance.” *Phys. Rev. Lett.* **97**(12) 120407 (2006).
136. D. E. Sheehy and L. Radzihovsky. “BEC-BCS Crossover in ”Magnetized” Feshbach-Resonantly Paired Superfluids.” *Phys. Rev. Lett.* **96** 060401–1–4 (2006).

137. S. Inouye, M. R. Andrews, J. Stenger, H.-J. Miesner, D. M. Stamper-Kurn, and W. Ketterle. "Observation of Feshbach resonances in a Bose-Einstein condensate." *Nature* **392** 151 (1998).
138. J. M. Kinast. *Thermodynamics and Superfluidity of a Strongly Interacting Fermi Gas*. Ph.D Thesis, Duke University (2006).
139. I. P. Kaminow. *An Introduction to Electro-Optic Devices*. Academic Press, Inc., U.S. (1974).
140. F. E. Terman. *Radio Engineering*. McGraw-Hill Book Company, Inc., New York and London (1937).